

Linear amplification analysis for extraction of coherent structures in wall-bounded turbulent flows



Vikrant Gupta

Department of Engineering
University of Cambridge

This dissertation is submitted for the degree of
Doctor of Philosophy

Fitzwilliam College

July 2014

I would like to dedicate this thesis to the memory of my grand parents.

Declaration

I hereby declare that except where specific reference is made to the work of others, the contents of this dissertation are original and have not been submitted in whole or in part for consideration for any other degree or qualification in this, or any other University. This dissertation is the result of my own work and includes nothing which is the outcome of work done in collaboration, except where specifically indicated in the text. This dissertation contains less than 65000 words including appendices, bibliography, footnotes, tables and equations and has less than 150 figures.

Vikrant Gupta
July 2014

Acknowledgements

I would like to express my gratitude to my supervisor Dr. Matthew Juniper for his guidance and providing me freedom to pursue research in turbulence. I would also like to thank him for patiently teaching me how to write in correct and easy to understand English. I am very grateful to Rolls Royce and EPSRC for funding me through Dorothy Hodgkin Postgraduate award and to ERC for the extended funding. I would like to thank to Ford of Britain Trust for travel grants to pay for my conference expenses and to Fitzwilliam college for extra assistance through E. D. Davies Scholarship.

I am very grateful to all the academics I had chance to meet during my PhD. I would particularly like to acknowledge Dr. Ricardo Garcia-Mayoral, Dr. Will Bainbridge, and Dr. Yongyun Hwang. I am also fortunate to get to work with many people during my PhD. Their knowledge and way of thinking helped me a lot to grow as a researcher. For that I acknowledge Mr. Tifenn Brandily, Mr. Hannes Brauckmann, Mr. Mike Simpson, and Mr. Ali Ersoz. I am also very grateful to my thesis examiners Dr. Ati Sharma and Prof. Stewart Cant, whose inputs had been most useful.

I would like to acknowledge my colleagues and friends Outi, Ubaid, and Rao, with whom I had many fun and intensive discussions in fluid mechanics. I recognise the support of my friends who made the stay in Cambridge fun. Most of all I thank my housemate Giulio, then I thank my dear friends Karthik, Simon, Irene, Ale, Pau, Chris, Luca, John, Florian, Rao, Ubaid, Outi, Tifenn, and Iain. I would like to specifically acknowledge the support and help of Larry, he had been very kind to book shared double rooms during the conferences so that I could get free accommodations.

In the end I would like to thank my parents and sisters. Their biggest concern had been when will I finish my PhD studies and get a job. It helped me keep focus.

Abstract

Coherent structures in turbulent flows provide a means of understanding turbulence in terms of large organised motions. Understanding the mechanism of formation of coherent structures can be helpful in suppressing or enhancing the turbulence in a flow by means of active or passive control devices. Knowledge of the Reynolds number scaling of the size and energy content of coherent structures can extend the knowledge to high Reynolds number flows, which are out of reach of the present computational and experimental facilities.

In this thesis, linear amplification and eigenvalue stability analyses are performed by linearising the Navier–Stokes or Reynolds-averaged Navier–Stokes (RANS) equations over the mean flow profiles in several wall-bounded turbulent shear flows. It is investigated whether the linear optimal modes or the leading eigenmodes approximate the coherent structures in fully nonlinear turbulent flows. This is done by comparing various kinematic properties of the optimal modes, such as the shape and energy spectra, with those of the observed coherent structures in turbulent channel and pipe flows in the first half of the thesis.

The use of the linearised Navier–Stokes equations in the regions of high mean shear in the flows is justified based on rapid distortion theory. In the linearised RANS equations-based analysis, turbulence models are used to account for the effect of wave-induced perturbations in the Reynolds stress on the behaviour of small external wave motions. The turbulence models used in this thesis are the eddy viscosity model (EVM) and the explicit algebraic Reynolds stress model (EARSIM). The focus of this thesis is to investigate whether this effect of wave-induced perturbations in the Reynolds stress needs to be included in stability analysis of wall-bounded turbulent flows.

The linear amplification analysis based on the Navier–Stokes equations finds three main types of structures in turbulent channel flows. The first type are the small streamwise wavelength ($\lambda_x^+ = 200 - 800$) structures, which are found to scale in inner units and have preferred spanwise wavelength equal to around one hundred wall-units. These properties match well with those of observed near-wall structures. The second type are the intermediate streamwise wavelengths (from $\lambda_x^+ > 800$ to $\lambda_x < 3$) structures which correspond to hairpin vortical and large-scale streaky like structures. The peak in energy amplification in

this wavelength range found from the analysis matches well with that from DNS. Various kinematic properties, such as the inclination angle of streaks with the wall, also match with those of large-scale-motions (LSMs) observed in experiments. The third type are the large streamwise wavelength ($\lambda_x \geq 6$) structures. The preferred spanwise wavelength of these structures ($\lambda_z|_{peak} \approx 2$), their scaling in outer units, and the fact that they extend to the wall match with the observed features of very-large-scale-motions (VLSMs). All these results show that the most optimal modes obtained from the linearised Navier–Stokes equations, without any turbulence model or eddy viscosity, share many important features with those of observed coherent structures in turbulent channel flows.

In comparison, the results from the EVM- and EARSM-based linear amplification analyses find only two types of coherent structures. One type are of the small wavelengths, which correspond to the near-wall structures, and the other type are of the large wavelengths, which correspond to the VLSMs. These analyses, however, find minima in energy spectra in the intermediate wavelength region, where DNS and the Navier–Stokes equations-based analysis find maxima in energy spectra.

In axially rotating turbulent pipe flows, it is found from the linearised Navier–Stokes equations-based analysis that rotation causes the widening of streaks and prevents the formation of quasi-streamwise vortices. These results match well with observations from DNS, which further shows the usefulness of the linearised Navier–Stokes equations.

In the second part of the thesis, stability analyses based on the linearised Navier–Stokes and RANS equations are applied in more complex flows. Based on the results from the stability analyses for flows in gas-turbine systems, it is found that for such flows the inclusion of turbulence models in stability analysis has no significant qualitative effect on the results. This is because these instabilities are driven by regions of high mean shear for which analysis based on the linearised Navier–Stokes equations is sufficient. It is also found from stability analysis that an expansion at the nozzle exit and swirl in the flow are destabilising, and therefore increase hydrodynamic instability.

Based on the preliminary comparisons of stability results and observations from DNS in Taylor-Couette flows, it is again concluded that the linearised Navier–Stokes equations-based analysis is better at capturing intermittent coherent structures as compared to the linearised RANS equations-based analysis.

It is concluded in this thesis that the linearised Navier–Stokes equations-based analysis, which does not require any turbulence model, can be used to find information about coherent structures in high mean shear flows, such as the flows in gas-turbine fuel-injectors or wall-bounded turbulent flows.

Contents

Contents	xi
List of Figures	xv
List of Tables	xxxiii
Nomenclature	xxxiii
1 Introduction	1
1.1 Coherent structures in turbulent shear flows	2
1.2 Simplified approaches for extraction of coherent structures	3
1.2.1 Exact solutions of Navier–Stokes equations	3
1.2.2 Input-output analysis	4
1.2.3 Energy amplification analysis	4
1.3 Relevance to gas-turbines and general scope	6
1.4 Thesis structure	6
2 Extraction of coherent structures in turbulent channel flow from linear amplification analysis	9
2.1 Introduction	9
2.1.1 Relation with other linear amplification approaches	12
2.1.2 Complimentary simplified approaches	17
2.1.3 Outline	18
2.2 Methodology for calculation of transient growth in turbulent channel flow .	18
2.3 Non-modal amplification analysis at small wavelengths	20
2.3.1 Optimal modes and near-wall structures	22
2.4 Non-modal amplification analysis at higher wavelengths	24
2.4.1 Intermediate wavelength optimal modes	26

2.4.2	Transition range optimal modes	31
2.4.3	Large wavelength optimal modes	31
2.5	Summary and Conclusion	35
3	RANS-based linear amplification analysis	39
3.1	Introduction	39
3.1.1	Outline	41
3.2	Linearised RANS equations	41
3.2.1	Frozen eddy viscosity models	42
3.2.2	Full eddy viscosity models	43
3.2.3	Frozen explicit algebraic Reynolds stress model	44
3.3	Turbulent channel flow	45
3.4	Linearised RANS-based amplification analysis	48
3.4.1	Optimal mode shapes	51
3.5	RANS-based linearised equations to find coherent structures	56
3.6	Summary and conclusion	62
4	Effect of axial rotation on near-wall structures in turbulent pipe flow	65
4.1	Introduction	65
4.1.1	Regeneration cycle of near-wall structures and chapter outline . . .	67
4.2	Pipe flow	67
4.3	Formation of near-wall streaks from quasi-streamwise vortices	69
4.3.1	The $R_o = 0$ and $R_o = 0.5$ cases	71
4.3.2	Artificial velocity profiles	78
4.4	Breakdown of near-wall streaks	81
4.4.1	The non-rotating case and the cases with small artificial rotation . .	84
4.4.2	The $R_o = 0.5$ case and the cases with artificially reduced rotation . .	87
4.5	Summary and Conclusion	87
5	Hydrodynamic instabilities in gas turbine combustors	91
5.1	Introduction	91
5.1.1	Outline	94
5.2	Effects of turbulence models and compressibility in stability analysis of gas-turbine flows	94
5.2.1	Results	98
5.2.2	Conclusion	101

5.3	Stability results with RANS data as input	102
5.4	Effect of change in operating conditions on the instabilities in the S series .	104
5.4.1	Hydrodynamic instabilities in case-B and case-C	106
5.5	Effect of small design modifications on hydrodynamic instabilities	107
5.5.1	Main instability modes in the T series	109
5.6	Conclusions	109
6	Global stability analysis of turbulent Taylor-Couette flow	113
6.1	Introduction	113
6.2	Definitions and problem formulation	115
6.2.1	The linearised Navier–Stokes equations	116
6.2.2	Anisotropic eddy viscosity augmented linearised equations	120
6.3	Numerical details and the cases studied	122
6.4	Stability results for the $\mu = 0$ flow cases	124
6.5	Stability results for the $Re_s = 1733$ flow cases	135
6.6	Summary and further work	148
7	Conclusions	151
7.1	Summary of the work completed	151
7.2	Main conclusions	155
7.3	Further work	155
	References	157
	Appendix A Linear perturbation equations for secondary instability	167

List of Figures

- 2.1 The maximum transient growth, G_{max} , as a function of the spanwise (λ_z^+) and streamwise (λ_x^+) wavelengths. The peaks in G_{max} are at $\lambda_z^+ \approx 100$ for the $\lambda_x^+ = 250 - 800$ perturbations. For higher λ_x^+ perturbations the peaks are not at $\lambda_z^+ \approx 100$, but are at much higher λ_z^+ values. At the $\lambda_x = \infty$, the peak is at the $\lambda_z^+ = 540$, as reported in Ref. [1]. 13

- 2.2 The maximum transient growth, G_{max} , as a function of the spanwise (λ_z) and streamwise (λ_x) wavelengths calculated from the eddy viscosity based approach for the flow profiles (a) $Re_\tau = 2000$ from the empirical expression in Ref. [2] and (b) $Re_\tau = 2003$ from the DNS in Ref. [3]. The top axis is the spanwise wavelength in outer units (λ_z) and the bottom axis is the spanwise wavelength in inner units (λ_z^+), and the arrow is in the direction of increasing λ_x . The results in the two cases are very similar. This approach finds two peaks in G_{max} , one at $\lambda_z^+ \approx 100$, which corresponds to near-wall streaks, and the other at $\lambda_z \approx 2 - 4$, which corresponds to VLSMs, as mentioned in [2]. The main disadvantage of this approach is that it finds minima in energy amplification at the intermediate spanwise wavelengths, between $\lambda_z^+ \approx 100$ and $\lambda_z = 2$, where DNS show a peak in energy spectra [4]. Another smaller disadvantage of this approach is that it finds the optimal structures to be streamwise uniform (i.e. the $\lambda_x = \infty$) [4, 5]. 16

- 2.3 The maximum transient growth, G_{max} , as a function of the spanwise wavelength (λ_z^+) for the (a) $Re_\tau = 934$, (b) $Re_\tau = 2003$, and (c) $Re_\tau = 4079$ flow cases. The peaks in G_{max} are at $\lambda_z^+ \approx 100$, which is in agreement with the observations on the near-wall streaks spacing. The peak spanwise wavelength value, $\lambda_z^+|_{peak}$, increases with increasing λ_x . The values of G_{max} and $\lambda_z^+|_{peak}$ scale in wall units. 21

- 2.4 Amplitude of velocity components of the optimal modes at the $\lambda_x^+ = 400$ and $\lambda_z^+ = 90$. (a) The initial optimal modes are vortical structures like near-wall quasi-streamwise vortices, and (b) the final optimal modes are streaky structures like near-wall streamwise streaks. The shape of the optimal modes, represented by their velocity amplitudes, scale in wall units. . . . 22
- 2.5 Results for the $\lambda_x^+ = 400$ and $\lambda_z^+|_{peak} = 90$ in the $Re_\tau = 2003$ flow case. (a) The initial optimal mode in the $y-z$ plane, it has a vortical structure like that of near-wall quasi-streamwise vortices. (b) The final optimal mode in the $x-y$ plane (the y -axis is twice magnified). Regions with the positive streamwise velocity have the negative wall-normal velocity and vice-versa, so they belong to the Q4 and Q2 events. Here Q2 and Q4 refers to 2nd and 4th quadrants, respectively, of fluctuating u and v phase plots. 23
- 2.6 The maximum transient growth, G_{max} , at the higher wavelengths for the flows at (a) $Re_\tau = 934$, (b) $Re_\tau = 2003$, and (c) $Re_\tau = 4079$. the value of $\lambda_z|_{peak}$ varies from the intermediate wavelengths (from $\lambda_z^+ = 450$ to $\lambda_z = 1.5$) to the large wavelengths ($\lambda_z \approx 2$) depending upon the input λ_x . The value of $\lambda_z|_{peak}$ increases with increasing λ_x . The present analysis finds peaks in G_{max} at the intermediate wavelengths, while the EVM based analysis finds only minima in G_{max} at these intermediate wavelengths. The DNS data for turbulent channel flows shows peak in the energy spectra at these intermediate wavelength, which is in agreement with the present analysis. . . . 25
- 2.7 The preferred spanwise wavelength ($\lambda_z|_{peak}$) as functions of the input streamwise wavelength in (a) inner units and (b) outer units. Frame (b) shows that there is a jump in the value of $\lambda_z|_{peak}$ at $\lambda_x \approx 3$, after which $\lambda_z|_{peak}$ scales nearly in outer units. The jump region is indicated by dashed lines, and corresponding λ_x matches well with the threshold wavelength used in Ref. [6] for differentiating between the LSMs and VLSMs. The region before the jump does not scale in either inner or outer units, except an initial part which scales in inner units. 26

- 2.8 The normalised velocity amplitudes of the (a) initial and (b) final optimal modes at the $\lambda_x^+ = 1500$ and the corresponding $\lambda_z^+|_{peak}$, for the $Re_\tau = 934$ (dashed line), 2003 (solid line), and 4079 (squares) flow cases. The black colour is for the streamwise velocity component, grey is for the wall-normal velocity component and light-grey is for the azimuthal velocity component. These modes have similarities with the optimal modes shown in figure 2.4 and 2.9. The initial optimal modes, which have most of their energy in the spanwise velocity and have significant energy in the wall-normal velocity, are like vortical structures. The final optimal modes have most of their energy in the streamwise velocity like streaky structures. These modes extend to the wall but are dominant in the outer layer. 27
- 2.9 The normalised velocity amplitudes of the (a) initial and (b) final optimal modes at the $\lambda_x = 2$ and the corresponding $\lambda_z|_{peak}$, for the $Re_\tau = 934$ (dashed line), 2003 (solid line), and 4079 (squares) flow cases. These modes have similarities with the optimal modes shown in figures 2.4 and 2.8. The initial optimal modes, which have most of their energy in the spanwise velocity and have significant energy in the wall-normal velocity, are like vortical structures. The final optimal modes have most of their energy in the streamwise velocity like streaky structures. These modes extend to the wall but are dominant in the outer layer. 28
- 2.10 The $y^+|_{dominant}$ as functions of (a) λ_z^+ and (b) λ_x^+ . These plots show that structures get wider and longer as they move away from the wall. 29
- 2.11 Quiver plot of the final optimal mode at the $\lambda_x = 2$ and the corresponding $\lambda_z|_{peak} = 0.55$ in the $Re_\tau = 2003$ flow case in the $x - y$ plane. This plot shows that the mode contains packets of Q2 and Q4 events, which is observed in Ref. [7] for the streaky structures. The Q2 and Q4 events contribute towards the negative \overline{uv} -Reynolds stress component. 29
- 2.12 Low speed streaky regions in the final optimal modes at the (a) $\lambda_x^+ = 1500$ and (b) $\lambda_x = 2$ and the corresponding $\lambda_z|_{peak}$ in the $Re_\tau = 2003$ flow case are shown. The maximum amplitude ($= -0.5$) is arbitrarily decided to be one-sixth of the maximum amplitude in the final optimal mode. Inclination angles of the streaks with the wall are shown by the red dashed line, which are based on visualisation alone. The inclination of the streak in the $\lambda_x = 2$ optimal mode is close to the inclination of the $\Delta x \approx 2.5$ low-speed streak observed in Ref. [7]. 30

- 2.13 Velocity amplitudes of the (a) initial and (b) final optimal modes at the $\lambda_x = 4$ and the corresponding $\lambda_z|_{peak}$. (c) magnification of the near wall region, indicated by a square box in frame (b). The mode shapes are close to those of the optimal modes in the intermediate wavelength range. However, unlike those mode shapes, these structures do not extend to the wall as shown for the final optimal mode in frame (c). The mode shapes nearly scales in outer units like the VLSMs. 32
- 2.14 Velocity amplitudes of the (a) initial and (b) final optimal modes at the $\lambda_x = 20$ and the corresponding $\lambda_z|_{peak}$. (c) magnification of the near wall region, indicated by a square box in frame (b). The mode shapes scale closely in outer units, and extend to the wall. These are properties of the VLSMs. The velocity amplitude, however, is maximum at $y \approx 0.5$ while the VLSMs have most energy at the $y \approx 0.2$ 33
- 2.15 Velocity amplitudes of the (a) initial and (b) final optimal modes at the $\lambda_x = 20$ and the corresponding $\lambda_z|_{peak} = 3.4$ in the $Re_\tau = 2000$ (squares) and $Re_\tau = 2003$ (solid line) flow cases calculated from the eddy viscosity based approach. Although $\lambda_z|_{peak}$ is higher than the observed spanwise extent of the VLSMs, the wall-normal energy distribution in the final optimal mode closely matches with that of the VLSMs. The final optimal modes have most of their energy in the logarithmic layer, with maxima at $y \approx 0.3$, which matches well with the observation that the VLSMs are most energetic at $y \approx 0.2$ 34
- 2.16 The preferred λ_z corresponding to the various λ_x values from the present analysis (black dots) and the EVM-based analysis (red diamonds) in the $Re_\tau = 2003$ flow case are shown. For some λ_x values there are two points. This is because there are two peaks in G_{max} at those λ_x perturbations as shown in figure 2.2 (b). The dashed magenta line is for the streamwise velocity energy spectra in the near-wall region in Jimenez *et al.* (2004) [8]. The dashed blue line is for the streamwise velocity energy spectra in the $y = 0.1 - 0.3$ region in Jimenez & Hoyas (2008) [9] (the relation is known up to a constant of proportionality). The biggest drawback in the EVM-based analysis is that there are no red squares in the intermediate λ_z region. This is the range of the wavelengths where the LSMs are observed. The black dots from the present analysis show that they are in a good match with the slope of the blue line. 37

- 3.1 The Reynolds stress components estimated from the (a–d) EVM and (e–h) EARSM for the $Re_\tau = 934$ flow case. The solid lines are from the DNS data and the dashed lines are from the models. The EVM, by definition, is accurate at estimating the $\overline{u'v'}$ -component, but the EARSM is better at estimating all the other components. The error in the models is higher in the near-wall region, this is because all turbulence models are inaccurate in the near-wall region. 47
- 3.2 The maximum transient growth, G_{max} , in the three flow cases, (a, d) $Re_\tau = 180$, (b, e) $Re_\tau = 934$, and (c, f) $Re_\tau = 2003$, calculated from the (a–c) EVM- and (d–f) EARSM-based analyses are shown as functions of λ_x and λ_z . The top and bottom axes show the spanwise wavelengths in outer (λ_z) and inner (λ_z^+) units, respectively. The different lines in each frame correspond to the different λ_x perturbations, and the arrows indicate the direction of increase in λ_x . The most important feature in these plots is that there are two peaks in the G_{max} in all the cases. A primary peak at the higher λ_z values, which scales in outer units, and a secondary peak at the smaller λ_z^+ values, which scales in inner units. These results are similar to the results in Refs. [2, 10], where the optimal structures corresponding to the primary peak are compared with very-large-scale-motions (VLSMs) and the optimal structures corresponding to the secondary peak are compared with near-wall structures. 50
- 3.3 The normalised amplitudes of velocities in the initial and final optimal modes at the (a, b) $\lambda_x^+ = 400$ and $\lambda_z^+ = 85$ calculated from the EVM-based analysis, and at the (c, d) $\lambda_x^+ = 400$ and $\lambda_z^+ = 180$ calculated from the EARSM-based analysis. The dashed lines, solid lines, and squares correspond to the $Re_\tau = 180$, 934, and 2003 flows, respectively. The black, grey, and light-grey colours correspond to the streamwise, wall-normal, and azimuthal velocities, respectively. The shape of these modes show that they scale in inner units, except the streamwise velocity component in the initial optimal mode from the EARSM-based analysis in frame (c). The shapes of the optimal modes from the EVM- and EARSM-based analyses match with each other. The only noticeable difference is in the streamwise velocity component in the initial optimal modes. The shapes of the wall-normal velocity in the initial modes and the streamwise velocity in the final modes match well with those shown in figures 5(a) and (b), respectively, in Pujals *et al.* (2009) [2]. 53

- 3.4 Results for the $\lambda_x^+ = 400$ and $\lambda_z^+ = 85$ in the $Re_\tau = 180$ flow case from the EVM-based analysis. (a) The initial optimal mode is shown in the $Y^+ - Z^+$ plane, it has a vortical structure like that of near-wall quasi-streamwise vortices. (b) The final optimal mode is shown in the $X^+ - Y^+$ plane (the Y^+ -axis is twice magnified). The streaky structures with the positive stream-wise velocity have the negative wall-normal velocity and vice-versa. 54
- 3.5 Results for the $\lambda_x^+ = 400$ and $\lambda_z^+ = 180$ in the $Re_\tau = 180$ flow case from the EARSMS-based analysis. (a) The initial optimal mode is shown in the $Y^+ - Z^+$ plane, it has a vortical structure like that of near-wall quasi-streamwise vortices. (b) The final optimal mode is shown in the $X^+ - Y^+$ plane (the Y^+ -axis is twice magnified). The streaky structures with the positive stream-wise velocity have the negative wall-normal velocity and vice-versa. 55
- 3.6 The normalised amplitudes of velocities in the initial and final optimal modes at the (a, b) $\lambda_x = 20$ and $\lambda_z \approx 3.4$ calculated from the EVM-based analysis, and at the (c, d) $\lambda_x = 20$ and $\lambda_z \approx 4.25$ calculated from the EARSMS-based analysis. The dashed lines, solid lines, and squares correspond to the $Re_\tau = 180, 934$, and 2003 flows, respectively. The black, grey, and light-grey colours correspond to the streamwise, wall-normal, and azimuthal velocities, respectively. The shape of these modes show that they scale well in outer units, and that the shapes from the EVM- and EARSMS-based analyses also match with each other. The shapes of the wall-normal velocity in the initial modes and the streamwise velocity in the final modes from both the analyses match well with those shown in figures 5(c) and (d), respectively, in Pujals *et al.* (2009) [2]. 57
- 3.7 The normalised eigenvalue spectra in the $Re_\tau = 2003$ flow case for the $\lambda_x^+ = 400$ and $\lambda_z^+ = 85$ perturbations calculated from the (a, c) MV- and (b, d) EVM-based analyses. The top plots show a few leading eigenvalues with the $0.95 \leq \omega_{rs} \leq 1.05$, and the bottom plots show almost the complete spectra. These figures show that the EVM-based analysis not only damps the eigenvalues significantly, but also scatter them away from $\omega_{rs} = 1$. As a consequence fewer eigenvectors contribute in the formation of coherent structures. 59

- 3.8 The normalised eigenvalue spectra in the $Re_\tau = 2003$ flow case for the $\lambda_x = 2$ and $\lambda_z = 0.75$ perturbations calculated from the (a, c) MV- and (b, d) EVM-based analyses. The top plots show a few leading eigenvalues with the $0.95 \leq \omega_{rs} \leq 1.05$, and the bottom plots show almost the complete spectra. These figures show that the EVM-based analysis not only damps the eigenvalues significantly, but also scatter them away from $\omega_{rs} = 1$. The frame (d) shows that in the EVM-based analysis, the eigenvalues are divided into two regions based on their growth rate. There are significantly fewer eigenvalues in frame (b) as compared to those in the frame (a), which means that in the EVM-based analysis fewer eigenvectors contribute in the formation of coherent structures. 60
- 3.9 The normalised eigenvalue spectra in the $Re_\tau = 2003$ flow case for the $\lambda_x = 20$ and $\lambda_z = 3$ perturbations calculated from the (a, c) MV- and (b, d) EVM-based analyses. The top plots show a few leading eigenvalues with the $0.95 \leq \omega_{rs} \leq 1.05$, and the bottom plots show almost the complete spectra. These figures show that the EVM-based analysis not only damps the eigenvalues significantly, but also scatter them away from $\omega_{rs} = 1$. The frame (d) shows that in the EVM-based analysis, the eigenvalues are divided into two regions based on their growth rate. There are significantly fewer eigenvalues in frame (b) as compared to those in the frame (a), which means that in the EVM-based analysis fewer eigenvectors contribute in the formation of coherent structures. 61
- 4.1 The regeneration cycle of near-wall structures involves three main steps. This cycle can be started from any point, in the present study it is started from quasi-streamwise vortices. The first step is the generation of near-wall streaks by linear amplification of quasi-streamwise vortices via a lift-up mechanism. The second step is the breakdown of the near-wall streaks for the formation of x -dependent flow via modal or non-modal sinuous instabilities. The third step is a nonlinear process that leads to the formation of the quasi-streamwise vortices from the x -dependent flow. 68

- 4.2 (a) The mean axial velocity profile in fully developed turbulent pipe flow for the $Re = 2450$ at the four rotation numbers. The profiles in the wall region, when non-dimensionalised in wall units, do not change with rotation number. (b) The mean azimuthal velocity profile, normalised by their rotation number, for the three rotating cases. The normalised profiles are similar to each other. 69
- 4.3 The maximum transient growth, G_{max} , as functions of λ_x^+ and λ_z^+ in the (a) non-rotating and (b) rotating cases. The value of $\lambda_z^+|_{peak}$ is at around 100 wall units in both cases, which matches with the observed spanwise/azimuthal spacing of near-wall streaks. The higher $\lambda_z^+|_{peak}$ for the rotating case indicates widening of the streaks with rotation. 72
- 4.4 The normalised velocity amplitudes in the (a) initial and (b) final optimal modes of $\lambda_x^+ = 300$ and $m = -12$ (or $\lambda_z^+ = 89$) perturbations. Solid lines are for the non-rotating case, and the dashed lines are for the case $Re_{eff} = 0.05$, which has small artificial rotation added over the non-rotating case's flow profile (explained in Section 4.3.2). The initial optimal modes have most energy in the azimuthal and wall-normal velocity perturbations, and are matched with quasi-streamwise vortex. The final optimal modes have most energy in the axial velocity perturbations, and are matched with near-wall streaks. The shape of the optimal modes are very similar for the two cases. 74
- 4.5 The (a) initial optimal mode in the $y - \theta$ plane and (b) final optimal mode in the $x - y$ plane in the non-rotating case for the $\lambda_x^+ = 300$ and $m = -12$ (or $\lambda_z^+ = 89$) perturbations. The shapes of these modes confirm that the initial optimal mode corresponds to quasi-streamwise vortices, and the final optimal mode corresponds to sweeps and ejections, and hence to streaks. . . 75

- 4.6 The normalised velocity amplitudes in the (a) initial and (b) final optimal modes of the $\lambda_x^+ = 300$ and $m = -9$ (or $\lambda_z^+ = 102$) perturbations. Solid lines are for the $R_o = 0.5$ case. Dots and dashed lines are for the cases $R_{eff} = 0.475$ and $R_{eff} = 0$, respectively (explained in Section 4.3.2). In these two cases the rotation is artificially reduced or removed from the rotating case's flow profile. The mode shapes are similar to those for the non-rotating case. In the rotating case and the $R_{eff} = 0.475$ case, there are higher energy contributions from the streamwise velocity perturbations in the initial optimal mode and from the wall-normal and azimuthal velocity perturbations in the final optimal mode than those in the initial and final modes, respectively, in the non-rotating and $R_{eff} = 0$ cases. This implies that rotation causes an increase in amplification of the wall-normal and azimuthal velocity components more than in the streamwise velocity component. 76
- 4.7 The (a) initial optimal mode in the $y - \theta$ plane and (b) final optimal mode in the $x - y$ plane of the $\lambda_x^+ = 300$ and $m = -9$ (or $\lambda_z^+ = 102$) perturbations in the $R_o = 0.5$ case. The shapes of these modes are similar to the shapes of the corresponding modes in the non-rotating case shown in figure 4.5. . . . 77
- 4.8 The maximum transient growth, G_{max} , in the $\lambda_x^+ = 300$ perturbations in (a) the non-rotating case and the type I artificial cases, and (b) the $R_o = 0.5$ case and the type II artificial cases. Frame (a) shows that G_{max} increases as rotation is artificially added to the non-rotating case, and frame (b) shows that G_{max} decreases as rotation is artificially removed from the rotating case. These results show that the W_0 terms in the linearised perturbation equations contribute to the increase in transient growth. These results also show that $\lambda_z^+|_{peak}$ is entirely dependent upon the U_0 profile. 80
- 4.9 The maximum transient growth, G_{max} , in the system when the $v \frac{dU_0}{dr}$ term is artificially removed. There is very little transient growth in the system and none at $\lambda_z^+ \approx 100$. This shows that the W_0 terms do not cause transient growth by themselves. They need the $v \frac{dU_0}{dr}$ term. 81
- 4.10 (a) The cross-stream distribution of the streamwise velocity as observed for low-speed streak regions at the quiescent phase, which is during the minimum drag phase, in the minimal channel flow simulations. (b) Idealised version of (a). This figure is taken from Schoppa & Hussain (2002) [11]. . . 82

- 4.11 (a) The growth rate, ω_i , of the streak breakdown instability as a function of λ_x^+ for streaks with azimuthal wavenumber $M = 9 - 15$, equivalent to azimuthal spacing of 70-120, in the non-rotating flow case. The $M = 11$ ($\lambda_z^+ \approx 97$) streaks are most unstable to the breakdown instability at $\lambda_x^+ \approx 286$. (b) The growth rate of the streak breakdown instability in the $M = 11$ streaks in the three flow cases. The streak breakdown instability decreases as rotation in the flow increases, which shows that rotation of the pipe has a stabilising effect on streaks. 85
- 4.12 The streamwise vorticity component of the leading eigenmodes for the streak breakdown instability of the $M = 11$ streaks are plotted for the (a) $R_o = 0$ flow case at $\lambda_x^+ = 286$, (b) $R_{eff} = 0.025$ flow case at $\lambda_x^+ = 286$, and (c) $R_{eff} = 0.05$ flow case at $\lambda_x^+ = 242$. In frame (a) the three main regions in the structure are marked as crests, troughs, and streak flanks. As nonlinear effects get prominent, the streamwise vortex gets concentrated on one of the flanks and the generation of the quasi-streamwise vortices commences [11]. Rotation in the flow tilts the structure of streamwise vortices in one direction. This is to favour the formation of the vortices on the one side of the flanks, which is tilted in the direction of rotation. 86
- 4.13 The growth rate, ω_i , of the streak breakdown instability in the $M = 9$ streaks in the three flow cases ($R_o = 0.5$, $R_{eff} = 0.475$, and $R_{eff} = 0$). The streak breakdown instability increases as rotation is artificially removed, which confirms the stabilising effect of rotation. 87
- 5.1 The flow fields in the case-A of the S series gas-turbine injector-combustor system. The operating conditions in this case are set such that air and fuel are injected at the stoichiometric ratio. Frames (a–c) show the fields in the entire system while frames (d–f) show fields only in an upstream part of the geometry. Frames (a) and (d) show the axial velocity, (b) and (e) show the azimuthal velocity, and (c) and (f) show the temperature field. 95

- 5.2 The $m = -1$ instability mode in the central pipe calculated from the four stability analyses. They are represented in terms of the normalised perturbation kinetic energy multiplied by the local growth rate ω_i . Above the mode shape plots, the local absolute frequency (ω_r) and streamwise wavenumber (k_r) are plotted in black and red colour lines, respectively, as functions of the streamwise location. A comparison of frames (a) and (b) shows that compressibility does not affect this instability mode. Frames (c) and (d) show that turbulence models also have little qualitative effect. The difference is that the modes in (c) and (d) are slightly wider in the radial direction as compared to the modes in (a) and (b). The EVM-based analysis damps the mode significantly while the EARSMS-based analysis damps it relatively mildly. 99
- 5.3 The $m = -2$ instability mode in the central pipe calculated from the four stability analyses. They are represented in terms of the normalised perturbation kinetic energy multiplied by the local growth rate ω_i . Frames (a) and (b) show that the compressibility does not affect this instability mode. Frames (c) and (d) show that turbulence models also have little effect on the shape of the modes. According to the molecular viscosity- and the EARSMS-based analyses this mode is more unstable than the $m = -1$ mode. The EVM-based analysis, however, predicts this mode to be stabler than the $m = -1$ mode. 100
- 5.4 Frames (a–d) show the $m = -2$ instability modes in the $x \approx -1.5$ to 0 region and frames (e–h) show the $m = 2$ instability modes in the $x \approx -1.5$ to 0 region calculated from the four stability analyses. The $m = -2$ mode is dominant in the region with negative swirl while the $m = 2$ mode is dominant in the region with positive swirl. The positive values of the frequency and wavenumber for these modes imply that they both are co-rotating and counter-winding with respect to the local mean swirl in the flow. 101
- 5.5 (a) The axial velocity, (b) the azimuthal velocity, and (c) the temperature fields in the case-A of the S series obtained from the RANS simulation. They are qualitatively very similar to the fields obtained by time-averaging the URANS simulation data, as shown in figure 5.1. The only noticeable difference is that the RANS data has higher velocities and temperature fields and the gradients in the fields are also sharper. 103

- 5.6 The main instability modes obtained from the EARSIM-based analysis performed with the RANS data as input for the case-A in the S series system. (a) The $m = -1$ instability in the central injection, (b) the $m = -2$ instability in the central injection, (c) the $m = -2$ instability downstream of the central injection where the several incoming flows interact, and (d) the $m = +2$ instability downstream of the central injection where the several incoming flows interact. These modes are qualitatively very similar to the four instability modes shown in Section 5.2, where stability analysis of the same case is performed but with the time-averaged URANS data as input. The only difference is that the growth rates and frequencies are marginally higher, which is a result of the sharper shear layers. 104
- 5.7 The time-averaged fields are shown in case-B (frames a–c) and case-C (frames d–f) of the S series: (a) and (d) show the axial velocity, (b) and (e) show the azimuthal velocity, and (c) and (f) show the temperature field. The temperature field in case-B is colder than that in case-A, and that in case-C is colder than that in case-B. The velocity fields have the opposite trend. Case-B and case-C, on average, have higher velocity magnitudes than those in case-A. . 105
- 5.8 The thermoacoustic pressure oscillations in the three cases of the S series are shown: (a) case-A, (b) case-B, and (c) case-C. The amplitude and frequency of the thermoacoustic instability decreases monotonically as the fuel-air mixture is changed from stoichiometric to lean. 106
- 5.9 Frames (a–d) and (e–h) show dominant instability modes in case-B and case-C, respectively, of the S series injector-combustor system. These modes match very closely with the unstable modes in case-A of the series. The growth rate, however, is higher in case-B than that in case-A, and case-C has the highest growth rate among the three cases. The growth rate of hydrodynamic instability increases with increasing gradient in the mean shear layer. 107

- 5.10 The top and bottom rows show the axial and azimuthal velocity fields in the T series. All of them have the same colour-scale, which is calibrated as 0 to 2.25 for the axial velocity, and 0 to 1.5 for the azimuthal velocity (the positive azimuthal velocity indicates that the swirl is in the anti-clockwise direction). The flow through the central jet in the T series is non-swirling at a moderate flow velocity. In the downstream portion, three annular injections join the central injection and there are expansions in the system geometry. These later injections add swirl in the flow. 108
- 5.11 This instability mode is mainly caused by the shear around the centreline but also interacts with the shear between the other injected flow streams. It is winding and rotating in the anti-clockwise direction. The average wavelength of this mode is larger than the length of the combustor by an order of magnitude, which implies that this mode is unlikely to sustain a global instability. 110
- 5.12 This instability mode is caused by the inflection point in the mean axial velocity at the $r \approx 3$. It is winding in the clockwise direction and rotating in the anti-clockwise direction. Swirl near the $r = 3$ is in the anti-clockwise direction, so this mode is counter-winding and co-rotating with respect to the local mean swirl in the flow. The wavelength of this mode is larger than the length of the combustor by an order of magnitude, which implies that this mode is unlikely to sustain a global instability. 111
- 6.1 The region highlighted in grey is a representative cross-section in which the mean velocities, Reynolds stresses and eigenvectors in all the flow cases are presented. 117
- 6.2 Eigenvalues of azimuthal wavenumber $m = 0$ perturbations in the (a, b) $Re_s = 1733$ and $\mu = 0.4$, and (c, d) $Re_i = 11250$ and $\mu = 0$ cases calculated from the (a, c) MV-based analysis and (b, d) EARS-based analysis. The black dots are eigenvalues calculated with 40 Fourier modes and 60 grid-points in the r -direction and the red circles are eigenvalues calculated with 30 Fourier modes and 80 grid-points. The convergence is good in all the cases. In the higher Reynolds number case, the MV-based analysis calculations have small differences in the growth rates amongst the eigenvalues with the negative growth rates. 123

- 6.3 The mean velocity in the $\mu = 0$ cases. Each row presents the mean velocities in the (a) $Re_i = 1481$, (b) $Re_i = 3333$, (c) $Re_i = 7500$, and (d) $Re_i = 16875$ cases. Each column presents the (i) azimuthal (W), (ii) axial (U), and (iii) radial (V) mean velocity components in the above mentioned cases. By definition the mean azimuthal velocity of the inner cylinder is linearly proportional to Re_i , and the mean azimuthal velocity of the outer cylinder is zero. The mean axial and radial velocities are non-zero because Taylor vortices exist in the flow. 125
- 6.4 The Reynolds normal stress components in the $\mu = 0$ cases. Each row presents the Reynolds normal stress in the (a) $Re_i = 1481$, (b) $Re_i = 3333$, (c) $Re_i = 7500$, and (d) $Re_i = 16875$ cases. Each column presents the (i) WW , (ii) UU , and (iii) VV —components of the Reynolds normal stress. The magnitude of the Reynolds normal stress components increases with increasing Re_i 126
- 6.5 The Reynolds shear stress components in the $\mu = 0$ cases. Each row presents the Reynolds shear stress in the (a) $Re_i = 1481$, (b) $Re_i = 3333$, (c) $Re_i = 7500$, and (d) $Re_i = 16875$ cases. Each column presents the (i) WU , (ii) VW , and (iii) UV —components of the Reynolds shear stress. The magnitude of the Reynolds shear stress components increases with increasing Re_i 127
- 6.6 The growth rate of the leading eigenmodes for all the Re_i cases calculated from the (a) MV-based analysis (the first two eigenvalues are shown) and (b) EARSM-based analyses (only the first eigenvalues are shown). The MV-based analysis predicts an increase in the growth rate as Re_i increases, which means that the higher Re_i flows should be more intermittent. The EARSM-based analysis predicts a decrease in the growth rate as Re_i increases, which means that the higher Re_i flows should be less intermittent. The DNS data for these flows show that the turbulent intermittency increases with increasing Re_i , which means that the growth rate predictions from the MV-based analysis are in better agreement with the observation from the DNS. The figure also shows the azimuthal wavenumbers of the leading eigenmodes. . . 128
- 6.7 The first two leading eigenmodes of the (a, b) $m = 0$ and (c, d) $m = 1$ azimuthal wavenumbers in the $Re_i = 1481$ case calculated from the MV-based analysis. The MV and EARSM-based analyses give very similar growth rates and eigenmode shapes for this flow case. 130

- 6.8 The first two leading eigenmodes of the $m = 0$ azimuthal wavenumber in the $Re_i = 3333$ case calculated from the (a, b) MV- and (c, d) EARSM-based analyses. The first mode from the MV-based analysis matches with the second mode from the EARSM-based analysis, and the second mode from the MV analysis matches with the first mode from the MV-based analysis. 131
- 6.9 The first two leading eigenmodes of the $m = 0$ azimuthal wavenumber in the $Re_i = 5000$ case calculated from the (a, b) MV- and (c, d) EARSM-based analyses. The first mode from the MV-based analysis matches with the second mode from the EARSM-based analysis, and the second mode from the MV-based analysis matches with the first mode from the EARSM-based analysis. 132
- 6.10 The leading eigenmodes calculated from the MV-based analysis in the $Re_i = 7500$ of the azimuthal wavenumbers (a) $m = 0$ and (b) $m = 1$, in the $Re_i = 11250$ of the azimuthal wavenumber (c) $m = 1$, and in the $Re_i = 16875$ of the azimuthal wavenumbers (d) $m = 1$ and (e) $m = 5$. Unlike the eigenmodes in the lower Re_i cases, these modes are concentrated at a few spots, such as near the inner cylinder or the axial boundaries. 133
- 6.11 The leading eigenmodes of the azimuthal wavenumber (a, c) $m = 0$ and (b, d) $m = 1$ in the (a, b) $Re_i = 7500$ and (c, d) $Re_i = 16875$ cases calculated from the EARSM-based analysis. These eigenmodes match the corresponding azimuthal wavenumber eigenmodes in the lower Re_i cases. This is in contrast to the eigenmodes calculated from the MV-based analysis in these higher Re_i cases, which are concentrated at a few spots. 134
- 6.12 The mean velocities in the $Re_s = 1733$ cases. Each row presents the mean velocities in the (a) $\mu = -0.4$, (b) $\mu = -0.2$, (c) $\mu = 0.2$, and (d) $\mu = 0.4$ cases. Each column presents the (i) azimuthal (W), (ii) axial (U), and (iii) radial (V) mean velocity components in the above mentioned cases. The mean azimuthal velocity mainly depends upon the inner and outer cylinder rotation, which are determined by μ and Re_s . The mean axial and radial velocity profiles are the result of the formation of Taylor vortices. These profiles suggest that the Taylor vortices weaken when the outer cylinder rotates while keeping Re_s constant. 135

- 6.13 The mean velocities in the $Re_s = 1733$ cases. Each row presents the mean velocities in the (a) $\mu = -0.71$, (b) $\mu = -1$, and (c) $\mu = -2$ cases. Each column presents the (i) azimuthal (W), (ii) axial (U), and (iii) radial (V) mean velocity components in the above mentioned cases. The mean axial and radial velocities in the $\mu = -2$ case are very small, which implies that there are no Taylor vortices in this case. 136
- 6.14 The Reynolds normal stresses in the $Re_s = 1733$ cases. Each row presents the Reynolds normal stress components in the (a) $\mu = -0.4$, (b) $\mu = -0.2$, (c) $\mu = 0.2$, and (d) $\mu = 0.4$ cases. Each column presents the (i) WW , (ii) UU , and (iii) VV Reynolds normal stress components. For the negative μ cases, the Reynolds normal stress components first increase sharply when μ is changed from 0 to -0.2 then decrease slightly in the $\mu = -0.4$ case. For the positive μ cases, the Reynolds normal stress components increase when μ is changed from 0 to 0.2, the UU and VV components further increase in the $\mu = 0.4$ case, but the WW component decreases slightly. 137
- 6.15 The Reynolds shear stresses in the $Re_s = 1733$ cases. Each row presents the Reynolds shear stress in the (a) $\mu = -0.4$, (b) $\mu = -0.2$, (c) $\mu = 0.2$, and (d) $\mu = 0.4$ cases. Each column presents the (i) WU , (ii) VW , and (iii) UW Reynolds shear stress component. The Reynolds shear stress components first increase when μ is changed from 0 to -0.2 or 0.2, then decrease when further changed to $\mu = -0.4$ or 0.4. 138
- 6.16 The Reynolds normal stresses in the $Re_s = 1733$ cases. Each row presents the Reynolds normal stress in the (a) $\mu = -0.71$, (b) $\mu = -1$, and (c) $\mu = -2$ cases. Each column presents the (i) WW , (ii) UU , and (iii) VV Reynolds normal stress components. The Reynolds normal stress components decrease with increasing negative μ 139
- 6.17 The Reynolds shear stresses in the $Re_s = 1733$ cases. Each row presents the Reynolds shear stress in the (a) $\mu = -0.71$, (b) $\mu = -1$, and (c) $\mu = -2$ cases. Each column presents the (i) WU , (ii) VW , and (iii) UW Reynolds shear stress components. The Reynolds shear stress components decrease with increasing negative μ 139

- 6.18 The growth rates of the leading modes predicted by the (a) MV- and (b) EARSM-based analyses. The MV-based analysis predicts co-rotation to be destabilising, which means flows with positive μ should be more intermittent than the $\mu = 0$ flow case. The EARSM-based analysis predicts that small co-rotation ($\mu = 0.2$) is stabilising while the higher co-rotation ($\mu = 0.4$) is destabilising. This means that the flow with small co-rotation should be less intermittent than the $\mu = 0$ case, and the flow with higher co-rotation should be more intermittent than the $\mu = 0$ case. The MV-based analysis predicts counter-rotation to be destabilising except for the $\mu = -1$ case, which means that the flows with higher counter-rotation should be more intermittent except for the $\mu = -1$ flow case. The EARMS based analysis predicts that small counter-rotation is stabilising (up to the $\mu = -0.2$), while higher counter-rotation (up to the $\mu = -1$) is destabilising. Therefore the $\mu = -0.2$ should be less intermittent than the $\mu = 0$ case, and the flows with the $\mu \geq -0.4$ should be more intermittent than the lower negative μ flows. The growth rate for the $\mu = -2$ flow cases are for the primary instability, which means for the formation of Taylor vortices. 142
- 6.19 Standard deviation in the torque at the inner (blue squares) and outer (orange rhombuses) cylinders as functions of μ . The standard deviation is an indicator of the fluctuations in the torque with respect to the mean torque. The trends of standard deviation in the torque match qualitatively with the trend of growth rates predicted from the MV-based analysis in figure 6.18 (a). This figure is provided by Mr. Hannes Brauckmann, which is based on the DNS results presented in Ref. [12]. 143
- 6.20 The first two $m = 0$ eigenmodes in the $\mu = 0.2$ flow case calculated from the (a, b) MV- and (c, d) EARSM-based analyses. 144
- 6.21 The first eigenmodes in the $\mu = 0.4$ case of the azimuthal wavenumbers (a, b) $m = 0$ and (c, d) $m = 1$ calculated from the (a, c) MV- and (b, d) EARSM-based analyses. 144
- 6.22 The first eigenmodes in the $\mu = 0.4$ case of the azimuthal wavenumbers (a, b) $m = 2$ and (c, d) $m = 3$ calculated from the (a, c) MV- and (b, d) EARSM-based analyses. 145
- 6.23 The first $m = 1$ eigenmodes in the (a) $\mu = -0.2$, (b) $\mu = -0.4$, and (c) $\mu = -0.71$ flow cases calculated from the MV based analysis. 145

-
- 6.24 The first $m = 0$ eigenmodes in the (a) $\mu = -0.2$, (b) $\mu = -0.4$, and (c) $\mu = -0.71$ flow cases calculated from the EARSM-based analysis. 146
- 6.25 Eigenvectors in the $\mu = -1$ case: (a, b) the first two $m = 0$ eigenmodes calculated from the MV-based analysis, and (c, d, e) the first three $m = 0$ eigenmodes calculated from the EARSM-based analysis. 146
- 6.26 The first few $m = 0$ eigenmodes for the $\mu = -2$ flow case calculated from the MV- and EARSM-based analyses. The stability results for this case are for the primary instability, i.e for the formation of Taylor vortices. 147

List of Tables

- 5.1 Three cases of the S-series 104
- 5.2 The radii of the different sections in all the cases of the T series. 109
- 6.1 The leading eigenmodes in the $\mu = 0$ cases. The MV-based analysis predicts destabilisation with increasing Re_i , while the EARSM-based analysis predicts stabilisation with increasing Re_i 129
- 6.2 The growth rates of the leading eigenmodes in the $Re_s = 1733$ flow cases. . 141

Chapter 1

Introduction

“Coherent Structures are the embodiment of our desire to find order in apparent disorder.”

— A. K. M. Fazle Hussain [13]

One of the principal approaches in the study of turbulence is to understand it in terms of elementary large organised motions, which are known as coherent structures [14]. Although, there is no unanimously accepted definition of coherent structures, various researchers have explained them from their perspective. From a dynamical point of view, coherent structures are characterised as the deterministic aspect of turbulence, the other aspect of turbulence being stochastic [15–17]. For the purpose of quantitative measurements, Hussain (1986) [13] defined a coherent structure as a connected turbulent fluid mass with instantaneously phase-correlated vorticity over its spatial extent. A simple and appealing definition is given by Adrian (2007) [14], according to which coherent structures are large organised motions that persist for a long time. There is an emphasis on their persistence in time. Fluid continuity always ensures some degree of spatial coherence, but only those structures that live long enough are caught in flow visualisations and contribute significantly to the mean flow statistics to be important [14].

The idea to understand turbulence in terms of coherent structures receives particular attention because it provides much desired properties of universality and determinism to turbulent flows. For example all wall-bounded flows, such as flat-plate boundary layer flows, channel flows, and pipe flows, have similar near-wall vortical and streaky structures. The most prominent work in the direction of unifying turbulent flows based on experimental observations on coherent structures is of Townsend (1976) [18]. The main features of turbulent flow in wakes, jets, mixing zones, pipes, channels, boundary layers, and between rotating cylinders have been illuminated based on the principles developed in the book [18].

More recently, various simplified approaches have been developed to model coherent structures (summarised in Section 1.2). These simplified approaches provide a way to extend the understanding of turbulence to Reynolds numbers which are beyond the present computational and experimental resources, and their predictive properties provide a basis for developing active- or passive-control mechanisms for enhancing or reducing turbulence in the corresponding flows. One type of such simplified approaches that is based on the linearised Navier–Stokes or RANS equations is the topic of this study. Various energy amplification analyses, based on either the linearised Navier–Stokes or the linearised RANS equations, are developed and applied to extract coherent structures in a number of wall-bounded shear flows. The purpose of this study is to understand which of the energy amplification analyses is best suited to study different wall-bounded shear flows.

1.1 Coherent structures in turbulent shear flows

The literature on coherent structures, or large eddies, observed in turbulent shear flows is enormous. Townsend (1951) [19] were the first to recognise the presence of coherent structures in wall-turbulence. Inspired by the work of Townsend, Grant (1958) [20] also found large organised eddies in a wake flow behind a circular cylinder and in a flat plate boundary layer flow. Kline *et al.* (1967) [21] were the very first researchers to do an extensive visual and quantitative research on coherent structures in the near-wall region in boundary layer flows. They reported the formation of low-speed streaks by a lift-up mechanism, and also reported that average spanwise spacing between the streaks is nearly 100 wall units. This result on the spanwise spacing has been confirmed by many researchers [22–27], Smith and Metzler (1983) [27] reported 100 wall units to be the average and 80 wall units to be the most probable spanwise spacing.

Other structures found in wall turbulence are hairpin vortices [28–30] and turbulent bulges in the outer layer of the turbulent boundary layer [31]. With the advancement in experimental facilities, such as of particle image velocimetry and laser doppler velocimetry, many large coherent structures in the outer layer of wall turbulence are captured and quantitatively described. Large-scale-motions (LSM), which are eddies of streamwise extent of around 1–3 times the characteristic flow dimension (such as boundary layer thickness or channel half-width) are found and explained by many researchers in a recent few years [6, 7, 14, 32–35]. Structures larger than LSMs, with streamwise extent of up to 15–20 times the characteristic flow dimension, have also been found and their mechanism of formation has been speculated in Refs. [6, 14, 32, 34–38]. There are several notable reviews on coher-

ent structures in wall turbulence which can be referred for further reading [39–43]. Apart from wall-turbulence coherent structures have been reported in several free shear turbulent flows as well [44–47].

1.2 Simplified approaches for extraction of coherent structures

In the turbulent regime flows become very sensitive to initial conditions and random perturbations. Consequently, instantaneous flow solutions considered in isolation provide little insight about the flow dynamics. In such cases, simplified approaches based on the governing Navier–Stokes equations or the Reynolds-averaged Navier–Stokes equations have been developed to understand the flow dynamics, such as the transition to turbulence, mechanism of the formation of organised coherent structures, and their sustaining mechanisms in apparently disorganised flow. Such simplified approaches in literature could be roughly classified into three classes.

1.2.1 Exact solutions of Navier–Stokes equations

In the first class, turbulent flows are treated as deterministic chaotic systems as compared to in a statistical manner in the traditional theory [48]. This approach is based on the fact that although the Navier–Stokes equations for a fluid flow are infinite-dimensional, the small-scale motions are smoothed by viscosity and the flow can be approximately treated as a finite-dimensional dynamical system. Coherent structures are thought of as lower dimensional manifolds in whose neighbourhood the fluid flow system spends a substantial fraction of its time [49]. Therefore, a turbulent flow can be described by substantially lower-order models based on coherent structures in the flow.

In the past two decades, a number of coherent structures in simple turbulent flows are found as exact nonlinear travelling wave solutions [48, 50–59] or as exact periodic wave solutions [60–63] of the Navier–Stokes equations. These numerically computed exact solutions of the Navier–Stokes equations are found to theoretically describe the transition to turbulence as well as fully turbulent flows in terms of lower-order dynamical systems. A review concerning the application of this approach to the transition to turbulence can be read from Eckhardt *et al.* (2007) [56], and to fully turbulent flows can be read from Kawahara *et al.* (2011) [48].

1.2.2 Input-output analysis

In the second class, the Reynolds-number scaling of turbulent quantities and coherent structures are found from forcing analysis. Waves perturbations, which are parameterised by either wave speeds [5, 64, 65] or by temporal frequencies [66–70] Refs added, are fed in to the system and their responses are studied.

The general solution of the linearised equations of a dynamical system contains two parts, and are shown in equation 2 in Schmid (2007) [71] for the linearised incompressible Navier–Stokes equations. The first part is the response to initial perturbations, which is considered in the third class of the approaches discussed in Section 1.2.3. This part is also called the homogeneous solution and quantifies the inherent energy amplification of perturbations in the system through energy transfer from the mean flow. The second part is the response to an external forcing, which is considered in input-output analyses. This part is also called the particular solution and quantifies the outside influence on disturbance growth, resonance behaviour, and pattern selection. An advantage of input-output analysis is that it can naturally include the neglected terms in the governing equations, such as the nonlinear terms. This is done by including the neglected terms in the input forcing, which may make the input forcing function very complex. McKeon & Sharma (2010) [5] formulated the problem to make minimal assumptions in their analysis of fully developed turbulent pipe flows, and examined the response to forcing parameterised by wavenumbers in the two inhomogeneous directions and the wave speed. Recently, Sharma & McKeon (2013) [64] and Moarref *et al.* (2013) [65] extended the same analysis to find various coherent structures in turbulent pipe flow and Reynolds number scaling of energy spectra in turbulent channel flow, respectively. Sharma & McKeon (2013) [64] used combinations of the leading response modes to predict hairpin vortices and other structures. Moarref *et al.* (2013) [65] used weighting function based on the DNS data at low Reynolds number channel flows, and predicted the Reynolds number and wall-normal variations of energy in the streamwise velocity at high Reynolds numbers.

1.2.3 Energy amplification analysis

In the third class, coherent structures are found as the most amplified modes of the linearised Navier–Stokes equations [1, 72–75] or the linearised RANS equations [2, 10, 68, 76–80]. The present study is focused on the development of such analyses and their application in various wall-bounded turbulent flows.

The Navier–Stokes equations linearised over the mean velocity profile have been used

for linear stability analysis of perturbations for a long time since the early work of Malkus (1956) [72]. A formal justification for such analyses, however, came much later when the theory of rapid distortion (RDT) was developed [81, 82]. Hunt and Carruthers (1990) [81] showed that use of the linearised Navier–Stokes equations to simulate large coherent structures is justified in the regions of high mean shear. This is because in these regions the linear terms act much more quickly than the nonlinear terms. Energy amplification analysis based on the linearised Navier–Stokes equations is formulated in Chapter 2 and is used in Chapters 2, 4, 5, and 6. The literature in this area is also discussed in further detail in Chapter 2.

The use of turbulence models to augment the linearised Navier–Stokes equations was first introduced by Reynolds & Hussain (1972) [76]. They used a triple decomposition of the flow fields as $f = \bar{f} + \tilde{f} + f'$, where \bar{f} is the time time-averaged flow fields part, \tilde{f} is the organised wave perturbations part, and f' is the turbulent fluctuations part. The organised wave perturbations \tilde{f} are defined using phase-averaging and represent the external wave perturbations. The turbulent fluctuations (f') contribute to the Reynolds stress components in the flow, which are defined as $\overline{u'_i u'_j}$, where over-line represents the time-averaging, superscript $'$ represents the fluctuating part, u represents the velocity field, and subscripts i and j represent the spatial directions. Reynolds & Hussain (1972)'s purpose was to include the effect of wave-induced perturbations in the Reynolds stress on the behaviour of small external wave perturbations. They concluded that a simple eddy viscosity model, with a constant eddy viscosity profile, is effective in modelling the wave-induced perturbations in the Reynolds stress, and the resulting analysis predicts the behaviour of external wave perturbations that is not substantially different from the actual behaviour. They also proposed that there is a need for better models to obtain quantitatively better results. In Chapter 3, the explicit algebraic Reynolds stress models (EARSMS)-based linearised RANS equations are derived, and the corresponding analyses are used in Chapters 3, 5, and 6. The literature in this area is also discussed in further detail in Chapter 3.

In the present study, analysis based on the linearised Navier–Stokes equations and analyses based on the EVM- and EARSMS-based linearised RANS equations, where the effect of wave-induced fluctuations in Reynolds stress is included in the analysis, are implemented for several wall-bounded turbulent shear flows. These analyses are performed to find coherent structures, or hydrodynamic instabilities, in the flows and wherever possible the results are compared with the experimental or numerical results in the literature. The focus of this study is on understanding which of the analyses best suit the wall-bounded turbulent shear flows.

1.3 Relevance to gas-turbines and general scope

The main reason for studying hydrodynamic instabilities in gas-turbine flows is for their role in entrainment of fuel into air, which is important for air-fuel mixing at the molecular level for combustion [83–85]. Another reason is because hydrodynamic instabilities may also interact with thermoacoustic oscillations, which can cause pressure oscillations to grow to dangerously high levels [86]. The difficulty in studying hydrodynamic instabilities comes because flows inside gas-turbines are in the turbulent regime and the systems' geometries are usually complicated. This makes studying them computationally expensive, such that DNS is practically impossible and LES is possible only at a few steps in the design process. RANS and URANS are popular methods because they calculate the mean velocity and Reynolds stresses in a turbulent flow in a feasible time as required in the design process. These methods, however, are very dissipative, particularly in commercial solvers. The RANS solvers give no information about hydrodynamic instabilities in the flows, and the URANS solvers give information only about low frequency oscillations in the flows. Therefore, approaches based on the linearised Navier–Stokes or RANS equations, which require only the mean velocity and Reynolds stress fields as input, to find hydrodynamic instabilities in gas-turbine injector-combustor systems are desirable. Such approaches are applied for studying hydrodynamic instabilities in gas-turbine flows in Chapter 5.

Apart from gas-turbines, another important application of modelling coherent structures is for drag-reduction in aerodynamic flows. Moarref and Jovanovic (2012) [87] have derived a model-based active control for drag-reduction in turbulent channel flow. Their active-control is based on the linearised $K - \varepsilon$ model RANS equations, which are shown to capture coherent structures in channel flow [2, 10]. Meliga *et al.* (2012) [88] have also obtained sensitivity results in 2D wave flow past a square cylinder by using the linearised RANS equations based global stability analysis. It is, therefore, expected that successful demonstrations of various linearised equations based analyses can serve as the basis for the application of tools from linear algebra in fluid flows.

1.4 Thesis structure

This thesis is divided into seven chapters. In chapter 2, energy amplification analysis based on the linearised Navier–Stokes equations is applied on turbulent channel flows. The effect of the nonlinear terms is approximated by using the streamwise wavelength of perturbations as input to the analysis. In this analysis only molecular viscosity is used, i.e. no eddy

viscosity or any other turbulence model is used in the analysis. The results are compared with the observations from experiments and DNS in turbulent boundary layers. In chapter 3, the linearised RANS equations are derived based on different turbulent models. These models include the eddy viscosity models (EVMs), which are first-order turbulence closure models, and the explicit algebraic Reynolds stress models (EARSMS), which are second-order turbulence closure models. This is the first study in the literature where a second-order turbulence model is used to derive the linearised RANS equations for the purpose of stability analysis. The EARSMS- and EVM-based analyses are implemented on turbulent channel flows, and the results are compared with those in the literature. In Chapter 4, the linearised Navier–Stokes equations based stability analysis and secondary stability analysis are performed to study the effect of rotation on near-wall coherent structures in turbulent pipe flow. In Chapter 5, analyses based on the linearised Navier–Stokes and linearised RANS equations are applied for flows inside gas-turbine injector-combustor systems. The effect of small modifications in systems’ operating conditions and designs on hydrodynamic instabilities are predicted, and the results from the various analyses are compared to find which one best suit these flows. In Chapter 6, analyses based on the linearised Navier–Stokes and EARSMS-based linearised RANS equations are applied on Taylor-Couette flow to find intermittent coherent structures that develop on the top of Taylor vortices. Some preliminary comparisons are made between the stability analyses results with those from the DNS. Lastly, Chapter 7 presents the conclusion and further work.

Chapter 2

Extraction of coherent structures in turbulent channel flow from linear amplification analysis

Fully developed turbulent channel flow is the most studied flow case in the literature on extracting coherent structures. In this Chapter, a simple approach is presented for finding coherent structures in turbulent channel flows, which, to an extent, serves as a basis in the analyses used in Chapters 4, 5, and 6. This chapter also presents a detailed review on other approaches in the literature.

2.1 Introduction

Simplified approaches for understanding and controlling coherent structures in turbulent flows have recently gained much attention. These approaches are desired for their applicability at high Reynolds numbers, where DNS or experiments are either not possible or not accurate, and for their simplification, which helps in understanding the dynamics of coherent structures. Various simplified approaches in the literature could be roughly classified into three classes. In the first class, coherent structures are found as nonlinear travelling wave or periodic solutions of the Navier–Stokes equations [48, 54–57, 62]. In the second class, coherent structures are found from an input-output analysis where the waves are parameterised either by wave speeds [5, 64, 65] or by temporal frequencies [66–68]. In the third class, coherent structures are found as the most amplified modes of the linearised Navier–Stokes equations [1, 72–75] or of the linearised RANS equations [2, 10, 68, 76–80].

The success of the approaches that are based on linearised equations in finding coherent structures has motivated the application of other linear analysis tools in turbulent flows. For example, sensitivity analysis of a wake flow behind a 2-D square cylinder is performed in Ref. [88]. They used the Spallart-Allmaras model to derive the RANS equations for the flow, and the linearised RANS equations are then used to calculate sensitivity of the flow to a small control cylinder. Their results compare well with the experimental measurements in the same flow [89]. The linearised $K - \epsilon$ model-based RANS equations are used in deriving model-based control for suppressing near-wall structures in channel flow [87]. Application of a passivity theorem, as a result of which each wavenumber perturbations can be controlled individually, is used to derive a linear control strategy for successful relaminarisation of a low Reynolds number turbulent channel flow in Ref. [90]. Kim (2007) [91] reviewed the usefulness of linear systems approach in turbulent flow control, which further emphasises the importance of the linear dynamics in turbulence. These sensitivity and control applications further motivate for the development of simplified approaches in turbulent flows.

In this chapter an approach is presented for extracting coherent structures in turbulent channel flows. In this approach the most amplified perturbations and the corresponding initial optimal modes of the linearised Navier–Stokes equations are interpreted as approximations of coherent structures in fully nonlinear turbulent channel flows. The effect of the neglected nonlinear terms is modelled as the input streamwise wavelengths of the perturbations, where the input values are based on experimental and DNS observations. The use of the linearised Navier–Stokes equations is justified based on the rapid distortion theory [81, 82, 92]. Hunt & Carruthers (1990) [81] showed that application of the linearised Navier–Stokes equations in reproducing large-scale turbulent structures is justifiable in the high mean shear flow regions, because in such regions the time-scale at which the linear terms act is much smaller than the time-scale at which the nonlinear terms act. Lee, Kim, & Moin (1990) [82] showed that to be true for the formation of streaks in flows where the mean shear is as high as in the near-wall region in wall-bounded turbulent flows. Recently, Jimenez (2013) [92], based on the same theory, further stretched the applicability of the linearised Navier–Stokes equations into the logarithmic layer, and through physical arguments also explained the role of linear processes in the formation of coherent structures in this region.

A simple mathematical description for the justification of the RDT in the regions of high mean shear is presented in Lee, Kim, & Moin (1990) [82], and is presented here. The

ensemble-averaged (or Reynolds-averaged) velocity is labelled U_i , and fluctuating velocity and pressure fields are labelled u_i and p , respectively. The Reynolds stress terms are represented as $\overline{u_i u_j}$. The equation for the evolution of the fluctuating velocity fields is written as below.

$$\frac{\partial u_i}{\partial t} + U_j \frac{\partial u_i}{\partial x_j} = \left[-\frac{\partial p}{\partial x_i} + \nu \frac{\partial^2}{\partial x_j \partial x_j} u_i \right] - \underbrace{\left[u_j \frac{\partial}{\partial x_j} U_i \right]}_L - \underbrace{\left[\frac{\partial}{\partial x_k} (u'_k u'_i) - \overline{u'_k u'_i} \right]}_{NL} \quad (2.1)$$

where the terms labelled L and NL are the principal linear and nonlinear driving terms, respectively. In the flow region, where the timescale of the L term is much smaller than the timescale of the NL term, the contribution from the NL term can be ignored. This means that the evolution of the fluctuating field can be predicted based on the linearised Navier–Stokes equations. The timescale of the L term is straightforward to obtain. It is equal to the inverse of the mean shear, $\frac{1}{S}$, where S is the mean shear. The timescale of the NL term is defined as $\frac{l}{q}$, where l is a length scale and q is the turbulence kinetic energy. Lee, Kim, & Moin (1990) [82] took dissipation length scale l_d to be the length scale and argued that it gives a good indication of differences in turbulence structures. The dissipation length scale is given as: $l_d = \frac{q^3}{\varepsilon}$, where $\varepsilon = \nu \frac{\partial u_i}{\partial x_j} \frac{\partial u_i}{\partial x_j}$ is the dissipation rate of the turbulence kinetic energy. Based on these definitions, the ratio of the NL -term timescale to the L -term timescale is given as: $S^* = \frac{Sq^2}{\varepsilon}$. This ratio is shown to be big in the near-wall region as well as in the logarithmic layer in Jimenez (2013) [92].

The modelling of the effect of the neglected nonlinear terms as the input streamwise wavelength of perturbations is based on the results of Kim & Lim (2000) [93], and the regeneration cycle proposed in Refs. [11, 94]. Kim & Lim (2000) [93] showed that while the linear terms are essential in the formation and maintenance of streaks, it is nonlinear mechanisms that are responsible for the proper streak spacing. It is also known from the regeneration cycle that the streaky structures form from near-wall vortical structures, as also predicted from linear amplification analysis results of Butler & Farrell (1993) [1]. Schoppa & Hussain (2002) [11] showed that the near-wall vortical structures, also called quasi-streamwise vortices, have the streamwise lengths equal to a few hundred wall-units, this is also mentioned in Ref. [42] and observed in Ref. [95]. In the present study, these results are interpreted as that the nonlinear mechanisms that are responsible for the proper streak spacing act through selecting the streamwise length of the vortical structures. There-

fore, the streamwise wavelengths are used as input in the present analysis. Although the results in Ref. [93] and the regeneration cycle are only for near-wall structures, in the present approach the modelling of the effect of the nonlinear terms as the input streamwise wavelength is extended in the entire channel. This is partly justified based on the similarity of coherent structures and in the mechanism of their formation in the entire wall-bounded flow [30, 92].

Of course, such a modelling of the effect of the neglected nonlinear terms is only rudimentary. Nevertheless various kinematic properties of the resulting optimal modes are in good agreement with those of coherent structures as discussed in this chapter. The present approach is very close to many approaches in the literature, particularly those in Refs. [1, 2, 10, 73]. Therefore the key differences and benefits of the present approach over the existing linear amplification approaches are separately discussed. In this process, the present approach is also discussed in detail.

2.1.1 Relation with other linear amplification approaches

Butler & Farrell (1993) [1] were the first to perform non-modal stability analysis on the mean flow profile in turbulent channel flow. Their purpose was to find streaks in the near-wall region whose spanwise spacing, L_z^+ , scales in wall units (i.e. it is independent of the Reynolds number if non-dimensionalized using the kinematic viscosity, ν , and the friction velocity, $u_\tau = \sqrt{\nu(\frac{dU}{dy}|_{wall})}$). The widely accepted value is $L_z^+ \approx 100$ [21, 27]. Butler & Farrell (1993) [1] found that the global maximum in the transient growth is at the spanwise wavelength $\lambda_z^+ = 540$ (not 100) and streamwise wavelength $\lambda_x^+ = \infty$. The maximum transient growth (G_{max}) calculations for the same flow profile are performed here and the results, for the streamwise uniform as well as finite wavelength perturbations, are shown in figure 2.1. Butler & Farrell (1993) [1] pointed out that the optimization time ($\tau^+ = 2342$) required for this process is very long, and that, after a certain time, the nonlinear terms will act to prevent the linear transient growth. They estimated this time to be $\tau_e^+ = 80$, and referred to it as an eddy turnover time. When the optimisation time was limited to the τ_e^+ , they found the peak in the transient growth to be at the $\lambda_z^+ = 100$ and $\lambda_x^+ = \infty$.

This limiting of the optimisation time, however, is challenged both quantitatively and conceptually. Kim & Lim (2000) [93] showed that nonlinear time-marching simulations for a turbulent channel flow start to become significantly different from the corresponding linear time-marching simulations in time only half as long as the τ_e^+ . This raises a question

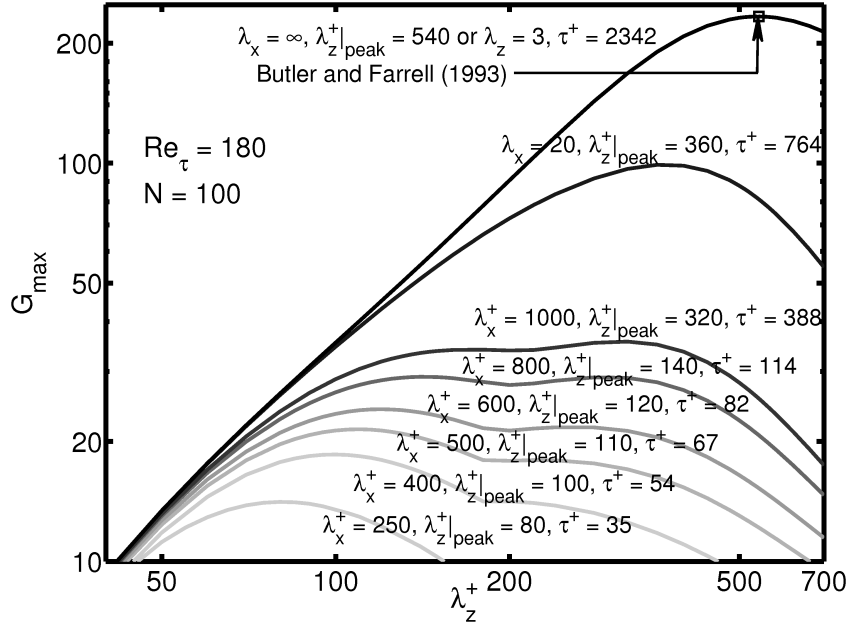


Fig. 2.1 The maximum transient growth, G_{\max} , as a function of the spanwise (λ_z^+) and streamwise (λ_x^+) wavelengths. The peaks in G_{\max} are at $\lambda_z^+ \approx 100$ for the $\lambda_x^+ = 250 - 800$ perturbations. For higher λ_x^+ perturbations the peaks are not at $\lambda_z^+ \approx 100$, but are at much higher λ_z^+ values. At the $\lambda_x = \infty$, the peak is at the $\lambda_z^+ = 540$, as reported in Ref. [1].

on the estimated τ_e^+ . Chernyshenko and Baig (2005) [73] raised a question on the given reason for limiting the optimisation time. They pointed out that the flow is fully nonlinear all the time, so to argue that nonlinear mechanisms are significant only after a certain time during the formation of each streak is unrealistic. Besides these shortcomings, the results in Ref. [1] predict the formation of streaks that are streamwise uniform, while the observed streaks are around 1000 wall-units long. The present approach overcomes all these shortcomings by using the streamwise wavelength as input instead of the optimisation time. Firstly, the streamwise lengths of coherent structures are much more easily observed than the optimisation time. Secondly, use of the streamwise wavelength as input does not restrict the nonlinearity to be significant only after a certain time in the process. In fact it divides the role of the linear and nonlinear terms as concluded in Ref. [93], and is in good agreement with the notion of the most widely accepted regeneration cycle of near-wall structures [11, 94, 96].

The current understanding of the formation of near-wall structures is that low-speed streaks of $L_x^+ \approx 1000$ (length in the streamwise direction) below $y^+ = 40 - 50$ (wall-normal location) are formed by relatively short quasi-streamwise vortices, which are $\mathcal{O}(100)$ wall-

units long [11, 42, 95]. The quasi-streamwise vortices on the one side transport high speed fluid towards the wall, known as sweeps, and on the other side lift low speed fluid away from the wall, known as ejections. The lifted low speed fluid from the ejections, when left behind, elongates and forms the near-wall streaks. The ejections and sweeps, therefore, are indirect indicators of the streaks [11]. The next step in the regeneration cycle is the formation of the streamwise vortices back from the lifted streaks. Schoppa & Hussain (2002) [11] show that the preferred streamwise wavelength of these vortices is $\lambda_x^+ \approx 300$, which, perhaps coincidentally, closely matches with the minimal channel length required for sustaining turbulence [97].

It is known from the results in Refs. [1, 2, 10] and from the results presented in figure 2.5, that linear amplification analysis captures the formation of sweeps and ejections like structures from quasi-streamwise vortices like structures. Therefore, the streamwise wavelengths of a few hundred wall units ($\lambda_x^+ = 200 - 800$) are used as input in the present analysis. These input wavelengths are close to the streamwise length of the observed near-wall vortical structures [11, 42, 95], and are smaller than the streamwise length of the observed streaks (≈ 1000) [8]. Figure 2.1 shows that when the streamwise wavelength of perturbations is fixed in between 200 – 800 wall-units, the most amplified spanwise wavelength is naturally close to 100. In Section 2.3, it is shown to be the case in other Reynolds number flows as well.

Another closely related linear amplification analysis to find near-wall structures is of Chernyshenko & Baig (2005) [73]. They tested two conceptual models for the sustainment of near-wall structures. In the first model, the pattern of streaks is dictated by the pattern of wall-normal motions via a lift-up mechanism, which is also in agreement with the regeneration cycle [11, 94]. In the second model, the pattern of streaks is dictated by the selective properties of the linearised Navier–Stokes operator alone. They presented numerical results which supported the second model over the first. This is re-iterated in a follow-up article by the same group - in a developed turbulent flow the selective properties of the linearised Navier–Stokes operator are stronger than the selective properties of the nonlinear terms - [98]. Chernyshenko & Baig (2005) [73] were right to point out that the linearised Navier–Stokes operator have important selective properties as demonstrated in various linear amplification and harmonic forcing papers [1, 2, 5, 10], but it does not agree with the numerical experiments of Kim & Lim (2000) [93], who showed that the nonlinear terms are essential for the streaks to form in the right pattern. In contrast to Chernyshenko &

Baig (2005) [73]’s analysis, in the present approach while it is recognised that the linearised Navier–Stokes operator has strong selective properties and select the preferred λ_z^+ , it is also recognised that the nonlinear terms select the preferred λ_x^+ during the formation of vortices. Therefore the present approach, to an extent, accommodates both the conceptual models suggested by Chernyshenko & Baig (2005) [73].

The latest linear amplification approach to find coherent structures in turbulent channel flow is where the molecular viscosity is replaced by an eddy viscosity in the linearised Navier–Stokes equations. Because this is the state-of-the-art approach it is necessary to show whether there is any advantage of using the present approach over this approach. The use of the eddy viscosity models in stability analysis was first introduced by Reynolds & Hussain (1972) [76]. This was to account for the effect of wave-induced perturbations in the Reynolds stress on the behaviour of small external wave-perturbations. Del-Alamo & Jimenez (2006) [10] were the first to use eddy viscosity model in non-modal stability analysis to find coherent structures in wall-bounded turbulence, and later Pujals *et al.* (2009) [2] introduced a correction in Ref. [10]’s analysis. Pujals *et al.* (2009) [2] found that such linear amplification analysis naturally gives two peaks in the maximum transient growth (G_{max}). One is at $\lambda_z^+ \approx 100$, which scales in inner units and identified to correspond to near-wall streaks, and the other is at $\lambda_z \approx 4$, which scales in outer units and identified to correspond to very-large-scale-motion (VLSMs). Calculations of G_{max} using their approach are performed here for two flow profiles: (a) the $Re_\tau = 2000$ empirical profile used in Pujals *et al.* (2009) [2] and (b) the $Re_\tau = 2003$ DNS profile calculated in Ref. [3]. The results from the two profiles are similar and are shown in figure 2.2.

The major drawback in the results from the eddy viscosity based approach is pointed out in Jimenez (2009) [4]. It is that in the intermediate spanwise wavelengths region, which is in between the two peaks at $\lambda_z^+ \approx 100$ and $\lambda_z = 2$, there is minimum energy amplification as shown in figure 2.2, while DNS show a peak in the energy spectra in this intermediate wavelength region. Jimenez (2009) [4] suspected that the reason for this is that the eddy viscosity used in the analysis is too high to model the energy-containing eddies correctly. In the original work of Reynolds & Hussain (1972) [76], they used a triple decomposition $u = \bar{u} + \tilde{u} + u''$, where \bar{u} is the time-averaged field, \tilde{u} is the organised part of the motion defined using phase-averaged field, and u'' corresponds to the disorganised part, to derive the linearised RANS equations. In Ref. [76], the organised component \tilde{u} was part of an externally introduced perturbation in the flow, while turbulent coherent structures, such as

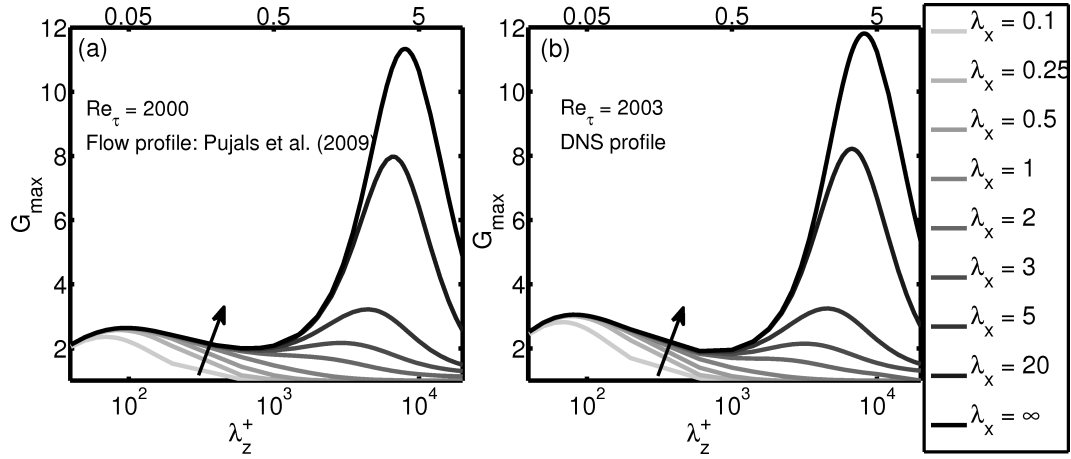


Fig. 2.2 The maximum transient growth, G_{max} , as a function of the spanwise (λ_z) and streamwise (λ_x) wavelengths calculated from the eddy viscosity based approach for the flow profiles (a) $Re_\tau = 2000$ from the empirical expression in Ref. [2] and (b) $Re_\tau = 2003$ from the DNS in Ref. [3]. The top axis is the spanwise wavelength in outer units (λ_z) and the bottom axis is the spanwise wavelength in inner units (λ_z^+), and the arrow is in the direction of increasing λ_x . The results in the two cases are very similar. This approach finds two peaks in G_{max} , one at $\lambda_z^+ \approx 100$, which corresponds to near-wall streaks, and the other at $\lambda_z \approx 2 - 4$, which corresponds to VLSMs, as mentioned in [2]. The main disadvantage of this approach is that it finds minima in energy amplification at the intermediate spanwise wavelengths, between $\lambda_z^+ \approx 100$ and $\lambda_z = 2$, where DNS show a peak in energy spectra [4]. Another smaller disadvantage of this approach is that it finds the optimal structures to be streamwise uniform (i.e. the $\lambda_x = \infty$) [4, 5].

streaks, are inherently present in the flow [98]. The time-averaging and phase-averaging both smooth the streaks out, so they are included in u'' and not to be predicted as part of \tilde{u} . Blesbois *et al.* (2013) [98] argued that if the streaks are to be predicted as part of the solution of the equations for \tilde{u} , then the streaks should not be included in u'' , and hence their contribution in the Reynolds stress components should also not be included.

Some researchers consider that using the eddy viscosity based approach is important because the mean velocity is a steady solution of the RANS equations and not of the Navier–Stokes equations. Therefore, it is the RANS equations, which contain an eddy viscosity in place of the molecular viscosity, that should be linearised for stability analysis. While it is true that steady solutions of the eddy viscosity based RANS equations are close to the mean flow profiles in turbulent channel flow, it is not a reason that stability analysis based on these equations can predict coherent structures in the flow. In fact, one of the features of very large coherent structures, such as the VLSMs, is that they are not amenable to models, such as the EVMs, that calculate the Reynolds stress from the local mean velocity gradients. As also pointed out in Guala *et al.* (2006) [6], very-large motions are hardly local and are therefore not amenable to being represented by gradient transport models.

In comparison, the approach presented in this chapter is simply based on the rapid distortion theory and is backed by a number of papers [1, 73, 81, 82, 93] [McKeon and Sharma ref. removed]. It is shown in Section 2.4, that apart from the peaks at $\lambda_z^+ \approx 100$ and $\lambda_z \approx 2$ the present approach also finds peaks in energy amplification in the intermediate spanwise wavelengths region, and various kinematic properties of the corresponding optimal structures are in good agreement with those of the observed coherent structures. Another drawback in the eddy viscosity based approach is that the transient growth is maximum for the streamwise uniform perturbations, i.e. $\lambda_x = \infty$, however the near-wall streaks have a finite streamwise wavelength (≈ 1000) [4, 5]. This second drawback is not a problem in the present approach because λ_x is an input based on experimental or DNS observations.

2.1.2 Complimentary simplified approaches

As explained in Section 1.2.2 of Chapter 1, input-output analyses are other popular simplified approaches to find information on coherent structures in turbulent flows [5, 64–67]. These analyses are considered complimentary to the present one, because where the present analysis gives the homogeneous solution of the linearised Navier–Stokes equations, which quantifies the inherent energy amplification of perturbations in the system through energy

transfer from the mean flow, the input-output analyses give the particular solution, which quantifies the outside influence on disturbance growth, resonance behaviour, and pattern selection [71].

2.1.3 Outline

In Section 2.2, the formulation of the present approach for turbulent channel flows is shown. In Section 2.3, non-modal amplification analysis at the small input streamwise wavelengths is performed. In Section 2.4, non-modal amplification analysis at the intermediate and large streamwise wavelengths is performed.

2.2 Methodology for calculation of transient growth in turbulent channel flow

The streamwise, wall-normal, and spanwise directions, respectively, are represented by (x, y, z) coordinates. The mean flow velocity in the channel is given as $(U(y), 0, 0)$, and the linear perturbations are assumed to be of the form $(u(y), v(y), w(y)) \exp\{-i\omega t + 2\pi i x/\lambda_x + 2\pi i z/\lambda_z\}$. The friction Reynolds number is defined as $Re_\tau = u_\tau h/\nu$. The bottom wall of the channel is located at $y = 0$. The wall-normal location (y) and wavelengths (λ_x and λ_z) are always non-dimensionalized in outer units, i.e. by h . Any variable represented with a superscript⁺ is non-dimensionalised in wall units, i.e. by ν and u_τ .

The linearised Navier–Stokes equations are given as:

$$\begin{aligned}
 \frac{\partial u}{\partial t} &= -\nu \frac{dU}{dy} - ik_x U u - ik_x p + \frac{1}{Re_\tau} \left[\frac{\partial^2 u}{\partial y^2} - k_z^2 u - k_x^2 u \right] \\
 \frac{\partial v}{\partial t} &= -ik_x U v - \frac{\partial p}{\partial y} + \frac{1}{Re_\tau} \left[\frac{\partial^2 v}{\partial y^2} - k_z^2 v - k_x^2 v \right] \\
 \frac{\partial w}{\partial t} &= -ik_x U w - ik_z p + \frac{1}{Re_\tau} \left[\frac{\partial^2 w}{\partial y^2} - k_z^2 w - k_x^2 w \right] \\
 0 &= ik_x u + \frac{\partial v}{\partial y} + ik_z w
 \end{aligned} \tag{2.2}$$

where k_x and k_z are equal to $\frac{2\pi}{\lambda_x}$ and $\frac{2\pi}{\lambda_z}$, respectively. The Orr–Sommerfeld and Squire equations are derived from the linearised Navier–Stokes equations for the present analysis,

and are given as:

$$\omega \begin{bmatrix} -k_z^2 - k_x^2 + \frac{d^2}{dy^2} & 0 \\ 0 & I \end{bmatrix} \begin{bmatrix} v \\ \Omega \end{bmatrix} = \begin{bmatrix} \frac{1i}{Re_\tau} \left(k_z^4 + \frac{d^4}{dy^4} - 2k_z^2 \frac{d^2}{dy^2} \right) + k_x \left(-k_z^2 U + U \frac{d^2}{dy^2} - \frac{d^2 U}{dy^2} \right) & 0 \\ -\frac{2i}{Re_\tau} k_x^2 \left(\frac{d^2}{dy^2} - k_z^2 \right) - k_x^3 U + \frac{1i}{Re_\tau} k_x^4 & \\ k_z \frac{dU}{dy} & \frac{1i}{Re_\tau} \left(\frac{d^2}{dy^2} - k_z^2 \right) + k_x U - \frac{1i}{Re_\tau} k_x^2 \end{bmatrix} \begin{bmatrix} v \\ \Omega \end{bmatrix}, \quad (2.3)$$

where Ω is the wall-normal vorticity, i represents the imaginary unit, and I is the identity operator. Chebyshev spectral method with Gauss-Lobatto points in the y -direction is used for discretisation. The fact that v and Ω are anti-symmetric and symmetric, respectively, with respect to the centre of the channel is used and discretisation is performed only for half of the domain. Chebyshev differentiation matrices are used for the differential operators in the equation [99].

The purpose of this formulation is to calculate the maximum transient growth, G_{max} , given below.

$$G_{max} = \sup \frac{|u(t)|^2 + |v(t)|^2 + |w(t)|^2}{|u(0)|^2 + |v(0)|^2 + |w(0)|^2} \quad (2.4)$$

where $|\cdot|^2$ represents the L_2 -norm. The maximum transient growth, G_{max} , is maximized not only over all the initial conditions but also over the time t . In order to calculate G_{max} , first the eigenvalues and eigenvectors of equation 3.16 are calculated. The Matlab function ‘eig’ is used to calculate the eigenvalues (not the eigenvectors), the eigenvectors corresponding to the calculated eigenvalues are then calculated using the Matlab function ‘eigs’ because it is numerically cheaper.

The maximum transient growth is calculated based on the knowledge of eigenvalues and eigenvectors, by using the formulation given in Ref. [100]. The system eigenvectors are labelled f_i and the corresponding eigenvalues are labelled ω_i . The calculated eigenvectors, f_i , are modified such that they are composed of the $(u(y), v(y), w(y))$ velocity components. The matrices F and $\Lambda(t)$ are formed as below.

$$F = [f_1 \ f_2 \ f_3 \ \dots \ f_M] \quad (2.5)$$

$$\Lambda(t) = \text{diag}(\exp(-i\omega_1 t) \exp(-i\omega_2 t) \exp(-i\omega_3 t) \dots \exp(-i\omega_M t)) \quad (2.6)$$

The maximum transient growth at time t is then equal to $SVD(F\Lambda F^{-1})$ [100]. The matrix F , however, is not necessarily a square matrix. The F^{-1} is therefore calculated as $(F^*F)^{-1}F^*$, where F^* is the complex conjugate transpose of F . In the matlab numerical code the maximum transient growth at time t is calculated by using the command given below.

$$G_{max}(t) = \text{svds}(F\Lambda(t)/(F^*F)F^*, 1) \quad (2.7)$$

The maximum transient growth, G_{max} , is calculated by finding the maxima of $G_{max}(t)$ by repeating the calculations for several values of t . The codes are verified by reproducing the results of Butler & Farrell (1993) [1], presented in figure 2.1, and of Pujals & Cossu (2009) [2], presented in figure 2.2 (a).

The maximum transient growth, G_{max} , is calculated for a fixed input λ_x over a range of λ_z values. The spanwise wavelength, λ_z , at the maximum in G_{max} is labelled $\lambda_z|_{peak}$. This value of $\lambda_z|_{peak}$ is assumed to be the preferred spanwise wavelength of coherent structures in the flow at the corresponding streamwise wavelength. The kinematic properties of the initial and final optimal modes at $\lambda_z|_{peak}$ and λ_x are matched with those of the observed coherent structures at approximately similar wavelengths in the flow. This process is then repeated for a number of input streamwise wavelengths.

2.3 Non-modal amplification analysis at small wavelengths

Figure 2.3 shows the maximum transient growth, G_{max} , as a function of λ_z and λ_x for channel flows at the $Re_\tau = 934, 2003$, and 4079 . The input λ_x^+ used is of $\mathcal{O}(100)$, which is based on the observed streamwise length of quasi-streamwise vortices [11, 42, 95]. Calculations at the higher wavelengths are presented in Section 2.4. The flow profiles for these cases are taken from the DNS data of Refs. [3, 101, 102]. Linear amplification calculations are performed with 150 grid-points and 280 eigenvectors for the $Re_\tau = 934$ and 2003 cases. Values of G_{max} calculated with 150 grid-points converge to a reasonable accuracy; it is checked that the change in G_{max} is smaller than 10^{-2} when some of the calculations are repeated with 170 grid-points and 320 eigenvectors. Calculations for the $Re_\tau = 4079$ case are performed with 195 grid-points and 380 eigenvectors. Its convergence is checked by repeating a few calculations with 180 grid-points and 350 eigenvectors, and the change in

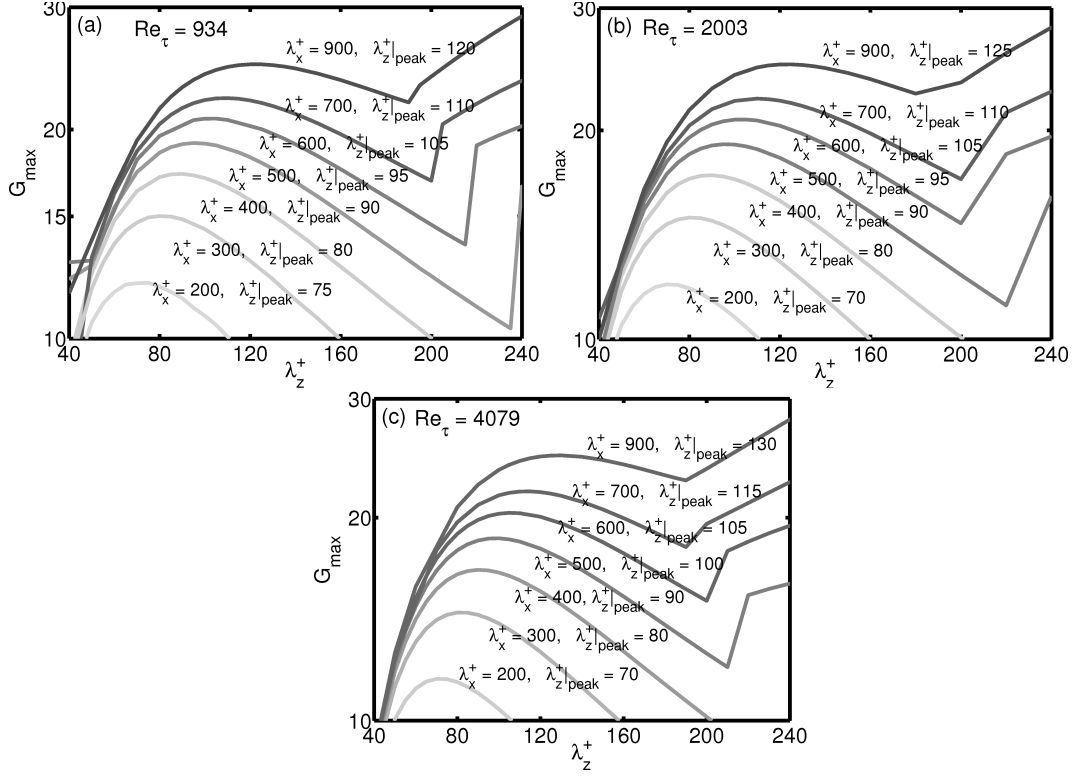


Fig. 2.3 The maximum transient growth, G_{max} , as a function of the spanwise wavelength (λ_z^+) for the (a) $Re_\tau = 934$, (b) $Re_\tau = 2003$, and (c) $Re_\tau = 4079$ flow cases. The peaks in G_{max} are at $\lambda_z^+ \approx 100$, which is in agreement with the observations on the near-wall streaks spacing. The peak spanwise wavelength value, $\lambda_z^+|_{peak}$, increases with increasing λ_x^+ . The values of G_{max} and $\lambda_z^+|_{peak}$ scale in wall units.

G_{max} remains smaller than 10^{-2} .

The results for these Reynolds number flows are very similar to each other as well as to those for the $Re_\tau = 180$ flow shown in figure 2.1. A peak in the transient growth exists at $\lambda_z^+ \approx 100$, and shifts to higher λ_z^+ for higher λ_x^+ perturbations. The values of G_{max} and $\lambda_z^+|_{peak}$ scale well in wall units. The optimisation time is in the range $\approx 30 - 100$, and also scales in wall-units. The jumps in G_{max} at higher λ_z^+ show that the solutions switch to a different mode. This does not happen in the $Re_\tau = 180$ case perhaps because it is a low Reynolds number flow and therefore the scale separation is not present in the flow. The preferred spanwise wavelength from linear amplification analysis ($\lambda_z^+|_{peak} = 100$) is close to the observed spanwise spacing of near-wall structures as reported in Ref. [27] and in many others. It is examined whether other kinematic properties of the optimal modes at $\lambda_z^+|_{peak}$ match with those of near-wall structures.

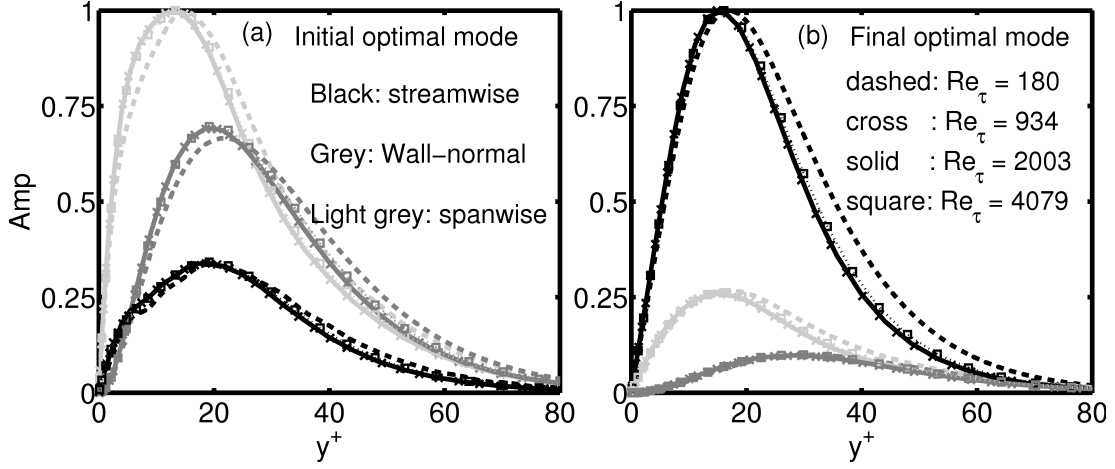


Fig. 2.4 Amplitude of velocity components of the optimal modes at the $\lambda_x^+ = 400$ and $\lambda_z^+ = 90$. (a) The initial optimal modes are vortical structures like near-wall quasi-streamwise vortices, and (b) the final optimal modes are streaky structures like near-wall streamwise streaks. The shape of the optimal modes, represented by their velocity amplitudes, scale in wall units.

2.3.1 Optimal modes and near-wall structures

Figure 2.4 presents velocity amplitudes of the optimal modes at the $\lambda_z^+ = 90$ and $\lambda_x^+ = 400$ in the four Reynolds number cases. This λ_z^+ is the $\lambda_z^+|_{peak}$ for the three higher Reynolds number flow cases, whereas $\lambda_z^+|_{peak}$ in the $Re_\tau = 180$ flow is 100. This difference in the $Re_\tau = 180$ flow case is because this flow's profile is an empirical fit given in Ref. [1], while the other three flow profiles are from DNS data. For the same reason, there is a small difference in the shapes of the optimal modes in the $Re_\tau = 180$ flow case as compared with those in the other Reynolds number cases. Although not shown here, $\lambda_z^+|_{peak}$ and the corresponding optimal modes in the $Re_\tau = 180$ DNS flow profile case are checked to match with those in the higher Reynolds number cases. This shows that these small differences are not because the $Re_\tau = 180$ flow is a lower Reynolds number case.

The velocity amplitudes represent the wall-normal distribution of perturbation energy in the optimal modes. Figure 2.4 shows that the peak in energy in these modes is at $y^+ \approx 15 - 20$ and most of their energy is in the region $y^+ < 60$, which shows that these modes exist in the near-wall region. Figure 2.4 (a) shows the velocity amplitudes of the initial optimal modes. They have most of their energy in the spanwise and wall-normal velocity components, and the initial optimal mode in the $Re_\tau = 2003$ flow case is plotted in the $y - z$ plane in figure 2.5 (a). The shape of this mode shows that it is like a vortical structure with vorticity in the streamwise direction, which is a property of quasi-streamwise vortices.

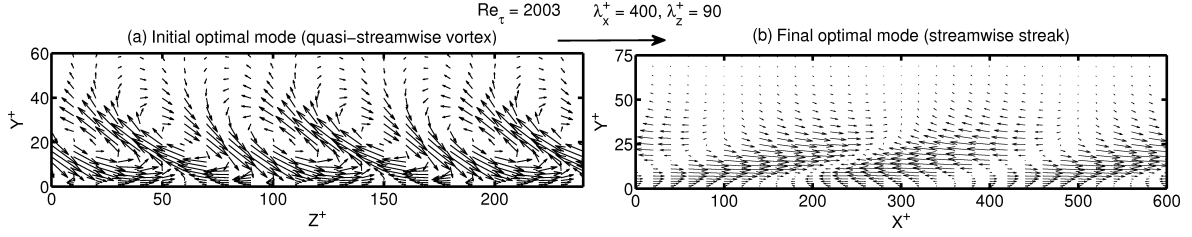


Fig. 2.5 Results for the $\lambda_x^+ = 400$ and $\lambda_z^+|_{peak} = 90$ in the $Re_\tau = 2003$ flow case. (a) The initial optimal mode in the $y-z$ plane, it has a vortical structure like that of near-wall quasi-streamwise vortices. (b) The final optimal mode in the $x-y$ plane (the y -axis is twice magnified). Regions with the positive streamwise velocity have the negative wall-normal velocity and vice-versa, so they belong to the Q4 and Q2 events. Here Q2 and Q4 refers to 2nd and 4th quadrants, respectively, of fluctuating u and v phase plots.

These vortices have a wall-normal component of velocity, which on the one side transports high speed fluid towards the wall and on the other side lifts low speed fluid away from the wall. These energetic processes are known as sweeps and ejections. The velocity amplitudes of the final optimal modes are shown in figure 2.4 (b). These mode have most of their energy in the streamwise velocity component, and the final optimal mode in the $Re_\tau = 2003$ flow case is plotted in the $x-y$ plane in figure 2.5 (b). The shape of this mode shows that it consists of packets of Q4 (positive u and negative v) and Q2 (negative u and positive v) events, which are the properties of sweeps and ejections, respectively. The lifted low speed fluid after the ejections elongates and forms near-wall low-speed streaks, and the high speed fluid after the sweeps forms near-wall high-speed streaks. Therefore, the sweeps and ejections are indirect indicators of the near-wall streaks [11]. Figures 2.4 and 2.5 show that the present approach captures the formation of the sweeps and ejections like structures, and hence of the near-wall streaks, from the quasi-streamwise vortices like structures.

Linear amplification analysis gives information about which wavelength structures in flows are preferred, i.e. get more energy amplification from the mean flow. Based on λ_x^+ and the corresponding $\lambda_z^+|_{peak}$, a relation for peak in the energy spectra is obtained. Because these optimal structures are mainly influential in the near-wall region, this relation is compared with the one observed in the near-wall region in DNS. Jimenez *et al.* (2004) [8] showed that spectra of energy in streamwise velocity at $y^+ = 16$ has a peak that follows the relation: $\lambda_z^+ = 13 (\lambda_x^+)^{1/3}$. This is very close to the peak in energy predicted by the present linear amplification analysis: $\lambda_z^+|_{peak} \approx 12.5 (\lambda_x^+)^{1/3}$. This relation is based on the $\lambda_z^+|_{peak}$ results for the flow cases $Re_\tau = 934, 2003$, and 4079 , such that the square of the deviation in $\lambda_z^+|_{peak}$ is minimised by adjusting the pre-multiplication factor while keeping the exponent

(= 1/3) constant.

2.4 Non-modal amplification analysis at higher wavelengths

Figure 2.6 presents the maximum transient growth, G_{max} , for the (a) $Re_\tau = 934$, (b) 2003, and (c) 4079 flows as functions of λ_z and λ_x . The input streamwise wavelengths are in the range from $\lambda_x^+ = 800$ to $\lambda_x = 20$. The peaks in energy amplification are at the spanwise wavelengths ($\lambda_z|_{peak}$) that depend upon the input λ_x . In figure 2.3 it is shown that peaks in G_{max} are at the small spanwise wavelengths $\lambda_z^+ \approx 100$ when the input $\lambda_x^+ = 200 - 800$, and in figure 2.6 it is shown that peaks in G_{max} are at the large spanwise wavelengths $\lambda_z \approx 2$ when the input $\lambda_x = 4 - 20$. These peaks correspond to the two peaks in G_{max} from the eddy viscosity based analysis shown in Pujals *et al.* (2009) [2], and also shown in figure 2.2. Apart from these two peaks, the present analysis also finds peaks in G_{max} at the intermediate spanwise wavelengths from $\lambda_z^+ \approx 450$ to $\lambda_z \approx 1.75$ when the input streamwise wavelengths are from $\lambda_x^+ = 800$ to $\lambda_x \approx 3$. The eddy viscosity-based analysis, however, finds minimum in G_{max} in this wavelength region. The inferred energy spectra from the present analysis, therefore, have a maximum in energy at these intermediate spanwise wavelength, while the inferred energy spectra from the eddy viscosity based analysis have a minimum in energy in the same range. DNS show a maximum in energy spectra in this intermediate spanwise wavelength range [3, 9], which matches better with the results from the present analysis as compared to those from the eddy viscosity based analysis.

Figure 2.7 shows $\lambda_z|_{peak}$ as function of λ_x in (a) wall-units and (b) in outer units. $\lambda_z|_{peak}$ increases monotonically with λ_x . At $\lambda_x \approx 3$, $\lambda_z|_{peak}$ suddenly jumps to a higher value as indicated by the dashed lines. Interestingly this λ_x matches with the threshold wavelength used to differentiate the LSMs and VLSMs in Guala *et al.* (2006) [6]. They used $\lambda_x \approx 3$, based on the net force spectra, while Bailey & Smits (2010) [35] used $\lambda_x \approx 6$, based on the energy autospectra, as the threshold wavelength. In this chapter, the features of the optimal modes are discussed by grouping them in three wavelength regions. The first region is $\lambda_x^+ = 800$ to $\lambda_x = 2.75$ before the $\lambda_z|_{peak}$ jump and is labelled intermediate wavelength range. This is also the range of wavelengths where hairpin vortices and the LSMs are reported in experiments and DNS. The second region is $2.75 < \lambda_x < 6$ and is labelled transition wavelength range, some researchers include this in the LSMs while the others in the VLSMs. The third region is $\lambda_x > 6$ and is labelled large wavelength range, this is the range of wavelengths where the VLSMs are reported. The transient growth calculations are performed only up to the $\lambda_x = 20$ perturbations.

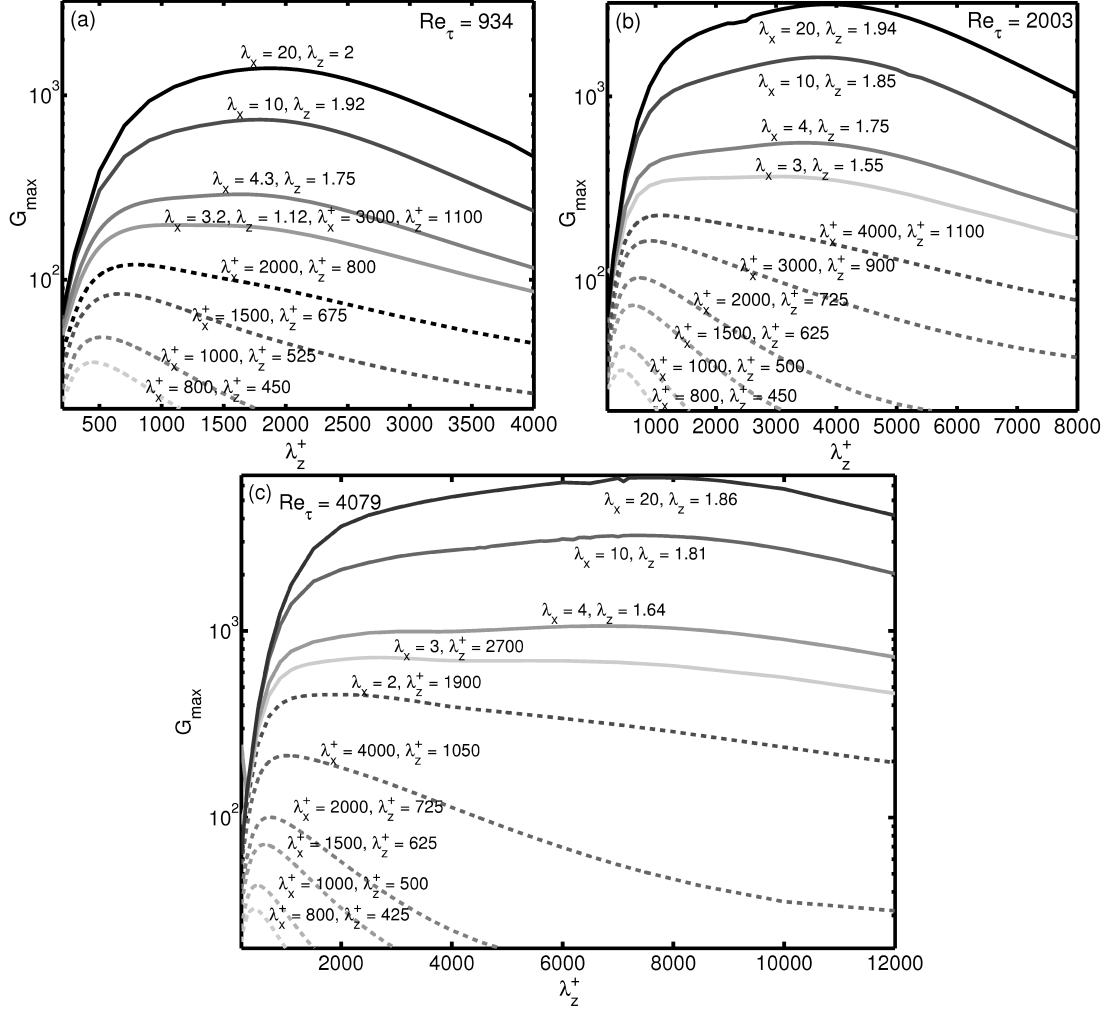


Fig. 2.6 The maximum transient growth, G_{max} , at the higher wavelengths for the flows at (a) $Re_\tau = 934$, (b) $Re_\tau = 2003$, and (c) $Re_\tau = 4079$. the value of $\lambda_z|_{peak}$ varies from the intermediate wavelengths (from $\lambda_z^+ = 450$ to $\lambda_z = 1.5$) to the large wavelengths ($\lambda_z \approx 2$) depending upon the input λ_x . The value of $\lambda_z|_{peak}$ increases with increasing λ_x . The present analysis finds peaks in G_{max} at the intermediate wavelengths, while the EVM based analysis finds only minima in G_{max} at these intermediate wavelengths. The DNS data for turbulent channel flows shows peak in the energy spectra at these intermediate wavelength, which is in agreement with the present analysis.

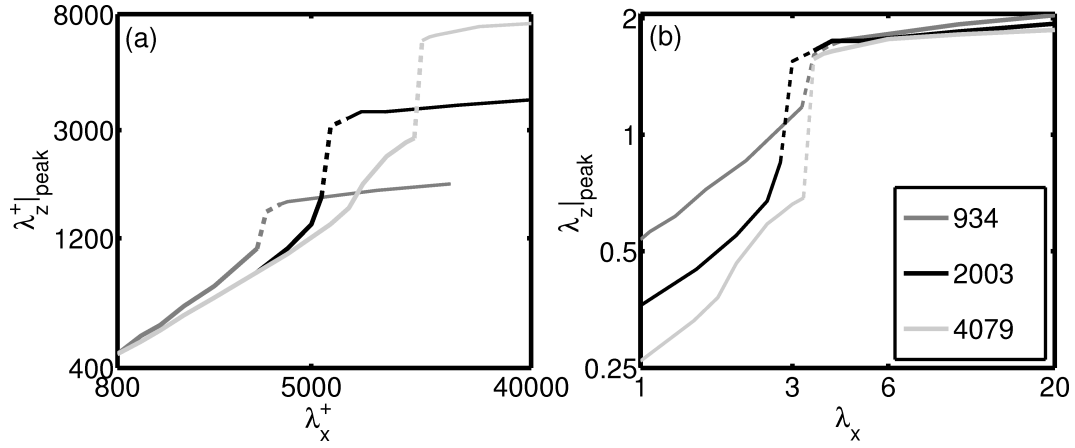


Fig. 2.7 The preferred spanwise wavelength ($\lambda_z|_{peak}$) as functions of the input streamwise wavelength in (a) inner units and (b) outer units. Frame (b) shows that there is a jump in the value of $\lambda_z|_{peak}$ at $\lambda_x \approx 3$, after which $\lambda_z|_{peak}$ scales nearly in outer units. The jump region is indicated by dashed lines, and corresponding λ_x matches well with the threshold wavelength used in Ref. [6] for differentiating between the LSMs and VLSMs. The region before the jump does not scale in either inner or outer units, except an initial part which scales in inner units.

It is investigated whether the optimal modes and the inferred energy spectra from the present linear amplification analysis match with those of coherent structures observed in experiments and DNS. In the present analysis, the wall-normal location at which a final optimal mode contains most energy (in the streamwise velocity) is labelled $y^+|_{dominant}$, and it is assumed to be the wall-normal location of the corresponding optimal modes.

2.4.1 Intermediate wavelength optimal modes

The intermediate wavelength is the region of λ_x before the jump in $\lambda_z|_{peak}$, which is from the $\lambda_x^+ = 800$ to $\lambda_x = 2.75$. As mentioned several times in this chapter, the major advantage of the present approach is that it finds peaks in the G_{max} in this wavelength range while the eddy viscosity based approach finds only minima in the same wavelength range. In order to show that this really is an advantage, it is essential to show that kinematic properties of the optimal modes and energy spectra match with those of coherent structures found in experiments and DNS.

Two pairs of the optimal modes are presented in figures 2.8 and 2.9 for all the three Reynolds number cases. The first pair is at the $\lambda_x^+ = 1500$ and the second pair is at the $\lambda_x = 2$. The spanwise wavelengths of the optimal modes are the corresponding $\lambda_z|_{peak}$ values in each case, which are 0.72 and 0.83 in outer units (675 and 775 in wall units) in the

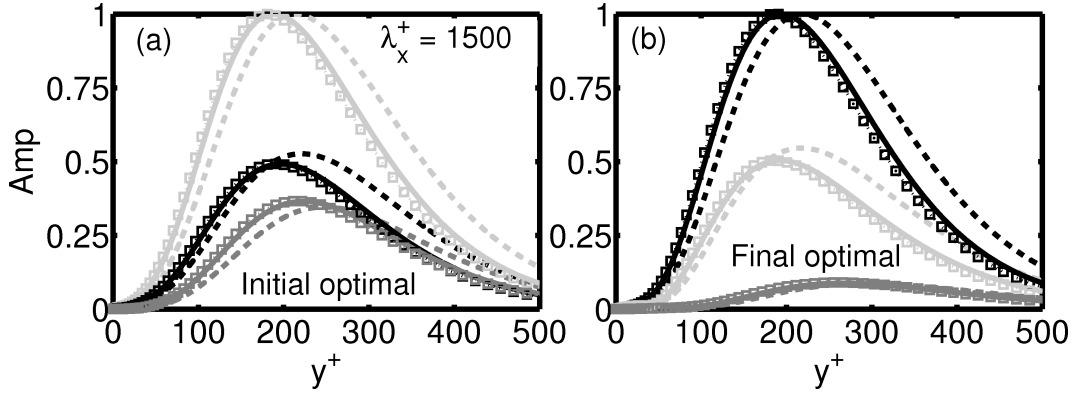


Fig. 2.8 The normalised velocity amplitudes of the (a) initial and (b) final optimal modes at the $\lambda_x^+ = 1500$ and the corresponding $\lambda_z^+|_{peak}$, for the $Re_\tau = 934$ (dashed line), 2003 (solid line), and 4079 (squares) flow cases. The black colour is for the streamwise velocity component, grey is for the wall-normal velocity component and light-grey is for the azimuthal velocity component. These modes have similarities with the optimal modes shown in figure 2.4 and 2.9. The initial optimal modes, which have most of their energy in the spanwise velocity and have significant energy in the wall-normal velocity, are like vortical structures. The final optimal modes have most of their energy in the streamwise velocity like streaky structures. These modes extend to the wall but are dominant in the outer layer.

$Re_\tau = 934$ case, 0.31 and 0.55 in outer units (625 and 1100 in wall units) in the $Re_\tau = 2003$ case, and 0.15 and 0.47 in outer units (625 and 1900 in wall units) in the $Re_\tau = 4079$ case.

These optimal modes have similarities with the optimal modes in the near-wall region shown in figure 2.4. The initial optimal modes have most energy in the azimuthal velocity component and significant energy in the wall-normal velocity component, which shows they are vortical type structures. The final optimal modes have most energy in the streamwise velocity component, which shows they are streaky structures. These results are interpreted such that the initial vortical structures get linearly amplified to form the final streaky structures. Such interpretation of the results is in accordance with the observations reported in Refs. [7, 14, 30, 32]. In their interpretation, vortical structures are referred to as hairpins or half-formed hairpins and these hairpin vortices produce low-speed streaky structures in the outer layer (and there are almost equal number of high-speed streaky structures as well). The longer streaky structures are formed by a combined action of several hairpin vortices, called packets of hairpin vortices whose formation mechanism is proposed in [33]. Various kinematic properties of the optimal structures with those of observed coherent structures are compared to further investigate the match between them.

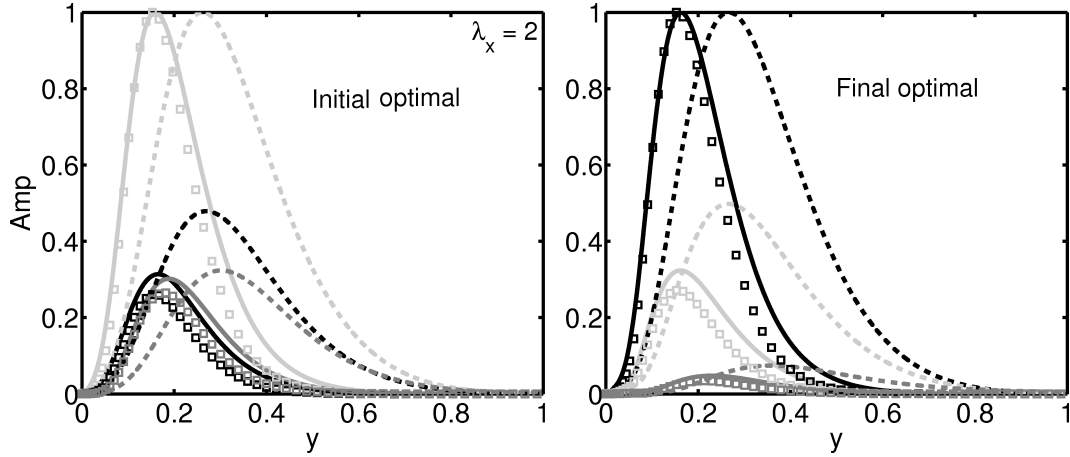


Fig. 2.9 The normalised velocity amplitudes of the (a) initial and (b) final optimal modes at the $\lambda_x = 2$ and the corresponding $\lambda_z|_{peak}$, for the $Re_\tau = 934$ (dashed line), 2003 (solid line), and 4079 (squares) flow cases. These modes have similarities with the optimal modes shown in figures 2.4 and 2.8. The initial optimal modes, which have most of their energy in the spanwise velocity and have significant energy in the wall-normal velocity, are like vortical structures. The final optimal modes have most of their energy in the streamwise velocity like streaky structures. These modes extend to the wall but are dominant in the outer layer.

Figures 2.8 and 2.9 show that the optimal modes at the $\lambda_x^+ = 1500$ are closer to the wall as compared to the optimal modes at the $\lambda_x = 2$. In figures 2.10 (a) and (b) $y^+|_{dominant}$ of the final optimal modes as functions of their λ_z^+ and λ_x^+ , respectively, are shown. These plots show that as the structures move away from the wall they get wider and longer. It has also been observed for structures in the same wavelength region in Ref. [6] (figure 4(d) of their paper) and in Ref. [35] (figure 6 of their paper), and Ref. [9] also quoted that generally the structures get longer and wider as they separate from the wall. Based on figure 2.10, the best fit, on minimising the standard deviation, for these optimal modes' width and length with their wall-normal location is found to be $\lambda_z^+ \propto y^+|_{dominant}$ and $\lambda_x^+ \propto (y^+|_{dominant})^{1/0.56}$, respectively. It is also inferred that the maximum in energy spectra for optimal modes from these results is $(\lambda_z)^{1.79} \propto \lambda_x$. The peak in energy spectra found in DNS data at the $Re_\tau = 2003$ has relations $\lambda_z^2 \propto \lambda_x$ for the streamwise velocity autospectra and $\lambda_z \propto \lambda_x$ for the wall-normal velocity and spanwise velocity autospectra as shown in figure 2 of Ref. [9]. Given that the streamwise velocity component contains most of the energy, relation for the peak in energy spectra of optimal modes found from the present analysis is in a reasonably good agreement with the observed peak in energy spectra in DNS shown in Ref [9]. It is also noted that $\lambda_z \propto y$ agrees with the self-similar eddies proposed by Townsend [18]. The relation $\lambda_x \propto (y^+|_{dominant})^{1/0.56}$ still shows the self-similar nature of the eddies but does not

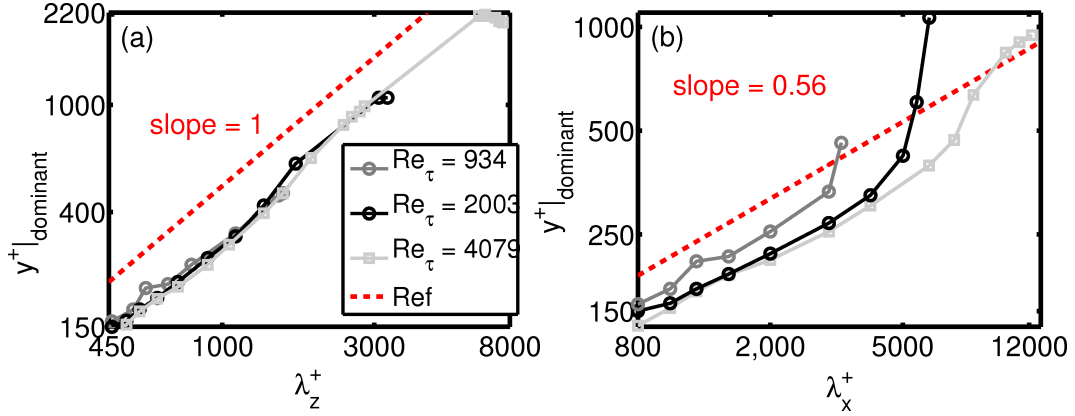


Fig. 2.10 The $y^+|_{\text{dominant}}$ as functions of (a) λ_z^+ and (b) λ_x^+ . These plots show that structures get wider and longer as they move away from the wall.

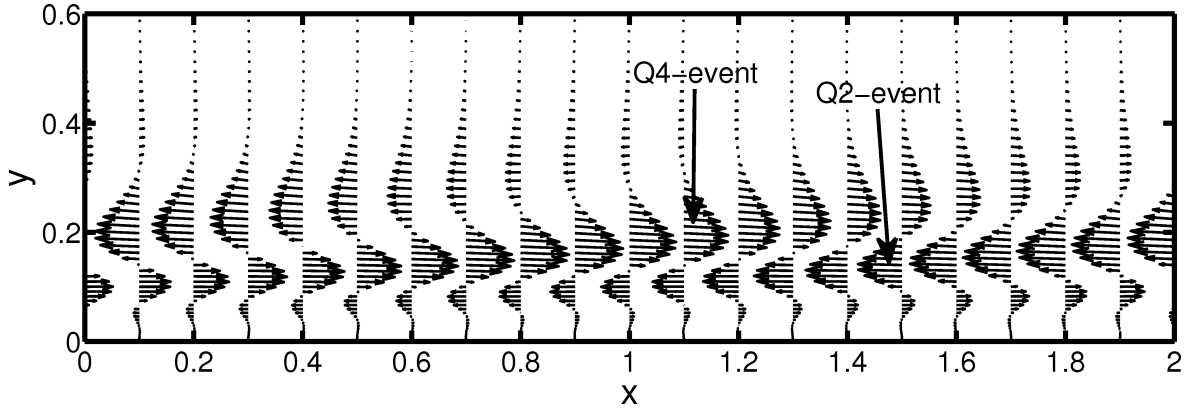


Fig. 2.11 Quiver plot of the final optimal mode at the $\lambda_x = 2$ and the corresponding $\lambda_z|_{\text{peak}} = 0.55$ in the $Re_\tau = 2003$ flow case in the $x-y$ plane. This plot shows that the mode contains packets of Q2 and Q4 events, which is observed in Ref. [7] for the streaky structures. The Q2 and Q4 events contribute towards the negative \overline{uv} -Reynolds stress component.

match with the relation proposed by Townsend [18]. This mismatch in λ_x scaling is also noted in Ref. [65].

Figure 2.11 shows a quiver plot of velocity vectors in the streamwise-wall-normal plane for the optimal mode at the $\lambda_x = 2$ and $\lambda_z|_{\text{peak}} = 0.55$ in the $Re_\tau = 2003$ case. This figure shows that the streaky structures in the final optimal mode consist of Q2 (negative u and positive v) and Q4 (positive u and negative v) events. This is very important because almost all the observed streaky structures in experiments consist of the Q2 or Q4 events, and this is why the \overline{uv} -Reynolds stress component is negative [7].

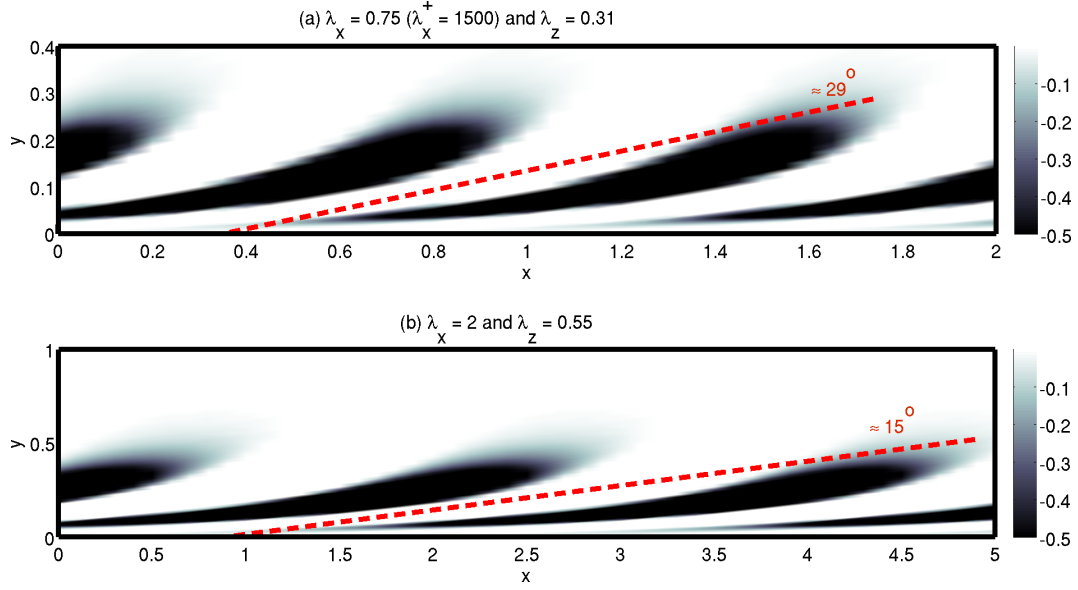


Fig. 2.12 Low speed streaky regions in the final optimal modes at the (a) $\lambda_x^+ = 1500$ and (b) $\lambda_x = 2$ and the corresponding $\lambda_z|_{peak}$ in the $Re_\tau = 2003$ flow case are shown. The maximum amplitude ($= -0.5$) is arbitrarily decided to be one-sixth of the maximum amplitude in the final optimal mode. Inclination angles of the streaks with the wall are shown by the red dashed line, which are based on visualisation alone. The inclination of the streak in the $\lambda_x = 2$ optimal mode is close to the inclination of the $\Delta x \approx 2.5$ low-speed streak observed in Ref. [7].

Figure 2.12 shows approximately the angle of inclination of low-speed streaky parts of the final optimal modes at the (a) $\lambda_x = 0.75$ and $\lambda_z|_{peak} = 0.31$ and (b) $\lambda_x = 2$ and $\lambda_z|_{peak} = 0.55$ in the $Re_\tau = 2003$ flow case. The maximum negative amplitude in the figure ($= -0.5$) is arbitrarily decided as one-sixth of the maximum amplitude in the optimal mode for a good visualisation. The comparison of the inclination angle with that in experiments can only be approximate, because even in experiments the inclination angle depends upon arbitrary choices of threshold amplitude, therefore only a quick approximation of the inclination angle, as indicated by the red line that is based on visualisation alone, is considered. This figure shows that the larger low-speed streak has a smaller inclination angle with the wall, and also that the inclination angle of the larger streak matches with that of the $\Delta x \approx 2.5$ streak ($\approx 11^\circ$) reported in figure 8 of Ref. [7].

Another noticeable property of the final optimal modes shown in figures 2.8 and 2.9 is that the v -velocity component is vanishingly small near the wall, while the u - and w -velocity components extend to the wall. This is in line with the observations of Ref. [9], where it is reported that the v -autospectra is detached from the wall while the u - and w -autospectra are attached.

Based on the match of these various kinematic properties; such as peak in the energy spectra, the shapes of the initial and final optimal modes, and the inclination angle; it is concluded that the optimal structures predicted by the present approach are good approximations of the observed coherent structures. It is, therefore, also concluded that the present analysis has an advantage over the EVM-based analysis, because the latter analysis does not find these coherent structures. The EVM-based analysis finds only minima in energy amplification in the intermediate wavelength region, as seen in figure 2.2, and hence predict no optimal structures in this region.

2.4.2 Transition range optimal modes

The transition range is the region of streamwise wavelengths ($2.75 < \lambda_x < 6$), which is considered as the LSMs in Ref. [35] while considered as the VLSMs in Ref. [6]. The optimal modes at the $\lambda_x = 4$, which is right after the region where the $\lambda_z|_{peak}$ jumps, and the corresponding $\lambda_z|_{peak}$ in the three Reynolds number cases are shown in figure 2.13. It is observed that their shape is similar to those of the structures in the intermediate wavelength range shown in figures 2.8 and 2.9. However unlike them these structures do not reach to the wall. This is shown more clearly in frame (c) for the final optimal mode. Their spanwise wavelength ($\lambda_z \approx 1.70$) is close to those of the large wavelength optimal modes in Section 2.4.3, which is similar to those of the VLSMs (one-third of pipe circumference) found in Ref. [35]. The final optimal modes have some similarities with detached LSMs reported in Ref. [35]. They observe that the detached LSMs are as wide as the VLSMs, while unlike the VLSMs they do not extend to the wall.

2.4.3 Large wavelength optimal modes

The large wavelength range includes the $\lambda_x = 6$ to $\lambda_x = 20$ (calculations are performed only up to the $\lambda_x = 20$). The observed eddies in this range are referred to as VLSMs, and the VLSMs as large as $L_x = 14 - 25$ have been reported in experiments [32, 36, 37]. The optimal modes at the $\lambda_x = 20$ and the corresponding $\lambda_z|_{peak}$ for the three flow cases $Re_\tau = 934$, 2003, and 4079 are presented in figure 3.6. These structures scale closely in outer units in terms of their shape and size. The final optimal modes extend to the wall, as shown in frame (c) more clearly. These are the properties of the VLSMs, they scale in outer units [14, 32, 35] and extend to the wall. The spanwise wavelength of the optimal modes also match with the observations in Ref. [35], who find the VLSMs to be approximately one-third of the pipe circumference ($\frac{1}{3}2\pi \approx 2$). The optimal modes, however, have most of their

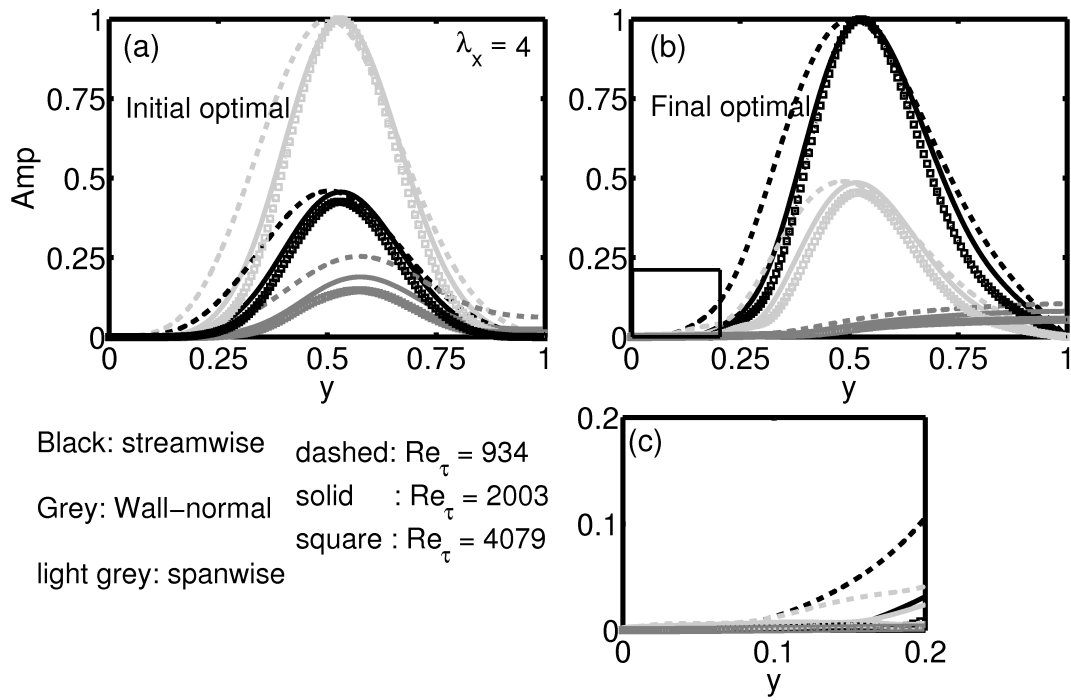


Fig. 2.13 Velocity amplitudes of the (a) initial and (b) final optimal modes at the $\lambda_x = 4$ and the corresponding $\lambda_z|_{peak}$. (c) magnification of the near wall region, indicated by a square box in frame (b). The mode shapes are close to those of the optimal modes in the intermediate wavelength range. However, unlike those mode shapes, these structures do not extend to the wall as shown for the final optimal mode in frame (c). The mode shapes nearly scales in outer units like the VLSMs.

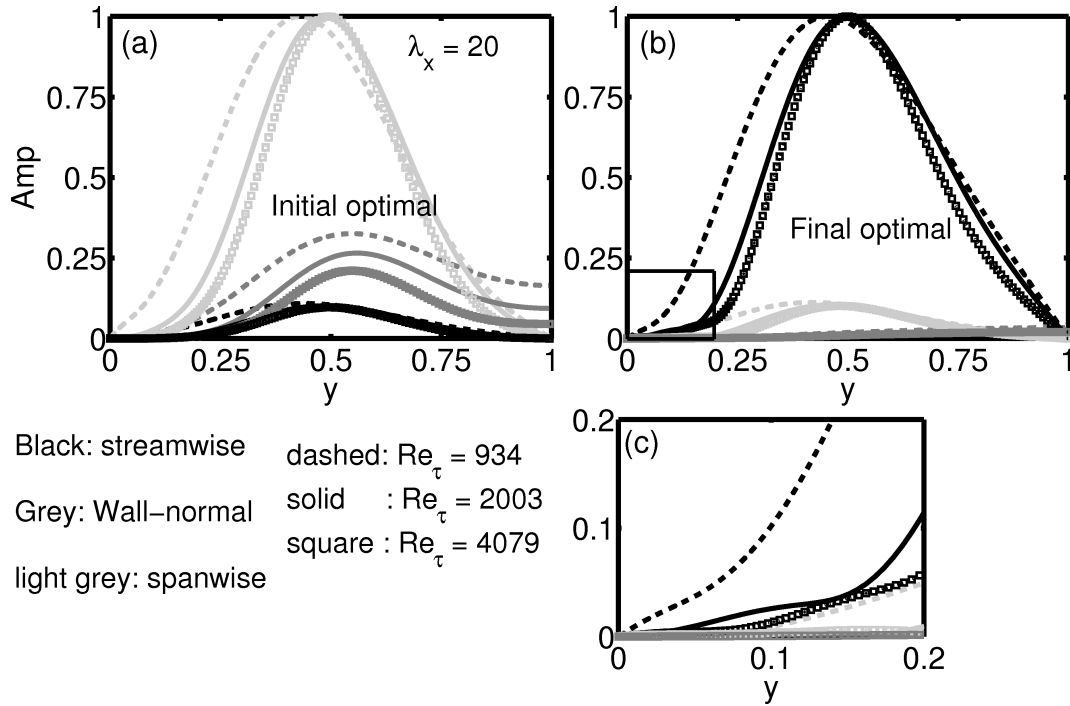


Fig. 2.14 Velocity amplitudes of the (a) initial and (b) final optimal modes at the $\lambda_x = 20$ and the corresponding $\lambda_z|_{peak}$. (c) magnification of the near wall region, indicated by a square box in frame (b). The mode shapes scale closely in outer units, and extend to the wall. These are properties of the VLSMs. The velocity amplitude, however, is maximum at $y \approx 0.5$ while the VLSMs have most energy at the $y \approx 0.2$.

energy outside the logarithmic layer (with maximum at $y \approx 0.5$), whereas it is clear from experimental observations that VLSMs have most of their energy inside the logarithmic layer (with maximum at $y \approx 0.2$) [6, 34]. It seems that the present analysis is poor at approximating the shape of the VLSMs in terms of their wall-normal energy distribution. The reason for that is because the present analysis is applicable only in the region of high mean shear, the VLSMs, however, exist from high mean shear near-wall region to zero mean shear centre of the channel. Their region of existence, therefore, is outside the zone of applicability of rapid distortion theory, on which the present analysis is based.

The optimal modes at the $\lambda_x = 20$ and the corresponding $\lambda_z|_{peak} = 3.4$ in the $Re_\tau = 2000$ and $Re_\tau = 2003$ flow cases calculated from the eddy viscosity based analysis are shown in figure 2.16. The value of $\lambda_z|_{peak}$ is around two times higher than the observed azimuthal width of the VLSMs (≈ 2) in Ref. [35], but the modes have most of their energy in the logarithmic layer ($y \approx 0.3$) like that of the VLSMs. The optimal mode shapes shift closer to the wall in the eddy viscosity-based approach because the eddy viscosity is lower in the

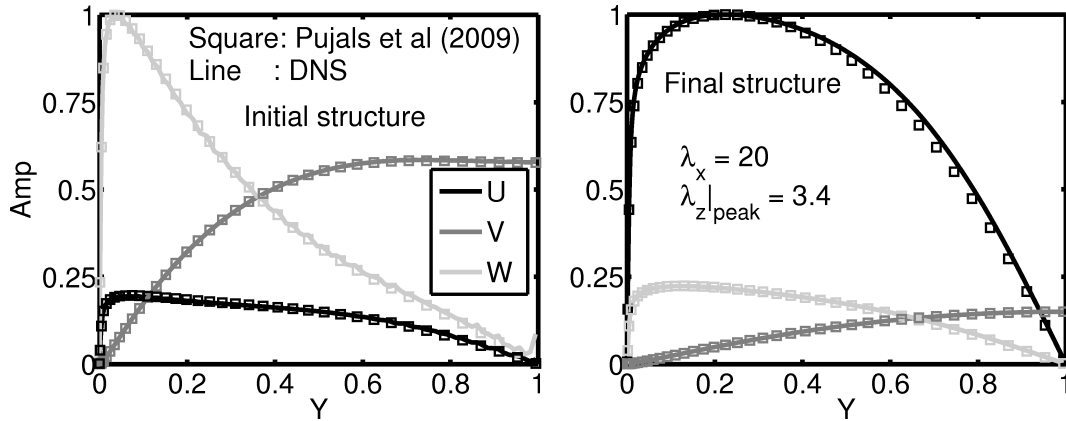


Fig. 2.15 Velocity amplitudes of the (a) initial and (b) final optimal modes at the $\lambda_x = 20$ and the corresponding $\lambda_z|_{peak} = 3.4$ in the $Re_\tau = 2000$ (squares) and $Re_\tau = 2003$ (solid line) flow cases calculated from the eddy viscosity based approach. Although $\lambda_z|_{peak}$ is higher than the observed spanwise extent of the VLSMs, the wall-normal energy distribution in the final optimal mode closely matches with that of the VLSMs. The final optimal modes have most of their energy in the logarithmic layer, with maxima at $y \approx 0.3$, which matches well with the observation that the VLSMs are most energetic at $y \approx 0.2$.

near-wall region and increases towards the centre. The modes, therefore, are damped higher in the region closer to the centre than they are in the region closer to the wall.

The origin of the VLSMs is a topic of debate in many recent papers. One popular theory is that the VLSMs are formed by merging of the LSMs and there are many experiments to support this theory, such as in Refs. [6, 32, 38]. Adrian (2007) [14] discussed that if merging of the LSMs is the sole source of formation of the VLSMs, it does not satisfactorily explain how the VLSMs contain the substantial turbulent kinetic energy and Reynolds shear stress as observed in Refs. [6, 32, 36]. Based on the experiments of Ref. [35], Smits *et al.* (2011) [43] also discussed that it is unlikely that the VLSMs form from the merging of the LSMs. Adrian (2007) [14] also pointed out that the formation of the VLSMs through merging of the LSMs opposes the classical Kolmogorov energy cascade concept, which is supported at high Reynolds numbers showing transfer of energy from large to small scales. Therefore, there must be a mechanism for the production of kinetic energy at the largest scale. The present approach, along with other linear amplification approaches [2, 10], supports the idea that there is a mechanism for the production of the turbulent kinetic energy at the large scales through energy transfer from the mean flow shear.

2.5 Summary and Conclusion

In this chapter, linear amplification analysis is performed on the Navier–Stokes equations linearised over the mean velocity profile to extract coherent structures in turbulent channel flows. The effect of the neglected nonlinear terms is modelled as the input streamwise wavelengths of perturbations, where the input values are based on experimental and DNS observations. Nonlinear processes, such as energy transfer from large-scale coherent structures to small-scale background turbulence and merging or breaking up of primary structures to form new coherent structures, are not accounted for by the present analysis. Therefore, the analysis is limited only to primary forms of coherent structures. The most amplified perturbations and the corresponding initial optimal modes from the analysis are interpreted as approximations of coherent structures in fully nonlinear turbulent channel flows. It is acknowledged that modelling the effect of the neglected nonlinear terms as the input streamwise wavelengths is very rudimentary, nevertheless various kinematic properties of the optimal modes and the maxima in energy amplification from the analysis match with those of the observed coherent structures in wall-bounded turbulence DNS and experiments.

The first type of structures found from the present analysis are at the small streamwise wavelengths ($\lambda_x^+ = 200 - 800$) in Section 2.3. The peak in the transient growth, G_{max} , for structures in this small streamwise wavelengths range is at the spanwise wavelength equal to one hundred wall-units ($\lambda_z^+|_{peak} \approx 100$) as shown in figure 2.3. This matches well with the observed spanwise spacing of near-wall streaks in experiments [21, 27]. Moreover, the corresponding initial and final optimal modes are of the shape of near-wall vortical and near-wall streaky structures, respectively, as shown in figures 2.4 and 2.5. Therefore, it is concluded that the present analysis captures the formation of the near-wall streaks from the quasi-streamwise vortices. The maxima in energy spectra in the near-wall region from the present analysis, which is based on λ_x^+ and the corresponding $\lambda_z^+|_{peak}$ values, is found to closely follow the relation $\lambda_z^+|_{peak} \approx 12.5(\lambda_x^+)^{1/3}$, which is in a good match with the observed peak in streamwise energy spectra in the near-wall region in Jimenez *et al.* (2004) [8] ($\lambda_z^+|_{peak} \approx 13(\lambda_x^+)^{1/3}$).

The second type of structures found from the present analysis are at the intermediate streamwise wavelengths (from $\lambda_x^+ > 800$ to $\lambda_x^+ < 3$) in Section 2.4.1. The peaks in the transient growth, G_{max} , for the structures in this streamwise wavelength range vary from the $\lambda_z^+ = 425$ to $\lambda_z \approx 1$ as shown in figures 2.6 and 2.7. On the basis of their shapes (shown in figures 2.8 and 2.9), the initial and final optimal modes are compared with large

vortical structures and the LSMs, respectively. Various kinematic properties of the optimal structures are shown to be in a good match with those of the observed structures. It is found that these optimal structures get wider in the spanwise direction and longer in the streamwise direction as they get away from the wall as shown in figure 2.10. This property matches with those of the LSMs found in Refs. [6, 35]. The peak in energy spectra, based on $\lambda_z^+|_{peak}$ and the corresponding λ_x^+ , from the present analysis is found to be $(\lambda_z^+)^{1.79} \propto \lambda_x^+$, which also matches with the energy spectra in Ref. [9]. Other properties, such as inclination angle of the low-speed streaky parts with the wall and the phase between the wall-normal and streamwise velocity components, also match with those of the LSMs.

Another interesting result from the present analysis is that there is a jump in $\lambda_z^+|_{peak}$ value at the $\lambda_x \approx 3$ as shown by the dashed lines in figure 2.7. This value of the streamwise wavelength matches with that of the threshold wavelength used in Guala *et al.* (2006) to differentiate between the LSMs and VLSMs.

The third type of structures from the present analysis are at the large streamwise wavelength ($\lambda_x \geq 6$) in Section 2.4.3. The preferred spanwise wavelength of these structures ($\lambda_z|_{peak} \approx 2$), their scaling in outer units, and the fact that they extend to the wall match with the observed features of the VLSMs. Unlike VLSMs, which are most energetic in the logarithmic layer, however, these optimal modes have most of their energy outside the logarithmic layer.

The main conclusion of the analysis presented in this chapter is that this analysis is simpler than the EVM-based approach in the literature yet the results are in better match with DNS and experiments. This is summarised in figure 2.16, where the preferred λ_z corresponding to various λ_x values from the present analysis (black dots) and the EVM-based analysis (red diamonds) in the $Re_\tau = 2003$ flow case are plotted. For some λ_x values there are two points, this is because there are two peaks in G_{max} at those λ_x perturbations as shown in figure 2.2 (b) for the EVM-based analysis. The dashed magenta line is for the streamwise velocity energy spectra in the near-wall region in Jimenez *et al.* (2004) [8]. The dashed blue line is for the streamwise velocity energy spectra in the $y = 0.1 - 0.3$ region in Jimenez & Hoyas (2008) [9] (the relation is known up to a constant of proportionality). It is seen in this figure that in the small streamwise wavelength region ($\lambda_x^+ \leq 800$), where the near-wall structures are observed, the black dots from the present analysis are very close to the magenta line while the red diamonds from the EVM-based analysis are all at the $\lambda_z = 75 - 85$. The bigger drawback from the EVM-based analysis is that there are no red squares in the intermediate λ_z region. This is the range of wavelengths where the LSMs are observed. The black dots from the present analysis show that they are in a good match with

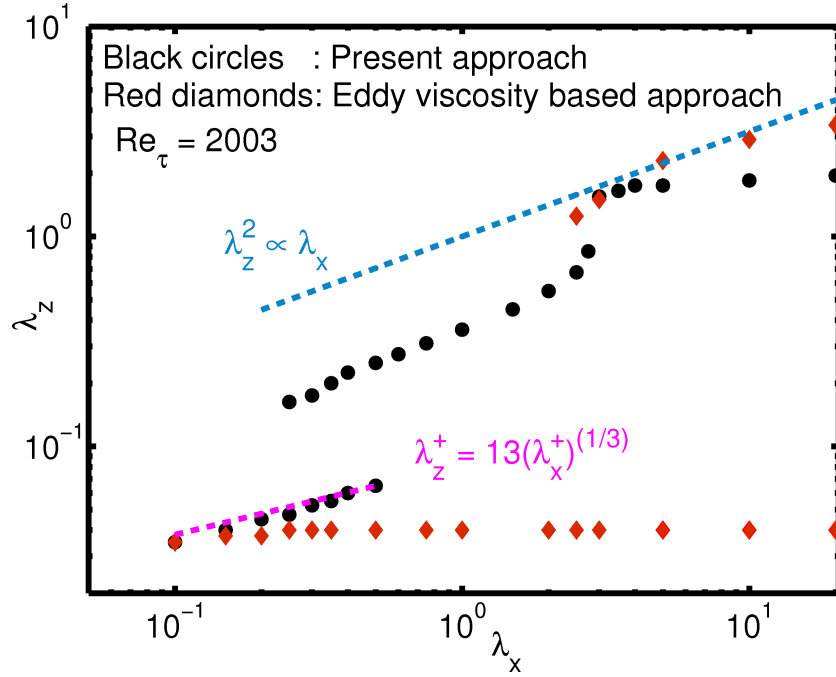


Fig. 2.16 The preferred λ_z corresponding to the various λ_x values from the present analysis (black dots) and the EVM-based analysis (red diamonds) in the $Re_\tau = 2003$ flow case are shown. For some λ_x values there are two points. This is because there are two peaks in G_{max} at those λ_x perturbations as shown in figure 2.2 (b). The dashed magenta line is for the streamwise velocity energy spectra in the near-wall region in Jimenez *et al.* (2004) [8]. The dashed blue line is for the streamwise velocity energy spectra in the $y = 0.1 - 0.3$ region in Jimenez & Hoyas (2008) [9] (the relation is known up to a constant of proportionality). The biggest drawback in the EVM-based analysis is that there are no red squares in the intermediate λ_z region. This is the range of the wavelengths where the LSMs are observed. The black dots from the present analysis show that they are in a good match with the slope of the blue line.

the slope of the blue line, and various kinematic properties of the corresponding optimal modes are shown to be in good match with the observed LSMs in Section 2.4.1. Beyond the $\lambda_x = 5 - 6$ and $\lambda_z = 2 - 3$, there are no reliable spectra from experiments or DNS, therefore, the results from the analyses in that wavelength range cannot be compared against any relation.

A major consequence of the results shown in this chapter is that the present analysis can be used in control applications in place of the EVM-based analysis, such as in Moarref & Jovanovic (2012) [87]. Another consequence is that the present analysis can be used for obtaining energy spectra in high Reynolds number flows, provided that the mean velocity is known for those flows.

Chapter 3

RANS-based linear amplification analysis

In Chapter 2, stability analysis based on the linearised Navier–Stokes equations is used. The focus of this Chapter is on stability analysis based on the linearised RANS equations.

3.1 Introduction

The Navier–Stokes equations linearised over the turbulent mean flow profile for stability analysis have been in use for a long time since the work of Malkus (1956) [72]. Reynolds & Hussain (1972) [76], however, were the first to introduce the use of turbulence models to augment the linearised Navier–Stokes equations. Their purpose was to include the effect of wave-induced perturbations in the Reynolds stress on the behaviour of small external wave perturbations. They concluded that a simple eddy viscosity model, with a constant eddy viscosity profile, is effective in modelling the wave-induced perturbations in the Reynolds stress, and the resulting analysis predicts the behaviour of external wave perturbations that is not substantially different from their actual behaviour. They also proposed that there is a need for better models to obtain quantitatively better results.

Recently, del Alamo & Jimenez (2006) [10] used a similar EVM-based analysis as Reynolds & Hussain (1972) [76] to predict coherent structures in turbulent channel flows, and their analysis is later corrected by Pujals *et al.* (2009) [2]. Cossu *et al.* (2009) and Willis *et al.* (2010) [68, 79] also used similar analyses to find coherent structures in turbulent boundary layer and pipe flows, respectively. These researchers predicted near-wall structures and very-large-scale-motions (VLSMs) in these flows with some success. Crouch *et al.* (2007) and Crouch *et al.* (2009) [77, 78] used the Spalart-Allmaras model-based

linearised RANS equations to successfully predict the onset of transonic buffet in high Reynolds number flows around a circular cylinder and aerofoils, respectively. Meliga *et al.* (2012) and Moarref & Jovanovic (2012) [87, 88] have further extended the application of the linearised RANS-based analyses by applying them for sensitivity analysis of a 2-D wake flow past a square cylinder and for designing model-based control for the drag reduction in a turbulent channel flow, respectively. Success of the above mentioned studies encourages the development in the direction of the linearised RANS-based analyses.

In this chapter, EARSM-based linearised RANS equations are derived for the purpose of stability analysis, where the EARSM stands for Explicit algebraic Reynolds stress model. The EARSMs are also known as anisotropic eddy viscosity models (AEVMs) and are similar to eddy viscosity models (EVMs). Both type of the models are based on the effective-viscosity hypothesis, according to which the Reynolds stress components depend upon local velocity gradients alone. The EARSMs, however, are based on the general form of the hypothesis, which is given in Refs. [103], and are second-order turbulence models, while the EVMs are based on a simpler form of the hypothesis, given in Refs. [104], and are first-order turbulence models. To my knowledge, this is the only study where a set of the second-order turbulence model-based linearised RANS equations for the purpose of stability analysis are derived. An advantage of using second-order turbulence models is that they have a wider range of application than that of first-order turbulence models. In terms of accuracy in the mean flow calculations, the EARSMs sit somewhere between the EVMs and differential Reynolds stress models (DRSMs) [105, 106].

The EARSM used in this chapter is developed by Gatski & Speziale (1993) [107]. In order to verify the derivation and the associated codes, the EARSM-based linearised RANS equations are applied for energy amplification analysis of turbulent channel flow. The results are compared with those from the EVM-based analysis, also derived in this chapter, and from Pujals *et al.* (2009) [2]. The results are in good qualitative agreement. There are only small quantitative differences, which are, of course, expected from any two stability analyses based on different turbulence models.

In Chapter 2 and in Refs. [4, 98], it is discussed that an eddy viscosity profile based on the full Reynolds stress is too high to be used in stability analysis of channel flow to find coherent structures. Blesbois *et al.* (2013) [98] pointed out that in the original paper of Reynolds & Hussain (1972) [76], the linearised RANS equations were derived for external wave perturbations. Coherent structures in turbulent channel flows, however, are implicitly present, and therefore are not expected to be found from the stability analysis based on the linearised RANS equations. This point is briefly discussed in Section 3.5 in the light of the

derivations for the linearised RANS equations presented in Section 3.2. The damping effect of using the eddy viscosity profile on eigenvalue spectra of wave perturbations in a turbulent channel flow is also shown.

3.1.1 Outline

This chapter is divided into six sections. In Section 3.2, the linearised RANS equations are derived, and the term that represents the wave-induced perturbations in the Reynolds stress is expressed using different turbulence models. The models used in this chapter are the EVM and EARSM. In Section 3.3, the linearised RANS equations for turbulent channel flows are derived. In Section 3.4, the EVM- and EARSM-based linearised RANS equations are applied for energy amplification analysis of turbulent channel flows. In order to verify the derivations and the associated codes for the EARSM-based analysis, the results from the two analyses are compared with each other and with those in the literature. In Section 3.5, the application of the linearised RANS-based analysis to find coherent structures is discussed, and the damping effect of the EVM-based analysis on eigenvalue spectra in a turbulent channel flow is shown.

3.2 Linearised RANS equations

Like Reynolds & Hussain (1972) [76], the triple decomposition of the velocity and pressure fields as $u_i = \bar{u}_i + \tilde{u}_i + u'_i$ and $p = \bar{p} + \tilde{p} + p'$, respectively, are used. Over-line indicates the time-averaged flow fields part, over-tilde indicates the organised wave perturbations part, which are defined using phase-averaging, and superscript ' indicates the disorganised turbulent fluctuations part. On substituting the above decomposition into the Navier–Stokes equations, the time-averaged momentum and continuity equations, respectively, for an incompressible flow are written as:

$$\begin{aligned} \bar{u}_j \partial_j \bar{u}_i &= -\partial_i \bar{p} + \frac{1}{Re} \partial_{jj} \bar{u}_i - \partial_j \overline{u'_i u'_j} - \partial_j \overline{\tilde{u}_i \tilde{u}_j} \\ \partial_j \bar{u}_j &= 0 \end{aligned} \quad (3.1)$$

where ∂_j and ∂_{jj} represent partial differentiation and double partial differentiation in the spatial direction j , respectively. For a statistically stationary flow, and in absence of the organised wave-perturbations, these equations are identical to the Reynolds-averaged Navier–Stokes equations. A statistically stationary turbulent flow is the one in which the mean

quantities, which are defined using ensemble-averaging, do not change with time, and fortunately most turbulent flows are statistically stationary. The term in the momentum equation ($\overline{u'_i u'_j}$), called the Reynolds stress, represents stress in the mean flow equations because of the turbulent fluctuations. Similar to the time-averaged equations, the phase-averaged Navier–Stokes equations are obtained as:

$$\begin{aligned}\partial_t (\tilde{u}_i) &= -(\overline{u_j} + \tilde{u}_j) \partial_j (\overline{u_i} + \tilde{u}_i) - \partial_i (\overline{p} + \tilde{p}) + \frac{1}{Re} \partial_{jj} (\overline{u_i} + \tilde{u}_i) - \partial_j \widetilde{u'_i u'_j} \\ \partial_j (\overline{u_j} + \tilde{u}_j) &= 0\end{aligned}\quad (3.2)$$

And by subtracting the time-averaged equations, the equations for phase-averaged fields are obtained as:

$$\begin{aligned}\partial_t (\tilde{u}_i) &= -\overline{u_j} \partial_j \tilde{u}_i - \tilde{u}_j \partial_j \overline{u_i} - \partial_i \tilde{p} + \frac{1}{Re} \partial_{jj} \tilde{u}_i + \partial_j (\overline{\tilde{u}_i \tilde{u}_j} - \tilde{u}_i \tilde{u}_j) - \partial_j (\widetilde{u'_i u'_j} - \overline{u'_i u'_j}) \\ \partial_j \tilde{u}_j &= 0\end{aligned}\quad (3.3)$$

In the momentum equation, the last term ($\widetilde{u'_i u'_j} - \overline{u'_i u'_j}$) is interpreted as the wave-induced fluctuations in the Reynolds stress and is labelled r_{ij} in Reynolds & Hussain (1972) [76]. This term is modelled for the small wave perturbations (\tilde{u}_i and \tilde{p}) using turbulence closure models [76], and for such small wave perturbations the second last term ($\overline{\tilde{u}_i \tilde{u}_j} - \tilde{u}_i \tilde{u}_j$) is neglected to obtain the linearised perturbations equations.

In this chapter, the r_{ij} term is derived using the frozen eddy viscosity models, exactly as done in Reynolds & Hussain (1972) [76], and using the frozen EARSIM, similar to as done in Ref. [76]. The term frozen means that turbulent quantities, such as the turbulent kinetic energy (K), turbulence dissipation rate (ϵ), and eddy viscosity profile (ν_t), do not change with the organised wave perturbations. The derivation with full eddy viscosity models, where the assumptions of a frozen model are relaxed, is also discussed but application of such analysis is outside the scope of this study.

3.2.1 Frozen eddy viscosity models

The eddy viscosity models are first-order turbulence closure models. They are based on an effective-viscosity hypothesis, given by Boussinesq (1977) [104], according to which the

Reynolds stress components are given as:

$$\overline{u'_i u'_j} = \frac{2}{3} K \delta_{ij} - \nu_t (\partial_j \overline{u_i} + \partial_i \overline{u_j}) \quad (3.4)$$

where ν_t is the eddy viscosity profile. A common way to calculate the eddy viscosity profile is as $\nu_t = C_\mu \frac{K^2}{\varepsilon}$, where C_μ is a constant which is usually set as 0.09. This definition of eddy viscosity profile is based on homogeneous turbulence, and therefore in very non-homogeneous parts of turbulent flows, such as in the near-wall region, some corrections are required. In simple shear flows, such as in a channel flow, the eddy viscosity profile can simply be calculated as: $\nu_t = -\frac{\overline{u'_i u'_j}}{d\overline{u_i}/dx_j}$, where i is the direction of the mean velocity and j is the direction in which the mean velocity varies [105].

The mean strain rate and rotation rate tensors ($\overline{S_{ij}}$ and $\overline{\Omega_{ij}}$), and the phase-averaged strain rate and rotation rate tensors ($\widetilde{S_{ij}}$ and $\widetilde{\Omega_{ij}}$) are defined in equations 3.5 and 3.6, respectively.

$$\overline{S_{ij}} = \frac{1}{2} (\partial_j \overline{u_i} + \partial_i \overline{u_j}), \quad \overline{\Omega_{ij}} = \frac{1}{2} (\partial_j \overline{u_i} - \partial_i \overline{u_j}) \quad (3.5)$$

$$\widetilde{S_{ij}} = \frac{1}{2} (\partial_j (\overline{u_i} + \tilde{u}_i) + \partial_i (\overline{u_j} + \tilde{u}_j)), \quad \widetilde{\Omega_{ij}} = \frac{1}{2} (\partial_j (\overline{u_i} + \tilde{u}_i) - \partial_i (\overline{u_j} + \tilde{u}_j)) \quad (3.6)$$

The expression for the Reynolds stress components in 3.4 is re-written as:

$$\overline{u'_i u'_j} = \frac{2}{3} K \delta_{ij} - 2\nu_t \overline{S_{ij}} \quad (3.7)$$

The expression for r_{ij} is derived as:

$$r_{ij} = \widetilde{u'_i u'_j} - \overline{u'_i u'_j} = -2\nu_t (\widetilde{S_{ij}} - \overline{S_{ij}}) = -\nu_t (\partial_j \tilde{u}_i + \partial_i \tilde{u}_j) \quad (3.8)$$

This expression of r_{ij} is substituted in equation 3.3, and the nonlinear term is ignored in the equation, to derive the equations for linear perturbations as:

$$\begin{aligned} \partial_t (\tilde{u}_i) &= -\overline{u_j} \partial_j \tilde{u}_i - \tilde{u}_j \partial_j \overline{u_i} - \partial_i \tilde{p} + \frac{1}{Re} \partial_{jj} \tilde{u}_i + \partial_j [\nu_t (\partial_j \tilde{u}_i + \partial_i \tilde{u}_j)] \\ \partial_j \tilde{u}_j &= 0 \end{aligned} \quad (3.9)$$

3.2.2 Full eddy viscosity models

In the full eddy viscosity model-based linearised RANS equations, the assumption that the turbulent quantities, such as K , ε , and ν_t , remain constant is relaxed. Therefore, differential

equations for the turbulent quantities, such as in the Spalart-Allmaras or $K - \varepsilon$ models, need to be linearised and solved. This requires either obtaining the mean flow from the RANS equations, or find a suitable model to which the given mean flow profile, from DNS or experiments, is an approximate solution. This is out of the scope of the present study. In most chapters of this thesis the mean flow profiles come from DNS data, and for Chapter 5 from a commercial software package ANSYS Fluent. The focus in this study is instead on using a second-order turbulence model in deriving the linearised RANS equations.

3.2.3 Frozen explicit algebraic Reynolds stress model

The EARSMs are second order turbulence closure models. They are based on the general form of the effective-viscosity hypothesis, according to which the Reynolds stress anisotropy tensor ($\bar{\mathbf{a}}$) can be written in terms of ten tensorially independent combination groups composed of $\bar{\mathbf{S}}$ and $\bar{\mathbf{\Omega}}$, as shown in equation 3.10. All the higher order combination groups are reduced with the aid of the Cayley-Hamilton theorem [103].

$$\begin{aligned} \bar{\mathbf{a}} = & \quad \bar{G}_1 \bar{\mathbf{S}} + \bar{G}_2 (\bar{\mathbf{S}} \bar{\mathbf{\Omega}} - \bar{\mathbf{\Omega}} \bar{\mathbf{S}}) + \bar{G}_3 \left(\bar{\mathbf{S}}^2 - \frac{1}{3} \text{tr}\{\bar{\mathbf{S}}^2\} \mathbf{I} \right) + \bar{G}_4 \left(\bar{\mathbf{\Omega}}^2 - \frac{1}{3} \text{tr}\{\bar{\mathbf{\Omega}}^2\} \mathbf{I} \right) + \\ & \bar{G}_5 \left(\bar{\mathbf{\Omega}} \bar{\mathbf{S}}^2 - \bar{\mathbf{S}}^2 \bar{\mathbf{\Omega}} \right) + \bar{G}_6 \left(\bar{\mathbf{S}} \bar{\mathbf{\Omega}}^2 + \bar{\mathbf{\Omega}}^2 \bar{\mathbf{S}} - \frac{2}{3} \text{tr}\{\bar{\mathbf{S}} \bar{\mathbf{\Omega}}^2\} \mathbf{I} \right) + \bar{G}_7 \left(\bar{\mathbf{\Omega}} \bar{\mathbf{S}} \bar{\mathbf{\Omega}}^2 - \bar{\mathbf{\Omega}}^2 \bar{\mathbf{S}} \bar{\mathbf{\Omega}} \right) + \\ & \bar{G}_8 \left(\bar{\mathbf{S}} \bar{\mathbf{\Omega}} \bar{\mathbf{S}}^2 - \bar{\mathbf{S}}^2 \bar{\mathbf{\Omega}} \bar{\mathbf{S}} \right) + \bar{G}_9 \left(\bar{\mathbf{S}}^2 \bar{\mathbf{\Omega}}^2 + \bar{\mathbf{\Omega}}^2 \bar{\mathbf{S}}^2 - \frac{2}{3} \text{tr}\{\bar{\mathbf{S}}^2 \bar{\mathbf{\Omega}}^2\} \mathbf{I} \right) + \\ & \bar{G}_{10} \left(\bar{\mathbf{\Omega}} \bar{\mathbf{S}}^2 \bar{\mathbf{\Omega}}^2 - \bar{\mathbf{\Omega}}^2 \bar{\mathbf{S}}^2 \bar{\mathbf{\Omega}} \right), \\ \text{and} \quad & \bar{a}_{ij} = \frac{\overline{u'_i u'_j}}{K} - \frac{2}{3} \delta_{ij}. \end{aligned} \quad (3.10)$$

where the \bar{G}_i -coefficients are functions of the known independent invariants of $\bar{\mathbf{S}}$ and $\bar{\mathbf{\Omega}}$ [107, 108], and \mathbf{I} is the identity tensor such that all non-diagonal elements are zero and all diagonal elements are equal to one. The Reynolds stress components in the EARSMs depend on $\bar{\mathbf{S}}$ as well as $\bar{\mathbf{\Omega}}$ tensors, and the relation is nonlinear. If only the first term in equation 3.10 for $\bar{\mathbf{a}}$ is retained, then the EARSM reduces to the EVM.

The \bar{G} -coefficients are calculated by substituting equation 3.10 into an algebraic form of equations for the Reynolds stresses that are obtained by imposing an equilibrium hypothesis in which the convection and diffusion terms are zero:

$$\frac{\overline{u'_i u'_j}}{K} (\mathcal{P} - \varepsilon) = \mathcal{P}_{ij} - \varepsilon_{ij} + \Pi_{ij}, \quad (3.11)$$

where \mathcal{P} ($= \mathcal{P}_{ii}/2$) is the turbulent production rate, ε ($= \varepsilon_{ii}/2$) is the turbulent dissipation

rate, \mathcal{P}_{ij} is the production tensor, ε_{ij} is the dissipation rate tensor, and Π_{ij} is the pressure strain rate tensor. The procedure to calculate the \overline{G} -coefficients requires further assumptions to obtain the explicit equations. In this chapter the solutions obtained by Gatski & Speziale (1993) [107] to calculate the \overline{G} -coefficients from the mean flow data are used.

The expression for r_{ij} is derived as:

$$r_{ij} = \widetilde{u'_i u'_j} - \overline{u'_i u'_j} = K (\widetilde{a_{ij}} - \overline{a_{ij}}) := K \widetilde{b_{ij}} \quad (3.12)$$

where $\widetilde{\mathbf{a}}$ is given as:

$$\begin{aligned} \widetilde{\mathbf{a}} = & \quad \widetilde{G}_1 \widetilde{S} + \widetilde{G}_2 (\widetilde{S} \widetilde{\Omega} - \widetilde{\Omega} \widetilde{S}) + \widetilde{G}_3 (\widetilde{S}^2 - \frac{1}{3} tr\{\widetilde{S}^2\} \mathbf{I}) + \widetilde{G}_4 (\widetilde{\Omega}^2 - \frac{1}{3} tr\{\widetilde{\Omega}^2\} \mathbf{I}) + \\ & \quad \widetilde{G}_5 (\widetilde{\Omega} \widetilde{S}^2 - \widetilde{S}^2 \widetilde{\Omega}) + \widetilde{G}_6 (\widetilde{S} \widetilde{\Omega}^2 + \widetilde{\Omega}^2 \widetilde{S} - \frac{2}{3} tr\{\widetilde{S} \widetilde{\Omega}^2\} \mathbf{I}) + \widetilde{G}_7 (\widetilde{\Omega} \widetilde{S} \widetilde{\Omega}^2 - \widetilde{\Omega}^2 \widetilde{S} \widetilde{\Omega}) + \\ & \quad \widetilde{G}_8 (\widetilde{S} \widetilde{\Omega} \widetilde{S}^2 - \widetilde{S}^2 \widetilde{\Omega} \widetilde{S}) + \widetilde{G}_9 (\widetilde{S}^2 \widetilde{\Omega}^2 + \widetilde{\Omega}^2 \widetilde{S}^2 - \frac{2}{3} tr\{\widetilde{S}^2 \widetilde{\Omega}^2\} \mathbf{I}) + \\ & \quad \widetilde{G}_{10} (\widetilde{\Omega} \widetilde{S}^2 \widetilde{\Omega}^2 - \widetilde{\Omega}^2 \widetilde{S}^2 \widetilde{\Omega}), \\ \text{and} \quad & \quad \widetilde{G}_i = F_i (\widetilde{S}, \widetilde{\Omega}) \end{aligned} \quad (3.13)$$

where F_i are the functions to obtain \overline{G}_i from \overline{S} and $\overline{\Omega}$ as:

$$\overline{G}_i = F_i (\overline{S}, \overline{\Omega}).$$

The expression for r_{ij} in equation 3.12 is substituted into equation 3.3, and the nonlinear terms are neglected, to obtain the linear perturbation equations as:

$$\begin{aligned} \partial_t (\tilde{u}_i) = & -\overline{u}_j \partial_j \tilde{u}_i - \tilde{u}_j \partial_j \overline{u}_i - \partial_i \tilde{p} + \frac{1}{Re} \partial_{jj} \tilde{u}_i - \partial_j (K \widetilde{b_{ij}}) \\ \partial_j \tilde{u}_j = & 0 \end{aligned} \quad (3.14)$$

Equations 3.9 and 3.14 are the general form of the EVM- and EARSM-based linearised RANS equations, respectively. Their specific forms depend upon the turbulence model used for calculations of v_i or \overline{G}_i , and on the flow case under study.

3.3 Turbulent channel flow

Turbulent channel flow is studied here as a case study to show the application of the EARSM-based linearised RANS equations in energy amplification analysis to find coherent struc-

tures. This flow case is chosen because: (i) coherent structures in turbulent channel flow are well studied in the literature, (ii) several analyses based on the linearised Navier–Stokes or RANS equations are applied on turbulent channel flow [1, 2, 10, 72, 73, 76], and (iii) it has a simple flow geometry. In the geometry considered here, the streamwise, wall-normal, and spanwise directions are labelled (x, y, z) , respectively. The mean stream is in the x –direction and the flow is homogeneous in the x – and z –directions. The channel half-width is h , with the x –axis on the bottom wall. The mean velocity, turbulent fluctuations, and linear harmonic perturbations, respectively, are given as:

$$\begin{aligned}\bar{u}_i &= [\bar{u}(y), 0, 0], \quad \bar{p} = \bar{p}(y), \\ u'_i &= [u', v', w'](x, y, z, t), \quad p' = p'(x, y, z, t), \quad \text{and} \\ \tilde{u}_i &= [\tilde{u}, \tilde{v}, \tilde{w}](y) \exp[-i\omega t + ik_x x + ik_z z], \quad \tilde{p} = \tilde{p}(y) \exp[-i\omega t + ik_x x + ik_z z].\end{aligned}\quad (3.15)$$

where ω is a complex number, and k_x and k_z are real numbers. The streamwise wavelength of perturbations is $\lambda_x = \frac{2\pi}{k_x}$, and the spanwise wavelength of perturbations is $\lambda_z = \frac{2\pi}{k_z}$. The kinematic viscosity is labelled ν_t , and the friction Reynolds number is defined as $Re_\tau = \frac{hu_\tau}{\nu}$, where friction velocity is defined as $u_\tau = \sqrt{\nu \frac{d\bar{u}(0)}{dy}}$. All the lengths presented are non-dimensionalised in outer units, which is done by dividing by h . When they are non-dimensionalised in inner units they are divided by ν/u_τ , and the non-dimensionalised streamwise and spanwise wavelengths are represented as λ_x^+ and λ_z^+ , and the non-dimensionalised axes in the streamwise, wall-normal, and spanwise directions are represented as X^+ , Y^+ , and Z^+ , respectively.

The ν_t profile and $\overline{G_i}$ –coefficients need to be calculated from the mean flow data for the implementation of the EVM- and EARSM-based linearised RANS equations, respectively. The DNS data used are for channel flows at the $Re_\tau = 180, 934$, and 2003, which are available online from Refs. [3, 101]. The eddy viscosity profile is calculated as $\nu_t = -\frac{\overline{u'v'}}{d\bar{u}/dy}$. The $\overline{G_i}$ –coefficients are calculated as in equation (49) in Gatski & Speziale (1993) [107]. The accuracy of these models in reproducing the Reynolds stress tensor is checked for the $Re_\tau = 934$ flow case, and the results are shown in figure 3.1. The top and bottom rows are the estimations from the EVM and EARSM, respectively. The solid lines are the exact Reynolds stress from the DNS data, and the dashed lines are estimated from the models.

The EVM, by definition, is exact at estimating the $\overline{u'v'}$ –component, as seen in the frame (a), but the error is large in all the three normal Reynolds stress components estimations. The other two Reynolds stress components ($\overline{v'w'}$ and $\overline{w'u'}$) are identically zero in turbulent channel flows. The EARSM is overall more accurate at estimating the Reynolds stress.

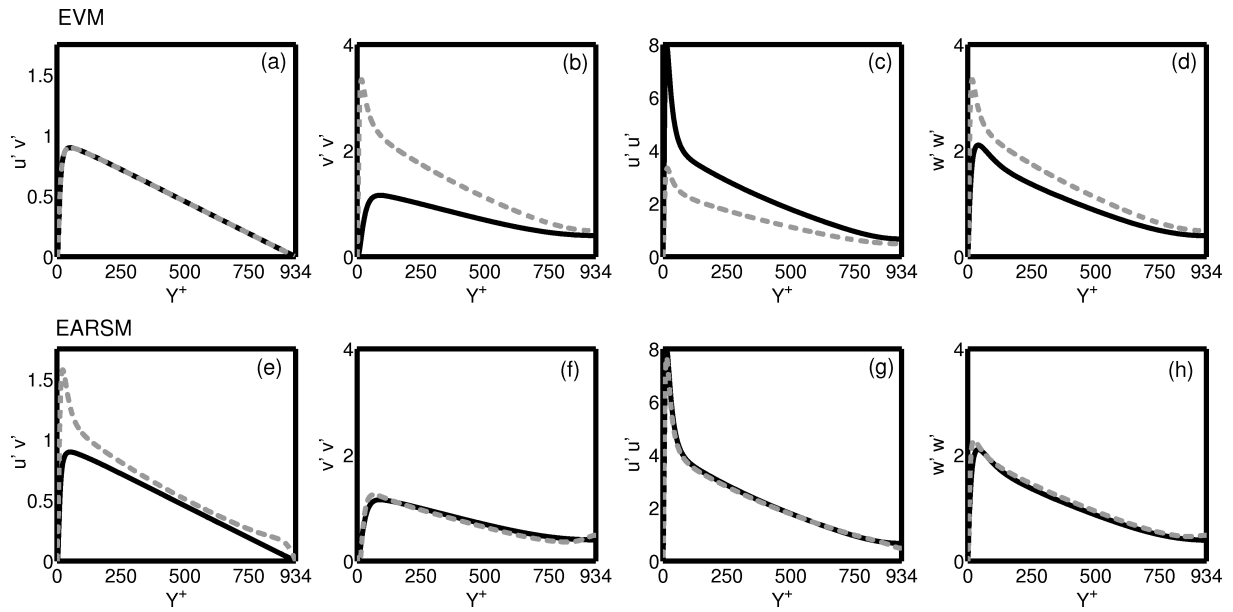


Fig. 3.1 The Reynolds stress components estimated from the (a–d) EVM and (e–h) EARSM for the $Re_\tau = 934$ flow case. The solid lines are from the DNS data and the dashed lines are from the models. The EVM, by definition, is accurate at estimating the $\overline{u'v'}$ –component, but the EARSM is better at estimating all the other components. The error in the models is higher in the near-wall region, this is because all turbulence models are inaccurate in the near-wall region.

Except for the $\overline{u'v'}$ -component, it estimates all the other component more accurately. The EVMs have isotropic eddy viscosity, which is calculated based on the dominant component, while the EARSMs have anisotropic eddy viscosity, i.e. different turbulent viscosity in each direction. The dominant Reynolds stress component in turbulent channel flows is $\overline{u'v'}$, and therefore the EVM is accurate only at estimating this component, while the EARSM is better at estimating all the other components. Another noticeable factor in these estimates is that the difference between the Reynolds stress from the DNS and from the models is maximum near the wall. This is because all turbulence models are inaccurate in the near-wall region, and require artificial corrections.

3.4 Linearised RANS-based amplification analysis

The mean flow velocity and linear perturbations from equation 3.15, along with the calculated v_t are substituted in equation 3.9 to obtain the EVM-based linearised equations. Then the Orr-Somerfeld equations were obtained and an eigenvalue problem is formulated as below.

$$\omega \begin{bmatrix} -k_z^2 - k_x^2 & \\ +\frac{d^2}{dy^2} & 0 \\ 0 & I \end{bmatrix} \begin{bmatrix} \tilde{v} \\ \tilde{\Omega} \end{bmatrix} = \begin{bmatrix} 1i \left(v_t k_z^4 + v_t \frac{d^4}{dy^4} - 2k_z^2 v_t \frac{d^2}{dy^2} + k_z^2 \frac{d^2 v_t}{dy^2} \right) \\ + 1i \left(\frac{d^2 v_t}{dy^2} \frac{d^2}{dy^2} 2 \frac{dv_t}{dy} \frac{d^3}{dy^3} - 2k_z^2 \frac{dv_t}{dy} \frac{d}{dy} \right) - k_x^3 U \\ + k_x \left(-k_z^2 U + U \frac{d^2}{dy^2} - \frac{d^2 U}{dy^2} \right) + 1i v_t k_x^4 & 0 \\ -ik_x^2 \left(2v_t \frac{d^2}{dy^2} - 2v_t k_z^2 + 2 \frac{dv_t}{dy} \frac{d}{dy} - \frac{d^2 v_t}{dy^2} \right) & \\ & k_z \frac{dU}{dy} & 1i v_t \left(\frac{d^2}{dy^2} - k_z^2 \right) \\ & & + k_x U - 1i v_t k_x^2 \end{bmatrix} \begin{bmatrix} \tilde{v} \\ \tilde{\Omega} \end{bmatrix}, \quad (3.16)$$

where $\tilde{\Omega}$ is the wall-normal vorticity, i represents the imaginary unit, and I is the identity operator.

The calculated $\overline{G_i}$ are substituted in equation 3.14 to obtain the EARSM-based linearised equations, which is also formulated as an eigenvalue problem.

$$\omega \begin{bmatrix} I & 0 & 0 & 0 \\ 0 & I & 0 & 0 \\ 0 & 0 & I & 0 \\ 0 & 0 & 0 & 0 \end{bmatrix} \begin{bmatrix} \tilde{u} \\ \tilde{v} \\ \tilde{w} \\ \tilde{p} \end{bmatrix} = [NS] \begin{bmatrix} \tilde{u} \\ \tilde{v} \\ \tilde{w} \\ \tilde{p} \end{bmatrix} + [T] \begin{bmatrix} \tilde{u} \\ \tilde{v} \\ \tilde{w} \end{bmatrix} \quad (3.17)$$

where $[NS]$ represents the Navier–Stokes equations, which is given by the continuity equation and first four terms in the momentum equation written in equation 3.14, and $[T]$ represents the turbulence term, which is given by the last term in the momentum equation written in equation 3.14. This equation is re-written as a generalised eigenvalue problem.

$$\omega [B] \begin{bmatrix} \tilde{u} \\ \tilde{v} \\ \tilde{w} \\ \tilde{p} \end{bmatrix} = [A] \begin{bmatrix} \tilde{u} \\ \tilde{v} \\ \tilde{w} \\ \tilde{p} \end{bmatrix} \quad (3.18)$$

Chebyshev spectral method with Gauss-Lobatto points in the y -direction is used for discretisation. The fact that \tilde{v} is anti-symmetric and \tilde{u} , \tilde{w} , and \tilde{p} are symmetric with respect to the centre of the channel is used, and discretisation is performed only for half of the domain. Chebyshev differentiation matrices are used for the differential operators in the equation [99]. The Matlab function ‘eig’ is used to calculate the eigenvalues (not the eigenvectors), the eigenvectors corresponding to the calculated eigenvalues are then calculated using the Matlab function ‘eigs’ because it is numerically cheaper.

The maximum transient growth, $G_{max} = \sup \frac{\tilde{u}^2(t) + \tilde{v}^2(t) + \tilde{w}^2(t)}{\tilde{u}^2(0) + \tilde{v}^2(0) + \tilde{w}^2(0)}$, is maximised over the amplification time t as well as the initial condition. It is calculated based on the formulation given in Ref. [100]. The procedure of its calculation based on the system’s eigenvalues and eigenvectors is described in Section 2.2.

Figure 3.2 shows the maximum transient growth, G_{max} , in the three flow cases, (a, d) $Re_\tau = 180$, (b, e) $Re_\tau = 934$, and (c, f) $Re_\tau = 2003$, calculated from the (a–c) EVM- and (d–f) EARSM-based analyses as functions of λ_x and λ_z . The top and bottom axes show the spanwise wavelengths in outer (λ_z) and inner (λ_z^+) units, respectively. The different lines in each frame correspond to the different λ_x perturbations, and the arrows indicate the direction of increase in λ_x . The λ_x in the $Re_\tau = 180$ flow case are $\lambda_x^+ = 200, 400, 900, 1800$, and 3600 . The λ_x in the $Re_\tau = 934$ flow case are $\lambda_x^+ = 400$, and $\lambda_x = 1, 2, 5$, and 20 . The λ_x in the $Re_\tau = 2003$ flow case are $\lambda_x^+ = 400$, and $\lambda_x = 0.5, 1, 2, 5$, and 20 . The calculations from the EARSM based analysis are performed with 150 grid-points for all the cases. Some calculations are repeated with 130 or 170 grid-points, and the change in G_{max} is up to $\mathcal{O}(10^{-2})$. The calculations in the EVM based analysis are performed with 150 grid-points for the $Re_\tau = 2003$ and 934 cases, and are checked by repeating some calculations with 130 grid-points, and with 130 grid-points for the $Re_\tau = 180$ case, and are checked by repeating some calculations with 110 grid-points. The change in G_{max} is up to $\mathcal{O}(10^{-2})$ in all the cases.

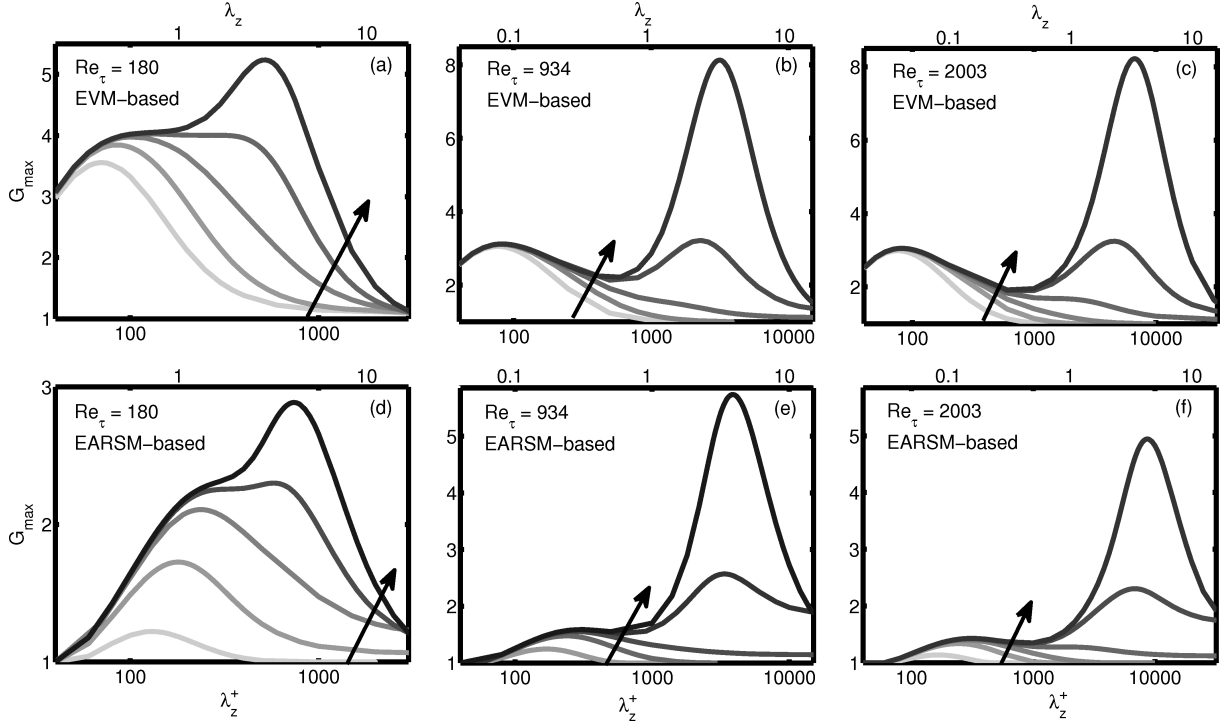


Fig. 3.2 The maximum transient growth, G_{max} , in the three flow cases, (a, d) $Re_\tau = 180$, (b, e) $Re_\tau = 934$, and (c, f) $Re_\tau = 2003$, calculated from the (a–c) EVM- and (d–f) EARS-based analyses are shown as functions of λ_x and λ_z . The top and bottom axes show the spanwise wavelengths in outer (λ_z) and inner (λ_z^+) units, respectively. The different lines in each frame correspond to the different λ_x perturbations, and the arrows indicate the direction of increase in λ_x . The most important feature in these plots is that there are two peaks in the G_{max} in all the cases. A primary peak at the higher λ_z values, which scales in outer units, and a secondary peak at the smaller λ_z^+ values, which scales in inner units. These results are similar to the results in Refs. [2, 10], where the optimal structures corresponding to the primary peak are compared with very-large-scale-motions (VLSMs) and the optimal structures corresponding to the secondary peak are compared with near-wall structures.

The most important feature in figure 3.2 is that both the analyses find that there are two peaks in G_{max} for all the flow cases. A primary peak at the larger spanwise wavelength, which scales in outer units, and a secondary peak at the smaller spanwise wavelength, which scales in inner units. These results are very similar to the results in Pujals *et al.* (2009) and del-Alamo & Jimenez (2006) [2, 10], who also use the EVM-based analysis. A difference between the present EVM-based analysis and that of Pujals *et al.* (2009) [2] is that in the former analysis the DNS data for channel flow are used while in the latter analysis empirical profiles of the eddy viscosity and mean velocity for channel flow are used. Therefore, the results are expected to be quantitatively little different but qualitatively similar. This is shown in figure 2 of Chapter 2. In Refs. [2, 10], the optimal structures corresponding to the primary peak are compared with very-large-scale-motions (VLSMs) and the optimal structures corresponding to the secondary peak are compared with near-wall structures.

Apart from this important similarity between the results from the two analyses, there are some minor quantitative and qualitative differences in the results. The EVM-based analysis predicts the primary peak at $\lambda_z|_{peak} \approx 3.4$ while the EARSMS-based analysis predicts it at $\lambda_z|_{peak} \approx 4.25$. The EVM-based analysis predicts the secondary peak at $\lambda_z^+|_{peak} \approx 80$ while the EARSMS-based analysis predicts it at $\lambda_z^+|_{peak} \approx 140 - 200$ depending upon λ_x^+ . The observed width of VLSMs in pipe flow is found to be around 2 outer units [35], and the spanwise spacing of near-wall streaks is observed to be nearly 100 wall units [21, 27]. Therefore, results from the EVM-based analysis are quantitatively closer to the observations. A qualitative difference between the results is that the secondary peak from the EVM-based analysis is predicted to be at the $\lambda_z^+|_{peak} = 75 - 85$, which does not depend much upon λ_x^+ , while it increases with increasing λ_x^+ in the EARSMS-based analysis. In DNS data, it has been observed that the larger structures are also wider [8], therefore, this property is captured better by the EARSMS-based analysis. Another difference in the results is that G_{max} from the EARSMS-based analysis is smaller than that from the EVM-based analysis, and both are much smaller than G_{max} from the molecular viscosity (MV)-based analysis in Chapter 2. The reason that the EARSMS damps more than the EVM is because the viscosity in the dominant direction, which is of the $\overline{u'v'}$ -Reynolds stress, is over-estimated by the EARSMS as seen in figure 3.1.

3.4.1 Optimal mode shapes

Figure 3.3 shows the normalised amplitudes of velocities in the initial and final optimal modes correspond to the secondary peaks in G_{max} . Frames (a) and (b) show the modes at

the $\lambda_x^+ = 400$ and $\lambda_z^+ = 85$ calculated from the EVM-based analysis, and frames (c) and (d) show the modes at the $\lambda_x^+ = 400$ and $\lambda_z^+ = 180$ calculated from the EARSMS-based analysis. The dashed lines, solid lines, and squares correspond to the $Re_\tau = 180, 934$, and 2003 flows, respectively. The black, grey, and light-grey colours correspond to the streamwise, wall-normal, and azimuthal velocities, respectively. These plots show that these modes exist in the near-wall region and they scale in inner units, except the streamwise velocity component in the initial optimal modes from the EARSMS-based analysis shown in frame (c). The shapes of the optimal modes from the EVM- and EARSMS-based analyses match with each other. The only noticeable difference is in the streamwise velocity component in the initial optimal modes. The shapes of the wall-normal velocity in the initial modes and the streamwise velocity in the final modes match well with those correspond to the secondary peak shown in figures 5(a) and (b) in Pujals *et al.* (2009) [2].

In summary, the optimal modes that correspond to the secondary peaks (i) scale in inner units, (ii) lie in the near-wall region, and (iii) have small wavelengths of the order of the size of near-wall structures as observed in Refs. [8, 21, 27]. Because these features are consistent with those of near-wall structures, these optimal modes are compared with the near wall structures in previous studies [1, 2, 10, 73]. The optimal modes that correspond to the secondary peaks in the $Re_\tau = 180$ flow case from the EVM- and EARSMS-based analyses are shown in two-dimensional planes in figures 3.4 and 3.5, respectively. Frames (a) in both the figures show the initial optimal modes in the spanwise–wall-normal plane. These figures show that the mode shapes are like vortical structures in the near-wall region. They match with quasi-streamwise vortices. Frames(b) in both the figures show the final optimal modes in the streamwise–wall-normal plane. These figures show the mode shapes are streaky structures. The regions with the positive streamwise velocity have the negative wall-normal velocity. These regions match with sweeps, which form high-speed streaks. The regions with the negative streamwise velocity have the positive wall-normal velocity. These regions match with ejections, which form low-speed streaks.

Figure 3.6 shows the normalised amplitudes of velocities in the initial and final optimal modes correspond to the primary peak in G_{max} . Frames (a) and (b) show modes at the $\lambda_x = 20$ and $\lambda_z \approx 3.4$ calculated from the EVM-based analysis, and frames (c) and (d) show modes at the $\lambda_x = 20$ and $\lambda_z \approx 4.25$ calculated from the EARSMS-based analysis. The dashed lines, solid lines, and squares correspond to the $Re_\tau = 180, 934$, and 2003 flows, respectively. The black, grey, and light-grey colours correspond to the streamwise, wall-normal, and azimuthal velocities, respectively. These plots show that the final optimal modes have most energy in the streamwise velocity and it peaks in the logarithmic layer

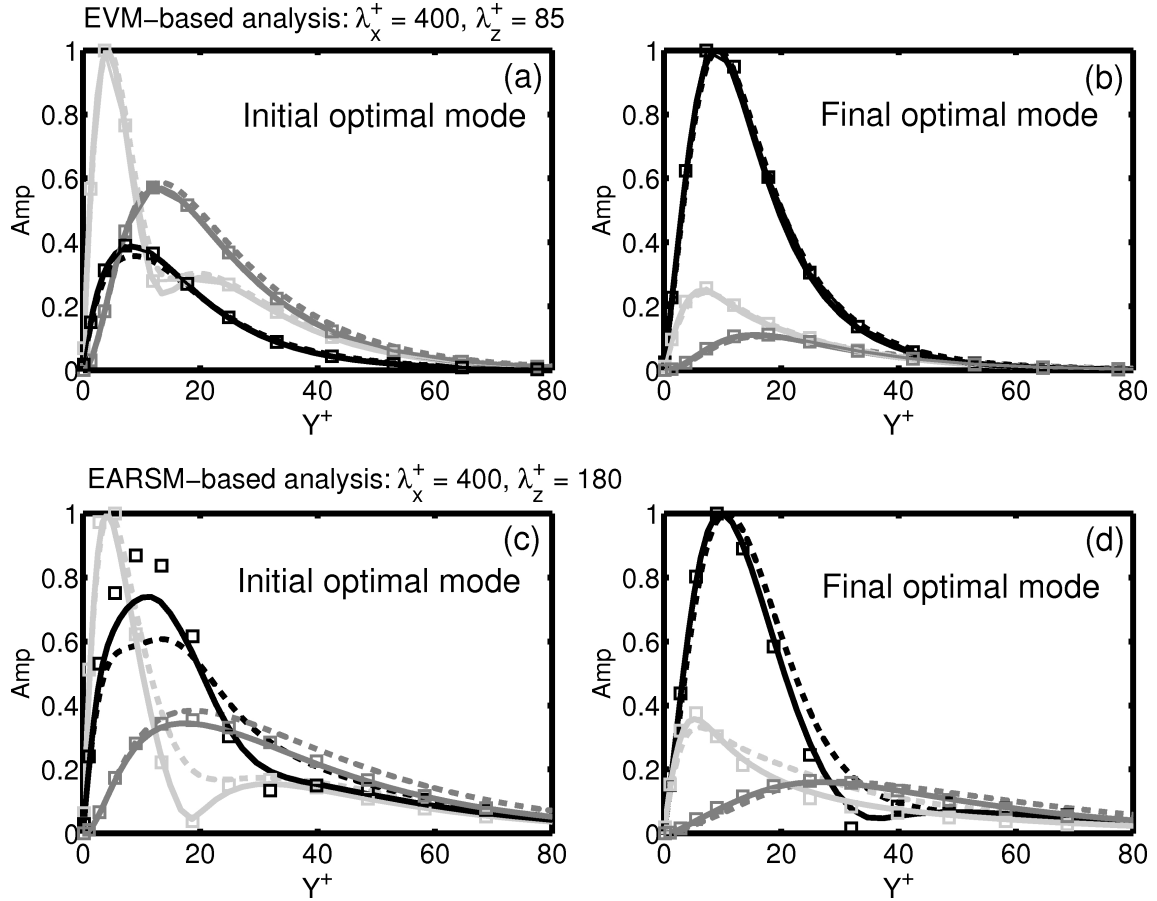


Fig. 3.3 The normalised amplitudes of velocities in the initial and final optimal modes at the (a, b) $\lambda_x^+ = 400$ and $\lambda_z^+ = 85$ calculated from the EVM-based analysis, and at the (c, d) $\lambda_x^+ = 400$ and $\lambda_z^+ = 180$ calculated from the EARS-based analysis. The dashed lines, solid lines, and squares correspond to the $Re_\tau = 180, 934$, and 2003 flows, respectively. The black, grey, and light-grey colours correspond to the streamwise, wall-normal, and azimuthal velocities, respectively. The shape of these modes show that they scale in inner units, except the streamwise velocity component in the initial optimal mode from the EARS-based analysis in frame (c). The shapes of the optimal modes from the EVM- and EARS-based analyses match with each other. The only noticeable difference is in the streamwise velocity component in the initial optimal modes. The shapes of the wall-normal velocity in the initial modes and the streamwise velocity in the final modes match well with those shown in figures 5(a) and (b), respectively, in Pujals *et al.* (2009) [2].

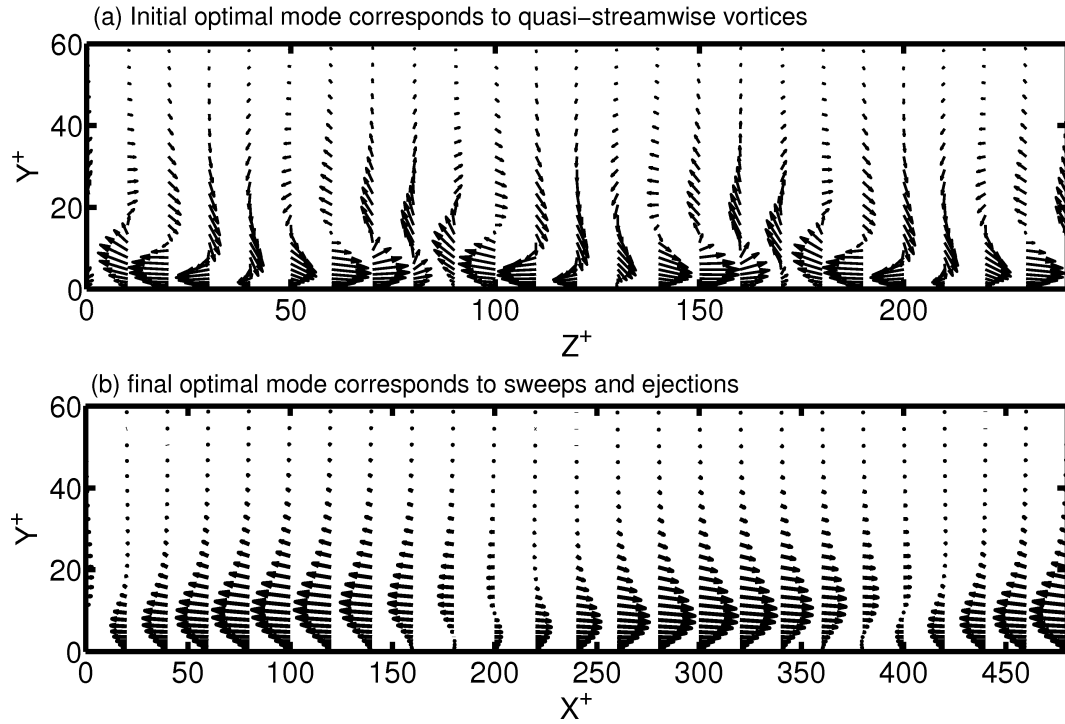


Fig. 3.4 Results for the $\lambda_x^+ = 400$ and $\lambda_z^+ = 85$ in the $Re_\tau = 180$ flow case from the EVM-based analysis. (a) The initial optimal mode is shown in the $Y^+ - Z^+$ plane, it has a vortical structure like that of near-wall quasi-streamwise vortices. (b) The final optimal mode is shown in the $X^+ - Y^+$ plane (the Y^+ -axis is twice magnified). The streaky structures with the positive streamwise velocity have the negative wall-normal velocity and vice-versa.

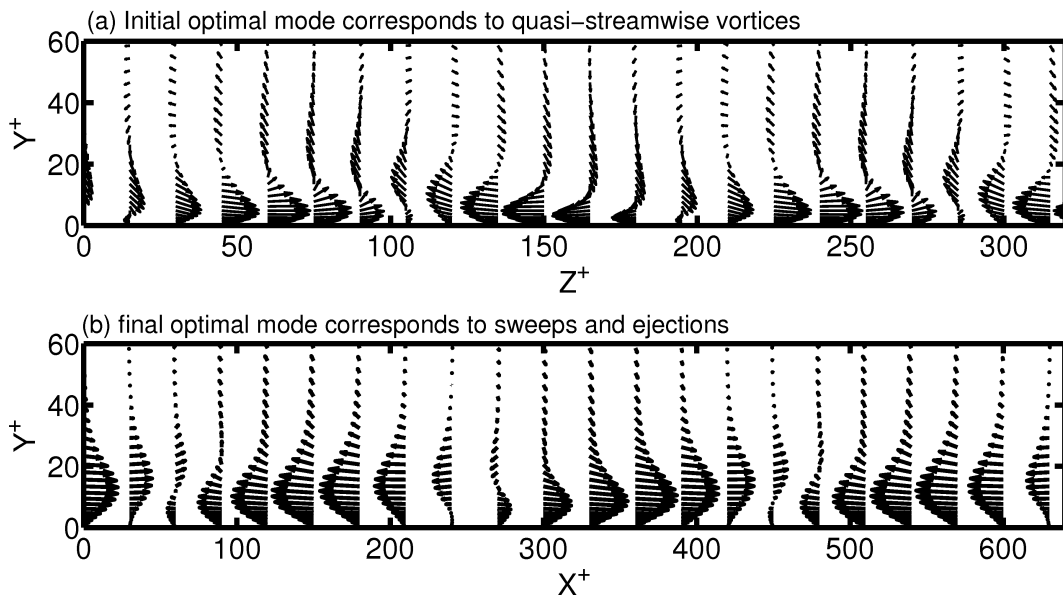


Fig. 3.5 Results for the $\lambda_x^+ = 400$ and $\lambda_z^+ = 180$ in the $Re_\tau = 180$ flow case from the EARS-based analysis. (a) The initial optimal mode is shown in the $Y^+ - Z^+$ plane, it has a vortical structure like that of near-wall quasi-streamwise vortices. (b) The final optimal mode is shown in the $X^+ - Y^+$ plane (the Y^+ -axis is twice magnified). The streaky structures with the positive streamwise velocity have the negative wall-normal velocity and vice-versa.

at $y \approx 0.2 - 0.3$. The shapes of the optimal modes from the EVM- and EARSMS-based analyses match with each other. The wall-normal velocity in the initial optimal modes and the streamwise velocity in the final optimal modes match with those shown in figures 5(c) and (d), respectively, in Pujals *et al.* (2009) [2].

In summary, the optimal modes that correspond to the primary peak (i) scale in outer units, (ii) lie in the entire channel but have most of their energy in the logarithmic layer, and (iii) have very large wavelengths. Because these features are consistent with those of VLSMs, these optimal modes are compared with the VLSMs in Refs. [2, 10]. The origin of the VLSMs has been a topic of discussion in many recent studies. Some researchers conclude that they form from the merging of smaller large-scale-motions (LSM) while others believe that they form independently. This is discussed in detail with references in Chapter 2. The results in this chapter, and in Refs. [2, 10], suggest that VLSMs can form independently of the smaller structures.

There is a good overall agreement between the results from (i) the present EVM-based analysis (ii) the present EARSMS-based analysis, and (iii) the EVM-based analysis in Pujals *et al.* (2009) [2]. The aim of this linear amplification analysis is to verify the present EARSMS-based analysis. It is a much more complicated turbulence model as compared to the EVM, and the match in the results from the EARSMS-based analysis with those from the EVM-based analyses confirms that the derivations and associated codes used in the present chapter are correct. The EARSMS-based analyses, similar to the present one, are used in Chapter 5 for flows in gas-turbine injector-combustor systems and in Chapter 6 for Taylor-Couette flows.

3.5 RANS-based linearised equations to find coherent structures

For the purpose of this discussion, coherent structures in turbulent flows are characterised into two types. The first type are intermittent coherent structures, such as streaks and vortices in channel flow or other large eddies in statistically stationary turbulent flows. Their contribution in the velocity and pressure fields averages out in the time-averaged as well as the phase-averaged fields, therefore they are part of the fluctuating fields u'_i and p' . The second type are almost constant frequency coherent structures, such as vortex shedding in a turbulent flow behind a cylinder. Their contribution in the velocity and pressure fields averages out in the time-averaged fields, but not in the phase-averaged fields. They, therefore,

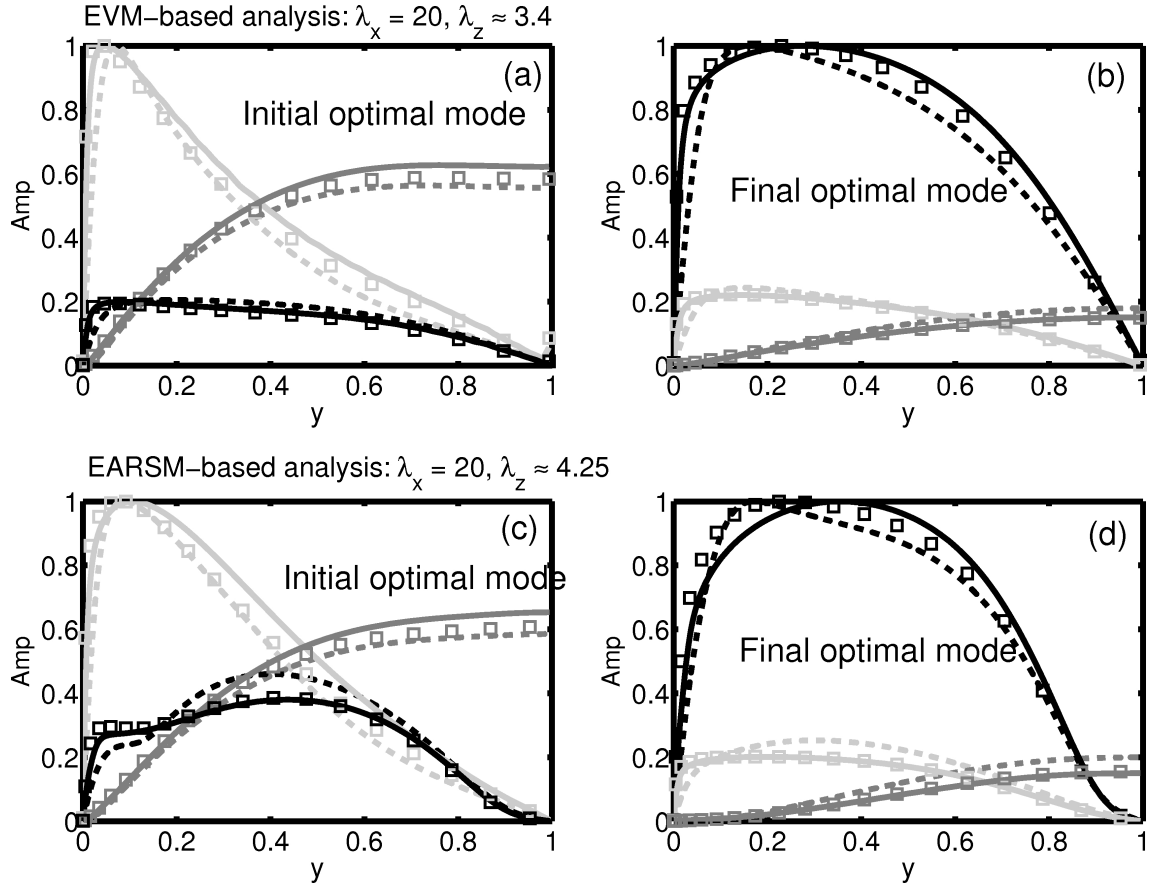


Fig. 3.6 The normalised amplitudes of velocities in the initial and final optimal modes at the (a, b) $\lambda_x = 20$ and $\lambda_z \approx 3.4$ calculated from the EVM-based analysis, and at the (c, d) $\lambda_x = 20$ and $\lambda_z \approx 4.25$ calculated from the EARS-based analysis. The dashed lines, solid lines, and squares correspond to the $Re_\tau = 180, 934$, and 2003 flows, respectively. The black, grey, and light-grey colours correspond to the streamwise, wall-normal, and azimuthal velocities, respectively. The shape of these modes show that they scale well in outer units, and that the shapes from the EVM- and EARS-based analyses also match with each other. The shapes of the wall-normal velocity in the initial modes and the streamwise velocity in the final modes from both the analyses match well with those shown in figures 5(c) and (d), respectively, in Pujals *et al.* (2009) [2].

are part of the phase-averaged fields \tilde{u}_i and \tilde{p} .

It is seen in Section 3.2, that the linearised RANS equations are derived for the phase-averaged fields \tilde{u}_i and \tilde{p} . The linearised RANS-based analyses, therefore, are suitable for prediction of the second type of coherent structures but not for the first type of coherent structures. If an analysis, similar to the linearised RANS-based analysis, has to be derived for predicting the first type of coherent structures, then in such analysis their contribution should be included in \tilde{u}_i and \tilde{p} fields not in u'_i and p' fields. Consequently, in such analysis the Reynolds stress components will be much lower.

In the present EVM-based analysis for turbulent channel flows, and also in the other EVM-based analyses in the literature [2, 10], however, the eddy viscosity profiles are calculated based on the total Reynolds stress components. Such eddy viscosity profiles are too high for the prediction of coherent structures [4]. This is seen in the transient growth calculations. The maximum transient growth, G_{max} , calculated from the EVM-based analysis are very small, while G_{max} calculated from the molecular viscosity (MV)-based analysis in Chapter 2 are much larger. Another, and much graver, consequence of such high eddy viscosity profile is that it finds only minima in energy amplification for all the intermediate wavelengths. The intermediate wavelength region is the region between the two peaks found from the EVM-based analysis. The DNS data for channel flow show a peak in energy spectra in the same wavelength region. The observed coherent structures in this wavelength region are called hairpin vortices and LSMs, and they are predicted well by the MV-based stability analysis in Chapter 2.

The damping effect of using the eddy viscosity profile such as in the present analysis is shown in figures 3.7, 3.8, and 3.9 for the perturbations of the small ($\lambda_x^+ = 400$ and $\lambda_z^+ = 85$), intermediate ($\lambda_x = 2$ and $\lambda_z = 0.75$), and large ($\lambda_x = 20$ and $\lambda_z = 3$) wavelengths in the $Re_\tau = 2003$ flow case. It is not possible to say anything conclusively from the eigenvalue spectra alone. Nonetheless they provide some insight about the damping in the EVM-based analysis. The left side plots (a and c) show eigenvalues calculated from the MV-based analysis and the right side plots (b and d) show eigenvalues calculated from the EVM-based analysis. The eigenvalues are divided into three types based on the wall-normal position (y_s) where the corresponding eigenvectors have most energy. The red circles correspond to eigenvalues in the near-wall region ($y_s \leq 40/Re_\tau$), the blue circles correspond to eigenvalues in the logarithmic layer ($y_s > 40/Re_\tau$ and $y_s < 0.3$), and the black circles correspond to eigenvalues outside the logarithmic layer ($y_s \geq 0.3$ and $y_s < 0.6$). Other eigenvalues ($y_s \geq 0.6$) are neglected because their contribute in the formation of coherent structures is not likely to be important. The vertical axis in the plots is the growth rate (ω_i), and the horizontal

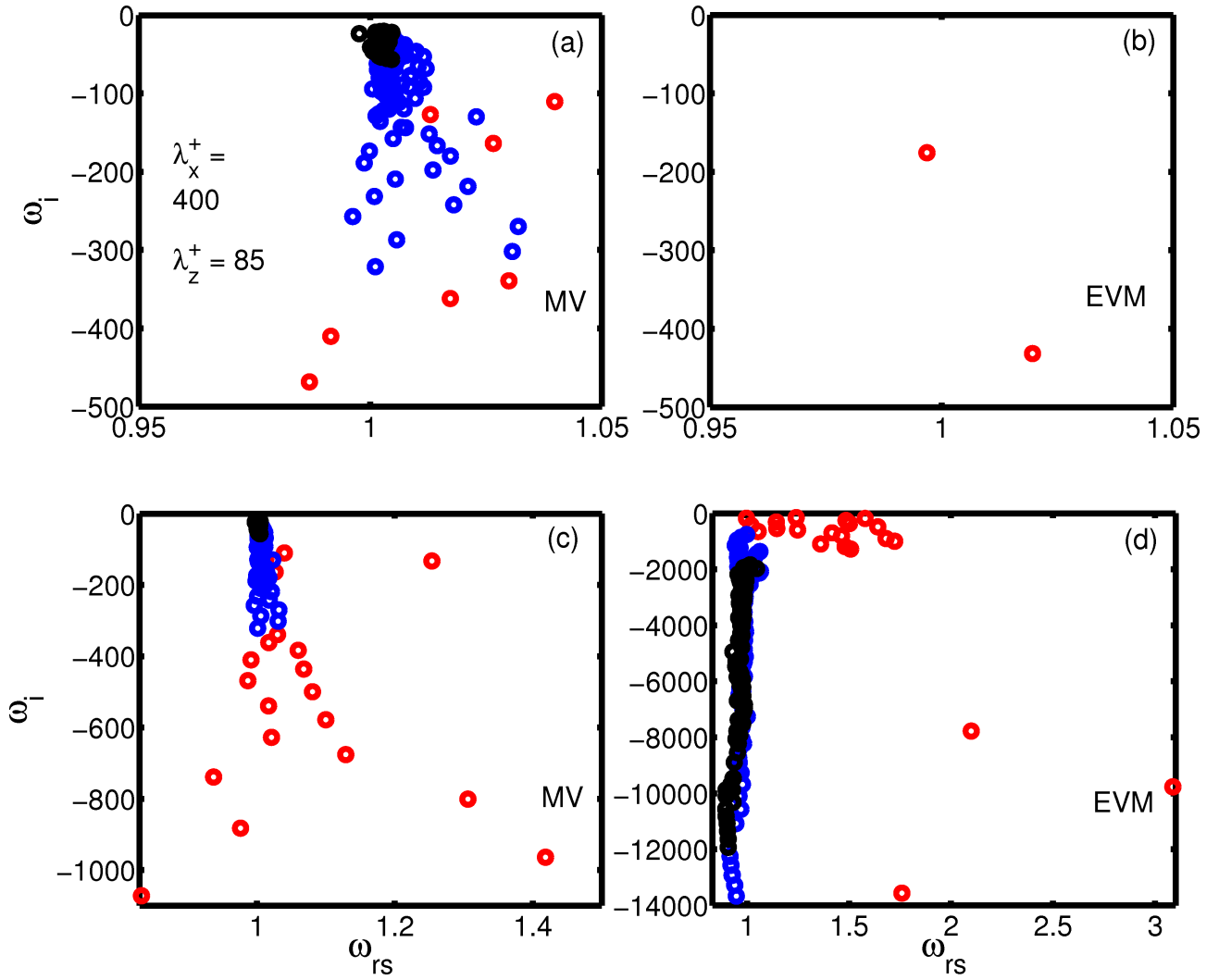


Fig. 3.7 The normalised eigenvalue spectra in the $Re_\tau = 2003$ flow case for the $\lambda_x^+ = 400$ and $\lambda_z^+ = 85$ perturbations calculated from the (a, c) MV- and (b, d) EVM-based analyses. The top plots show a few leading eigenvalues with the $0.95 \leq \omega_{rs} \leq 1.05$, and the bottom plots show almost the complete spectra. These figures show that the EVM-based analysis not only damps the eigenvalues significantly, but also scatter them away from $\omega_{rs} = 1$. As a consequence fewer eigenvectors contribute in the formation of coherent structures.

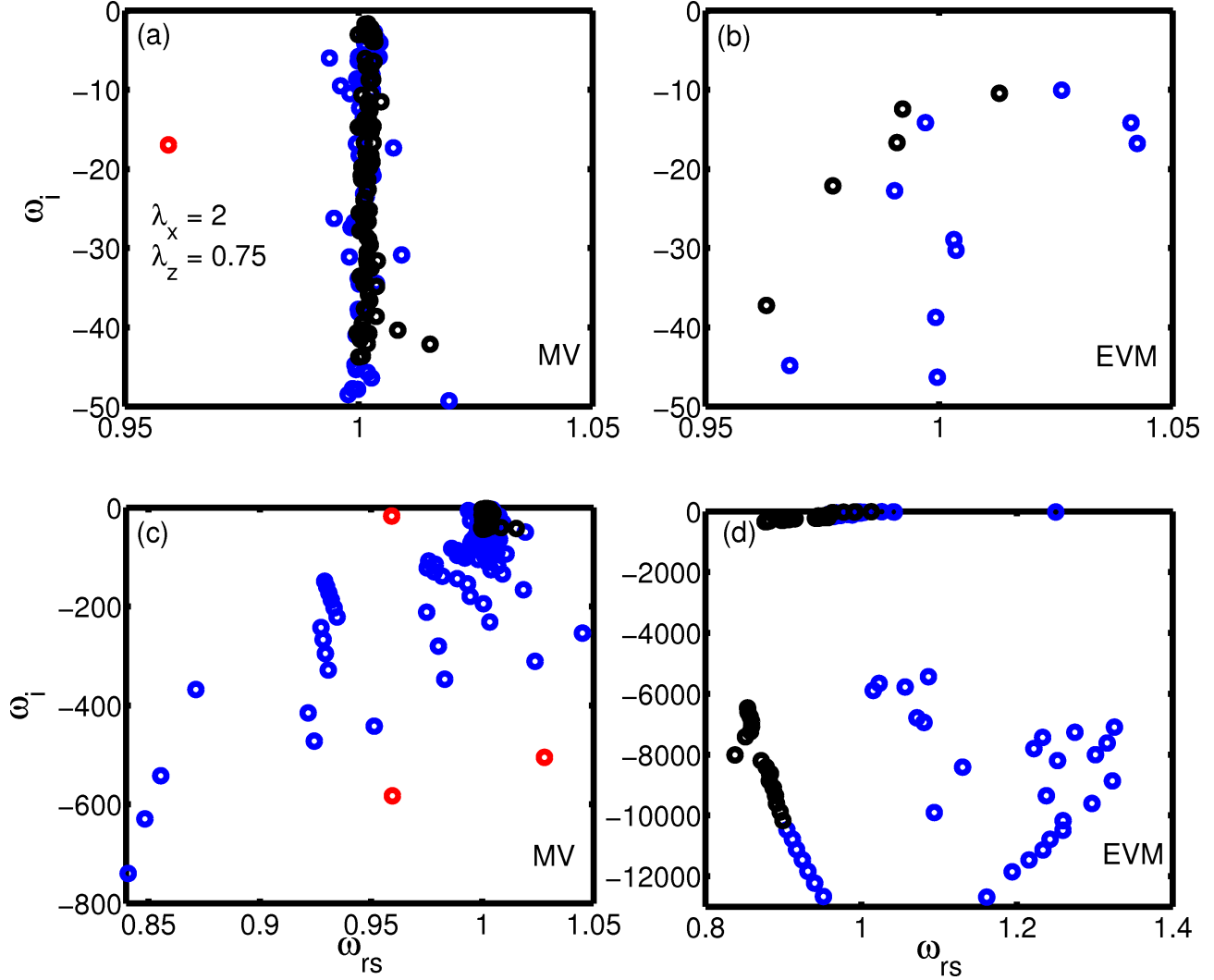


Fig. 3.8 The normalised eigenvalue spectra in the $Re_\tau = 2003$ flow case for the $\lambda_x = 2$ and $\lambda_z = 0.75$ perturbations calculated from the (a, c) MV- and (b, d) EVM-based analyses. The top plots show a few leading eigenvalues with the $0.95 \leq \omega_{rs} \leq 1.05$, and the bottom plots show almost the complete spectra. These figures show that the EVM-based analysis not only damps the eigenvalues significantly, but also scatter them away from $\omega_{rs} = 1$. The frame (d) shows that in the EVM-based analysis, the eigenvalues are divided into two regions based on their growth rate. There are significantly fewer eigenvalues in frame (b) as compared to those in the frame (a), which means that in the EVM-based analysis fewer eigenvectors contribute in the formation of coherent structures.

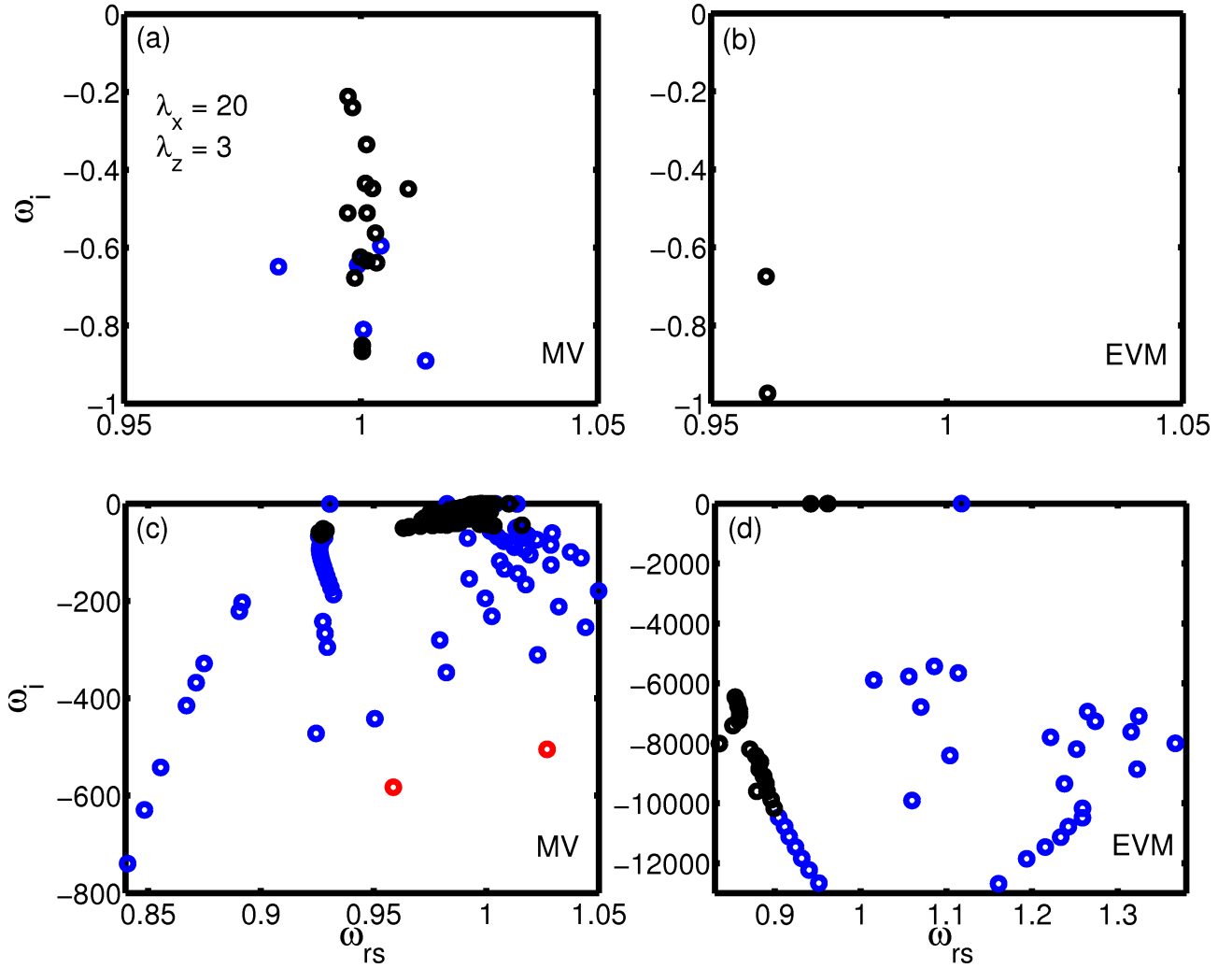


Fig. 3.9 The normalised eigenvalue spectra in the $Re_\tau = 2003$ flow case for the $\lambda_x = 20$ and $\lambda_z = 3$ perturbations calculated from the (a, c) MV- and (b, d) EVM-based analyses. The top plots show a few leading eigenvalues with the $0.95 \leq \omega_{rs} \leq 1.05$, and the bottom plots show almost the complete spectra. These figures show that the EVM-based analysis not only damps the eigenvalues significantly, but also scatter them away from $\omega_{rs} = 1$. The frame (d) shows that in the EVM-based analysis, the eigenvalues are divided into two regions based on their growth rate. There are significantly fewer eigenvalues in frame (b) as compared to those in the frame (a), which means that in the EVM-based analysis fewer eigenvectors contribute in the formation of coherent structures.

axis in the plots is the scaled frequency of eigenvalues (ω_{rs}). It is calculated as:

$$\omega_{rs} = \frac{\omega_r}{\bar{u}(y_s)k_x} \quad (3.19)$$

This represents the convective velocity of an eigenvector divided by the flow velocity at the location where the eigenvector has most energy. Because the coherent structures convect at the local flow speed, ω_{rs} is expected to be near 1. The top two plots (a and b) in the three figures show only a few leading eigenvalues with the $0.95 \leq \omega_{rs} \leq 1.05$. The bottom two plots (c and d) show the almost complete spectra. Only a few scattered eigenvalues with the ω_{rs} much greater than 1 are not shown.

There are three noticeable properties in these plots. The first is, as expected, that the EVM-based analysis has eigenvalues with the much smaller growth rate as compared to those from the MV-based analysis. The factor is of more than 10. The second is that eigenvalues from the EVM-based analysis, particularly in figures 3.8 and 3.9, are divided into two regions based on their growth rate. It shows that only a few eigenvectors in the EVM-based analysis contribute in the formation of coherent structures. The third is that the most of the eigenvalues from the MV-based analysis have the $\omega_{rs} = 1$, which shows that the corresponding eigenvectors can simulate the wave perturbations in the flow, while in the EVM-based analysis they are considerably scattered away from the $\omega_{rs} = 1$. The conclusion of this section is that the EVM-based analysis not only heavily damps the eigenvalues but it also scatters them away from $\omega_{rs} = 1$. The overall effect of this is seen as a reduction in transient growth in the system calculated from the EVM-based analysis. The spectra from the EARSM-based analysis are not shown here, but they have similar features as those in from the EVM-based analysis.

3.6 Summary and conclusion

In this chapter, the linearised RANS equations based on a second-order turbulence model (EARSM) are derived. In order to verify the derivation and the associated codes, these equations are applied for energy amplification analysis of turbulent channel flows to find coherent structures. The results from this analysis are compared with those from the EVM-based analysis derived in this chapter, and also with those of Pujals *et al.* (2009) [2].

The EARSM-based analysis finds that there are two peaks in the transient growth: a primary peak at the $\lambda_z \approx 4.25$, which scales in outer units, and a secondary peak at the $\lambda_z^+ \approx 170$, which scales in inner units. These results match qualitatively with those from the EVM-

based analyses. They also show a primary peak, which scales in outer units, and a secondary peak, which scales in inner units, in similar regions of wavelengths. Moreover, the shapes of the optimal modes from the EARSIM-based analysis are also in good agreement with those from the EVM-based analyses. This agreement of results from the analyses based on the two significantly different models verifies the derivation of the present EARSIM-based analysis, and the associated codes as well. The EARSIM-based analyses, similar to the present one, are used in Chapter 5 for flows in gas-turbine injector-combustor systems and in Chapter 6 for Taylor-Couette flows.

It is also discussed in this chapter, that analysis based on the linearised RANS equations is better suited for coherent structures that occur at an almost constant frequency, such as vortex shedding behind a cylinder, and not so suitable for coherent structures that occur intermittently, such as streaks and vortices in turbulent channel flows. The linearised RANS equations-based analysis over-damps the intermittent structures in a flow. The EVM-based analysis in turbulent channel flow is used as an example to show this damping effect. It is seen that the EVM-based analysis not only damps the eigenvalues significantly, but also scatters them away from $\omega_{rs} = 1$, where $\omega_{rs} = 1$ represents the modes which convect at local flow velocity. The overall effect of this is seen as a reduction in transient growth in the system calculated from the EVM-based analysis.

Chapter 4

Effect of axial rotation on near-wall structures in turbulent pipe flow

In this chapter, modal and non-modal stability analyses that are based on the linearised Navier–Stokes equations are used to study the formation of near-wall coherent structures in turbulent pipe flows and how rotation of the pipe around its own axis disrupts their formation. This chapter is in two parts. In the first part, the process of formation of streaks from quasi-streamwise vortices is studied. This analysis is similar to the analysis in Chapter 2, where linear amplification analysis is performed by linearising the Navier–Stokes equations around the mean velocity profile. The effect of the nonlinear terms in this analysis is modelled as the input streamwise wavelengths of perturbations, which are based on experimental and DNS observations on coherent structures. In the second part, the process of breakdown of low-speed streaks for the formation of quasi-streamwise vortices is studied. This analysis is similar to the modal stability analysis in Schoppa & Hussain (2002) [11], where the Navier–Stokes equations are linearised over an idealised realisation of the low-speed streaks.

4.1 Introduction

Turbulent boundary layers suffer from a higher skin-friction drag than their laminar counterparts. It is recognised that this higher skin-friction drag in turbulent flows is caused by coherent structures in the near-wall region. Consequently, there is commercial interest in suppressing these structures either through passive control, such as by modifying the flow boundaries by adding riblets [109], or through active control, such as by deterring sweeps or stabilising and preventing lifting of spanwise vorticity in the near-wall region [110].

Recently, many simplified approaches have been developed to understand and model coherent structures in turbulent flows [2, 5, 10, 48, 56, 68, 73, 75]. Out of these approaches the ones that are based on linearised equations are of particular interest in control applications. Moarref & Jovanovic (2012) [87] have implemented a linear model-based active-control in channel flow for achieving drag reduction. Their study is based on the studies of Lee, Kim, & Moin (1990) and Kim & Lim (2000) [82, 93], who showed the role of linear mechanisms in the formation and maintenance of streaks, and on the studies of del-Alamo & Jimenez (2006) and Pujals *et al.* (2009) [2, 10], who showed that the linearised RANS equations that are based on a simple eddy viscosity model qualitatively capture the features of coherent structures in turbulent channel flows. Sharma *et al.* (2011) [90] have also designed and implemented a linear control strategy for re-laminarisation of a low Reynolds number turbulent channel flow. Their linear control strategy is based on a passivity approach according to which it is possible to control each wavenumber perturbation individually.

Meliga *et al.* (2012) [88] have used linearised RANS equations-based global stability analysis to obtain the sensitivity of sinuous oscillations to the addition of a small control cylinder in a 2-D turbulent flow past a D-shaped cylinder. In their analysis they linearised a set of 2-D RANS equations around the mean flow, where the mean flow is obtained by time-averaging the unsteady solutions obtained from the same set of RANS equations. They showed that their results are in agreement with experimental observations of Ref. [89] for the same flow. Mettot *et al.* (2014) [111], somewhat contrarily to Meliga *et al.* (2012) Ref [88], have shown that an even simpler analysis, where the Navier–Stokes equations are linearised over the mean flow, is equally capable of predicting the sensitivity results that are in good agreement with the experiments. There are two main advantages of the latter study. The first is that it does not require the RANS equations to be linearised. The second is that solution for the mean flow can be obtained from any source, such as DNS, RANS, or experiments, while in the former study the mean flow profiles have to be obtained from the same set of equations as used in the stability analysis. Mettot *et al.* (2014) [111] obtained the mean velocity profile by time-averaging the unsteady solutions of a set of 3-D RANS equations.

The aim of the study in this chapter is to see (i) whether the linearised Navier–Stokes equations based analyses capture the process of formation of near-wall structures in a rotating turbulent pipe flow, and (ii) whether they explain the effects of axial rotation of the pipe on the near-wall structures. The main motivation for this study is to see whether the linearised equations based analyses in this chapter can be used as a basis for the application of more tools from linear dynamical systems in rotating turbulent pipe flows. The effect of

rotation in pipe flows is also interesting because of its difference in the laminar and turbulent regimes. Constant axial rotation of pipe around its own axis has a destabilising effect in laminar pipe flows as it brings the critical Reynolds number down [112]. Contrarily, in turbulent pipe flows the axial rotation is stabilising as it causes a reduction in near-wall structures, and brings the flow profile closer to the laminar parabolic shape flow profile [113]. Rotation of the pipe can be thought of as a passive control mechanism (not an optimal one though) and is similar to other control strategies in terms of the forcing mechanism, such as the forced large-scale counter-rotating vortices or wall-oscillations in Refs. [114–117]. Therefore, understanding the effect of rotation on coherent structures also sheds light on the mechanism of these other control strategies.

4.1.1 Regeneration cycle of near-wall structures and chapter outline

The most widely accepted mechanism for the formation and maintenance of near-wall structures in wall-bounded turbulent flows is the regeneration cycle summarised in figure 4.1 [8, 11, 94, 96, 118]. [Refs added.] There are three main steps in this cycle and the two of them are linear. These two linear processes - (i) the formation of near-wall streaks from quasi-streamwise vortices via a linear lift-up mechanism and (ii) the breakdown of the streaks for the formation of the quasi-streamwise vortices via a secondary instability - are studied using analyses based on the linearised Navier–Stokes equations in two parts of this chapter in Section 4.3 and Section 4.4, respectively. In Section 4.2, the mean velocity profiles in turbulent pipe flows are discussed, and the terminologies are introduced.

4.2 Pipe flow

The streamwise, radial, and azimuthal directions are represented by (x, r, θ) coordinates, respectively. The mean flow velocity is given as $(U_0(r), 0, W_0(r))$ in the (x, r, θ) directions, respectively. The Reynolds, friction Reynolds, and rotation numbers, respectively, are defined as:

$$Re = \frac{U_m R}{\nu}, \quad Re_\tau = \frac{u_\tau R}{\nu}, \quad \text{and} \quad R_o = \frac{W_0(R)}{U_m}.$$

where, U_m is the mean bulk velocity, R is the pipe radius, ν is the kinematic viscosity, and u_τ is the friction velocity defined as: $u_\tau := \sqrt{-\nu \left(\frac{dU_0(R)}{dr} \right)}$. From henceforth all variables are non-dimensionalized in outer units, i.e. by U_m and R , unless they are indicated by superscript⁺, in which case they are non-dimensionalized in wall (or inner) units, i.e. by u_τ

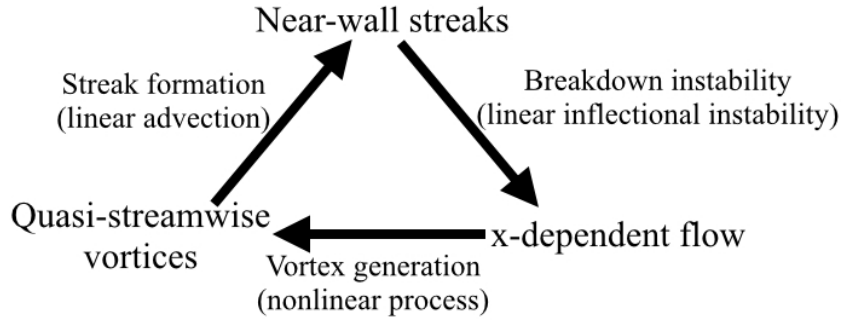


Fig. 4.1 The regeneration cycle of near-wall structures involves three main steps. This cycle can be started from any point, in the present study it is started from quasi-streamwise vortices. The first step is the generation of near-wall streaks by linear amplification of quasi-streamwise vortices via a lift-up mechanism. The second step is the breakdown of the near-wall streaks for the formation of x -dependent flow via modal or non-modal sinusoidal instabilities. The third step is a nonlinear process that leads to the formation of the quasi-streamwise vortices from the x -dependent flow.

and \mathbf{v} . The wall-normal distance is defined as $y = 1 - r$ in outer units and as $Y^+ = Re_\tau(1 - r)$ in inner units. Length in the azimuthal direction is defined as $z^+ = Re_\tau\theta$ in inner units.

The mean flow profiles are taken from the DNS results presented in Orlandi & Fatica (1997) [113] for the pipe flows at $Re = 2450$ and $R_o = 0, 0.5, 1$, and 2 . The (a) mean axial velocity profiles in inner units and (b) mean azimuthal velocity profiles, normalised by their rotation numbers, in inner units, are plotted in figures 4.2. The mean axial velocity profile in the near-wall region, when non-dimensionalised in inner units, does not change with the rotation number. The centreline velocity, however, increases with the rotation. The mean azimuthal velocity profiles, when normalised by their rotation numbers, are similar at all the rotation numbers. The profiles do not fall on the top of each other as found in the experiments in Refs. [119–121], but there is still a good match in the profiles [113].

The friction Reynolds numbers for the four cases, in order of increasing rotation number, are 170, 147, 149, and 157. It is highest for the non-rotating case, it decreases and then increases slightly again as the rotation increases. This shows that some rotation causes a decrease in the wall shear stress, and hence in the drag. This is because rotation causes a disruption in the regeneration process of near-wall structures. As a result there are fewer quasi-streamwise vortices and fewer near-wall streaks in the rotating cases as observed in Ref. [113]. In this chapter, two of the cases, which are $R_o = 0$ and $R_o = 0.5$, are studied. The study is limited only to these two cases because at higher rotation numbers ($R_o = 1$ and 2) the mean profiles themselves are linearly unstable. This suggests that the dominant mechanism for the formation of streaks might no longer be the same non-normal lift-up

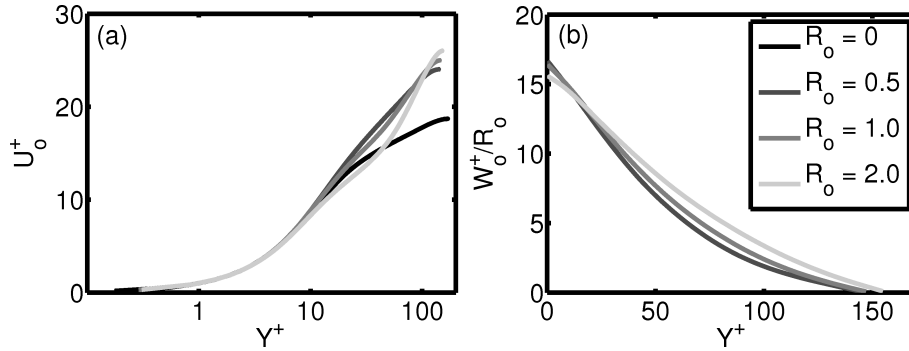


Fig. 4.2 (a) The mean axial velocity profile in fully developed turbulent pipe flow for the $Re = 2450$ at the four rotation numbers. The profiles in the wall region, when non-dimensionalised in wall units, do not change with rotation number. (b) The mean azimuthal velocity profile, normalised by their rotation number, for the three rotating cases. The normalised profiles are similar to each other.

mechanism, and a discussion on that is beyond the scope of this study.

4.3 Formation of near-wall streaks from quasi-streamwise vortices

Quasi-streamwise vortices are vortical structures that populate the near-wall region in wall-bounded turbulent flows [40]. These vortical structures have significant wall-normal velocity component, which on the one side brings high speed fluid towards the wall and on the other side lifts low speed fluid away from the wall. These events are known as sweeps and ejections, respectively. The lifted low speed fluid from the ejections elongates and forms low-speed near-wall streaks [42]. This process is dominantly linear because the quasi-streamwise vortices are amplified via a linear lift-up mechanism for the formation of the sweeps and ejections, and hence for the formation of the near-wall streaks. The role of linear mechanisms in the formation and maintenance of streaks is also shown in Refs. [82, 93]. Kim & Lim (2000) [93], however, also showed that streaks form at correct size only when the nonlinear terms are also included.

Energy amplification analysis based on the Navier–Stokes equations linearised over the mean velocity profile is performed here to study the formation of streaks and the effect of rotation on their formation. Based on Kim & Lim (2000) [93]’s conclusions, the effect of the nonlinear terms is modelled as the input streamwise wavelengths of the perturbations, where the input values are based on the observed quasi-streamwise vortices’ streamwise lengths. Such a modelling for the effect of the nonlinear terms is very rudimentary. Nonetheless

there is a good match in the optimal modes and energy spectra from the analysis with those in experiments and DNS.

The turbulent mean flow profile is uniform in the x – and θ –directions, so the perturbations $(u', v', w', p')(x, r, \theta, t)$ over it are assumed to be of the form:

$$(u(r), v(r), w(r), p(r)) \exp\{-i\omega t + ikx + im\theta\},$$

where the streamwise wavelength is given as $\lambda_x = 2\pi/k$, and the azimuthal wavelength is defined as $\lambda_z := 2\pi/m$ (λ_x and λ_z are non-dimensionalised by R). The linearised momentum and continuity equations for the perturbations are given below.

$$\begin{aligned} \frac{\partial u}{\partial t} &= -v \frac{dU_0}{dr} - im \frac{W_0}{r} u - ikU_0 u - ikp + \frac{1}{Re} \left[\frac{1}{r} \frac{\partial}{\partial r} \left(r \frac{\partial u}{\partial r} \right) - \frac{m^2}{r^2} u - k^2 u \right] \\ \frac{\partial v}{\partial t} &= -im \frac{W_0}{r} v + w \frac{2W_0}{r} - ikU_0 v - \frac{\partial p}{\partial r} + \frac{1}{Re} \left[\frac{1}{r} \frac{\partial}{\partial r} \left(r \frac{\partial v}{\partial r} \right) - \frac{m^2}{r^2} v - k^2 v - \frac{v}{r^2} - \frac{2im}{r^2} w \right] \\ \frac{\partial w}{\partial t} &= -\frac{v}{r} \frac{d}{dr} (rW_0) - im \frac{W_0}{r} w - ikU_0 w - \frac{im}{r} p + \frac{1}{Re} \left[\frac{1}{r} \frac{\partial}{\partial r} \left(r \frac{\partial w}{\partial r} \right) - \frac{m^2}{r^2} w - k^2 w - \frac{w}{r^2} + \frac{2im}{r^2} v \right] \\ 0 &= iku + \frac{1}{r} \frac{\partial}{\partial r} (rv) + \frac{im}{r} w \end{aligned} \quad (4.1)$$

In contrast to a non-rotating case, where the only linear coupling term is $v \frac{dU_0}{dr}$, a rotating case has additional linear coupling terms, which are $w \frac{2W_0}{r}$ in the v –momentum equation, and $\frac{v}{r} \frac{d}{dr} (rW_0)$ in the w –momentum equation. These terms represent linear interaction between the azimuthal and wall-normal velocity perturbations with the mean azimuthal velocity, respectively. They increase the non-normality of the operator and, as will be investigated, also the transient growth in the system.

For the numerical calculations, equations 4.1 are written as a generalised eigenvalue problem.

$$\omega [B] \begin{bmatrix} u \\ v \\ w \\ p \end{bmatrix} = [A] \begin{bmatrix} u \\ v \\ w \\ p \end{bmatrix} \quad (4.2)$$

Chebyshev spectral method is used with Gauss-Lobatto points in the wall-normal direction. Discretisation is performed by projecting the values of the quantities on the Gauss-Lobatto points. Chebyshev differentiation matrices are used for the differential operators in the equation [99]. Matlab function ‘eigs’ is used to calculate the eigenvalues and the

required number of eigenvectors.

The maximum transient growth is defined as:

$$G_{max} = \sup_{0 \leq t < \infty} \frac{|\sqrt{r}u(t)|^2 + |\sqrt{r}v(t)|^2 + |\sqrt{r}w(t)|^2}{|\sqrt{r}u(0)|^2 + |\sqrt{r}v(0)|^2 + |\sqrt{r}w(0)|^2}.$$

Many studies in the literature do not include the curvature effect in G_{max} , perhaps because this effect is small in the near-wall region and does not affect the results qualitatively. G_{max} is calculated based on the formulation given in Ref. [?]. Towards that purpose, first the eigenvectors are re-written such that they only include u , v , and w components and square root of radial component, r , is multiplied. An eigenvector corresponding to an eigenvalue, ω_i is given as:

$$f_i = [\sqrt{r}u_i \sqrt{r}v_i \sqrt{r}w_i],$$

where u_i , v_i , and w_i are the velocity components in the original eigenvector calculated from equation 4.2. Based on the calculated f_i and ω_i , the maximum transient growth is calculated in the same way as described in Section 2.2.

4.3.1 The $R_o = 0$ and $R_o = 0.5$ cases

Figure 4.3 presents the maximum transient growth, G_{max} , for the (a) non-rotating ($R_o = 0$) and (b) rotating ($R_o = 0.5$) cases. The G_{max} calculations are performed for the perturbations of $\lambda_x^+ = 100 - 700$. This choice of λ_x^+ is based on the streamwise length of the observed quasi-streamwise vortices, which is only a few hundred wall-units [11, 42, 95]. Schoppa & Hussain [11] showed through numerical calculations that their preferred length is approximately 300 wall-units, which, perhaps coincidentally, matches with the minimal channel length required to sustain wall-turbulence [97]. The maximum transient growth, G_{max} , calculations are performed with 80 grid-points and 150 eigenvectors. The convergence is checked by repeating a few calculations with 100 grid-points and 180 eigenvectors, the change in G_{max} is less than 0.1 percent and there is no change in the calculated $\lambda_z^+|_{peak}$ values.

Preferred azimuthal spacing of near-wall streaks

The peaks in G_{max} are at $\lambda_z^+ \sim 100$ for the non-rotating and rotating cases. This tallies with the observations that near-wall streaks with spanwise/azimuthal spacing of 100 wall units are preferred in wall-bounded turbulent flows [21, 27]. Figure 4.3 also shows that the $\lambda_z^+|_{peak}$ values are higher in the rotating case as compared to those in the non-rotating case,

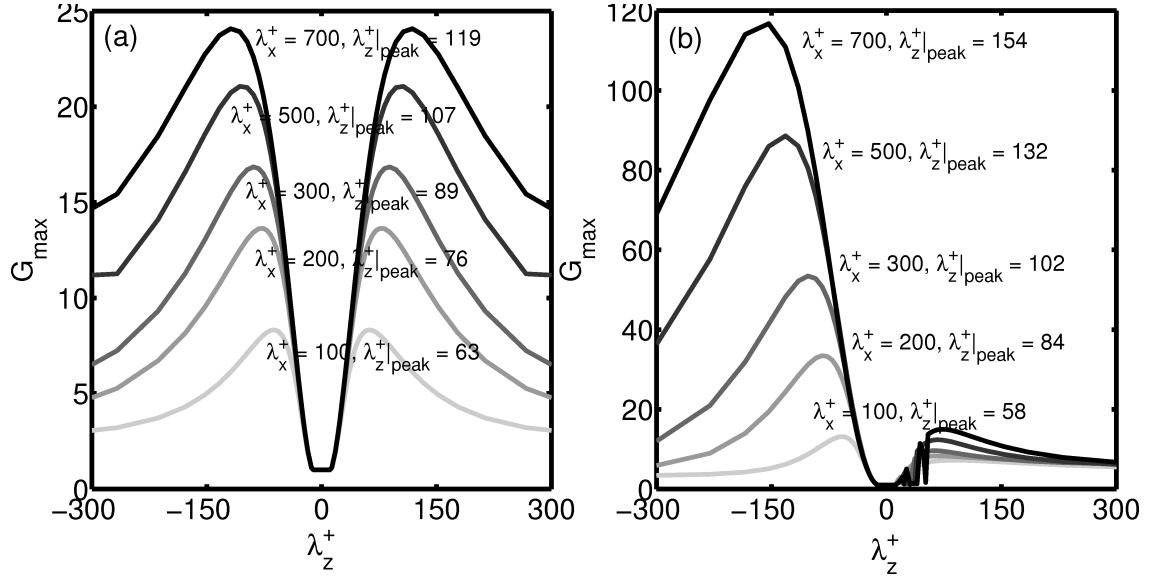


Fig. 4.3 The maximum transient growth, G_{max} , as functions of λ_x^+ and λ_z^+ in the (a) non-rotating and (b) rotating cases. The value of $\lambda_z^+|_{peak}$ is at around 100 wall units in both cases, which matches with the observed spanwise/azimuthal spacing of near-wall streaks. The higher $\lambda_z^+|_{peak}$ for the rotating case indicates widening of the streaks with rotation.

except for the $\lambda_x^+ = 100$ perturbations where it is slightly lower. The rotating flow, therefore, is expected to have wider near-wall streaks as compared to those in the non-rotating case. Such widening of streaks, or increase in their spacing, has also been observed in the DNS data of Orlandi & Fatica [113].

Co-winding and counter-winding streaks:

Linear amplification in the rotating case is higher for the negative m modes than it is for the positive m modes, unlike in the non-rotating case where it is symmetric in m . This implies that the flow with rotation favours the formation of co-winding streaks (k/m is of the opposite sign as that of U/W) over the formation of counter-winding streaks (k/m is of the same sign as that of U/W). Also the G_{max} values at the peaks are higher in the rotating case than they are in the non-rotating case. This means that if everything else in the regeneration cycle remains the same, the formation of near-wall streaks is more energetic in the rotating pipe flow than it is in the non-rotating flow. This is the opposite trend to that expected from the friction Reynolds number [113]. This will be further discussed later in the chapter.

Shape of the optimal modes

Figure 4.4 (solid lines) shows the normalised velocity amplitudes in the (a) initial and (b) final optimal modes of the $\lambda_x^+ = 300$ and $m = -12$ perturbations in the non-rotating case. The initial optimal mode has most of its energy in the azimuthal and wall-normal velocity components, which is a feature of quasi-streamwise vortices. The final optimal mode has most of its energy in the streamwise velocity component, which is a feature of near-wall streaks. This also indicates that the streamwise velocity component gets most amplified during the linear amplification process, which is expected because the linear coupling term, $-v \frac{dU_0}{dr}$, appears in the u -momentum equation. Figure 4.5 (a) shows a 2-d projection of the initial optimal mode in the $y - \theta$ plane ($y = 1 - r$). It confirms that the shape of the initial optimal mode is of the form of quasi-streamwise vortices. Figure 4.5 (b) shows a 2-d projection of the final optimal mode in the $x - y$ plane. This mode has regions of positive streamwise velocity and negative wall-normal velocity, where the negative wall-normal velocity means that the flow is towards the wall. These regions match with sweeps which are the initial form of high-speed streaks. This mode also has regions of negative streamwise velocity and positive wall-normal velocity. These regions match with ejections which are the initial form of low-speed streaks. The shapes of the optimal modes confirm that linear stability analysis captures the process of the formation of the sweeps and ejections, hence of the formation of the near-wall streaks, from the quasi-streamwise vortices.

Figure 4.6 (solid lines) shows the normalised velocity amplitudes in the (a) initial and (b) final optimal modes of the $\lambda_x^+ = 300$ and $m = -9$ perturbations in the rotating case. There is a higher contribution of energy from the streamwise velocity perturbation in the initial optimal mode than that in the non-rotating case. Also the final optimal mode has higher contributions from the azimuthal and wall-normal velocity perturbations than those in the non-rotating case. This implies that rotation causes an increase in amplification of the wall-normal and azimuthal velocity components more than of the streamwise velocity component. This is understandable as the additional linear coupling terms in the rotating case, which include W_0 , appear in the v - and w -momentum equations. The shapes of the initial and final optimal modes in the $y - \theta$ and $x - y$ planes are shown in frames 4.7 (a) and (b), respectively. The shapes of these modes are quite similar to those in the non-rotating case.

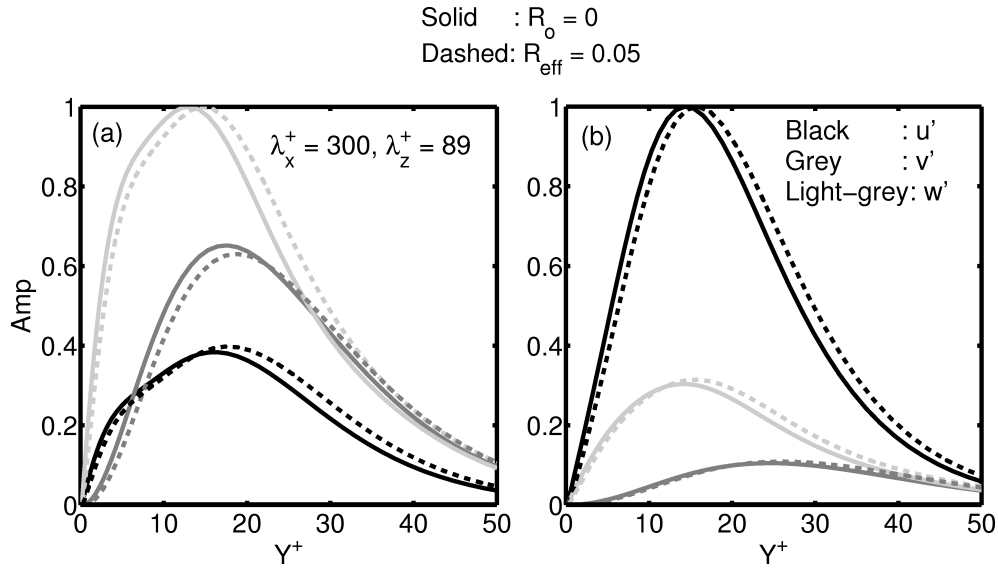


Fig. 4.4 The normalised velocity amplitudes in the (a) initial and (b) final optimal modes of $\lambda_x^+ = 300$ and $m = -12$ (or $\lambda_z^+ = 89$) perturbations. Solid lines are for the non-rotating case, and the dashed lines are for the case $R_{eff} = 0.05$, which has small artificial rotation added over the non-rotating case's flow profile (explained in Section 4.3.2). The initial optimal modes have most energy in the azimuthal and wall-normal velocity perturbations, and are matched with quasi-streamwise vortex. The final optimal modes have most energy in the axial velocity perturbations, and are matched with near-wall streaks. The shape of the optimal modes are very similar for the two cases.

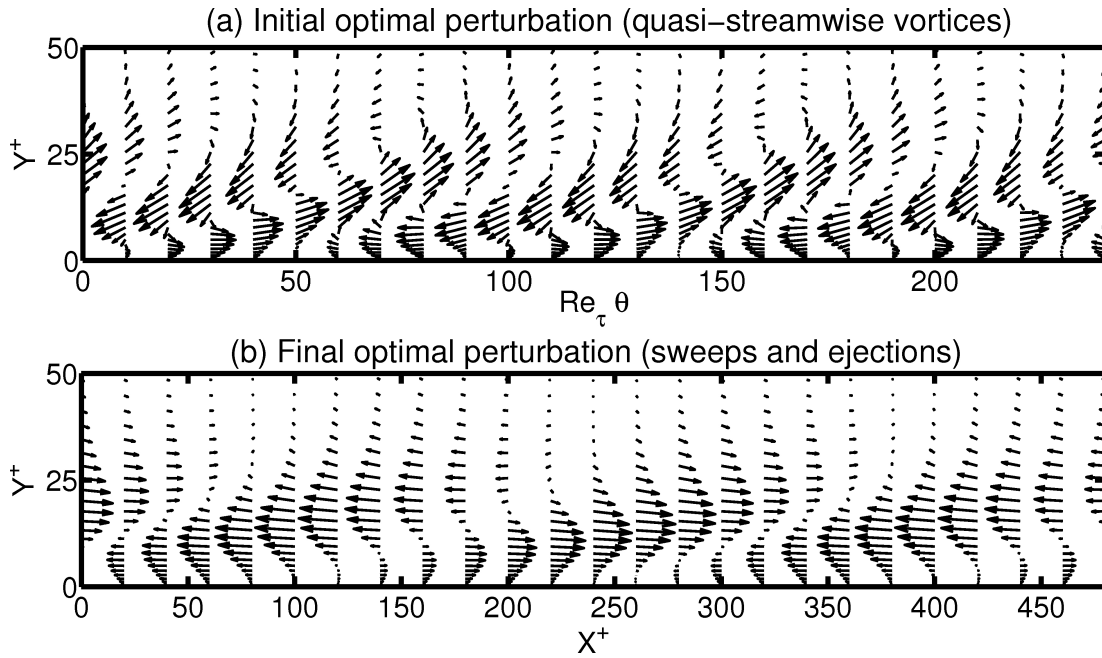


Fig. 4.5 The (a) initial optimal mode in the $y - \theta$ plane and (b) final optimal mode in the $x - y$ plane in the non-rotating case for the $\lambda_x^+ = 300$ and $m = -12$ (or $\lambda_z^+ = 89$) perturbations. The shapes of these modes confirm that the initial optimal mode corresponds to quasi-streamwise vortices, and the final optimal mode corresponds to sweeps and ejections, and hence to streaks.

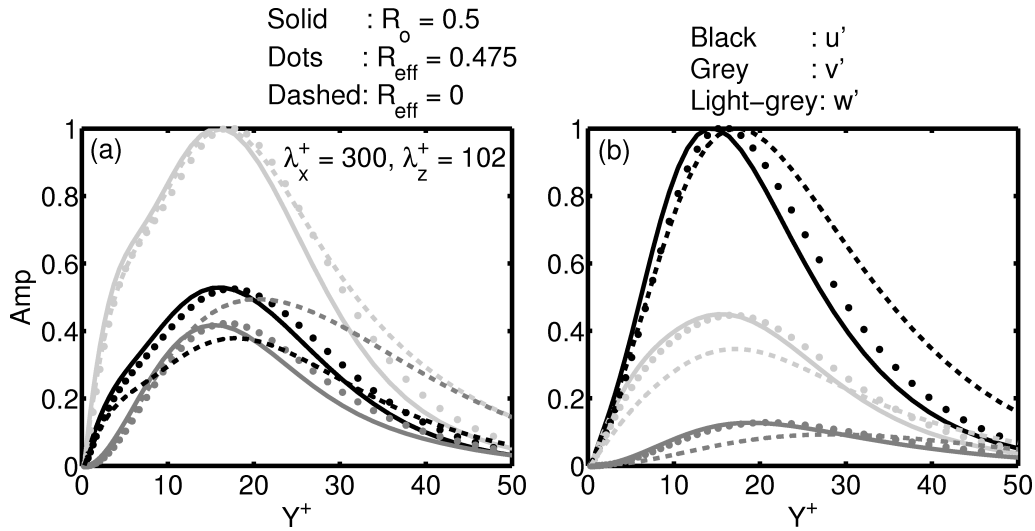


Fig. 4.6 The normalised velocity amplitudes in the (a) initial and (b) final optimal modes of the $\lambda_x^+ = 300$ and $m = -9$ (or $\lambda_z^+ = 102$) perturbations. Solid lines are for the $R_o = 0.5$ case. Dots and dashed lines are for the cases $R_{eff} = 0.475$ and $R_{eff} = 0$, respectively (explained in Section 4.3.2). In these two cases the rotation is artificially reduced or removed from the rotating case's flow profile. The mode shapes are similar to those for the non-rotating case. In the rotating case and the $R_{eff} = 0.475$ case, there are higher energy contributions from the streamwise velocity perturbations in the initial optimal mode and from the wall-normal and azimuthal velocity perturbations in the final optimal mode than those in the initial and final modes, respectively, in the non-rotating and $R_{eff} = 0$ cases. This implies that rotation causes an increase in amplification of the wall-normal and azimuthal velocity components more than in the streamwise velocity component.

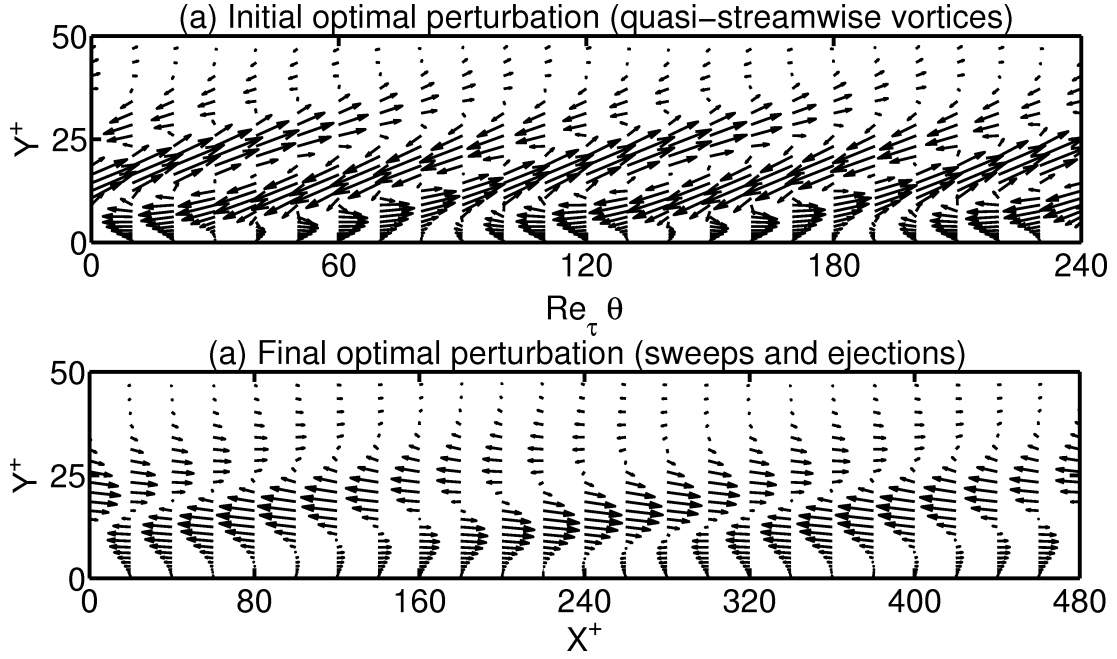


Fig. 4.7 The (a) initial optimal mode in the $y - \theta$ plane and (b) final optimal mode in the $x - y$ plane of the $\lambda_x^+ = 300$ and $m = -9$ (or $\lambda_z^+ = 102$) perturbations in the $R_o = 0.5$ case. The shapes of these modes are similar to the shapes of the corresponding modes in the non-rotating case shown in figure 4.5.

Scaling of near-wall streaks

Jimenez *et al.* [8] found from their DNS data for a turbulent channel flow that peak in spectra of energy in the streamwise velocity at $y^+ = 16$, which is where near-wall streaks have most energy, follows a relation as:

$$\lambda_z^+ = 13 (\lambda_x^+)^{1/3}.$$

Notably, the wavelengths at the peaks in G_{max} from the present analysis also follow a very similar relation:

$$\lambda_z^+|_{peak} = 13.18 (\lambda_x^+)^{1/2.98}.$$

This relation is obtained by using the $\lambda_z^+|_{peak}$ values for the $\lambda_x^+ = 100, 200, 300, 500$, and 700 perturbations, and by minimising the standard deviation in the pre-multiplication factor, which is equal to 0.22. Rotation in pipe causes widening of streaks. Scaling relation changes for the rotating case ($R_o = 0.5$), and is given as:

$$\lambda_z^+|_{peak} = 5.87 (\lambda_x^+)^{1/2}.$$

This relation is also obtained in the same way as that in the non-rotating case. The standard deviation in the pre-multiplication factor here is 0.0584. This relation indicates that near-wall streaks get wider in the rotating case.

In summary, it is seen that the present linear amplification analysis captures the main features of the process of formation of near-wall streaks from quasi-streamwise vortices. It shows that near-wall streaks have the preferred azimuthal wavelength of approximately 100 wall units. The initial and final optimal structures in the process are shown to be close to quasi-streamwise vortices and sweeps and ejections, respectively. The peak in energy spectra from the analysis matches with that from the DNS in Ref. [8]. It also reproduces the effects of rotation on streaks, such as their widening and preference for co-winding structures in rotating flow cases. These results match with the observations in Ref [113]. It, however, predicts that the transient growth increases with rotation, which would not tally with the reduction in skin-friction if everything else in the regeneration cycle of near-wall structures remains unchanged.

4.3.2 Artificial velocity profiles

Unlike in the non-rotating flows, the linear perturbation equations in the rotating flows, shown in equation 4.1, have several linear coupling terms. Each of these linear coupling terms enhances the system's non-normality, and could contribute in extracting energy from the mean flow to sustain turbulent coherent structures. In this Section, some of these terms in the linear perturbation equations are artificially increased or decreased to identify the contribution from each of them individually.

The artificial cases considered here are based on two assumptions. The first is that the mean azimuthal velocity profile (W_0), when normalized by the rotation number, remains nearly unchanged at all the rotation numbers as seen in figure 4.2 (b). The second assumption is that mean axial velocity profile (U_0), when non-dimensionalised in wall units, does not change much in the buffer layer with change in the rotation number. The types of artificial cases studied here are as follows:

I) Addition of small rotation to the non-rotating case: In these cases the mean streamwise velocity profile is the same as in the non-rotating case, and the mean azimuthal velocity profile is equal to either 5 percent or 10 percent of the W_0 in the rotating case ($R_o = 0.5$). Therefore giving the effective rotation numbers equal to 0.025 and 0.05 to these cases, and they are labelled $R_{eff} = 0.025$ and $R_{eff} = 0.05$, respectively.

II) Reduction of rotation from the rotating case ($R_o = 0.5$): There are two such cases and

in both of them the mean streamwise velocity is the same as in the rotating case ($R_o = 0.5$). In the first case, the mean azimuthal velocity is 95 percent of W_0 in the rotating case ($R_o = 0.5$), therefore giving it the effective rotation number equal to 0.475 (labelled $R_{eff} = 0.475$). In the second case, the mean azimuthal velocity is set as zero, therefore giving it the effective rotation number equal to 0 (labelled $R_{eff} = 0$).

III) Removal of the main linear coupling term: In these cases, the linear coupling term $v \frac{dU_0}{dr}$ is artificially removed from the linearised equations in the $R_o = 0$ and 0.5 cases. This is similar to one of the cases in Kim & Lim (2000) [93].

Type I artificial cases

Figure 4.8 (a) shows the maximum transient growth, G_{max} , for the $\lambda_x^+ = 300$ perturbations in the non-rotating flow case and the type I artificial cases. This figure shows that G_{max} increases when the rotation is artificially added to the non-rotating case. All these three flow cases have the same U_0 profile, therefore the change in G_{max} is necessarily caused by the W_0 terms. The normalised velocity amplitudes in the optimal modes for the $R_{eff} = 0.05$ case are shown by the dashed lines in figure 4.4. The optimal mode shapes are similar to those in the non-rotating case, except for a small difference in relative contribution of different velocity components. The initial optimal mode has slightly more contribution from the streamwise velocity and the final optimal mode has more contribution from the wall-normal and azimuthal velocity perturbations. This shows that the W_0 terms cause an increase in amplification of the wall-normal and azimuthal velocity perturbations more than an increase in amplification of the streamwise velocity perturbations. The value of $\lambda_z^+|_{peak}$ remains unaffected by the addition of the W_0 terms.

Type II artificial cases

Figure 4.8 (b) shows the maximum transient growth, G_{max} , for the $\lambda_x^+ = 300$ perturbations in the rotating flow case and the type II artificial cases. This figure shows a reduction in the maximum transient growth, G_{max} , when W_0 terms are reduced from the $R_o = 0.5$ case. This reduction is very small in the $R_{eff} = 0.475$ case, but it is very clear in the $R_{eff} = 0$ case. This confirms again that the W_0 terms cause an increase in the transient growth. In figure 4.6 dots and dashed lines are for the normalised velocity amplitudes of the initial and final optimal modes in the $R_{eff} = 0.475$ and $R_{eff} = 0$ cases, respectively. The mode shapes are quite similar as in the $R_o = 0.5$ case, but with the decrease in the W_0 terms there is a decrease in contributions of the streamwise velocity component in the initial optimal mode

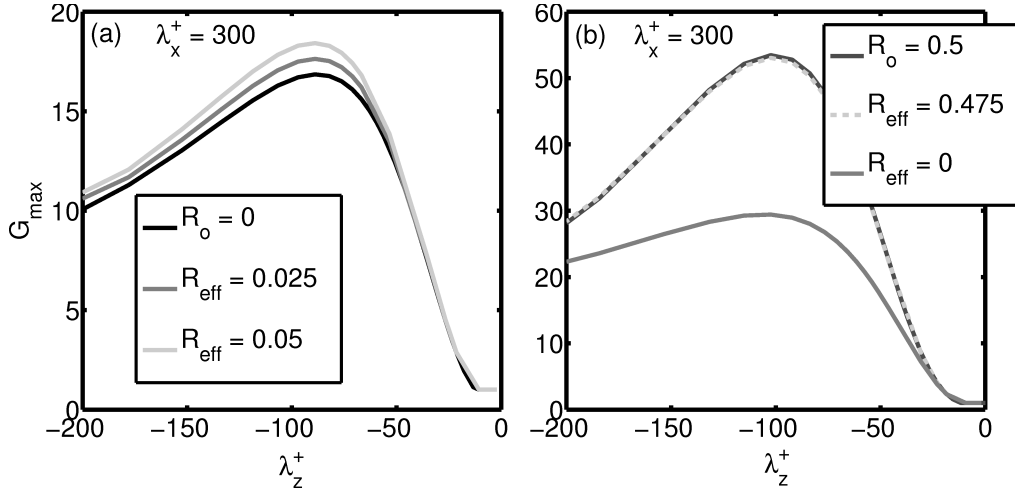


Fig. 4.8 The maximum transient growth, G_{max} , in the $\lambda_x^+ = 300$ perturbations in (a) the non-rotating case and the type I artificial cases, and (b) the $R_o = 0.5$ case and the type II artificial cases. Frame (a) shows that G_{max} increases as rotation is artificially added to the non-rotating case, and frame (b) shows that G_{max} decreases as rotation is artificially removed from the rotating case. These results show that the W_0 terms in the linearised perturbation equations contribute to the increase in transient growth. These results also show that $\lambda_z^+|_{peak}$ is entirely dependent upon the U_0 profile.

and of the wall-normal and azimuthal velocity components in the final optimal mode. This confirms again that the W_0 terms cause increase in amplification of the wall-normal and azimuthal velocity perturbations more than an increase in amplification of the streamwise velocity perturbations. The value of $\lambda_z^+|_{peak}$ remains the same even when the W_0 terms are completely removed. This shows that $\lambda_z^+|_{peak}$ is entirely determined by the U_0 profile.

Type III artificial cases

Kim & Lim (2000) [93] showed that turbulence in channel flow decays in the absence of the U_0 linear coupling term, which is similar to the $\nu \frac{dU_0}{dr}$ term. A major consequence of this result is that one only needs to suppress the coupling between the wall-normal velocity perturbations and the mean shear to control the flow, and this can be achieved by wall-suction and wall-blowing type actuators. In rotating pipe flows, however, there are additional linear coupling terms which could extract energy from the mean flow to possibly sustain turbulence even in the absence of the $\nu \frac{dU_0}{dr}$ term. To check this, the $\nu \frac{dU_0}{dr}$ coupling term is removed from the rotating case ($R_o = 0.5$) to see whether the additional linear coupling terms can independently extract energy from the mean flow. Figure 4.9 shows that there is very little transient growth in the system, and none at all at $\lambda_z^+ \approx 100$, in the absence of the $\nu \frac{dU_0}{dr}$ coupling term.

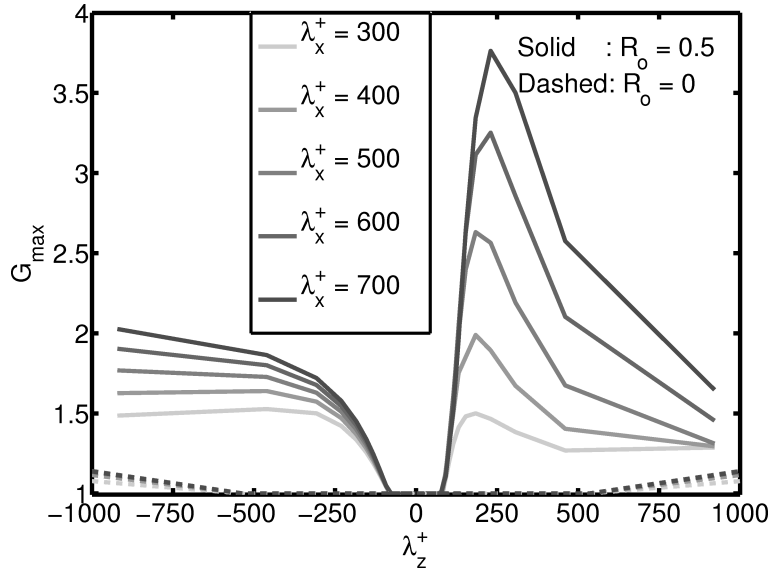


Fig. 4.9 The maximum transient growth, G_{max} , in the system when the $v \frac{dU_0}{dr}$ term is artificially removed. There is very little transient growth in the system and none at $\lambda_z^+ \approx 100$. This shows that the W_0 terms do not cause transient growth by themselves. They need the $v \frac{dU_0}{dr}$ term.

This shows that the additional linear coupling terms, which include W_0 , redistribute energy and enhance transient growth but they do not independently extract energy from the mean flow. Therefore, the original control strategy to just suppress the $v \frac{dU_0}{dr}$ term should also work in rotating pipe flows.

From the results discussed in this section, it is concluded that rotation of the pipe increases the transient growth in the system, which implies that if this were the only effect of rotation then near-wall streaks would be more energetic in rotating cases. However, we know that in rotating turbulent pipe flows the streaks are weaker and less frequent [113]. The streaks require quasi-streamwise vortices for their formation, and the formation of the quasi-streamwise vortices requires the streaks to breakdown as shown in the regeneration cycle in figure 4.1. This process is studied next to find whether this step can explain the reduction in near-wall structures in the rotating flow cases.

4.4 Breakdown of near-wall streaks

Lifted streaks are susceptible to sinuous (anti-symmetric) and varicose (symmetric) instabilities, which lead to their breakdown. Such streak instability is a common feature in laminar, transitional, and turbulent wall-bounded flows. Asai *et al.* (2002) [122] managed to produce

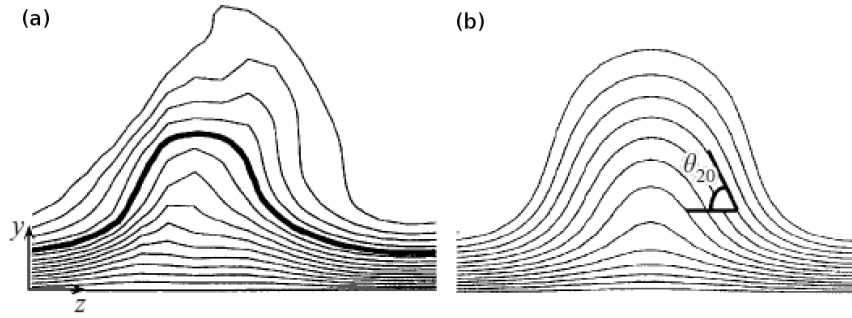


Fig. 4.10 (a) The cross-stream distribution of the streamwise velocity as observed for low-speed streak regions at the quiescent phase, which is during the minimum drag phase, in the minimal channel flow simulations. (b) Idealised version of (a). This figure is taken from Schoppa & Hussain (2002) [11].

single low-speed streaks in laminar boundary layer flows. They showed that when the streak is thin, as it is in the buffer layer, sinuous instability is dominant and eventually nonlinear processes lead to the formation of quasi-streamwise vortices. They also showed that when the streak is thicker, as it is in the logarithmic layer, varicose instability is dominant and eventually nonlinear processes lead to the formation of hairpin vortices. In this chapter, dynamics in the buffer layer is considered, where the streak thickness is approximately 100 wall units [21, 27], also shown in Section 4.3, and sinuous instability is dominant.

Lifted low-speed streaks in the near-wall region cause temporarily inflectional velocity profile, which give rise to modal sinuous instabilities [11, 94, 122]. This sinuous mode instability causes breakdown of the streaks, and an x -dependent flow is generated. Vorticity is then accumulated in certain regions of this x -dependent flow and quasi-streamwise vortices are eventually generated via nonlinear processes [11, 94]. Schoppa & Hussain [11] showed that the breakdown can also happen because of non-modal sinuous instability, especially when the streaks are not strong enough for modal instability. In this chapter, however, only modal instability and how axial rotation of the pipe affects this instability are examined.

Figure 4.10(a) shows the cross-stream distribution of the streamwise velocity as observed for low-speed streak regions at the quiescent phase, which is during the minimum drag phase, in the minimal channel flow simulations. Figure 4.10(b) is an idealised version of the actual distribution shown in frame (a) [11]. The velocity profile for the idealised distribution is given as, $U(y, z) = U_0(y) + \frac{\Delta u_0}{2} \cos(\beta_s z) g(y)$, $V = W = 0$, in Ref [11]. Because the near-wall region is largely unaffected by curvature of the pipe, the same flow profile for an idealised realisation of low-speed streaks in pipe flow is assumed in this study. It is given

below in cylindrical polar coordinates as:

$$\begin{aligned} U(r, \theta) &= U_0(r) + \frac{\Delta u_o}{2} \cos(M\theta)g(r) \\ V &= 0, \quad W(r) = W_0(r) \\ g(r) &= (1-r) \exp\left(-\eta(1-r)^2\right) = y \exp(-\eta y^2), \quad \text{where } y = 1-r. \end{aligned} \quad (4.3)$$

where η is such that the function $g(r)$ has a plateau at $y^+ \approx 20$, and M represents the azimuthal spacing of the streaks as: $\lambda_z^+ = \frac{2\pi}{M} Re_\tau$. The strength of a streak is defined through maximum normal vorticity: $\Omega_y|_{max} = 0.5M\Delta u_o$. A higher value of $\Omega_y|_{max}$ means a stronger streak.

The linear perturbations in the velocity profile are decomposed as:

$$\begin{aligned} u &= \sum_{n=0}^N [u_{nv}(r) \cos(nM\theta) + u_{ns}(r) \sin(nM\theta)] \\ v &= \sum_{n=0}^N [v_{nv}(r) \cos(nM\theta) + v_{ns}(r) \sin(nM\theta)] \\ w &= \sum_{n=0}^N [w_{nv}(r) \sin(nM\theta) + w_{ns}(r) \cos(nM\theta)] \\ p &= \sum_{n=0}^N [p_{nv}(r) \cos(nM\theta) + p_{ns}(r) \sin(nM\theta)] \\ (u', v', w', p') &= (u, v, w, p) \exp(-i\omega t + ikx) \end{aligned} \quad (4.4)$$

Subscripts nv and ns refer to the n^{th} varicose and n^{th} sinuous modes, respectively. The continuity and momentum equations are given in Appendix A. It is seen from the equations that the sinuous and varicose modes are linearly independent in non-rotating flow cases where $W_0 = 0$. The W_0 terms cause coupling between the sinuous and varicose modes, but they do not otherwise appear in the equations. Depending upon the W_0 profile, rotation can stabilise or destabilise the streaks. There is another effect of the axial rotation, which might be significant in the cases with high rotation number, but is outside the scope of the present study. This effect is through the change in the U -profile in equation A caused by rotation, i.e. through the change in the shape of the streaks in rotating cases.

To numerically solve the linear perturbation equations, Chebyshev spectral method with Gauss-Lobato points in the wall-normal direction are used. The leading eigenvalues and eigenvectors are found using the ‘eigs’ command in Matlab. The number of grid-points used is 80, and the number of sinuous and varicose modes used are 6. The convergence of

the leading eigenvalues is checked by repeating the calculations with 100 grid-points and 6 sinuous and varicose modes, and with 80 grid-points and 8 sinuous and varicose modes. The real and imaginary parts of the leading eigenvalues are found to be accurate to 3 significant figures.

There are two families of cases considered here. The first family is comprised of the non-rotating case and the $R_{eff} = 0.025$ and $R_{eff} = 0.05$ cases from the type I artificial cases explained in Section 4.3.2. From the results for these cases, it is seen how a small increase in rotation affects the breakdown instability of streaks. The second family is comprised of the rotating case ($R_o = 0.5$) and the $R_{eff} = 0.475$ and $R_{eff} = 0$ cases from the type II artificial cases explained in Section 4.3.2. The influence of rotation on the U -profile (by changing the shape of the streaks) is not considered. However, the results of these cases still show the effect of reducing the W_0 terms on the breakdown instability of streaks.

4.4.1 The non-rotating case and the cases with small artificial rotation

The streak strength is fixed at $\Omega_y|_{max} = 4.3$, which is similar to the values used in Ref. [11], and η is set at 40 for the first family of cases. Figure 4.11 (a) shows the growth rate, ω_i , of streak breakdown instability in the non-rotating case as a function of the perturbation wavelength λ_x^+ . Simulations are performed for streaks of azimuthal wavelength ≈ 100 , which is close to the observed spanwise spacing of near-wall streaks in boundary layer flows [21, 27]. This is done by fixing $M = 9 - 15$, which is equivalent to $\lambda_z^+ = 120 - 70$.

Streaks are most unstable for perturbations of $\lambda_x^+ \approx 300$, which implies that the most preferred length of the resultant quasi-streamwise vortices is approximately 300. This matches well with the results in Ref. [11], and with the length of the minimal channel required for sustenance of wall-turbulence [97]. The $M = 11$ ($\lambda_z^+ \approx 97$) streaks are most susceptible to the breakdown instability, with maximum growth rate for the $\lambda_x^+ \approx 286$ perturbations. It is also known from the results in Section 4.3, that quasi-streamwise vortices that are 300 – 400 wall units long in the streamwise directions get most amplified to form near-wall streaks with $\lambda_z^+ \approx 90 - 100$, which is equivalent to the $M = 11 - 12$ streaks. Based on the results in the present section and in Section 4.3, it is concluded that quasi-streamwise vortices of $\lambda_x^+ \approx 300 - 400$ and $\lambda_z^+ \approx 90 - 100$ are the most favoured ones in the near-wall structures' regeneration cycle. The streamwise length is chosen during the process of breakdown of streaks, and the azimuthal width is chosen during the process of formation of streaks.

The effect of rotation is examined for the $M = 11$ streaks. The results are shown in figure

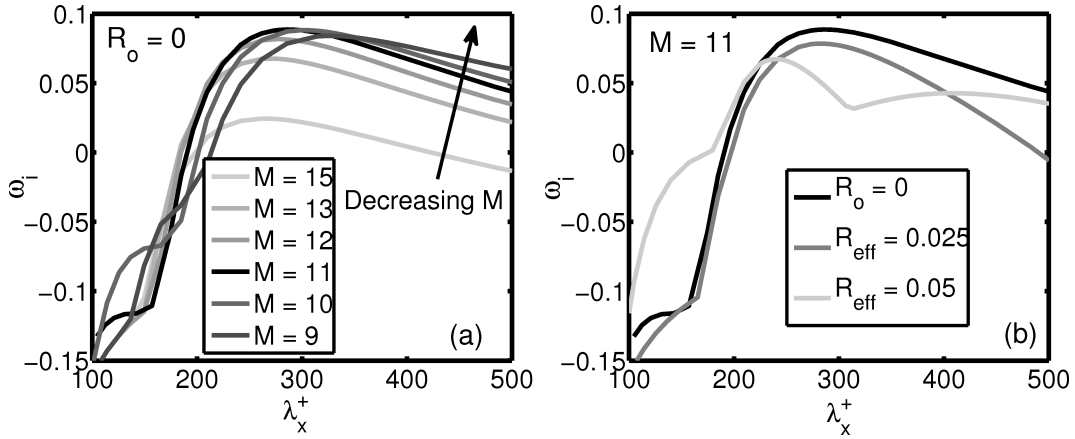


Fig. 4.11 (a) The growth rate, ω_i , of the streak breakdown instability as a function of λ_x^+ for streaks with azimuthal wavenumber $M = 9 - 15$, equivalent to azimuthal spacing of 70-120, in the non-rotating flow case. The $M = 11$ ($\lambda_z^+ \approx 97$) streaks are most unstable to the breakdown instability at $\lambda_x^+ \approx 286$. (b) The growth rate of the streak breakdown instability in the $M = 11$ streaks in the three flow cases. The streak breakdown instability decreases as rotation in the flow increases, which shows that rotation of the pipe has a stabilising effect on streaks.

4.11 (b) for the three flow cases ($R_o = 0$, $R_{eff} = 0.025$ and $R_{eff} = 0.05$). It is seen from the results that rotation has a stabilising effect on near-wall streaks. This means that rotation prevents the breakdown of streaks, and hence reduces the formation of quasi-streamwise vortices.

Figure 4.12 shows contours of the streamwise vorticity component of the leading eigenmodes for the streak breakdown instability of the $M = 11$ streaks in the (a) $R_o = 0$ flow case at $\lambda_x^+ = 286$, (b) $R_{eff} = 0.025$ flow case at $\lambda_x^+ = 286$, and (c) $R_{eff} = 0.05$ flow case at $\lambda_x^+ = 242$. The streamwise vorticity structure is divided into three regions: crests, troughs, and streak flanks, as marked in frame (a) and in Ref [11]. Nonlinear effects cause streamwise vortices to get concentrated on one of the flanks and the generation of the quasi-streamwise vortices commences [11]. Frames (b) and (c) show that the addition of rotation tilts the structure of streamwise vortices in the direction of rotation. This is to favour the formation of vortices which are tilted in the direction of rotation. It is seen in figure 4.7 that vortices tilted in the direction of rotation develop into streaks more favourably than those tilted in the other direction.

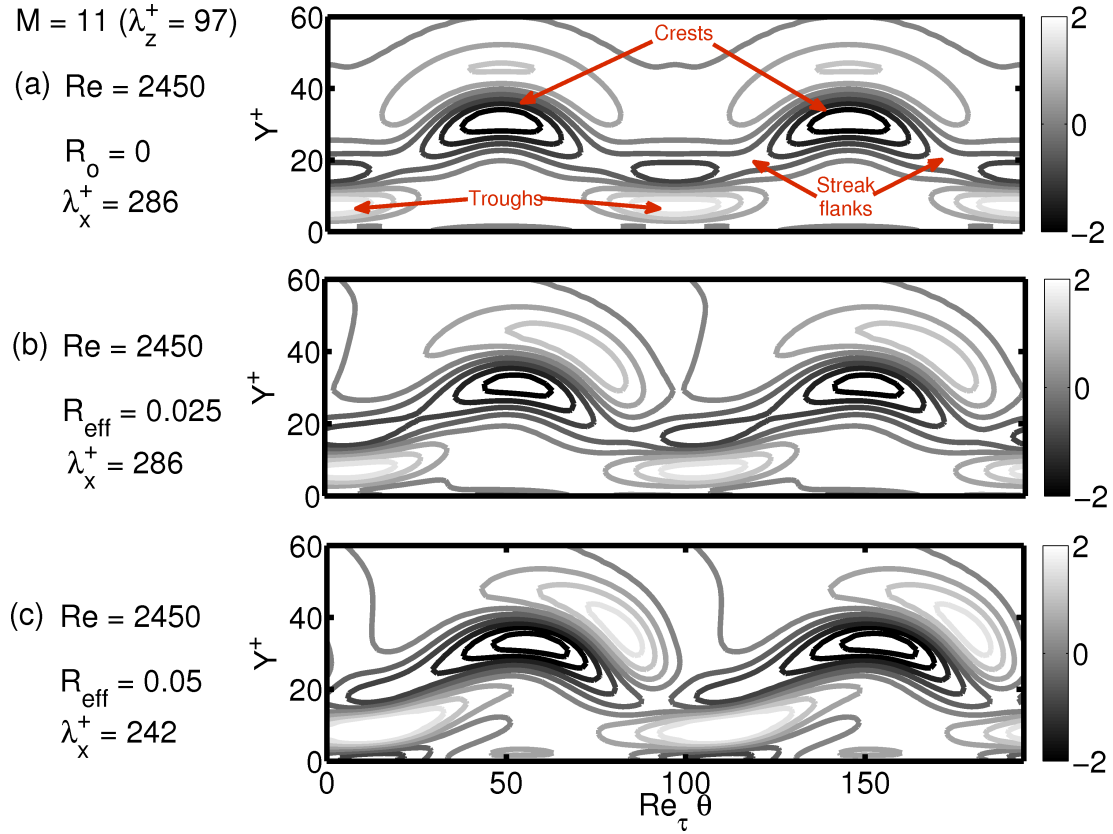


Fig. 4.12 The streamwise vorticity component of the leading eigenmodes for the streak breakdown instability of the $M = 11$ streaks are plotted for the (a) $R_o = 0$ flow case at $\lambda_x^+ = 286$, (b) $R_{eff} = 0.025$ flow case at $\lambda_x^+ = 286$, and (c) $R_{eff} = 0.05$ flow case at $\lambda_x^+ = 242$. In frame (a) the three main regions in the structure are marked as crests, troughs, and streak flanks. As nonlinear effects get prominent, the streamwise vortex gets concentrated on one of the flanks and the generation of the quasi-streamwise vortices commences [11]. Rotation in the flow tilts the structure of streamwise vortices in one direction. This is to favour the formation of the vortices on the one side of the flanks, which is tilted in the direction of rotation.

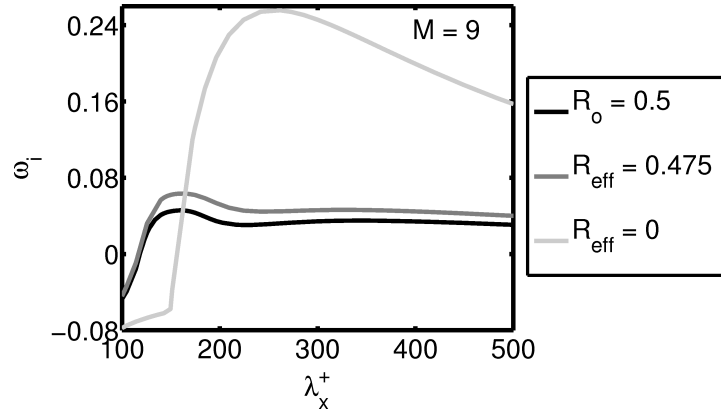


Fig. 4.13 The growth rate, ω_i , of the streak breakdown instability in the $M = 9$ streaks in the three flow cases ($R_o = 0.5$, $R_{eff} = 0.475$, and $R_{eff} = 0$). The streak breakdown instability increases as rotation is artificially removed, which confirms the stabilising effect of rotation.

4.4.2 The $R_o = 0.5$ case and the cases with artificially reduced rotation

The streak strength for this family of cases is fixed as $\Omega_y|_{max} = 4.3$, the same as in Section 4.4.1, and η is set as 22. As mentioned before, in the cases with high rotation the effect of rotation on the U -profile is not considered. These cases still include the effect of the W_0 terms on the streak breakdown instability, and purpose of examining these cases is to confirm whether rotation has a stabilising role on the streak breakdown instability. Figure 4.13 shows the effect of artificially removing the rotation on the growth rate of the streak breakdown instability of the $M = 9$ streaks. It shows that when 5 percent of the rotation is removed from the rotating profile ($R_{eff} = 0.475$), the growth rate increases. If the rotation is completely removed, the growth rate further increases significantly. These results confirm the stabilising effect of the rotation on the streak breakdown instability. Therefore, this shows that rotation prevents the formation of quasi-streamwise vortices.

4.5 Summary and Conclusion

In two parts of this chapter, stability analyses based on the linearised Navier–Stokes equations are performed to study the formation of near-wall structures in turbulent pipe flow, and to examine the effect of constant axial rotation of the pipe on their formation. In the first part in Section 4.3, the formation of streaks from quasi-streamwise vortices and the effect of rotation on this process are studied. This is done by performing energy amplification analysis based on the Navier–Stokes equations linearised over the mean velocity profile. The effect of the neglected nonlinear terms in this analysis is modelled as the input streamwise wave-

lengths of the perturbations. In the second part in Section 4.4, the breakdown instability of streaks, for the eventual formation of quasi-streamwise vortices, and the effect of rotation on this process are studied. This is done by performing secondary stability analysis based on the Navier–Stokes equations linearised over the mean velocity profile superimposed with an ideal realisation of low-speed streaks. The mean flow profiles in this study are taken from Ref. [113], and the profile for an ideal realisation of low-speed streaks is taken from Ref. [11].

It is shown in the first part in Section 4.3 that streaks with the azimuthal spacing of approximately 100 wall-units are preferred in the flows when they are formed from quasi-streamwise vortices that are a few hundred wall-units long in the streamwise direction. Both of these length scales match well with experimental observations in turbulent boundary layers. It is found that axial rotation of the pipe causes the widening of streaks, which agrees with the observations in Ref. [113]. Rotation also found to increase the transient growth, G_{max} , in the system. This increase in G_{max} is in accord with the destabilising role of rotation in laminar flows, but in turbulent flows the axial rotation is found to have a stabilising effect. It is observed in Ref. [113], that flow in axially rotating pipes have fewer near-wall structures than those in the same Reynolds number non-rotating pipe flow. In order to get further clarification on the role of rotation, its effect on the process of streak breakdown is examined.

It is shown in the second part in Section 4.4 that lifted low-speed streaks break down to form quasi-streamwise vortices that are around 300 wall units long in the streamwise direction. This matches with other theoretical calculations and experiments. It is also shown that axial rotation of the pipe has a stabilising role on the streaks breakdown instability, and therefore rotation prevents the formation of quasi-streamwise vortices. This explains how rotation can cause a reduction in near-wall structures. Based on the observations that the rotation has a stabilising role on near-wall structures, it is concluded that the stabilising role of the rotation on the process of breakdown of streaks dominates over the effect of the rotation in increasing the maximum transient growth, G_{max} , in the process of formation of streaks. In this Chapter, it is shown that simple linear stability analyses, without requiring any turbulence closure model, reproduce many important features in the process of formation of near-wall structures in turbulent pipe flow. They also explain the effect of axial rotation in the pipe on the near-wall structures in rotating flows.

There are some limitations of linear stability analysis in turbulent flows. One of them is that to perform linear stability analysis one needs the information on the mean flow profile. The mean flow profile, however, in turn needs either the full or a modelled information of

all coherent structures in the fully nonlinear flow. Therefore, linear stability analysis of turbulent flows is no longer a predictive analysis like in laminar flows, but it is a diagnostic analysis. If successful, such as in this chapter, it is useful in understanding the physics behind the formation and maintenance of coherent structures. It is also useful as a basis for further application of linear analysis tools, such as sensitivity analysis as shown in Refs. [88, 111] and in designing model-based active control as shown in Ref. [87].

Chapter 5

Hydrodynamic instabilities in gas turbine combustors

In this chapter approaches based on linearised equations are used to predict large hydrodynamic structures in turbulent flows inside gas-turbine injector-combustor systems. The main aim of this Chapter is to investigate whether the perturbations in the Reynolds stresses are sufficiently influential that they need to be included in stability analysis, when applied for finding hydrodynamic instabilities in gas-turbine injector-combustor flow systems. Local linear stability analysis is applied to complex flows inside gas-turbine injector-combustor systems [123–126]. In this Chapter, the calculations are performed using a software tool 'Instaflow'. This tool was originally developed by Dr Simon Rees and Dr Matthew P Juniper for local linear hydrodynamic stability analysis of flows [123].

Another aim of this chapter is to present the use of stability analysis in predicting the effect of changes in operating-condition/design on hydrodynamic structures in gas-turbine flows. Most results in this chapter were produced during a collaborative work between me, Mr Tifenn Brandily, Mr Mike Simpson, Mr Ali Ersoz, and Dr Matthew Juniper. Their help is deeply appreciated. Thanks must also go to Dr Will Bainbridge and Prof Stewart Cant for providing their Fluent codes to generate RANS and URANS data for the S series cases, and to Dr Fred Witham from Rolls-Royce for providing RANS data for the T series cases.

5.1 Introduction

Flows inside gas-turbines are often injected with swirl, and are at high Reynolds numbers. The swirl generates a radial pressure gradient, and when it comes out of an injector into a combustion chamber it produces a negative axial pressure gradient on expansion. This

causes the flow to reverse and a central recirculation zone (CRZ) usually forms. The recirculating flow brings the hot flow and reactants to the base of the flame, and enables the flame to be stabilised within the combustion chamber. Another common coherent structure in a combustion chamber is a precessing vortex core (PVC). It is formed when the recirculation bubble is unstable to non-axisymmetric perturbations. A review of these structures, and the physical mechanism behind their formation can be found in Ref. [127] and the references cited therein. Syred [127] noted that the formation of a PVC and other instabilities is a function of a number of parameters, such as the swirl number, the mode of fuel injection, the equivalence ratio, and small changes in injector design.

The motivation behind studying hydrodynamic instabilities and the resultant large-scale coherent structures in gas-turbine flows is for their role in entrainment of fuel into air, which is important for air-fuel mixing at the molecular level for combustion [83–85]. Apart from this desired effect on the air-fuel mixing, hydrodynamic instabilities may also interact with thermoacoustic oscillations. Combustion in a confined geometry is susceptible to thermoacoustic oscillations. These oscillations are result of a positive feedback mechanism between combustion and long wavelength pressure-waves inside the combustion chamber. If the mechanical energy injected during this positive feedback mechanism is higher than the acoustic damping then these oscillations grow, sometimes to dangerously high levels [86]. Thermoacoustic oscillations are particularly high in cases where the frequency of hydrodynamic instability is close to the natural acoustic frequency as shown in Refs. [128, 129]. This therefore is one more reason for studying hydrodynamic instabilities.

Flows inside gas-turbines are in the turbulent regime and the systems' geometries are usually complicated. This make studying them computationally expensive, such that DNS is practically impossible and LES is possible only at a few steps in the design process. RANS and URANS are popular methods because they calculate the mean velocity and Reynolds stresses in a turbulent flow in a feasible time as required in the design process. These methods however are very dissipative, particularly in commercial solvers. The RANS solvers give either little or no information about hydrodynamic instabilities in the flows, and the URANS solvers give information only about low frequency oscillations in the flows. The main purpose of this chapter is to apply approaches based on the linearised Navier–Stokes or RANS equations, which use the mean velocity and Reynolds stress fields as input, to find hydrodynamic instabilities in gas-turbine injector-combustor systems. These approaches include the molecular viscosity based stability analysis, eddy viscosity based stability analysis, and anisotropic eddy viscosity based stability analysis that are derived in Chapter 3. The molecular viscosity based analysis is derived by linearising the Navier–Stokes equa-

tions over the mean flow profile. The eddy and anisotropic eddy viscosity based analyses are derived by linearising the RANS equations over the mean flow profile. The latter two analyses include the wave-induced perturbations in the Reynolds stresses [76], plus all the terms in the first analysis. The similarities and differences in the results from these analyses are shown.

Another purpose of this chapter is to apply the molecular viscosity based stability analysis to analyse the effect of changes in equivalence ratio and design of injector geometries on hydrodynamic instabilities. Towards this purpose, three cases in the S series with various equivalence ratio and six cases in the T series with small design modifications are considered. The S and T series are groups of Rolls-Royce lean-burn injectors currently under development. Compressibility effects on hydrodynamic instabilities are also examined. For one of the cases, the mean flow is obtained both from time-averaging the URANS simulation data and from the RANS simulation data. The similarities in the results and the conceptual differences between the RANS and URANS are pointed out.

A major assumption in this chapter is that local linear stability analysis can be applied to complex flows inside gas-turbine injector-combustor systems. This assumption is based on the success of previous studies on similar flows in Refs. [123–126]. In local stability analysis the WKBJ approximation is applied. It means that the mean flow is assumed to be locally parallel. Therefore small local perturbations in the velocity and pressure, in axisymmetric mean flows, are assumed to be of the form: $\mathbf{u}(r) \exp(i(2\pi kx + m\theta - 2\pi\omega t))$. In this expression, $2\pi k$ and m are the axial and azimuthal wavenumbers, and $2\pi\omega$ is the angular frequency of corresponding perturbations. Each azimuthal wavenumber perturbation is considered separately by fixing the m as an integer.

The governing equations are solved with the no slip boundary condition at the walls to find the maximum absolute growth-rate. The solution pair (k, ω) is a set of complex numbers represented as $(k_r + ik_i, \omega_r + i\omega_i)$. In this expression $i = \sqrt{-1}$, the axial wavelength of the perturbation is $1/k_r$, the axial growth rate of the perturbation is $-2\pi k_i$, the frequency of the perturbations is $2\pi\omega_r$, and the growth rate of the perturbations is $2\pi\omega_i$. The regions of positive ω_i are called pockets of absolute instability. Broadly speaking, in order to provoke global instability, a pocket of absolute instability needs to be at least one quarter of the corresponding instability wavelength. A review of theory of local stability analysis, and its relation with global stability can be found in Ref. [130].

5.1.1 Outline

This Chapter is divided into six Sections. In Section 5.2, different stability analyses are briefly explained, and are applied to a case of the S series. The effects of compressibility and the wave-induced fluctuations in the Reynolds stresses in stability analysis are analysed. Section 5.3 discusses the conceptual differences between the RANS and URANS for statistically non-stationary turbulent flows. Stability analysis is performed by linearising the equations over the RANS data. The results are compared with the results presented from stability analysis performed by linearising the equations over the time-averaged URANS data in Section 5.2. In Section 5.4, the operating conditions in the S series are changed from stoichiometric to lean and to very lean by adjusting the fuel flow rate. The effect of the change in the operating conditions on hydrodynamic instabilities is analysed. In Section 5.5, six cases in the T series are studied. Each of these cases have small design differences. The effects of small design changes on hydrodynamic instabilities are pointed out.

5.2 Effects of turbulence models and compressibility in stability analysis of gas-turbine flows

Figure 5.1 shows the time-averaged velocity and temperature fields in the case-A of the injector-combustor system in the S series. This case of the S series has an operating condition such that air and fuel are injected at the stoichiometric ratio. Later, cases in the S series with lean fuel injection are also considered. A two-dimensional projection in the axial-radial plane of a limited part of the geometry is shown, which is chosen such that it starts from the centre and extends radially to the first wall in the radial direction. The results are obtained by time-averaging the solutions from the URANS simulations. A pressure-based solver of Fluent is used and the codes are provided by Dr Will Bainbridge [131]. The pressure-based solver refers to the general class of methods called projection methods, where the pressure equations, derived from the continuity and momentum equations, are solved to obtain numerical solutions of the Navier–Stokes equations [132].

The fields shown in the figure are a result of extensive post-processing. First, the time-averaged flow profiles are obtained by averaging the URANS data. In this study, the flow is assumed to be axisymmetric. In order to average the flow in the azimuthal direction, the data is interpolated onto a regular three-dimensional grid using the ‘TriScatteredInterp’ function in MATLAB. This interpolated function is then averaged in the azimuthal direction. The data is further smoothed to remove any numerical jumps, and special care is taken to ensure

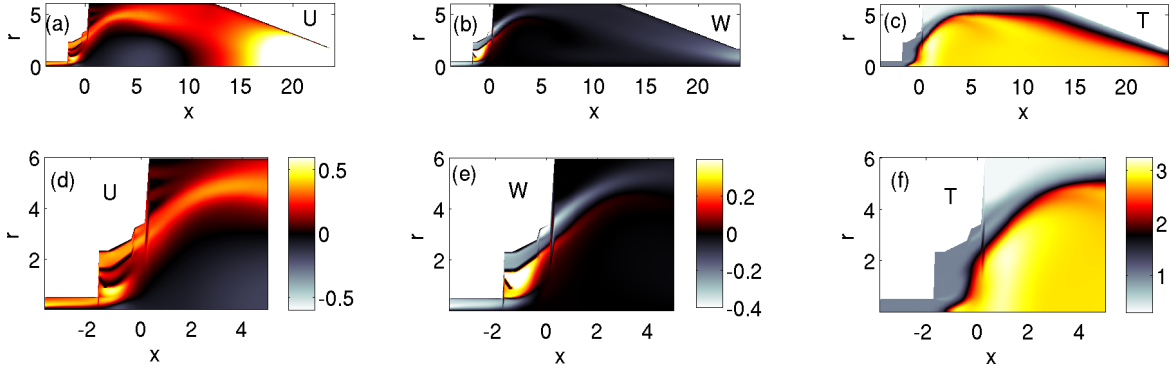


Fig. 5.1 The flow fields in the case-A of the S series gas-turbine injector-combustor system. The operating conditions in this case are set such that air and fuel are injected at the stoichiometric ratio. Frames (a–c) show the fields in the entire system while frames (d–f) show fields only in an upstream part of the geometry. Frames (a) and (d) show the axial velocity, (b) and (e) show the azimuthal velocity, and (c) and (f) show the temperature field.

that the swirl velocity and the first radial derivative of the axial velocity are zero at the centreline. In this chapter swirl velocity refers to the azimuthal velocity component of the flow.

Frames (a–c) show the axial and azimuthal velocities, and temperature fields in the geometry inclusive of the entire downstream portion. Frames (d–e) show the same fields as in (a–c) but only in an upstream part of the geometry, which is the most influential region of the flow. The geometry is sliced such that each slice contains the data at a discrete x -location. These slices are then studied separately using local stability analysis. In local stability analysis, the radial velocity is ignored. The flow after $x = 0.14$, however, has large radial velocity that cannot be ignored, and therefore local analysis is not performed for the flow downstream of $x = 0.14$.

The flow is turbulent. There are a number of stability analyses performed for various turbulent flows in the literature, and different approaches are found useful for different flows. A general form of the governing equations is formulated in this thesis, which is given below. Different approaches used in this Chapter use specific forms of these governing equations as explained below.

The linearised continuity equation is:

$$\Omega \frac{\rho}{P} p' - \Omega \frac{\rho}{T} T' = \rho k_x u' + \frac{1}{r} \frac{dr \rho v'}{dr} + \frac{m \rho}{r} w' + \frac{m \rho W}{r P} p' + \frac{\rho U k_x}{P} p' - \frac{m W \rho}{r T} T' - \frac{\rho U k_x}{T} T' \quad (5.1)$$

The linearised momentum equation in the axial direction is:

$$\Omega \rho u' = \frac{1i}{Re} \left(\frac{1}{r} \frac{d}{dr} r \frac{d}{dr} - \frac{m^2}{r^2} - \frac{4}{3} k_x^2 \right) u' + \rho \left(\frac{m}{r} W + k_x U \right) u' + \rho \frac{dU}{dr} v' - \frac{1i}{3Re} k_x \frac{1}{r} \frac{drv'}{dr} \\ - \frac{1i}{3Re} k_x \frac{m}{r} w' + k_x p' - \frac{\partial}{\partial x} r_{xx} - \frac{\partial}{\partial r} r_{xr} - \frac{\partial}{\partial \theta} r_{x\theta} \quad (5.2)$$

The linearised momentum equation in the radial direction is:

$$\Omega \rho w' = \rho W \frac{m}{r} w' - \frac{1i}{Re} \left[\left(1 + \frac{4}{3} m^2 \right) \frac{1}{r^2} - \frac{1}{r} \frac{d}{dr} r \frac{d}{dr} + k_x^2 \right] w' + \rho U k_x w' - \frac{1i}{3Re} \frac{mk_x}{r} u' \\ + \rho \frac{1}{r} \frac{drW}{dr} v' - \frac{1im}{3Re} \left(7 \frac{1}{r^2} + \frac{1}{r} \frac{d}{dr} \right) v' + \frac{m}{r} p' - \frac{\partial}{\partial x} r_{rx} - \frac{\partial}{\partial r} r_{rr} - \frac{\partial}{\partial \theta} r_{r\theta} \quad (5.3)$$

The linearised energy equation is:

$$\Omega \rho T' = \left[\frac{1i\gamma}{RePr} \left(\frac{1}{r} \frac{d}{dr} r \frac{d}{dr} - \frac{m^2}{r^2} - k_x^2 \right) + \frac{\rho m}{r} W + \rho U k_x \right] T' + 2i \frac{\gamma-1}{ReRg} \frac{dU}{dr} \frac{du'}{dr} + k_x \frac{\gamma-1}{Rg} P u' \\ + \rho \frac{dT}{dr} v' - 2i \frac{\gamma-1}{ReRg} m \left(\frac{d}{dr} \frac{W}{r} \right) v' + \frac{\gamma-1}{Rg} P \frac{1}{r} \frac{d}{dr} r v' - 2i k_x \frac{\gamma-1}{ReRg} \frac{dU}{dr} v' \\ + 2i \frac{\gamma-1}{ReRg} \left(\frac{dW}{dr} - \frac{W}{r} \right) \left(r \frac{d}{dr} \frac{w'}{r} \right) + \frac{m}{r} \frac{\gamma-1}{Rg} P w' - \frac{\partial}{\partial x} r_{\theta x} - \frac{\partial}{\partial r} r_{\theta r} - \frac{\partial}{\partial \theta} r_{\theta \theta} \quad (5.4)$$

where $(u', v', w', p', T', \rho')$ are the perturbations in the axial velocity, radial velocity, azimuthal velocity, pressure, temperature, and density, respectively. The pressure, temperature, and density variations are related as: $\frac{\rho'}{\rho} = \frac{p'}{P} - \frac{T'}{T}$. The frequency and wavenumber in the equation are related to ω and k as $\Omega = 2\pi\omega$, $k_x = 2\pi k$. Re is the Reynolds number based on the reference density, velocity, length, and viscosity values, Rg is the gas constant, Pr is the Prandtl number, and γ is the ratio of the specific heat at constant pressure to the specific heat at the constant volume. The r_{ij} terms in the momentum equations represent the perturbations in the Reynolds stresses, and are derived in Chapter 3.

The mean values of axial and azimuthal velocities are U and W , respectively, and those of pressure, density, temperature are P , ρ , and T , which are related as $P = \rho RgT$. The mean values in this Chapter are the time-averaged quantities. They are obtained by either averaging the URANS results over a long time, or by averaging the RANS results over several iterations. The averages used in this Chapter are not Favre-averaged, which are density weighted, but are simple time-averages theoretically defined as $\bar{\phi} = \frac{\int_0^{t_\infty} \phi(t) dt}{t_\infty}$, where the instantaneous variable ϕ is integrated over a sufficiently long time t_∞ .

In this Chapter, the following approaches are used for the flow in the case-A of the S series.

(i) Molecular viscosity based incompressible stability analysis (referred to as incompressible): The governing equation for mass and momentum are linearised around the mean flow profiles, which include the non-uniform mean density profile. Perturbations in the ve-

locity and pressure are considered, while perturbations in the temperature (or density) are ignored. The governing equations for such stability analysis are given in Ref. [133]. They can also be obtained by setting $\frac{dp}{dr}$, $\frac{dT}{dr}$, and ρ' , i.e. $\frac{p'}{p} - \frac{T'}{T}$, equal to zero, by setting $Rg = \infty$, and by ignoring the r_{ij} terms.

(ii) Molecular viscosity based compressible stability analysis (referred to as compressible): The governing equation for mass, momentum, and energy are linearised around the mean flow profiles, which include the non-uniform mean density profile. Perturbations in the temperature (or density) are also considered. The governing equations for such stability analysis are given in Ref. [133]. They can also be obtained by ignoring the r_{ij} terms in the above equations. The values of Rg , Pr , and γ are set as 287, 1, and 1.35, respectively, in this Chapter.

(iii) Eddy viscosity model based incompressible linear stability analysis (referred to as EVM): This analysis includes all the terms from analysis (i) plus the terms representing the wave induced perturbations in the Reynolds stresses. Perturbations in the Reynolds stresses are obtained by using an eddy viscosity model $\nu_t = 0.09 \frac{K^2}{\varepsilon}$, where ν_t is the eddy viscosity, K is the turbulent kinetic energy, and ε is the turbulence dissipation rate. This is a first-order turbulence model. The governing equations for this analysis can be obtained by using the r_{ij} expressions, which are derived in Section 3.2.1 in Chapter 3, in the above equations.

(iv) Explicit algebraic Reynolds stress model based incompressible linear stability analysis (referred to as EARSIM): Like analysis (iii), this analysis also includes all the terms from analysis (i) plus the terms representing the wave induced perturbations in the Reynolds stresses. Perturbations in the Reynolds stresses are obtained by using an explicit algebraic Reynolds stress model given by Wallin and Johansson [108]. This model belongs to the family of anisotropic eddy viscosity model, and is a second-order turbulence model. The governing equations for this analysis can be obtained by using the r_{ij} expressions, which are derived in Section 3.2.3 in Chapter 3, in the above equations.

Analyses (i) and (ii) are based on the predictive properties of stability analysis performed on the Navier–Stokes equations linearised over the mean flow profile. Lee, Kim and Moin [82] and Hunt and Carruthers [81] show that the linearised Navier–Stokes equations are good at reproducing large-scale coherent structures in high mean shear regions in turbulent flows. The flows inside gas-turbine injector-combustor systems are also characterised by the high mean shear regions, particularly in the upstream part of the geometry where several incoming flows at different velocities interact. Analysis (ii) examines whether compressibility effects are important in this flow. Analyses (iii) and (iv) are based on the linearised RANS equations, and are found to be useful in some flows [2, 10, 77, 78, 88]. They contain

also the wave-induced perturbations in the Reynolds stresses in addition to all the terms in the linearised Navier–Stokes equations. These analyses examine whether the wave-induced perturbations in the Reynolds stresses need to be included in stability analysis of gas-turbine injector-combustor systems.

5.2.1 Results

There are several absolutely unstable modes found from the above mentioned local stability analyses. Only a few of them, however, can sustain global instability, and only those unstable modes are discussed. These modes are classified based on their region of influence, azimuthal wavenumber (m), and frequency (ω_r). A general feature among all these modes is that they exist in the regions of high mean shear, which is not surprising because the mean shear is known to cause instabilities.

Instability in the upstream central pipe

The flow in the upstream central pipe is a high Reynolds number wake with a counter flow at the centre. The axial mean velocity profile is inflectional near the centre, and it has high mean shear as well. Consequently, there are several absolutely unstable modes that can sustain global instabilities. The flow is swirling in the clockwise direction, which, according to Ref. [134], facilitates modes winding in the anti-clockwise direction. In accordance with Ref. [134], it is found that these modes have negative m , positive k_r , and positive ω_r . Based on that these modes are winding in the anti-clockwise direction and rotating in the clockwise direction, which means that these modes are counter-winding and co-rotating with respect to the local mean swirl.

Figure 5.2 shows the $m = -1$ instability mode, in terms of the normalised disturbance kinetic energy multiplied by the local growth rate ω_i , calculated by the four stability analyses. Above the mode shape plots, their frequencies and streamwise wavenumbers are plotted in the black and red colour lines, respectively, as functions of their streamwise location. The number shown as ref in each frame is the maximum normalised growth rate for that mode, so the higher ref number means the more unstable mode. The average wavelength of this mode is around 2 units, and the length of the pocket of absolute instability is nearly 3 units. Because the pocket of absolute instability is larger than one-quarter of the wavelength, this mode has the potential to exist in the flow as a globally unstable mode.

The results from the incompressible and compressible stability analyses are very similar, even quantitatively. This shows that the compressibility is not an important factor in this part

of the geometry, this is because the flow is at a low Mach number. The modes calculated from the EVM- and EARSMS-based analyses are also very similar to the modes calculated from the molecular viscosity-based analyses. Quantitatively, however, these modes are less unstable. The EVM-based analysis damps the mode significantly while the EARSMS-based analysis damps it mildly. The only noticeable qualitative difference between the results is that the modes calculated from the EVM- and EARSMS-based analyses are slightly wider in the radial direction as compared to the modes from the molecular viscosity-based analyses. This is because the turbulent eddy viscosity is high in the central region, then decreases towards the wall, and reaches zero at the wall. As a result the part of the modes in the central region get more damped than the parts of the modes closer to the wall.

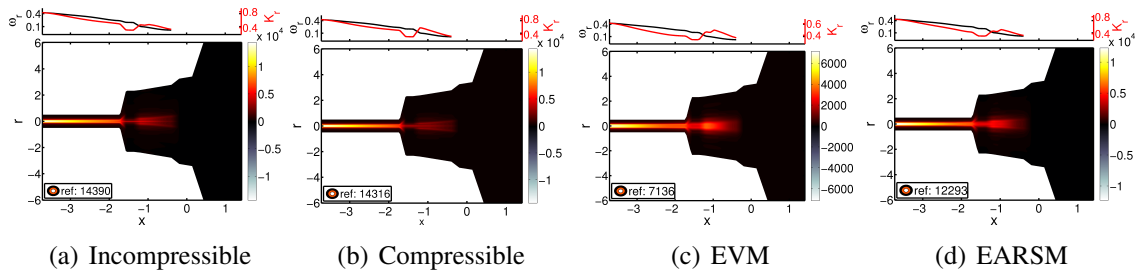


Fig. 5.2 The $m = -1$ instability mode in the central pipe calculated from the four stability analyses. They are represented in terms of the normalised perturbation kinetic energy multiplied by the local growth rate ω_i . Above the mode shape plots, the local absolute frequency (ω_r) and streamwise wavenumber (k_r) are plotted in black and red colour lines, respectively, as functions of the streamwise location. A comparison of frames (a) and (b) shows that compressibility does not affect this instability mode. Frames (c) and (d) show that turbulence models also have little qualitative effect. The difference is that the modes in (c) and (d) are slightly wider in the radial direction as compared to the modes in (a) and (b). The EVM-based analysis damps the mode significantly while the EARSMS-based analysis damps it relatively mildly.

Figure 5.3 shows the $m = -2$ instability mode in the central pipe. The mode shape is very similar to the $m = -1$ instability mode, but the frequency and streamwise wavenumbers are around two times higher, which is proportional to the change in the m . The mode shapes calculated from all the stability analyses are very similar to each other. According to the molecular viscosity- (compressible and incompressible) and the EARSMS-based analyses this mode is more unstable than the $m = -1$ mode. The EVM-based analysis, however, predicts this mode to be less unstable than the $m = -1$ mode. The $m = -3$ to -5 modes, not shown here, are predicted to be stable, or with a small pocket of absolute instability, by the EVM- and EARSMS-based analyses. Molecular viscosity-based analyses, however, show

them to be more unstable than the $m = -1$ mode, and less unstable than the $m = -2$ mode. This shows that turbulence model-based analyses damp the higher wavenumber modes more than they damp the lower wavenumber modes.

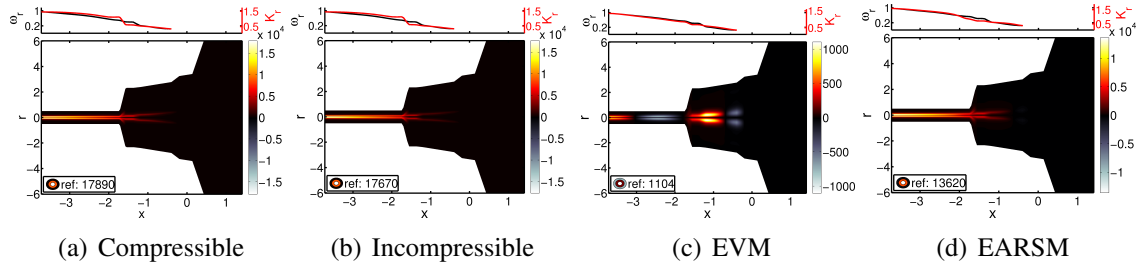


Fig. 5.3 The $m = -2$ instability mode in the central pipe calculated from the four stability analyses. They are represented in terms of the normalised perturbation kinetic energy multiplied by the local growth rate ω_i . Frames (a) and (b) show that the compressibility does not affect this instability mode. Frames (c) and (d) show that turbulence models also have little effect on the shape of the modes. According to the molecular viscosity- and the EARSM-based analyses this mode is more unstable than the $m = -1$ mode. The EVM-based analysis, however, predicts this mode to be stabler than the $m = -1$ mode.

Instabilities caused by the interaction of various incoming flows

Apart from the instabilities in the central pipe, there are a few unstable modes also between $x \approx -1.5$ to 0. There are several incoming flows at $x \approx -1.5$, and each of them injects flow at a different velocity. The incoming flow from the central region (up to $r \sim 0.45$) is a wake like flow with swirl in the clockwise direction. The incoming flow from the region $r \approx 0.45 - 1.5$ is at a relatively slower axial velocity and with swirl in the anti-clockwise direction. The incoming flow from the region $r > 1.5$ is at a relatively faster axial velocity and with swirl in the clockwise direction.

As a result of interaction of various incoming flows, there are two unstable modes in the flow with significantly long pockets of absolute instabilities. The four stability analyses, again, give very similar results. This again shows that compressibility effects are not important, and neither is the inclusion of the Reynolds stress perturbations in stability analysis of this flow.

The first is the $m = -2$ instability mode, shown in figures 5.4 (a–d). This mode is most dominant in the $1.5 < r < 2$ region. The positive streamwise wavenumber (k_r) implies that this mode is winding in the anti-clockwise direction, and the positive frequency (ω_r) implies that this mode is rotating in the clockwise direction. Because the mean swirl in this region

($1.5 < r < 2$) is in the clockwise direction, this mode is counter-winding and co-rotating with respect to the local mean swirl.

The second is the $m = +2$ instability mode, shown in figures 5.4 (e–h). This mode is dominant in the $0.4 < r < 1$ region. The positive streamwise wavenumber (k_r), the positive frequency (ω_r), and the positive azimuthal wavenumber (m) imply that this mode is winding in the clockwise direction and rotating in the anti-clockwise direction. Because the mean swirl in this region ($0.4 < r < 1$) is in the anti-clockwise direction, this mode is also counter-winding and co-rotating with respect to the local mean swirl.

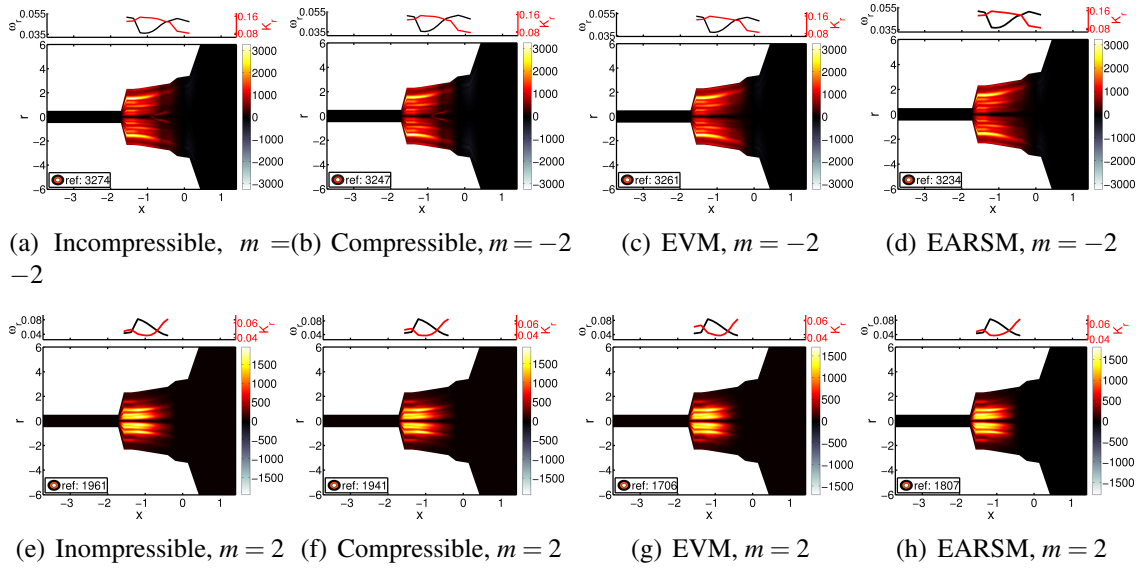


Fig. 5.4 Frames (a–d) show the $m = -2$ instability modes in the $x \approx -1.5$ to 0 region and frames (e–h) show the $m = 2$ instability modes in the $x \approx -1.5$ to 0 region calculated from the four stability analyses. The $m = -2$ mode is dominant in the region with negative swirl while the $m = 2$ mode is dominant in the region with positive swirl. The positive values of the frequency and wavenumber for these modes imply that they both are co-rotating and counter-winding with respect to the local mean swirl in the flow.

5.2.2 Conclusion

The conclusions based on the results presented in this Section are:

- i) Modes that are counter-winding and co-rotating with respect to the local swirl velocity are favoured in the flow.
- ii) Compressibility effects are not important, because the flow is at a low Mach number.

iii) Two turbulence models are used to account for the effect of the wave-induced perturbations in the Reynolds stress in stability analysis of the system. It is seen that the main effect of including the wave-induced perturbations in the Reynolds stress is to damp the unstable modes in the system. The EVM damps more than the EARSM. Also both the models damp the higher frequency/wavenumber modes more than they damp the lower frequency/wavenumber modes.

iv) The use of turbulence models in stability analysis has little effect on the mode shapes, wavenumbers, and frequencies. Therefore, in a qualitative analysis, such as the present one, the use of turbulence models is not required.

5.3 Stability results with RANS data as input

In the commercial CFD package ANSYS-Fluent, RANS solvers are used for obtaining the time-averaged solutions and URANS solvers are used for obtaining the ensemble-averaged solutions. Most turbulent flows are statistically stationary, which are defined as the flows in which the time-averaged equations (or quantities) are identical to the ensemble-averaged equations (or quantities). Therefore the two solvers, RANS and URANS, would give solutions close to each other. In turbulent flows that are not statistically stationary, such as vortex shedding flow behind a cylinder or the flow inside a gas-turbine combustor, ensemble-averaged quantities are time-dependent. For such flows, a URANS solver would give a time-dependent ensemble-averaged solution while a RANS solver, assuming that it gives a converged solution, would give a solution close to the time-average of the solution obtained from a URANS solver.

In Section 5.2, the time-averaged URANS simulation data are used as the input to perform stability analysis. The purpose of this section is to repeat the same calculations, but with the RANS simulation data as the input to perform stability analysis. The advantage of using the RANS solutions over the time-averaged URANS solutions is that calculation of the former takes much less computational time than that of the latter. Usually the data obtained from the RANS simulations have sharper shear layers than those in the time-averaged URANS data. Small differences in the spatio-temporal stability results obtained from using the RANS data as the input and from using the time-averaged URANS data as the input are pointed out in this section. Elsewhere in this chapter, the RANS and time-averaged URANS data are used indistinguishably.

Figure 5.5 shows the axial and azimuthal velocities and the temperature field in the case-A of the S series obtained from the RANS simulation. The fields presented here are

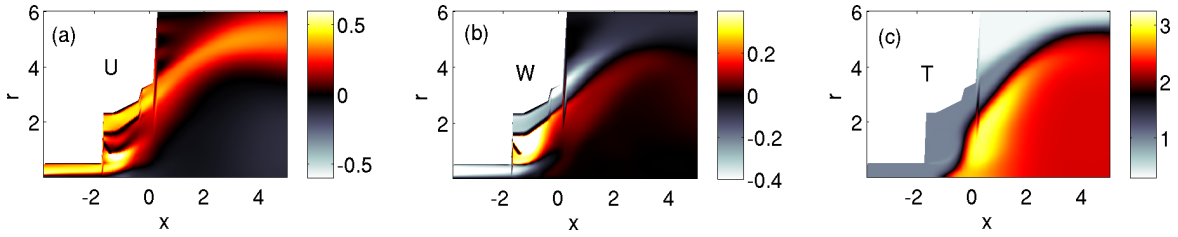


Fig. 5.5 (a) The axial velocity, (b) the azimuthal velocity, and (c) the temperature fields in the case-A of the S series obtained from the RANS simulation. They are qualitatively very similar to the fields obtained by time-averaging the URANS simulation data, as shown in figure 5.1. The only noticeable difference is that the RANS data has higher velocities and temperature fields and the gradients in the fields are also sharper.

compared with the fields presented in figure 5.1 (d–f), where the same fields are shown in the same part of the geometry for the same case but the data is obtained by time-averaging the URANS simulation results. The fields obtained from the RANS data are qualitatively similar to those obtained from the time-averaged URANS data. Quantitatively, they are slightly different. The RANS data has slightly higher velocities and temperature magnitudes. Another difference is that the mean shear is sharper in the RANS data than that in the time-averaged URANS data.

The EARSIM-based stability analysis is performed by linearising the equations over the mean flow obtained from the RANS simulation. The calculated instability modes are shown in figure 5.6. Not surprisingly, these modes are similar to the four modes shown when the calculations are performed using the time-averaged URANS data in Section 5.2. These modes are: (a) the $m = -1$ instability mode in the central pipe, (b) the $m = -2$ instability mode in the central pipe, (c) the $m = -2$ instability mode downstream of the central pipe where the several incoming flows interact, and (d) the $m = 2$ instability mode downstream of the central pipe where the several incoming flows interact. Qualitatively the mode shapes are very similar to the mode shapes obtained from stability analysis with the time-averaged URANS data as input. The only difference is that the growth rates and frequencies are marginally higher, which is a result of the sharper shear layers. The results seen in this section confirm that stability analysis over the RANS data gives very similar results to stability analysis over the time-averaged URANS data.

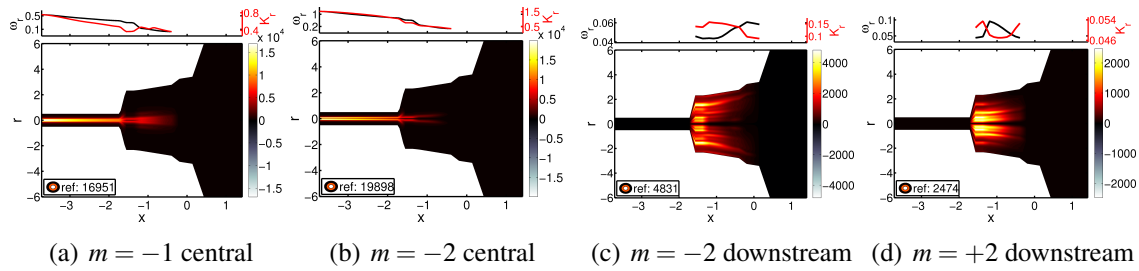


Fig. 5.6 The main instability modes obtained from the EARSM-based analysis performed with the RANS data as input for the case-A in the S series system. (a) The $m = -1$ instability in the central injection, (b) the $m = -2$ instability in the central injection, (c) the $m = -2$ instability downstream of the central injection where the several incoming flows interact, and (d) the $m = +2$ instability downstream of the central injection where the several incoming flows interact. These modes are qualitatively very similar to the four instability modes shown in Section 5.2, where stability analysis of the same case is performed but with the time-averaged URANS data as input. The only difference is that the growth rates and frequencies are marginally higher, which is a result of the sharper shear layers.

Table 5.1 Three cases of the S-series

Case	Air-fuel ratio	Entropy spot driven thermoacoustic oscillations
A	Stoichiometric	Highest
B	Lean	Moderate
C	Very lean	Absent

5.4 Effect of change in operating conditions on the instabilities in the S series

As already seen in Section 5.2, compressibility effects and inclusion of the Reynolds stress perturbations are not required in stability analysis in the S series. Therefore, in this section, only the molecular viscosity based compressible stability analysis is performed for flows in the S series at the different operating conditions. These cases are listed in table 5.1. Case-A has air and fuel injected at the stoichiometric ratio and is studied in Section 5.2, case-B has a lean mixture, and case-C has a leaner mixture than in case-B. The purpose is to demonstrate the application of stability analysis to study the effect of a change in the operating conditions on hydrodynamic instabilities in gas-turbine flows.

The mean flow is obtained by time-averaging the data calculated from the URANS simulations. The pressure-based Fluent solver is used in the simulations, with the same pressure difference maintained between the inlet and the outlet in all three cases. When the amount

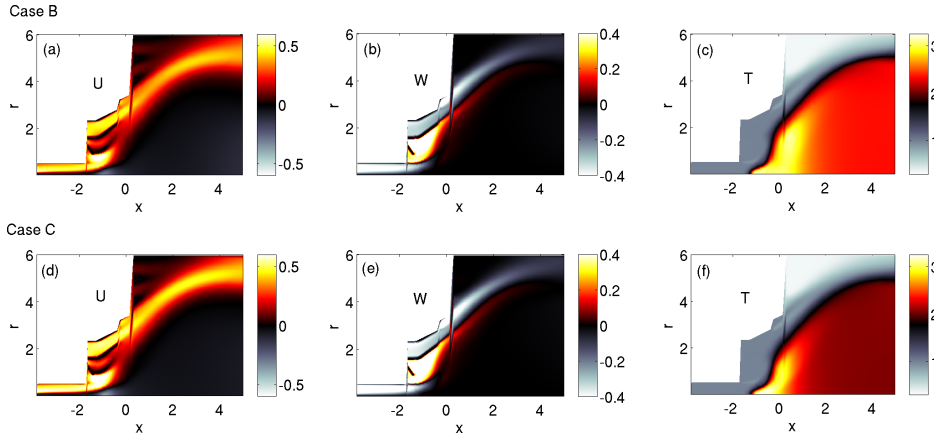


Fig. 5.7 The time-averaged fields are shown in case-B (frames a–c) and case-C (frames d–f) of the S series: (a) and (d) show the axial velocity, (b) and (e) show the azimuthal velocity, and (c) and (f) show the temperature field. The temperature field in case-B is colder than that in case-A, and that in case-C is colder than that in case-B. The velocity fields have the opposite trend. Case-B and case-C, on average, have higher velocity magnitudes than those in case-A.

of fuel injection is decreased in cases-B and C, the amount of heat release also decreases. This decreases the volumetric expansion in the flow, which decreases the change in velocity. For a given mass-flow rate it would decrease the pressure drop. However, the pressure drop is fixed, therefore the air mass flow rate increases as the fuel mass flow rate decreases. The axial and azimuthal velocities, and the temperature fields in cases-B and C are presented in figure 5.7. The temperature in case-B is colder than that in case-A, and that in case-C is colder than that in case-B. This is because temperature decreases monotonically with the decrease in fuel injection ratio. The velocity fields have the opposite trend. Case-B and case-C, on average, have higher velocity magnitudes than in case-A. The mean shear layers are also sharper in case-B than those in case-A, and case-C has the sharpest mean shear layers of the three cases.

Figure 5.8 shows the thermoacoustic oscillations in terms of normalised spatially averaged pressure in the three cases. These self-excited thermoacoustic oscillations, which are generated by coupling between the flame and the combustion cavity, in the same lean-burner geometry are discussed in [131, 135]. Large hot spots, or entropy spots, emerge from the edges of the flame, convect towards the nozzle and alter the mass flow rate in the nozzle. The nozzle is maintained at a fixed high pressure which causes the generation of an expansion

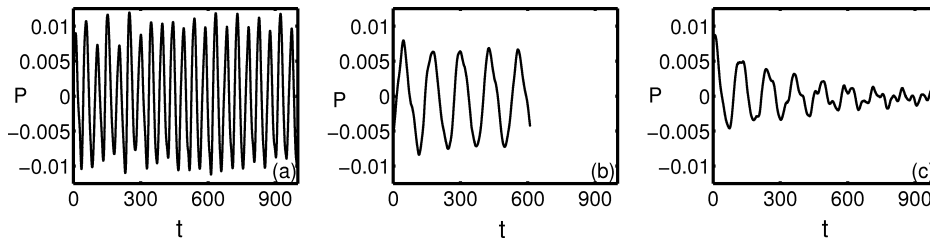


Fig. 5.8 The thermoacoustic pressure oscillations in the three cases of the S series are shown: (a) case-A, (b) case-B, and (c) case-C. The amplitude and frequency of the thermoacoustic instability decreases monotonically as the fuel-air mixture is changed from stoichiometric to lean.

wave that travels upstream towards the flame. The expansion wave causes further fluctuations in the flame and generates more hot spots, and the cycle continues. These entropy wave-driven thermoacoustic oscillations are axisymmetric. Case-A has these oscillations with highest amplitude and frequency (≈ 0.02) of the three cases. Case-B has slightly lower amplitude and frequency (≈ 0.01) than those in case-A. Case-C has a further lower frequency of the oscillations, and the amplitude decays to a very small value. This shows that the amplitude of thermoacoustic oscillations decreases monotonically as the amount of fuel injection is decreased. Another aim of this section is to investigate whether there is a link between the hydrodynamic instabilities in the upstream section of the system and these entropy wave generated large thermoacoustic oscillations in the downstream region of the system.

5.4.1 Hydrodynamic instabilities in case-B and case-C

Figure 5.9 shows hydrodynamic instability modes in case-B and case-C. The modes of instability in case-B and case-C are qualitatively similar to the instability modes in case-A, which are presented in Section 5.2. The only apparent difference is in the growth rate of the instabilities. Case-C is predicted to be the most unstable, while case-A is the least unstable of the three cases. This trend of hydrodynamic instability is consistent with the velocity field in the three cases. Case-C with the sharpest shear layers is the most unstable and case-A with the weakest shear layers is the least unstable. The trend of these hydrodynamic instabilities is exactly opposite of the trend of the thermoacoustic oscillations. The hydrodynamic instability modes found in these cases are at high frequencies and have non-zero m , while the thermoacoustic oscillations are at low frequency and are axisymmetric. The fact

that the two types of instability have very different frequencies and orthogonal mode shapes explains why there is no interaction between them and how they co-exist independently.

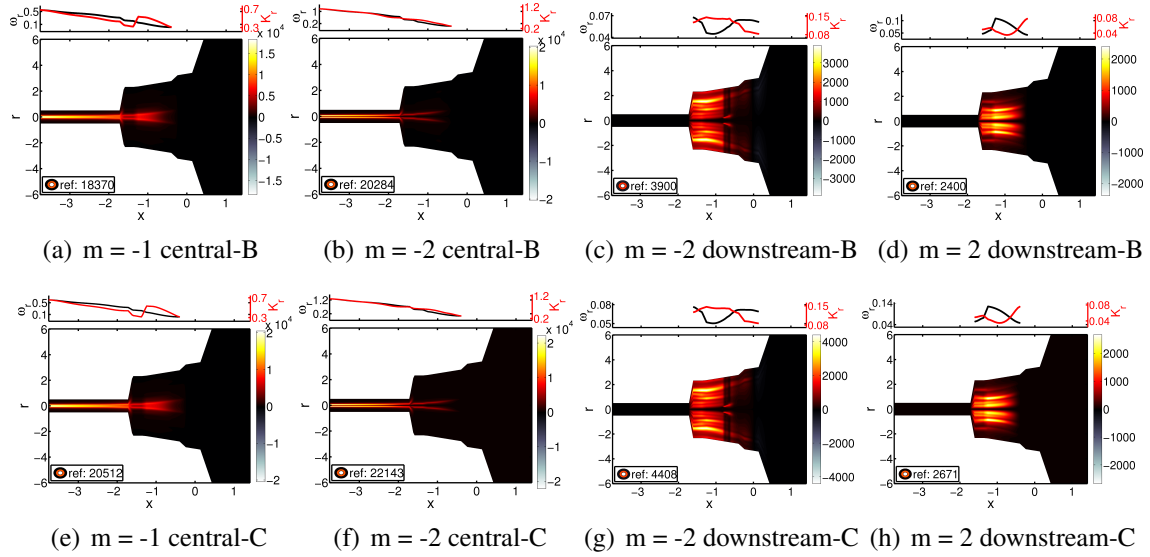


Fig. 5.9 Frames (a–d) and (e–h) show dominant instability modes in case-B and case-C, respectively, of the S series injector-combustor system. These modes match very closely with the unstable modes in case-A of the series. The growth rate, however, is higher in case-B than that in case-A, and case-C has the highest growth rate among the three cases. The growth rate of hydrodynamic instability increases with increasing gradient in the mean shear layer.

5.5 Effect of small design modifications on hydrodynamic instabilities

Six injector-combustor systems are considered in this section, for which the RANS data of non-reacting flows has been given by Dr Fred Witham from Rolls-Royce. All these systems have very similar geometry with small design modifications and are collectively called the T series. The axial and azimuthal velocities in them are shown in figure 5.10. The top row shows the axial velocity and the bottom row shows the azimuthal velocity fields. All of them have the same colour-scale, which is calibrated as 0 to 2.25 for the axial velocity, and 0 to 1.5 for the swirl velocity (positive azimuthal velocity indicates that swirl is in the anti-clockwise direction). The flow through the central jet in the T series is non-swirling at a moderate flow velocity. In the downstream portion, three annular incoming flows join the

central incoming flow, and there are expansions in the system geometry. The radii of the different sections in these systems is given in table 5.2.

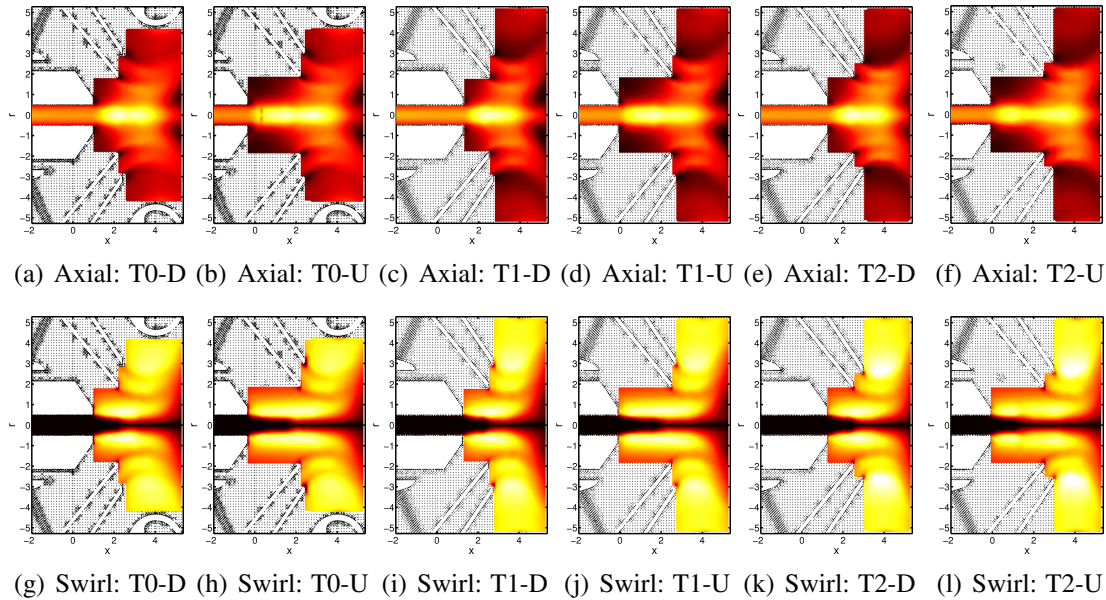


Fig. 5.10 The top and bottom rows show the axial and azimuthal velocity fields in the T series. All of them have the same colour-scale, which is calibrated as 0 to 2.25 for the axial velocity, and 0 to 1.5 for the azimuthal velocity (the positive azimuthal velocity indicates that the swirl is in the anti-clockwise direction). The flow through the central jet in the T series is non-swirling at a moderate flow velocity. In the downstream portion, three annular injections join the central injection and there are expansions in the system geometry. These later injections add swirl in the flow.

These systems are named: T0-D and T0-U, T1-D and T1-U, and T2-D and T2-U. The suffix D and U indicates the longer and shorter central injections, respectively. The numbers 0, 1, and 2 divide them based on the radii of the individual streams. Each of these systems have four sections, and R1, R2, R3, and R4 are the radii of those sections. Table 5.2 lists their values. The T0-D and T0-U have the smallest radius of the final section (R4), so they have the highest axial velocity among the T series systems. The higher axial velocity leads to lower absolute instability, because the axial flow sweeps the instabilities away. The expansion in the flow from R3 to R4 is maximum in the T2-D and T2-U, followed by the T1-D and T1-U, and is minimum in the T0-D and T0-U. The azimuthal velocity in the T series is maximum in the T2-D and T2-U, followed by the T1-D and T1-U, and is minimum in the T0-D and T0-U.

Table 5.2 The radii of the different sections in all the cases of the T series.

Case	R1	R2	R3	R4
T0-D	0.5	1.83	2.86	4.18
T0-U	0.53	1.87	3.03	4.20
T1-D	0.5	1.85	2.98	5.23
T1-U	0.5	1.83	2.94	5.23
T2-D	0.5	1.83	2.59	5.17
T2-U	0.5	1.85	2.57	5.23

5.5.1 Main instability modes in the T series

The two main instabilities in the T series are shown in figures 5.11 and 5.12. The first instability mode has $m = -1$. It is mainly caused by the mean shear around the centreline but also interacts with the mean shear between the other injected air streams. Based on the signs of the m , k_r , and ω_r , this mode is winding and rotating in the anti-clockwise direction. It is dominant in the central region, where swirl is very low. The second instability mode has $m = 2$ and is caused by the inflection point in the mean axial velocity at $r \approx 3$. Based on the signs of the m , k_r , and ω_r , this mode is winding in the clockwise direction and rotating in the anti-clockwise direction. The swirl near $r = 3$ is in the anti-clockwise direction, so this mode is counter-winding and co-rotating with respect to the local mean swirl in the flow.

The average wavelength of these instabilities, however, is larger than the length of the combustor by an order of magnitude. Therefore these instabilities are unlikely to sustain a global instability. Nevertheless a comparison of instabilities can be made to see the effect of the changes in the geometry. The T0-D and T0-U, with the smallest expansion and least swirl in the flow, are the least absolutely unstable cases. The T2-D and T2-U, with the large expansion and most swirl in the flow, are the most absolutely unstable cases. The T1-D and T1-U sit somewhere in between. They have large expansion as in the T2-U and T2-D, but only a moderate swirl in the flow. They are more unstable than the T0-D and T0-U, but less unstable than the T2-D and T2-U. Based on these results it is concluded that swirl in the flow and expansion in the geometry are destabilising.

5.6 Conclusions

The main conclusions of this chapter are:

1. For flows inside the gas-turbine injector-combustor systems inclusion of turbulence models in stability analysis, in order to account for the wave-induced fluctuations in the

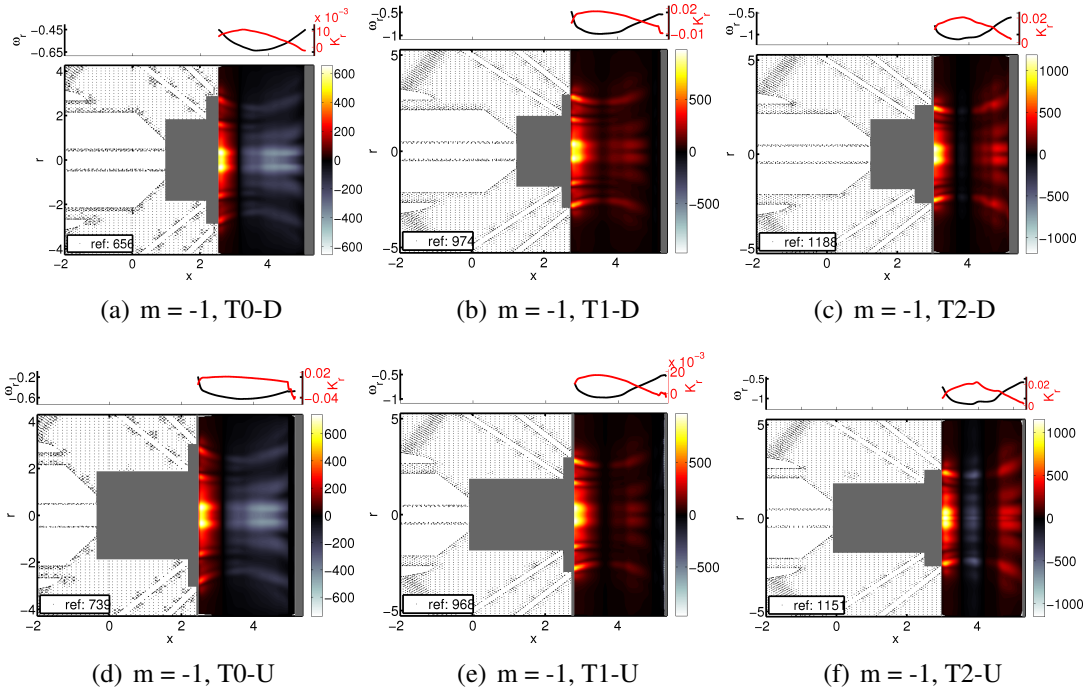


Fig. 5.11 This instability mode is mainly caused by the shear around the centreline but also interacts with the shear between the other injected flow streams. It is winding and rotating in the anti-clockwise direction. The average wavelength of this mode is larger than the length of the combustor by an order of magnitude, which implies that this mode is unlikely to sustain a global instability.

Reynolds stresses, has no significant qualitative effect on the results. Furthermore, they have little quantitative effect on the frequency of oscillations and the position of the perturbation kinetic energy, i.e. maximum of the eigenfunctions. This is because these instabilities are driven by the regions of high mean shear in which the linear processes dominate as shown in Refs [81, 82]. An implication of this is that only the mean flow velocity and density profiles are required in order to find information on large hydrodynamic instabilities in these flows. In order to use such tools reliably, it is important to validate the results from local analysis with those from global analysis and experiments or LES or DNS for a number of cases. In this direction, the recent results of Dr Outi Tammisola on global stability of flow in a gas-turbine injector-combustor system are encouraging as they match with the local stability results of Ref. [125], and also with the LES results.

2. The incompressible linearised governing equations give very similar results to the fully compressible linearised governing equations for these flows. This is because these flows are at the low Mach numbers (< 0.1).

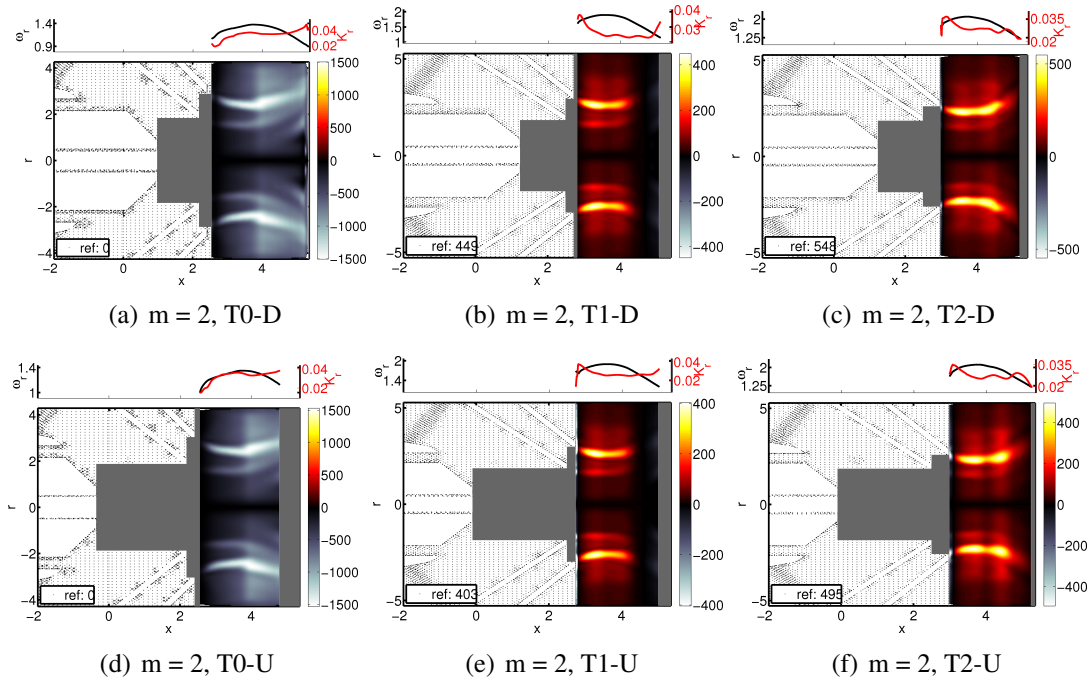


Fig. 5.12 This instability mode is caused by the inflection point in the mean axial velocity at the $r \approx 3$. It is winding in the clockwise direction and rotating in the anti-clockwise direction. Swirl near the $r = 3$ is in the anti-clockwise direction, so this mode is counter-winding and co-rotating with respect to the local mean swirl in the flow. The wavelength of this mode is larger than the length of the combustor by an order of magnitude, which implies that this mode is unlikely to sustain a global instability.

3. The stability analysis is performed by linearising the equations over the time-averaged URANS solutions and also by linearising over the RANS solutions. The results are qualitatively similar, except that the frequencies and growth rates are predicted to be a little higher when the RANS solutions are used. This is because the RANS solutions have sharper gradients, hence sharper mean shear layers, as compared to the time-averaged URANS solutions. It is concluded that if the RANS solver gives a converged solution, then stability analysis could be performed over the RANS solutions or the time-averaged URANS solutions almost indistinguishably.

4. Stability analysis is performed for three cases of the S series, one at the stoichiometric operating condition and the other two at lean and very lean operating conditions. The entropy wave-generated thermoacoustic oscillations in the first case have maximum amplitude and frequency, followed by the lean case, and the very lean case has nearly no thermoacoustic oscillations. The hydrodynamic instability modes in the upstream section of

the system, however, are found to have the opposite trend. This shows that thermoacoustic oscillations in the system and hydrodynamics instabilities in the upstream part co-exist in the system without affecting each other. This is because the hydrodynamic instability modes are at high frequencies and have non-zero azimuthal wavenumbers while the thermoacoustic oscillations are at low frequency and are axisymmetric.

5. The effect of small design changes in the T series on hydrodynamic instability modes is studied. Expansion at the nozzle exit and swirl in the flow are found to be destabilising. It is also seen from the S and T series results that most instability modes are counter-winding and co-rotating with respect to the local mean swirl in the flow.

Chapter 6

Global stability analysis of turbulent Taylor-Couette flow

In this Chapter, two stability analyses are performed over the mean flow profiles in Taylor-Couette flow. These mean flow profiles include Taylor-vortices and therefore are two-dimensional. They can be obtained by either time-averaging or ensemble-averaging the instantaneous flow fields. The two stability analyses are molecular viscosity (MV)-based stability analysis and an EARSM-based stability analysis. These analyses are derived in Chapter 3. This chapter extends the application of these stability analyses to a two-dimensional mean flow case. This work is part of an ongoing work in collaboration with Mr Hannes Brauckmann and Prof Bruno Eckhardt, who kindly provided the DNS data for the mean velocity, Reynolds stresses, and turbulent dissipation for all the cases considered here. The aim of the overall project is to understand whether model-based stability analyses could predict the intermittent turbulent structures in Taylor-Couette flow, and whether the predicted results on intermittent turbulent structures could be related to the observed fluctuating torque in the flow.

6.1 Introduction

The flow between two independently rotating concentric cylinders is among the most studied cases in fluid mechanics since the early work of Refs. [136–138], and is referred to as Taylor-Couette flow. The main reasons for the popularity of Taylor-Couette flow are its simple geometry and high symmetry, which make it experimentally easily accessible and mathematically well-defined. There are five independent parameters in this flow: the angular velocities of the two cylinders, their radii, and the aspect ratio of the geometry.

Standard bifurcation theory is used to describe transitions in this flow in considerable detail [139]. Based on the combinations of the above mentioned parameters, the flow can transition to several states such as Taylor vortex flow, wavy vortex flow, modulated vortex flow, corkscrew wavelet flow, and intermittent flow.

Interestingly, this flow shares many common features with Rayleigh-Bernard flow. Both flows are bounded between solid boundaries, driven by external forcing, and have similar vortical structures. Rayleigh-Bernard flow, however, is driven by buoyancy created by an externally maintained temperature difference between the two plates, while Taylor-Couette flow is driven by inertial terms created by externally maintained azimuthal velocities of the two cylinders. An analogy between the two flows was first drawn by Bradshaw [140] and later extended to the turbulent regime by Eckhardt, Grossmann, and Lohse [141]. Apart from academic interest another reason for the popularity of Taylor-Couette flow is its application in process technology [142].

Viscous fluid between the two cylinders causes molecular and convective transfer of the azimuthal momentum between the two cylinders. In this process, there is a net loss of angular momentum from one of the externally driven cylinders. This loss in angular momentum can be measured as torque [143]. Recent work concerning the understanding of scaling of the torque with Reynolds number, optimising the flow parameters to obtain maximum torque, and extending the research to higher Reynolds number regimes can be found in Refs. [12, 56, 144–146] and the references cited therein. The relationship between the torque and the azimuthal velocities of the cylinders is not simple. For example it is observed that small counter-rotation enhances the torque while large counter-rotation reduces it, and that co-rotating cases have different scaling of the torque with Reynolds number as compared to the scaling in counter-rotating cases. It is understood that the torque depends upon the size of Taylor vortices and on intermittent turbulent structures.

In the present study, two stability analyses are used as attempts to understand the relation between large-scale turbulent structures and torque. The first is based on the linearised Navier–Stokes equations such as in Refs. [1, 73]. The second is based on the linearised Navier–Stokes equations augmented with an anisotropic eddy viscosity model as shown in Chapter 3. This anisotropic eddy viscosity augmented stability analysis is, in principle, based on the eddy viscosity augmented stability analysis presented in Refs. [2, 10, 76]. This analysis is based on the linearised RANS equations, where the RANS equations are obtained using the EARSM model of Wallin and Johansson (2000) [108].

These two stability analyses are applied to fourteen Taylor-Couette flow cases for which the mean flow data is provided by Mr Hannes Brauckmann and Prof Bruno Eckhardt. The

mean flow is obtained such that it retains Taylor vortices, which form from instability in the flow caused by the rotation of the inner cylinder. The analyses presented here therefore are secondary stability analyses. The purpose of these analyses is to predict large-scale intermittent turbulent structures over Taylor-vortices in the flows. The similarity and differences between the predicted coherent structures from the two above mentioned stability analyses are presented here. A preliminary comparison of stability results with the observations from the DNS data, such as the trend of the leading eigenmode's growth rate with that of standard deviation in the torque data, is also presented.

This Chapter is divided into six sections. Section 6.2 gives the definitions and terminologies used in rest of the chapter. It also presents a formulation of the problem. Section 6.3 discusses the numerical details of the problem, and gives a brief description of the two families of the cases considered. Section 6.4 and 6.5 present the stability results, such as eigenvalues and eigenmodes, from the two analyses for the two families of the cases.

6.2 Definitions and problem formulation

The axial, radial, and azimuthal directions are labelled (x, r, θ) -directions, respectively. The radii of the inner and outer cylinders are r_i and r_o , the gap between the two is $d = r_o - r_i$, and the radius ratio is $\eta = r_i/r_o$. The aspect ratio is defined as $\Gamma = L_z/d$, where L_z is the length of the cylinders in the axial direction, and is set to 2. When the outer cylinder is at rest, this length supports a Taylor-vortex pair [12]. The angular velocities of the inner and outer cylinders are ω_i and ω_o , respectively. The ratio of the angular velocities is defined as $\mu = \omega_o/\omega_i$, and the kinematic viscosity is labelled ν . The inner cylinder Reynolds number (Re_i), outer cylinder Reynolds number (Re_o), and shear Reynolds number (Re_s) are defined as:

$$Re_i = \frac{dr_i\omega_i}{\nu}, \quad Re_o = \frac{dr_o\omega_o}{\nu}, \quad Re_s = \frac{2}{1+\eta}|\eta Re_o - Re_i| \quad (6.1)$$

The length is non-dimensionalised by d , and the figures presented in this chapter are re-scaled in the radial direction as $r = (r - r_i)/d$ and in the axial direction as $x = x/d$. The axial direction is periodic with the period of L_z in the DNS, and the mean velocity is obtained by averaging the data in time and in the azimuthal direction. This implies that the mean profiles are periodic in the x -direction and are independent of time and the θ -direction. This is exploited in the stability analysis presented here. The mean velocities (U, V, W) in

the (x, r, θ) –directions, respectively, are decomposed into the Fourier components:

$$U = \sum_{j=1}^{nom} U_j(r) \sin(jfx), V = \sum_{j=1}^{nom} V_j(r) \cos(jfx), W = W_0(r) + \sum_{j=1}^{nom} W_j(r) \cos(jfx) \quad (6.2)$$

where nom is the number of Fourier modes used to describe the mean velocity profiles, $f = 2\pi/L_z = \pi$, and U_j, V_j, W_0 and W_j are functions of r alone. The velocity perturbations (u', v', w') in the (x, r, θ) –directions, respectively, and the pressure perturbation (p') are:

$$\begin{aligned} u' &= \left(\sum_{j=1}^N H_j(r) \sin(jfx) \right) \exp[\omega t + im\theta] \\ v' &= \left(F_0(r) + \sum_{j=1}^N F_j(r) \cos(jfx) \right) \exp[\omega t + im\theta] \\ w' &= \left(G_0(r) + \sum_{j=1}^N G_j(r) \cos(jfx) \right) \exp[\omega t + im\theta] \\ p' &= \left(\sum_{j=1}^N P_j(r) \sin(jfx) \right) \exp[\omega t + im\theta] \end{aligned} \quad (6.3)$$

where N is the number of Fourier modes used to describe the perturbations, m , which is fixed as a real integer, is the azimuthal wavenumber, real part of ω is the growth rate, and its imaginary part is the frequency of the corresponding eigenvectors. Because the flow is not homogeneous in the x –direction, a Fourier mode in the x –direction is not an eigenmode but an eigenmode is a superposition of several Fourier modes. This will be clearer from the linearised equations.

6.2.1 The linearised Navier–Stokes equations

Stability analyses with the linearised Navier–Stokes or RANS equations are found to be good at predicting large-scale structures in turbulent flows, especially in the high mean shear regions, as shown in Refs. [1, 73–75, 81, 82, 92, 93, 111, 124, 125] and in Chapters 2–5. This property of the linearised Navier–Stokes equations-based analysis is exploited in determining large-scale structures that develop on the top of Taylor vortices in Taylor–Couette flows. For this purpose, the Navier–Stokes equations are linearised over the mean velocity profiles, which are obtained by time-averaging the data. The reference frame, during the time-averaging, has the same velocity as the Taylor vortices. The mean profiles,

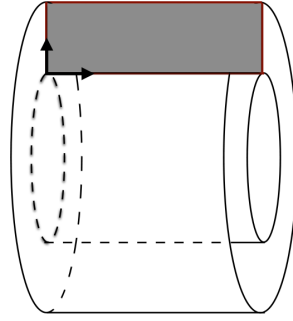


Fig. 6.1 The region highlighted in grey is a representative cross-section in which the mean velocities, Reynolds stresses and eigenvectors in all the flow cases are presented.

therefore, include Taylor-vortices in the flow. In figure 6.1 a schematic of Taylor-Couette flow geometry is shown. The mean velocity and Reynolds stress profiles are homogeneous in the azimuthal direction and periodic in the streamwise direction.

The region highlighted in grey is a representative cross-section in which the mean velocities, Reynolds stresses, and eigenmodes in Sections 6.4 and 6.5 are shown. The MV- and EARS- based stability analyses are performed over the mean profiles, which include Taylor-vortices. Therefore the instability results are for secondary large turbulent structures that develop on the top of Taylor-vortices. [Shifted the figure and part of the paragraph describing it before the equations.]

The momentum equation in the axial direction is:

$$\frac{\partial u'}{\partial t} = -V \frac{\partial u'}{\partial r} - v' \frac{\partial U}{\partial r} - \frac{W}{r} \frac{\partial u'}{\partial \theta} - U \frac{\partial u'}{\partial x} - u' \frac{\partial U}{\partial x} - \frac{\partial p'}{\partial x} + \frac{v}{r} \frac{\partial}{\partial r} \left(r \frac{\partial u'}{\partial r} \right) + \frac{v}{r^2} \frac{\partial^2 u'}{\partial \theta^2} + v \frac{\partial^2 u'}{\partial x^2} \quad (6.4)$$

On substituting Fourier modes for the mean velocity and perturbation quantities in this equa-

tion:

$$\begin{aligned}
-i\sigma H_l = & -\frac{2}{L_z} \int_0^{L_z} \sin(lfx) \sum_{k=1}^{nom} V_k \cos(kfx) \sum_{j=1}^N \frac{dH_j}{dr} \sin(jfx) dx + \frac{v}{r} \frac{d}{dr} \left(r \frac{dH_l}{dr} \right) - \frac{im}{r} W_0 H_l \\
& - \frac{2}{L_z} \int_0^{L_z} \sin(lfx) \sum_{k=1}^N F_k \cos(kfx) \sum_{j=1}^{nom} \frac{dU_j}{dr} \sin(jfx) dx - v \left(\frac{m^2}{r^2} + l^2 f^2 \right) H_l \\
& - \frac{2im}{rL_z} \int_0^{L_z} \sin(lfx) \sum_{k=1}^{nom} W_k \cos(kfx) \sum_{j=1}^N H_j \sin(jfx) dx + lfP_l \\
& - \frac{2}{L_z} \int_0^{L_z} \sin(lfx) \sum_{k=1}^{nom} U_k \sin(kfx) \sum_{j=1}^N \frac{dH_j}{dr} jf \cos(jfx) dx - F_0 \frac{dU_l}{dr} \\
& - \frac{2}{L_z} \int_0^{L_z} \sin(lfx) \sum_{k=1}^N H_k \sin(kfx) \sum_{j=1}^{nom} \frac{dU_j}{dr} jf \cos(jfx) dx
\end{aligned} \tag{6.5}$$

where $\sigma = i\omega$

The momentum equation in the radial direction is:

$$\begin{aligned}
\frac{\partial v'}{\partial t} = & -V \frac{\partial v'}{\partial r} - v' \frac{\partial V}{\partial r} - \frac{W}{r} \frac{\partial v'}{\partial \theta} - U \frac{\partial v'}{\partial x} - u' \frac{\partial V}{\partial x} + 2 \frac{W}{r} w' - \frac{\partial p'}{\partial r} + \frac{v}{r} \frac{\partial}{\partial r} \left(r \frac{\partial v'}{\partial r} \right) + \frac{v}{r^2} \frac{\partial^2 v'}{\partial \theta^2} \\
& + v \frac{\partial^2 v'}{\partial x^2} - v \frac{v'}{r^2} - 2 \frac{v}{r^2} \frac{\partial w'}{\partial \theta}
\end{aligned} \tag{6.6}$$

On substituting Fourier modes for the mean velocity and perturbation quantities in this equation.

$$\begin{aligned}
-i\sigma F_l = & -\frac{2}{L_z} \int_0^{L_z} \cos(lfx) \sum_{k=1}^N F_k \cos(kfx) \sum_{j=1}^{nom} \frac{dV_j}{dr} \cos(jfx) dx + \frac{v}{r} \frac{d}{dr} \left(r \frac{dF_l}{dr} \right) - \frac{im}{r} W_0 F_l \\
& - \frac{2}{L_z} \int_0^{L_z} \cos(lfx) \sum_{k=1}^{nom} V_k \cos(kfx) \sum_{j=1}^N \frac{dF_j}{dr} \cos(jfx) dx - v \left(\frac{m^2}{r^2} + 1 + l^2 f^2 \right) F_l \\
& - \frac{2im}{rL_z} \int_0^{L_z} \cos(lfx) \sum_{k=1}^{nom} W_k \cos(kfx) \sum_{j=1}^N F_j \cos(jfx) dx - \frac{2imv}{r^2} G_l - \frac{dP_l}{dr} \\
& + \frac{2}{L_z} \int_0^{L_z} \cos(lfx) \sum_{k=1}^{nom} U_k \sin(kfx) \sum_{j=1}^N F_j jf \sin(jfx) dx + \frac{2}{r} (G_l W_0 + G_0 W_l) \\
& + \frac{2}{L_z} \int_0^{L_z} \cos(lfx) \sum_{k=1}^N H_k \sin(kfx) \sum_{j=1}^{nom} V_j jf \sin(jfx) dx - F_0 \frac{dV_l}{dr} - \frac{dF_0}{dr} V_l \\
& + \frac{4}{rL_z} \int_0^{L_z} \cos(lfx) \sum_{k=1}^N G_k \cos(kfx) \sum_{j=1}^{nom} W_j \cos(jfx) dx - \frac{im}{r} F_0 W_l
\end{aligned} \tag{6.7}$$

and the equation for the F_0 -component is:

$$\begin{aligned}
 -2i\sigma F_0 = & -\sum_{j=1}^N F_j \frac{dV_j}{dr} - \sum_{j=1}^N V_j \frac{dF_j}{dr} - \frac{im}{r} \sum_{j=1}^N (F_j W_j + 2W_0 F_0) + \sum_{j=1}^N j f F_j U_j + \sum_{j=1}^N j f H_j V_j \\
 & + \frac{2}{r} \sum_{j=1}^N G_j W_j + 4 \frac{W_0 G_0}{r} - 2 \frac{dP_0}{dr} + \frac{2v}{r} \frac{d}{dr} \left(r \frac{dF_0}{dr} \right) - \frac{2v(m^2 + 1)}{r^2} F_0 - \frac{4imv}{r^2} G_0 \quad (6.8)
 \end{aligned}$$

The momentum equation in the azimuthal direction is:

$$\begin{aligned}
 \frac{\partial w'}{\partial t} = & -V \frac{\partial w'}{\partial r} - v' \frac{\partial W}{\partial r} - \frac{W}{r} \frac{\partial w'}{\partial \theta} - U \frac{\partial w'}{\partial x} - u' \frac{\partial W}{\partial x} - \frac{V}{r} w' - \frac{W}{r} w' - \frac{1}{r} \frac{\partial p'}{\partial \theta} + \frac{v}{r} \frac{\partial}{\partial r} \left(r \frac{\partial w'}{\partial r} \right) \\
 & + \frac{v}{r^2} \frac{\partial^2 w'}{\partial \theta^2} + v \frac{\partial^2 w'}{\partial x^2} - v \frac{w'}{r^2} + 2 \frac{v}{r^2} \frac{\partial v'}{\partial \theta} \quad (6.9)
 \end{aligned}$$

On substituting Fourier modes for the mean velocity and perturbation quantities in this equation.

$$\begin{aligned}
 -i\sigma G_l = & -\frac{2}{L_z} \int_0^{L_z} \cos(lfx) \sum_{k=1}^{nom} V_k \cos(kfx) \sum_{j=1}^N \frac{dG_j}{dr} \cos(jfx) dx + \frac{v}{r} \frac{d}{dr} \left(r \frac{dG_l}{dr} \right) - \frac{im}{r} P_l \\
 & - \frac{2}{L_z} \int_0^{L_z} \cos(lfx) \sum_{k=1}^N F_k \cos(kfx) \sum_{j=1}^{nom} \frac{dW_j}{dr} \cos(jfx) dx + \frac{2imv}{r^2} F_l - \frac{im}{r} (W_0 G_l + G_0 W_l) \\
 & - \frac{2im}{rL_z} \int_0^{L_z} \cos(lfx) \sum_{k=1}^{nom} W_k \cos(kfx) \sum_{j=1}^N G_j \cos(jfx) dx - v \left(\frac{m^2 + 1}{r^2} + l^2 f^2 \right) G_l \\
 & + \frac{2}{L_z} \int_0^{L_z} \cos(lfx) \sum_{k=1}^{nom} U_k \sin(kfx) \sum_{j=1}^N G_j j f \sin(jfx) dx - V_l \frac{dG_0}{dr} - F_l \frac{dW_0}{dr} \\
 & + \frac{2}{L_z} \int_0^{L_z} \cos(lfx) \sum_{k=1}^N H_k \sin(kfx) \sum_{j=1}^{nom} W_j j f \sin(jfx) dx - \frac{1}{r} (G_0 V_l + W_0 F_l) \\
 & - \frac{2}{rL_z} \int_0^{L_z} \cos(lfx) \sum_{k=1}^{nom} V_k \cos(kfx) \sum_{j=1}^N G_j \cos(jfx) dx - \left(\frac{dW_0}{dr} + \frac{W_0}{r} \right) F_0 \\
 & - \frac{2}{rL_z} \int_0^{L_z} \cos(lfx) \sum_{k=1}^N F_k \cos(kfx) \sum_{j=1}^{nom} W_j \cos(jfx) dx \quad (6.10)
 \end{aligned}$$

and the equation for the G_0 -component is:

$$\begin{aligned}
 -2i\sigma G_0 = & -\sum_{j=1}^N V_j \frac{dG_j}{dr} - \sum_{j=1}^N F_j \left(\frac{dW_j}{dr} + \frac{W_j}{r} \right) - \frac{im}{r} \sum_{j=1}^N G_j W_j + \sum_{j=1}^N jf G_j U_j + \sum_{j=1}^N jf H_j W_j \\
 & - \frac{1}{r} \sum_{j=1}^N G_j V_j - 2F_0 \left(\frac{dW_0}{dr} + \frac{W_0}{r} \right) - 2\frac{im}{r} (W_0 G_0 + P_0) + \frac{2\nu}{r} \frac{d}{dr} \left(r \frac{dG_0}{dr} \right) \\
 & - \frac{2\nu(m^2 + 1)}{r^2} G_0 - \frac{4im\nu}{r^2} F_0
 \end{aligned} \tag{6.11}$$

The continuity equation is:

$$\frac{\partial u'}{\partial x} + \frac{\partial v'}{\partial r} + \frac{v'}{r} + \frac{1}{r} \frac{\partial w'}{\partial \theta} = 0 \tag{6.12}$$

On substituting Fourier modes for perturbation quantities in this equation:

$$jf H_j + \frac{dF_j}{dr} + \frac{F_j}{r} + \frac{im}{r} G_j = 0 \tag{6.13}$$

and the relation between F_0 and G_0 from the continuity equations is:

$$\frac{dF_0}{dr} + \frac{F_0}{r} + \frac{im}{r} G_0 = 0 \tag{6.14}$$

Because the flow is not homogeneous in the x -direction, all the Fourier modes are to be solved simultaneously. The state vector is:

$$\left[\sum_{j=1}^N H_j(r), F_0(r), \sum_{j=1}^N F_j(r), G_0(r), \sum_{j=1}^N G_j(r), \sum_{j=1}^N P_j(r) \right] \tag{6.15}$$

Its size is $(4N + 2)$ times the number of grid-points in the r -direction. This analysis is referred to as MV-based analysis or just MV in the rest of the Chapter. The growth rates and eigenmodes obtained from the MV-based analysis are presented in Sections 6.4 and 6.5.

6.2.2 Anisotropic eddy viscosity augmented linearised equations

Another popular model-based stability analysis to predict large-scale structures in turbulent flows is based on augmenting the linearised Navier–Stokes equations with an eddy viscosity. Such an analysis was first presented in Reynolds and Hussain [76], and later used in Refs [2, 10] in channel flow. In such an analysis, the RANS equations are linearised instead of

the Navier–Stokes equations. The advantages and drawbacks of such an approach and a detailed literature review is discussed in detail in Chapters 2–4.

In this Chapter, an anisotropic eddy viscosity model (or EARSIM) given by Wallin and Johansson (2000) [108], labelled WJ model, is used. Therefore, the RANS equations based on the WJ model are linearised for stability analysis. This analysis is referred to as EARSIM-based analysis or just EARSIM in the rest of the Chapter. The detailed derivation of the linearised RANS equation based on an EARSIM is given in Chapter 3.

The Reynolds stress anisotropy tensor is labelled as \mathbf{a} , and its components are labelled a_{ww} , a_{uu} , a_{vv} , a_{wu} , a_{vw} , and a_{uv} . The Reynolds stress components are then given as:

$$\begin{aligned} WW &= \left(a_{ww} + \frac{2}{3}\right) K, \quad UU = \left(a_{uu} + \frac{2}{3}\right) K, \quad VV = \left(a_{vv} + \frac{2}{3}\right) K, \\ WU &= Ka_{wu}, \quad VW = Ka_{vw}, \quad UV = Ka_{uv}. \end{aligned} \quad (6.16)$$

where WW , UU , and VV are the azimuthal, axial, and radial Reynolds normal stress components, and WU , VW , and UV are the azimuthal-axial, radial-azimuthal, and axial-radial Reynolds shear stress components.

The linearised RANS equations also include the wave-induced perturbations in the Reynolds stresses in addition to all the terms in the linearised Navier–Stokes equations [76]. In this chapter, these perturbations in the Reynolds stresses are labelled a'_{ww} , a'_{uu} , a'_{vv} , a'_{wu} , a'_{vw} , and a'_{uv} , and the linearised RANS equations are given below. The derivations of these terms using an EARSIM model is shown in Chapter 3.

The linearised RANS equations are, in the axial direction:

$$\begin{aligned} \frac{\partial u'}{\partial t} &= -V \frac{\partial u'}{\partial r} - v' \frac{\partial U}{\partial r} - \frac{W}{r} \frac{\partial u'}{\partial \theta} - U \frac{\partial u'}{\partial x} - u' \frac{\partial U}{\partial x} - \frac{\partial p'}{\partial x} + \frac{v}{r} \frac{\partial}{\partial r} \left(r \frac{\partial u'}{\partial r} \right) + \frac{v}{r^2} \frac{\partial^2 u'}{\partial \theta^2} + v \frac{\partial^2 u'}{\partial x^2} \\ &\quad - \frac{\partial}{\partial r} (Ka'_{uv}) - \frac{1}{r} \frac{\partial}{\partial \theta} (Ka'_{wu}) - \frac{K}{r} a'_{uv} - \frac{\partial}{\partial x} (Ka'_{uu}), \end{aligned} \quad (6.17)$$

in the radial direction:

$$\begin{aligned} \frac{\partial v'}{\partial t} &= -V \frac{\partial v'}{\partial r} - v' \frac{\partial V}{\partial r} - \frac{W}{r} \frac{\partial v'}{\partial \theta} - U \frac{\partial v'}{\partial x} - u' \frac{\partial V}{\partial x} + 2 \frac{W}{r} w' - \frac{\partial p'}{\partial r} + \frac{v}{r} \frac{\partial}{\partial r} \left(r \frac{\partial v'}{\partial r} \right) + \frac{v}{r^2} \frac{\partial^2 v'}{\partial \theta^2} \\ &\quad + v \frac{\partial^2 v'}{\partial x^2} - v \frac{v'}{r^2} - 2 \frac{v}{r^2} \frac{\partial w'}{\partial \theta} - \left(\frac{\partial}{\partial r} + \frac{1}{r} \right) (Ka'_{vv}) - \frac{1}{r} \frac{\partial}{\partial \theta} (Ka'_{vw}) + \frac{K}{r} a'_{vw} - \frac{\partial}{\partial x} (Ka'_{uv}), \end{aligned} \quad (6.18)$$

and in the azimuthal direction:

$$\begin{aligned} \frac{\partial w'}{\partial t} = & -V \frac{\partial w'}{\partial r} - v' \frac{\partial W}{\partial r} - \frac{W}{r} \frac{\partial w'}{\partial \theta} - U \frac{\partial w'}{\partial x} - u' \frac{\partial W}{\partial x} - \frac{V}{r} w' - \frac{W}{r} w' - \frac{1}{r} \frac{\partial p'}{\partial \theta} + \frac{v}{r} \frac{\partial}{\partial r} \left(r \frac{\partial w'}{\partial r} \right) \\ & + \frac{v}{r^2} \frac{\partial^2 w'}{\partial \theta^2} + v \frac{\partial^2 w'}{\partial x^2} - v \frac{w'}{r^2} + 2 \frac{v}{r^2} \frac{\partial v'}{\partial \theta} - \left(\frac{\partial}{\partial r} + \frac{2}{r} \right) (K a'_{vw}) - \frac{1}{r} \frac{\partial}{\partial \theta} (K a'_{ww}) - \frac{\partial}{\partial x} (K a'_{wu}). \end{aligned} \quad (6.19)$$

The wave-induced perturbations in the Reynolds stresses, which are present as \mathbf{a}' in the equations above, are higher in the flows with higher Reynolds stresses. These additional \mathbf{a}' -terms usually have a stabilising effect on the flow. The growth rates and eigenmodes obtained from the EARSM-based analysis are presented in Sections 6.4 and 6.5.

6.3 Numerical details and the cases studied

The numerical solutions of the linearised equations are obtained by using a Chebyshev spectral method with Gauss-Lobato points in the r -direction. The Matlab command ‘sparse’ is used to store the matrices, which are obtained after discretisation of the operators, in a compact form. The leading 60 to 100 eigenvalues and eigenvectors are then found using the ‘eigs’ command in Matlab. The number of grid-points used is 60 to 80, and the number of Fourier modes used for the mean profiles and perturbations is 30 to 40. All solutions presented in this Chapter are obtained from a 2.9 GHz Intel Core i7 processor with 8GB-1600MHz RAM. The above mentioned numbers of Fourier modes and grid-points are nearly the maximum possible discretisation allowed by this computational resource, and are sufficient for the convergence of eigenvectors as shown in figure 6.2 below.

In this chapter, two families of the cases are considered. The mean flows for these cases are provided by Mr. Hannes Brauckmann and Prof Bruno Eckhardt. The first family has fixed $\mu = 0$ and changing Re_i , which means that the outer cylinder is at rest and the inner cylinder is rotating at several speeds. Seven cases of this family are considered by increasing the azimuthal velocity of the inner cylinder progressively. These cases have $Re_i = 1481, 2222, 3333, 5000, 7500, 11250$, and 16875 . Here the Re_i increases by a factor of 1.5 from one case to the next.

The second family has fixed $Re_s = 1733$ and changing μ , which means that the mean shear parameter in the flow is kept constant and the ratio of rotation of the two cylinders is varied. Eight cases are considered in this family. Two of them have co-rotating cylinders with $\mu = 0.2$ and 0.4 , one has a stationary outer cylinder ($\mu = 0$), and five cases have

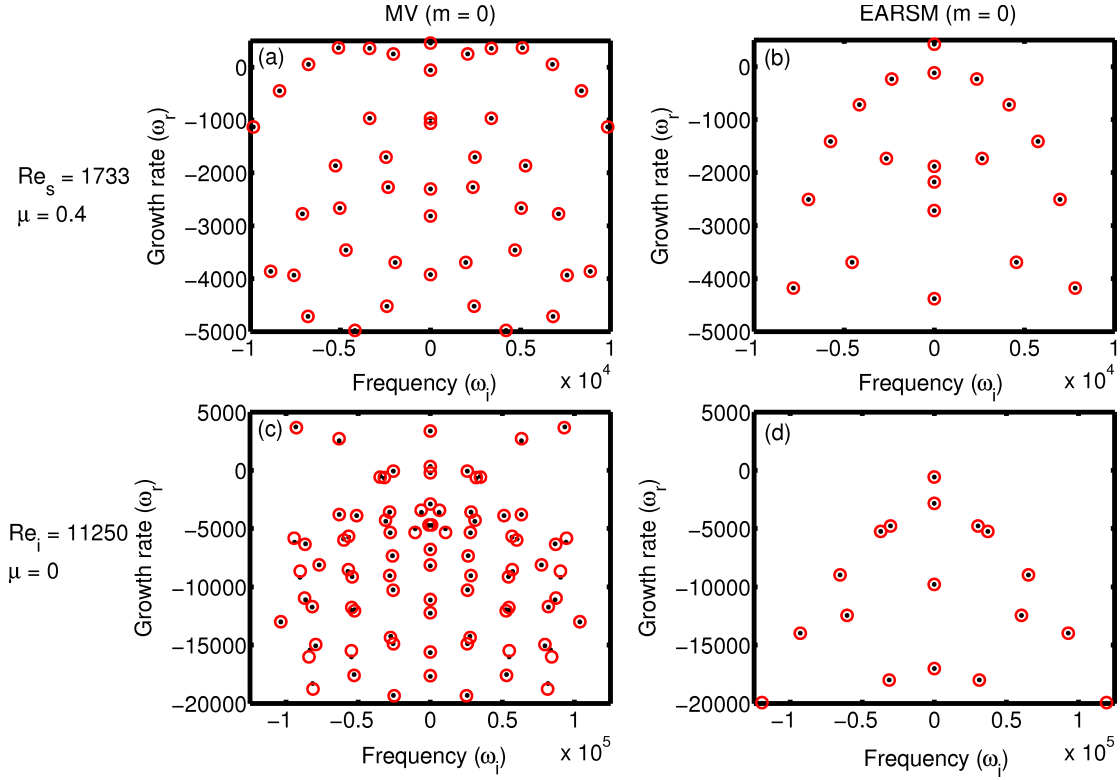


Fig. 6.2 Eigenvalues of azimuthal wavenumber $m = 0$ perturbations in the (a, b) $Re_s = 1733$ and $\mu = 0.4$, and (c, d) $Re_i = 11250$ and $\mu = 0$ cases calculated from the (a, c) MV-based analysis and (b, d) EARSMS-based analysis. The black dots are eigenvalues calculated with 40 Fourier modes and 60 grid-points in the r -direction and the red circles are eigenvalues calculated with 30 Fourier modes and 80 grid-points. The convergence is good in all the cases. In the higher Reynolds number case, the MV-based analysis calculations have small differences in the growth rates amongst the eigenvalues with the negative growth rates.

counter-rotating cylinders with $\mu = -0.2, -0.4, -0.71, -1$, and -2 . The case with $\mu = 0$ and $Re_s = 1733$ is common with the first case of the first family that has $\mu = 0$ and $Re_i = 1481$.

Figure 6.2 shows convergence of the leading eigenvalues in two cases: (a, b) a low Reynolds number case with $Re_s = 1733$ and $\mu = 0.4$, and (c, d) a high Reynolds number case with $Re_i = 11250$ and $\mu = 0$. These eigenvalues are obtained for perturbations of azimuthal wavenumber $m = 0$. The results in frames (a) and (c) are obtained using the MV-based analysis and the results in frames (b) and (d) are obtained using the EARSMS-based analysis. There are two sets of results: (i) the results shown by black dots are calculated with 40 Fourier modes and 60 grid-points in the r -direction and (ii) the results shown by red circles are calculated with 30 Fourier modes and 80 grid-points in the r -direction. The eigenvalues

barely change, which shows that the results are well converged. The one exception is the higher Reynolds number case ($Re_i = 11250$) calculations from the MV-based analysis. It has slight differences in the growth rates amongst the eigenvalues with the negative growth rates.

6.4 Stability results for the $\mu = 0$ flow cases

Figure 6.3 presents the mean velocity in four of the first family of cases, which are the $Re_i = 1481, 3333, 7500$ and 16875 cases. The mean azimuthal velocity (W) of the outer cylinder is fixed at zero, and W of the inner cylinder is linearly proportional to Re_i . Taylor-Couette flow with a rotating inner cylinder and a stationary outer cylinder is Rayleigh unstable. The instability in the flow causes the formation of Taylor-vortices, which get stronger with increasing Re_i . The mean axial and radial velocities plotted in the figure show the strength of Taylor-vortices. Faster rotation of the inner cylinder causes stronger Taylor-vortices, and therefore the U and V fields magnitudes also increase with Re_i . This increase in U and V is linearly proportional to Re_i , which means that the magnitude of the U and V fields also increases by a similar factor as the W fields with increasing Re_i .

Figures 6.4 and 6.5 show the Reynolds normal and shear stress components, respectively, in the four cases. The Reynolds stress components also increase with Re_i . Because they are second-order quantities, in general they are expected to increase in proportion to the square of the mean velocities, which means by $2.25^2 \approx 5$ from one case to the next. The increase is approximately 5 in all the cases, but is greater than 5 in between the $Re_i = 1481$ and $Re_i = 3333$ cases. All the Reynolds stress components are generally high in the region between two Taylor vortices, which coincides with the region of higher radial velocity. These regions are near $x = 0, 1$, and 2 . The increase in the Reynolds stress components implies an increase in the anisotropic eddy viscosity components, which usually have a stabilising effect on the eigenmodes calculated from the EARSME-based stability analysis.

Table 6.1 summarises the growth rates of the leading eigenvalues calculated from the MV- and EARSME-based analyses for the $m = 0, 1$, and 2 perturbations in all the cases and also for the $m = 4, 5$, and 6 perturbations in the $Re_i = 16875$ case. The calculations are performed at least up to $m = 3$ perturbations in all the cases to ensure that modes with the highest growth rates are captured. In the $Re_i = 1481$ case, there is almost no difference in the growth rates calculated from the two analyses up to the significant figures of the eigenvalues listed in the table. This is because the inertial terms, which are caused by the mean velocity, are much larger than the turbulent eddy viscosity terms, which are caused

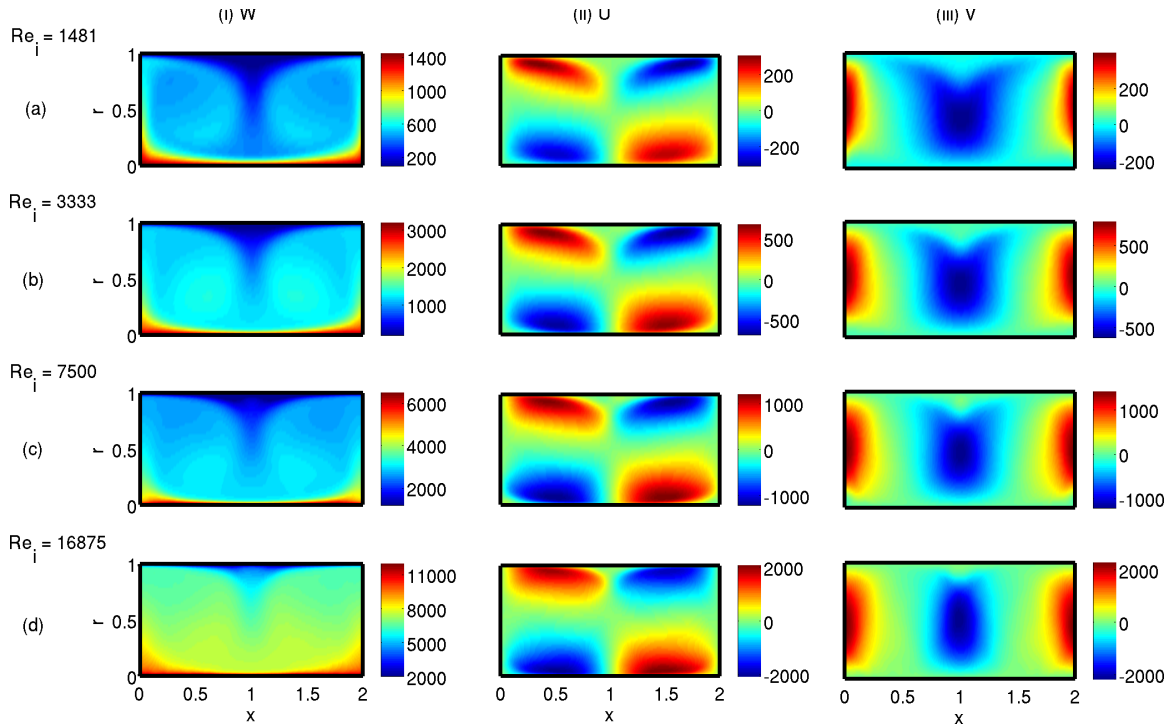


Fig. 6.3 The mean velocity in the $\mu = 0$ cases. Each row presents the mean velocities in the (a) $Re_i = 1481$, (b) $Re_i = 3333$, (c) $Re_i = 7500$, and (d) $Re_i = 16875$ cases. Each column presents the (i) azimuthal (W), (ii) axial (U), and (iii) radial (V) mean velocity components in the above mentioned cases. By definition the mean azimuthal velocity of the inner cylinder is linearly proportional to Re_i , and the mean azimuthal velocity of the outer cylinder is zero. The mean axial and radial velocities are non-zero because Taylor vortices exist in the flow.

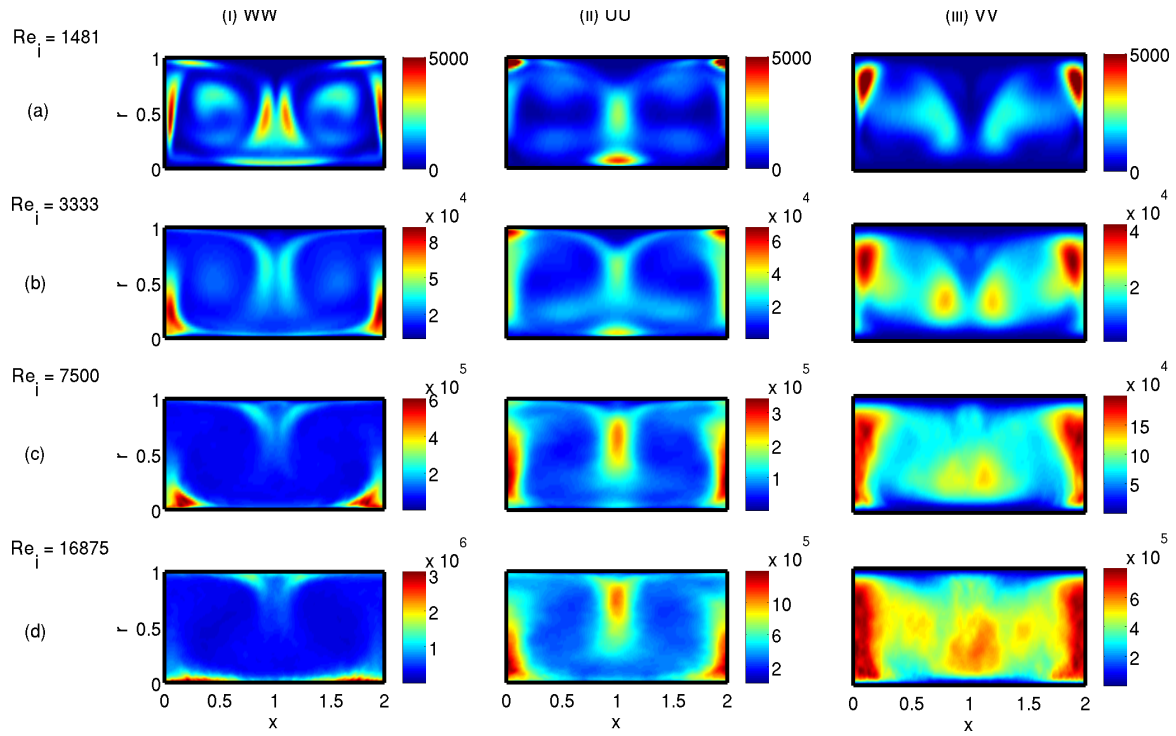


Fig. 6.4 The Reynolds normal stress components in the $\mu = 0$ cases. Each row presents the Reynolds normal stress in the (a) $Re_i = 1481$, (b) $Re_i = 3333$, (c) $Re_i = 7500$, and (d) $Re_i = 16875$ cases. Each column presents the (i) WW , (ii) UU , and (iii) VV —components of the Reynolds normal stress. The magnitude of the Reynolds normal stress components increases with increasing Re_i .

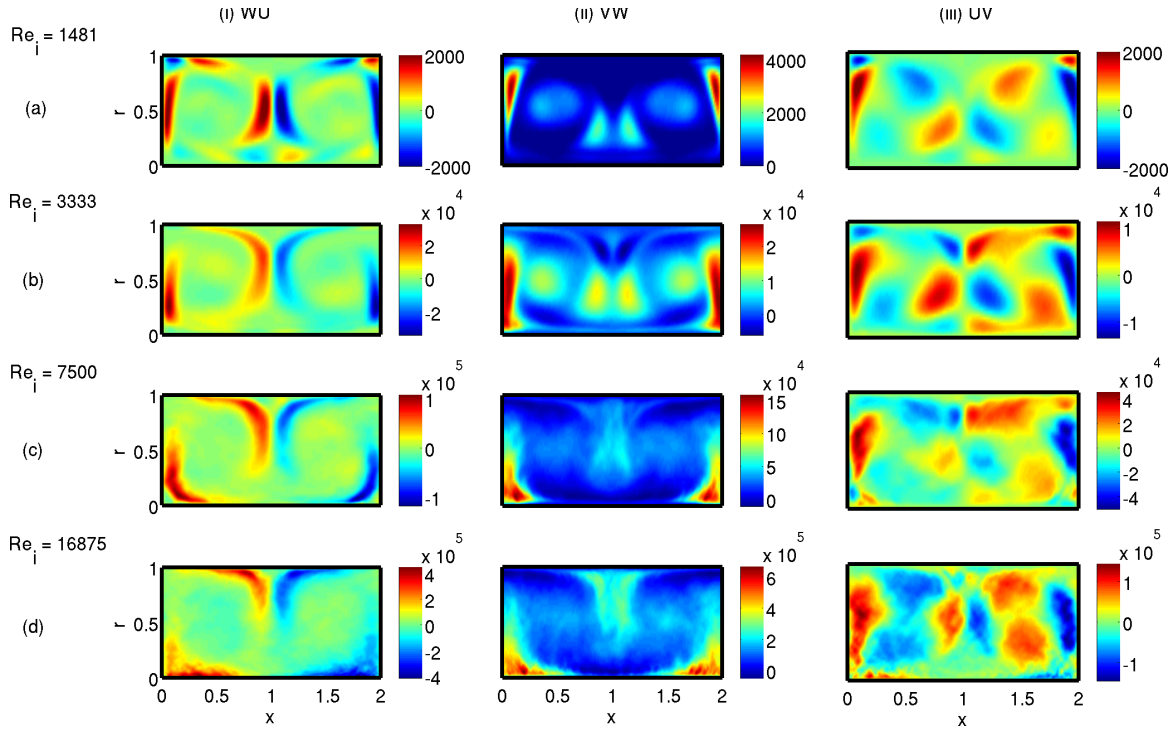


Fig. 6.5 The Reynolds shear stress components in the $\mu = 0$ cases. Each row presents the Reynolds shear stress in the (a) $Re_i = 1481$, (b) $Re_i = 3333$, (c) $Re_i = 7500$, and (d) $Re_i = 16875$ cases. Each column presents the (i) WU , (ii) VW , and (iii) UV —components of the Reynolds shear stress. The magnitude of the Reynolds shear stress components increases with increasing Re_i .

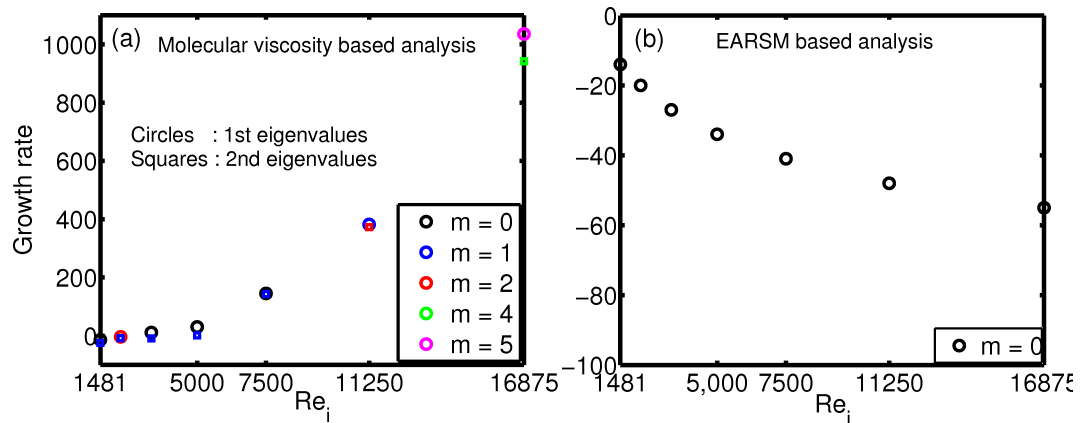


Fig. 6.6 The growth rate of the leading eigenmodes for all the Re_i cases calculated from the (a) MV-based analysis (the first two eigenvalues are shown) and (b) EARSM-based analyses (only the first eigenvalues are shown). The MV-based analysis predicts an increase in the growth rate as Re_i increases, which means that the higher Re_i flows should be more intermittent. The EARSM-based analysis predicts a decrease in the growth rate as Re_i increases, which means that the higher Re_i flows should be less intermittent. The DNS data for these flows show that the turbulent intermittency increases with increasing Re_i , which means that the growth rate predictions from the MV-based analysis are in better agreement with the observation from the DNS. The figure also shows the azimuthal wavenumbers of the leading eigenmodes.

by the Reynolds stresses. The results from the two analyses have similarities with each other until the $Re_i = 5000$ case. This is seen in terms of the frequencies of the leading eigenvectors, which match well with each other. For the flows with $Re_i \geq 7500$, the stability results from the two analyses have no similarities.

Figure 6.6 shows variation of the growth rate of the leading eigenmodes with Re_i calculated from the (a) MV- and (b) EARSM-based analyses. The figure also indicates the azimuthal wavenumbers of the leading eigenmodes. The EARSM-based analysis predicts that the eigenmodes with $m = 0$ are least stable in all the cases, while the MV-based analysis predicts that the azimuthal wavenumber of the most unstable eigenmode increases with increasing Re_i , with the exception of the $Re_i = 2222$ case. One major qualitative difference in the results between the two analyses is that the MV-based analysis predicts an increase in the growth rate with increasing Re_i , while the EARSM-based analysis predicts a decrease in the growth rate with increasing Re_i . Based on these results, the MV-based analysis predicts that the $\mu = 0$ flow cases should become more intermittent at higher Re_i and the EARSM-based analysis predicts that the $\mu = 0$ flow cases should become less intermittent at higher Re_i . Based on the DNS data, fluctuations on top of Taylor vortices become stronger with increasing Re_i . Therefore, it is concluded that the stability results from the MV-based anal-

Table 6.1 The leading eigenmodes in the $\mu = 0$ cases. The MV-based analysis predicts destabilisation with increasing Re_i , while the EARSME-based analysis predicts stabilisation with increasing Re_i .

Case	Azimuthal wavenumber					
Re_i	$m = 0$		$m = 1$		$m = 2$	
	MV	EARSME	MV	EARSME	MV	EARSME
1481	$-14 + 0i$	$-14 + 0i$	$-25 + 316i$	$-25 + 316i$	$-36 - 1956i$	$-36 - 1956i$
	$-33 + 1025i$	$-33 + 1025i$	$-32 + 814i$	$-32 + 814i$	$-36 + 616i$	$-36 + 616i$
	$-39 + 495i$	$-39 + 495i$	$-35 - 1729i$	$-35 - 1729i$	$-47 + 119i$	$-47 + 119i$
	$m = 0$		$m = 1$		$m = 2$	
	MV	EARSME	MV	EARSME	MV	EARSME
2222	$-12 + 0i$	$-20 + 0i$	$-8 - 2558i$	$-59 - 457i$	$-4 - 2897i$	$-70 + 185i$
	$-17 + 0i$	$-49 + 0i$	$-24 + 462i$	$-101 - 295i$	$-23 + 462i$	$-107 - 2880i$
	$-37 + 2239i$	$-79 + 716i$	$-41 + 1201i$	$-114 - 1827i$	$-41 + 1201i$	$-123 + 901i$
	$m = 0$		$m = 1$		$m = 2$	
	MV	EARSME	MV	EARSME	MV	EARSME
3333	$11 + 0i$	$-27 + 0i$	$-9 + 785i$	$-105 + 774i$	$-12 + 337i$	$-94 + 334i$
	$-16 + 0i$	$-73 + 0i$	$-50 + 1978i$	$-150 - 468i$	$-40 + 1530i$	$-251 - 1061i$
	$-69 + 1389i$	$-144 + 1166i$	$-66 - 3998i$	$-218 - 1522i$	$-95 - 2436i$	$-263 - 3290i$
	$m = 0$		$m = 1$		$m = 2$	
	MV	EARSME	MV	EARSME	MV	EARSME
5000	$30 + 0i$	$-34 + 0i$	$1 + 1132i$	$-173 + 1102i$	$-47 + 419i$	$-178 + 396i$
	$-13 + 0i$	$-118 + 0i$	$-50 + 2818i$	$-222 - 662i$	$-96 + 2189i$	$-380 - 2636i$
	$-47 + 1945i$	$-238 + 1720i$	$-60 + 1236i$	$-322 + 1220i$	$-101 + 679i$	$-399 - 591i$
	$m = 0$		$m = 1$		$m = 2$	
	MV	EARSME	MV	EARSME	MV	EARSME
7500	$145 + 4459i$	$-41 + 0i$	$143 + 3414i$	$-223 + 1179i$	$112 + 2256i$	$-280 + 106i$
	$36 + 6578i$	$-181 + 0i$	$53 + 5603i$	$-281 - 977i$	$13 + 4680i$	$-390 + 423i$
	$-45 + 2362i$	$-276 + 2143i$	$22 + 1270i$	$-347 + 1423i$	$-12 + 6920i$	$-443 - 3663i$
	$m = 0$		$m = 1$		$m = 2$	
	MV	EARSME	MV	EARSME	MV	EARSME
11250	$308 + 7814i$	$-48 + 0i$	$382 - 6300i$	$-310 - 1538i$	$373 + 4748i$	$-375 - 585i$
	$284 + 0i$	$-238 + 0i$	$335 + 8915i$	$-348 + 1055i$	$361 + 7353i$	$-548 - 5151i$
	$229 + 0i$	$-401 + 2554i$	$286 + 3737i$	$-474 - 4747i$	$338 + 9973i$	$-553 - 3115i$
	$m = 0$		$m = 1$		$m = 2$	
	MV	EARSME	MV	EARSME	MV	EARSME
16875	$744 + 16814i$	$-55 + 0i$	$850 + 14454i$	$-453 - 2385i$	$880 + 12086i$	$-469 - 1639i$
	$742 + 10172i$	$-355 + 0i$	$817 + 21298i$	$-476 + 928i$	$805 + 5372i$	$-665 - 7351i$
	$692 + 13522i$	$-548 + 3278i$	$763 - 7789i$	$-640 - 5378i$	$799 + 8651i$	$-763 - 4771i$
	$m = 4$		$m = 5$		$m = 6$	
	MV	EARSME	MV	EARSME	MV	EARSME
16875	$942 + 10548i$		$1036 + 12015i$		$895 + 2383i$	
	$909 + 3892i$		$931 + 8223i$		$883 + 5804i$	
	$872 - 17292i$		$912 + 15097i$		$867 + 14348i$	

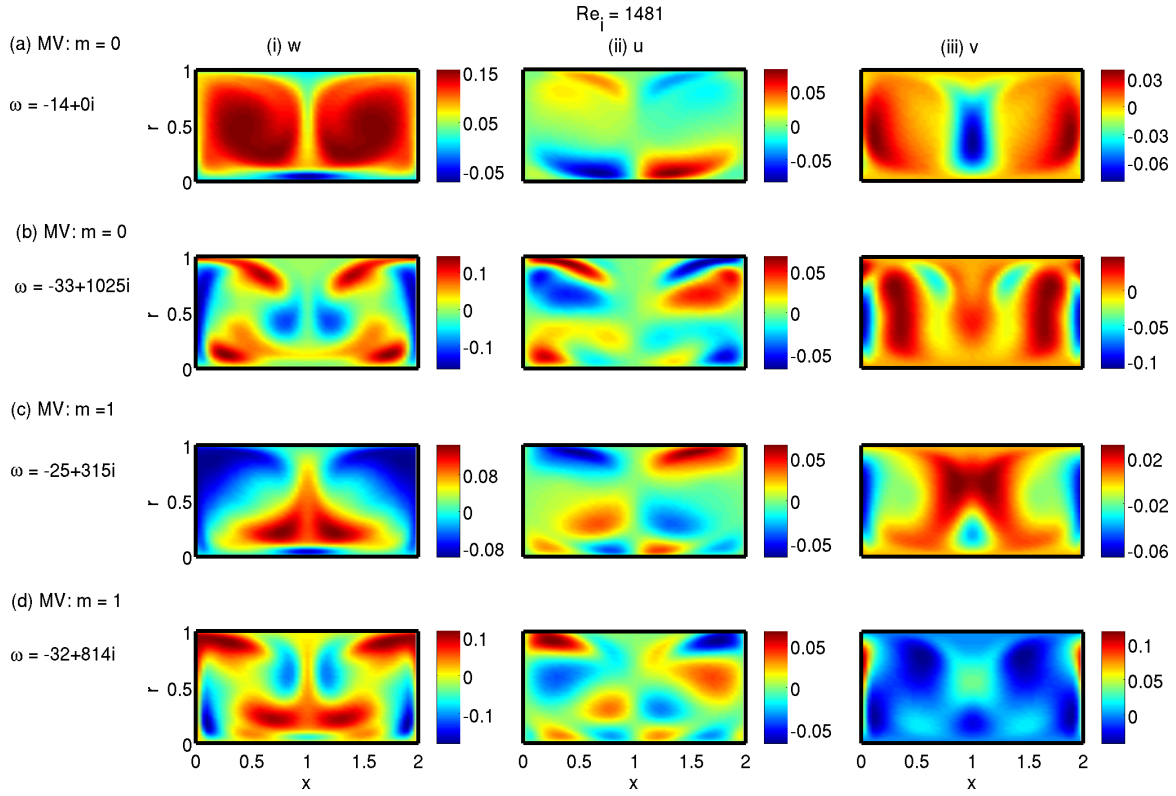


Fig. 6.7 The first two leading eigenmodes of the (a, b) $m = 0$ and (c, d) $m = 1$ azimuthal wavenumbers in the $Re_i = 1481$ case calculated from the MV-based analysis. The MV and EARS-M-based analyses give very similar growth rates and eigenmode shapes for this flow case.

ysis are in better agreement with the observations on the strength of intermittent structures from the DNS data.

A possible reason behind the bad predictions from the EARS-M-based analysis could be that the anisotropic eddy viscosity used is too high and therefore damps more than it should. This has been seen for channel flows as well in Chapters 2 and 3, and is discussed in Refs. [4, 98]. These researchers explain that if coherent structures are to be found from the stability analysis then their contribution in the Reynolds stresses should not be included. Therefore, the wave-induced perturbations in the Reynolds stresses in the linearised equations should only include the contribution from small-scale turbulence. Consequently, the anisotropic eddy viscosity used in the stability analysis should be much smaller than that used in the present EARS-M-based analysis.

Figure 6.7 presents the first two leading eigenmodes of the (a, b) $m = 0$ perturbations and of the (c, d) $m = 1$ perturbations calculated from the MV-based analysis. As mentioned before, results from the EARS-M-based analysis are very similar to those from the MV-based

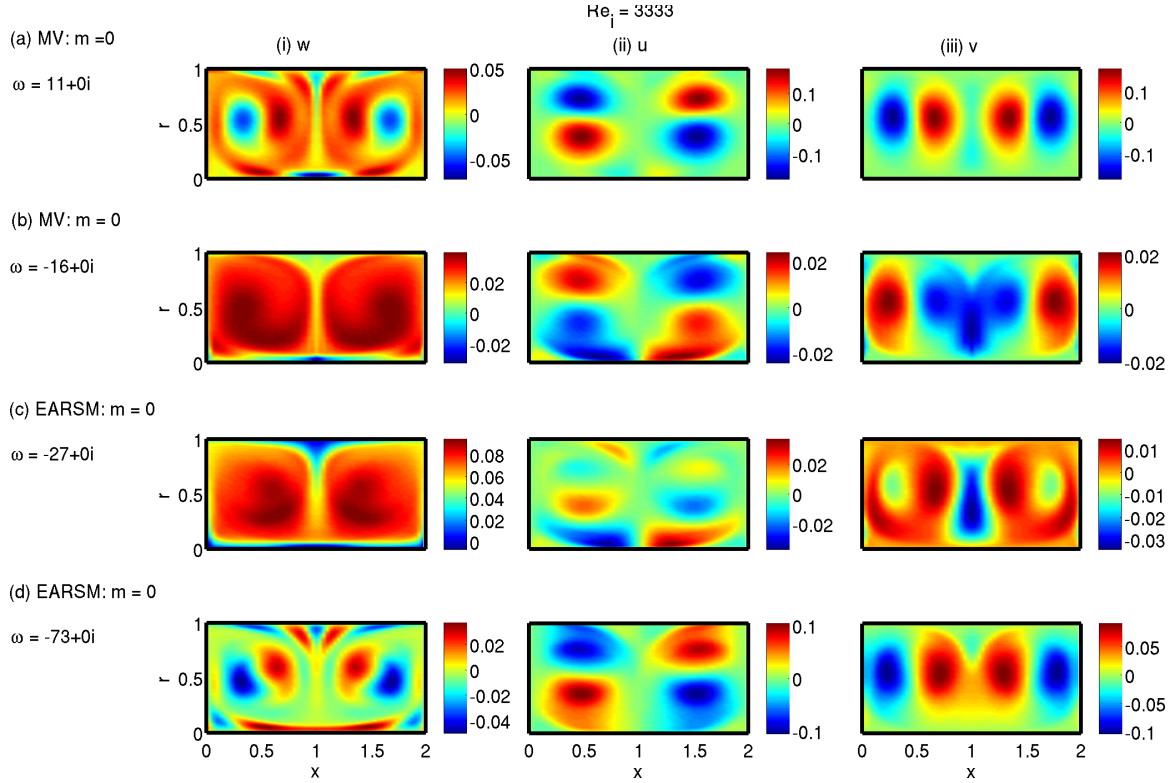


Fig. 6.8 The first two leading eigenmodes of the $m = 0$ azimuthal wavenumber in the $Re_i = 3333$ case calculated from the (a, b) MV- and (c, d) EARS-based analyses. The first mode from the MV-based analysis matches with the second mode from the EARS-based analysis, and the second mode from the MV analysis matches with the first mode from the MV-based analysis.

analysis for this case. Figures 6.8 and 6.9 show the leading eigenmodes from the MV- and EARS-based analyses for the flows at $Re_i = 3333$ and 5000, respectively. These figures show the similarity in eigenmodes from the two analyses. The stability results from the two analyses do not have any similarities for the flows with $Re_i \geq 7500$. Figures 6.10 and 6.11 show the leading eigenmodes calculated from the MV- and EARS-based analyses, respectively, for the flows with $Re_i \geq 7500$. Figure 6.10 shows that the leading eigenmodes predicted from the MV-based analysis for the higher Re_i cases are more localised than those for the lower Re_i flows, i.e. they are concentrated at a few spots. This is also in agreement with the observations from the DNS data, which show that intermittent turbulent structures, although they become stronger, decrease in size in the higher Re_i flow cases.

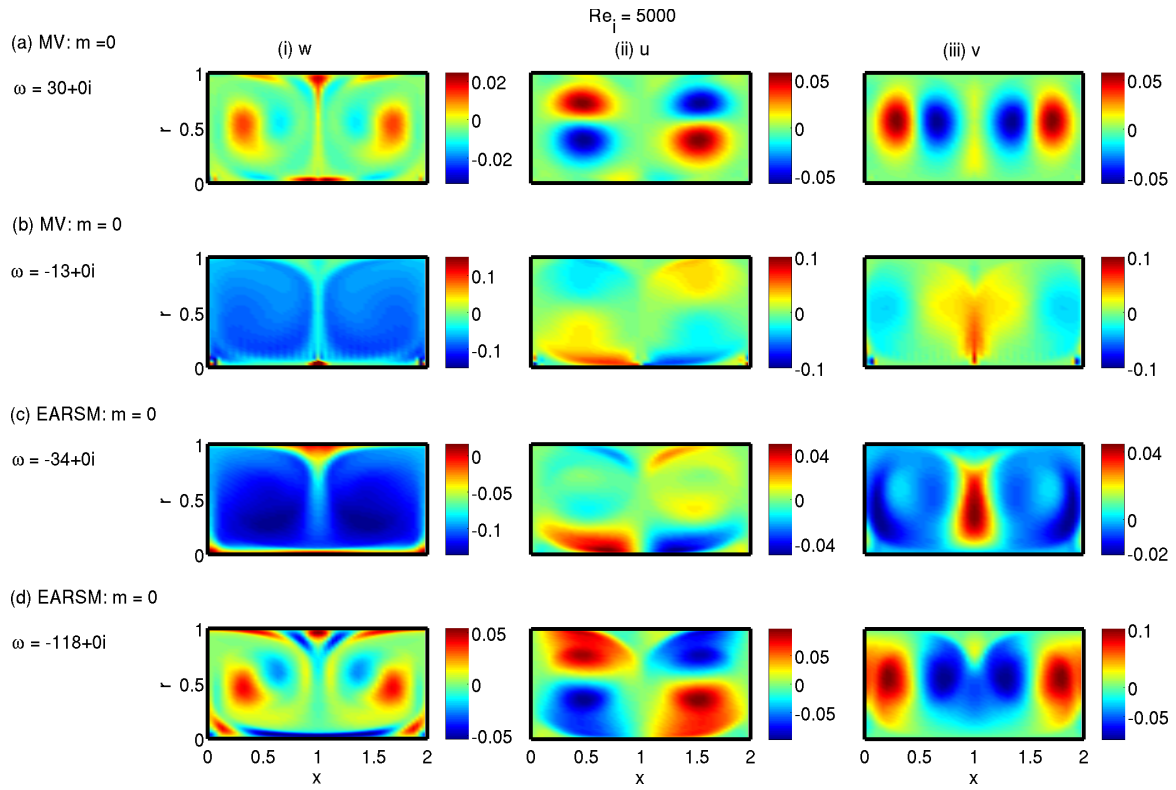


Fig. 6.9 The first two leading eigenmodes of the $m = 0$ azimuthal wavenumber in the $Re_i = 5000$ case calculated from the (a, b) MV- and (c, d) EARSIM-based analyses. The first mode from the MV-based analysis matches with the second mode from the EARSIM-based analysis, and the second mode from the MV-based analysis matches with the first mode from the EARSIM-based analysis.

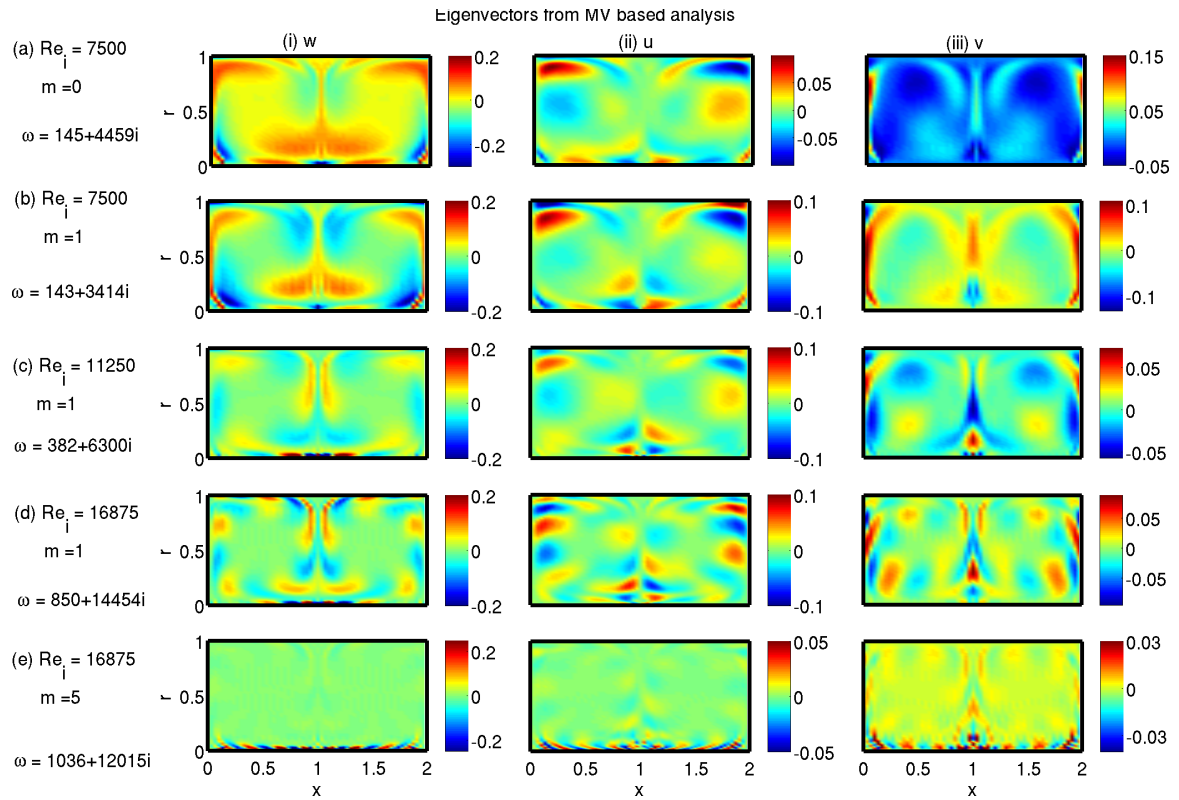


Fig. 6.10 The leading eigenmodes calculated from the MV-based analysis in the $Re_i = 7500$ of the azimuthal wavenumbers (a) $m = 0$ and (b) $m = 1$, in the $Re_i = 11250$ of the azimuthal wavenumber (c) $m = 1$, and in the $Re_i = 16875$ of the azimuthal wavenumbers (d) $m = 1$ and (e) $m = 5$. Unlike the eigenmodes in the lower Re_i cases, these modes are concentrated at a few spots, such as near the inner cylinder or the axial boundaries.

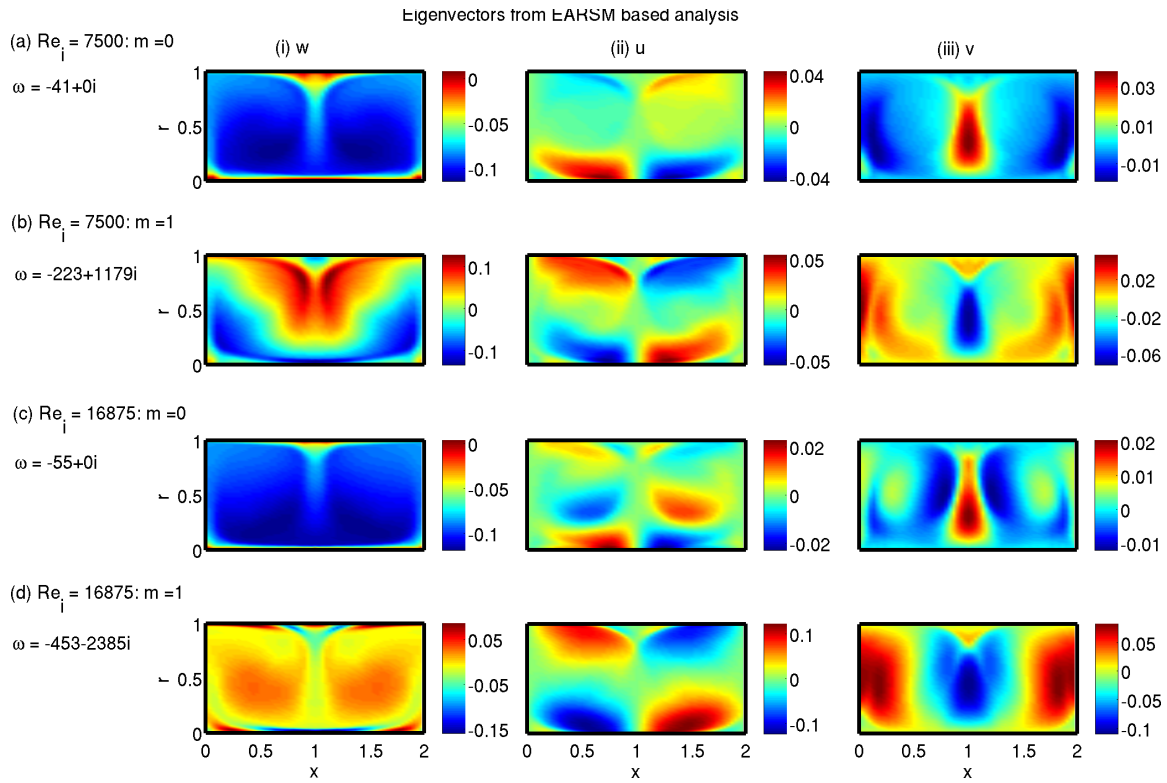


Fig. 6.11 The leading eigenmodes of the azimuthal wavenumber (a, c) $m = 0$ and (b, d) $m = 1$ in the (a, b) $Re_i = 7500$ and (c, d) $Re_i = 16875$ cases calculated from the EARSIM-based analysis. These eigenmodes match the corresponding azimuthal wavenumber eigenmodes in the lower Re_i cases. This is in contrast to the eigenmodes calculated from the MV-based analysis in these higher Re_i cases, which are concentrated at a few spots.

6.5 Stability results for the $Re_s = 1733$ flow cases

Figure 6.12 presents the mean velocities for the $\mu = -0.4, -0.2, 0.2$, and 0.4 cases and figure 6.13 presents the mean velocities for the $\mu = -0.71, -1$, and -2 cases. The flow between a rotating outer cylinder and a stationary inner cylinder is known to be Rayleigh stable. As compared to the $\mu = 0$ case, Taylor vortices are weakened in the cases with the non-zero μ . This is seen through the fact that the U and V velocities in these cases are smaller in magnitude than those in the $\mu = 0$ case. Moreover, the U and V fields in the negative μ cases are weaker than those in the positive μ cases of equal magnitude, which shows that Taylor vortices in the counter-rotating cases are weaker than those in the co-rotating cases. Finally, in the $\mu = -2$ case, the stabilising effect of the outer cylinder overtakes the destabilising effect of the inner cylinder and there are no significant Taylor vortices in the flow.

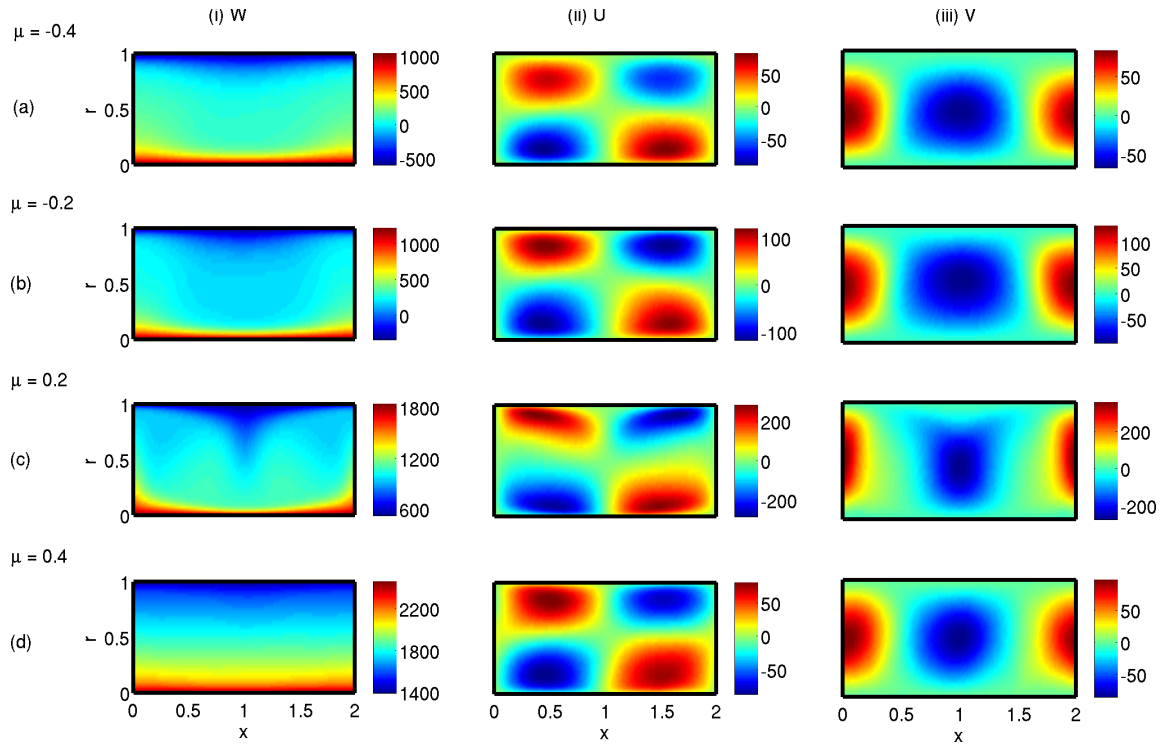


Fig. 6.12 The mean velocities in the $Re_s = 1733$ cases. Each row presents the mean velocities in the (a) $\mu = -0.4$, (b) $\mu = -0.2$, (c) $\mu = 0.2$, and (d) $\mu = 0.4$ cases. Each column presents the (i) azimuthal (W), (ii) axial (U), and (iii) radial (V) mean velocity components in the above mentioned cases. The mean azimuthal velocity mainly depends upon the inner and outer cylinder rotation, which are determined by μ and Re_s . The mean axial and radial velocity profiles are the result of the formation of Taylor vortices. These profiles suggest that the Taylor vortices weaken when the outer cylinder rotates while keeping Re_s constant.

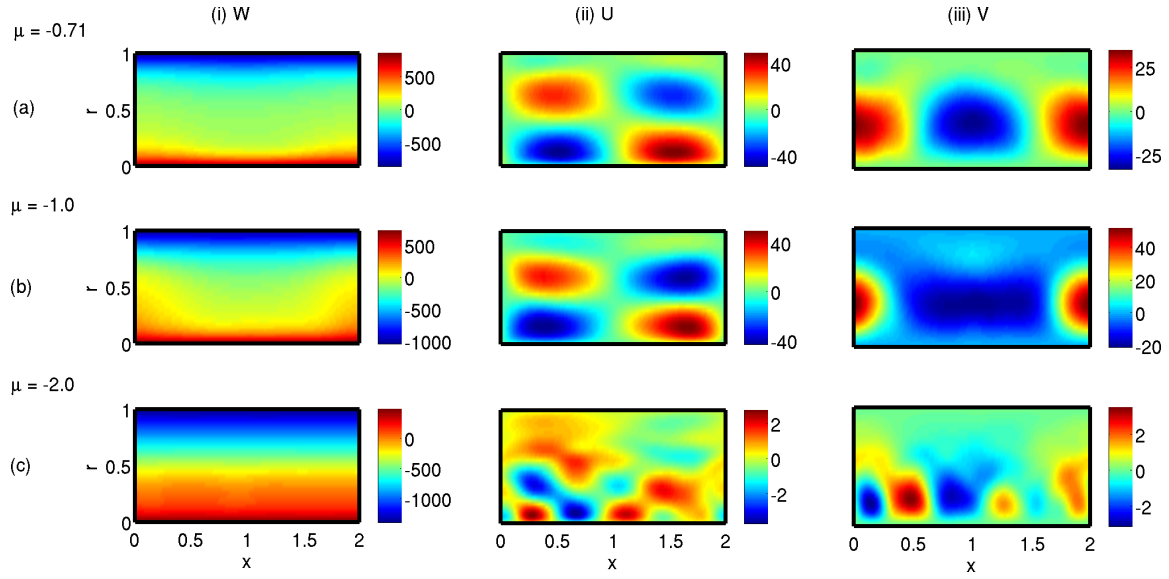


Fig. 6.13 The mean velocities in the $Re_s = 1733$ cases. Each row presents the mean velocities in the (a) $\mu = -0.71$, (b) $\mu = -1$, and (c) $\mu = -2$ cases. Each column presents the (i) azimuthal (W), (ii) axial (U), and (iii) radial (V) mean velocity components in the above mentioned cases. The mean axial and radial velocities in the $\mu = -2$ case are very small, which implies that there are no Taylor vortices in this case.

Figures 6.14 and 6.15 present the Reynolds normal and shear stress components, respectively, for the (a) $\mu = -0.4$, (b) -0.2 , (c) 0.2 , and (d) 0.4 cases. Figure 6.16 and 6.17 present the Reynolds normal and shear stress components, respectively, for the (a) $\mu = -0.71$, (b) -1.0 , and (c) -2.0 cases. In the positive μ cases, the WW , WU , VW , and UV Reynolds stress components increase from the $\mu = 0$ to 0.2 cases then decrease for the $\mu = 0.4$ case. The other two components (UU and VV) increase continuously from the $\mu = 0$ to 0.4 cases. In the negative μ cases, all the Reynolds stress components increase very sharply from the $\mu = 0$ to -0.2 cases and then gradually decrease until the last case ($\mu = -2.0$).

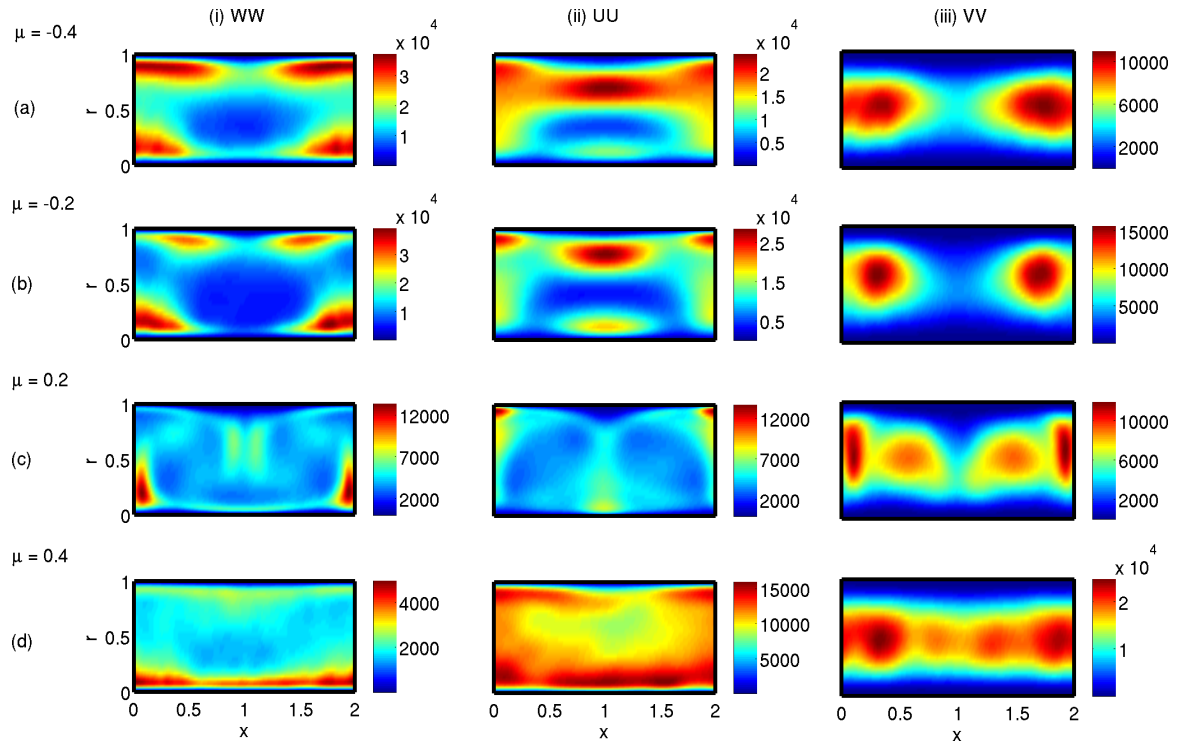


Fig. 6.14 The Reynolds normal stresses in the $Re_s = 1733$ cases. Each row presents the Reynolds normal stress components in the (a) $\mu = -0.4$, (b) $\mu = -0.2$, (c) $\mu = 0.2$, and (d) $\mu = 0.4$ cases. Each column presents the (i) WW , (ii) UU , and (iii) VV Reynolds normal stress components. For the negative μ cases, the Reynolds normal stress components first increase sharply when μ is changed from 0 to -0.2 then decrease slightly in the $\mu = -0.4$ case. For the positive μ cases, the Reynolds normal stress components increase when μ is changed from 0 to 0.2, the UU and VV components further increase in the $\mu = 0.4$ case, but the WW component decreases slightly.

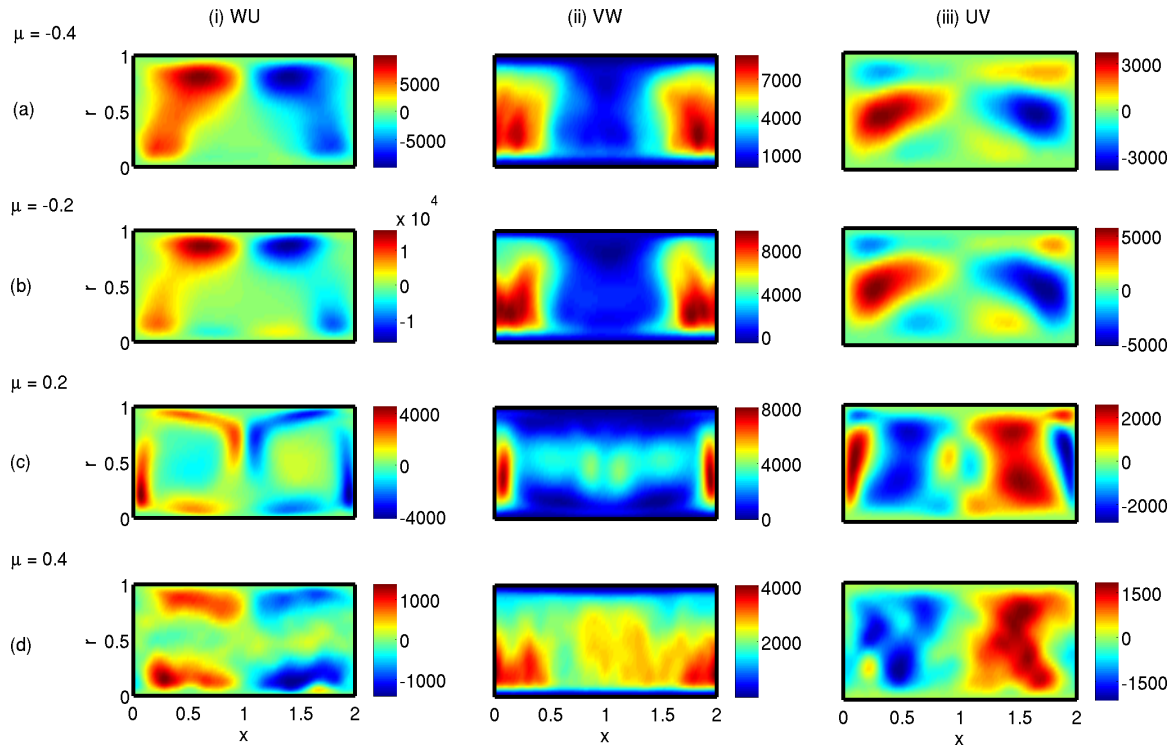


Fig. 6.15 The Reynolds shear stresses in the $Re_s = 1733$ cases. Each row presents the Reynolds shear stress in the (a) $\mu = -0.4$, (b) $\mu = -0.2$, (c) $\mu = 0.2$, and (d) $\mu = 0.4$ cases. Each column presents the (i) WU , (ii) VW , and (iii) UV Reynolds shear stress component. The Reynolds shear stress components first increase when μ is changed from 0 to -0.2 or 0.2 , then decrease when further changed to $\mu = -0.4$ or 0.4 .

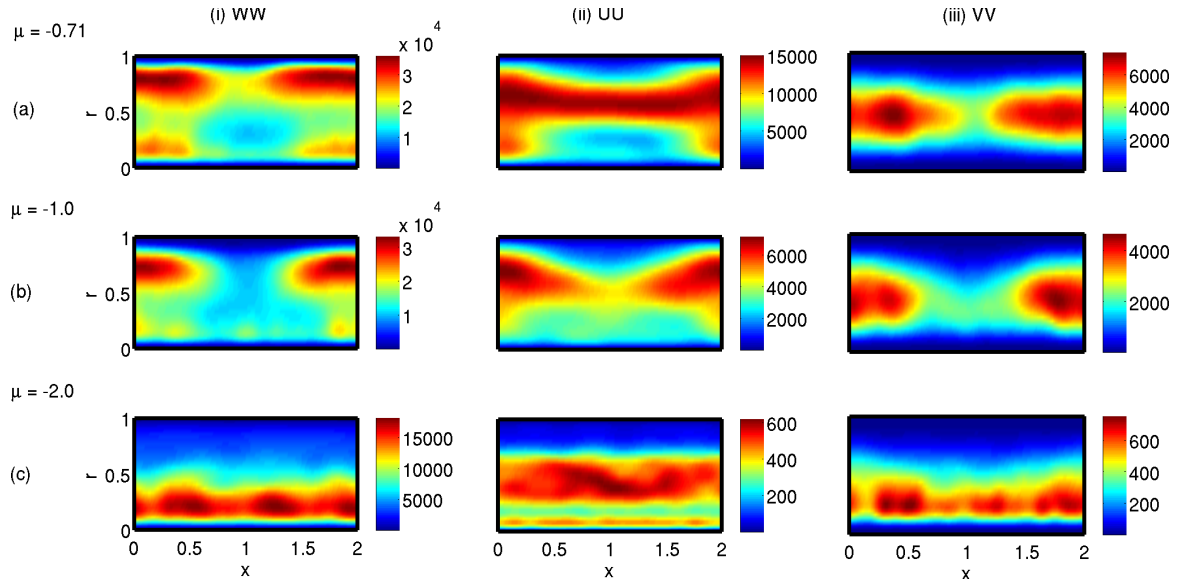


Fig. 6.16 The Reynolds normal stresses in the $Re_s = 1733$ cases. Each row presents the Reynolds normal stress in the (a) $\mu = -0.71$, (b) $\mu = -1$, and (c) $\mu = -2$ cases. Each column presents the (i) WW , (ii) UU , and (iii) VV Reynolds normal stress components. The Reynolds normal stress components decrease with increasing negative μ .

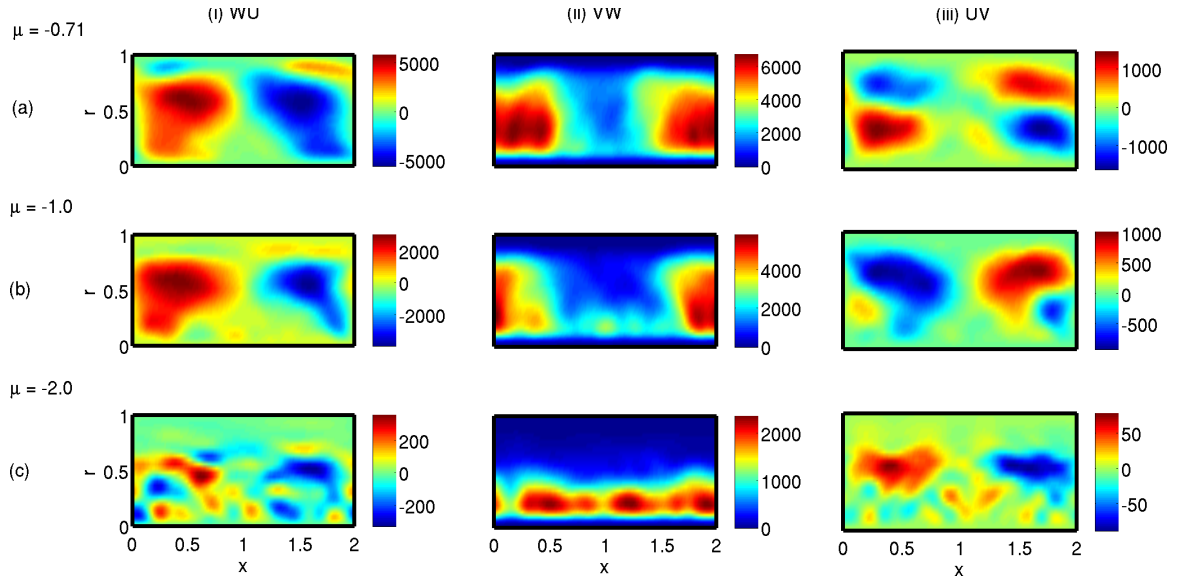


Fig. 6.17 The Reynolds shear stresses in the $Re_s = 1733$ cases. Each row presents the Reynolds shear stress in the (a) $\mu = -0.71$, (b) $\mu = -1$, and (c) $\mu = -2$ cases. Each column presents the (i) WU , (ii) VW , and (iii) UV Reynolds shear stress components. The Reynolds shear stress components decrease with increasing negative μ .

Table 6.2 summarises the growth rates of the leading eigenvalues calculated from the

MV- and EARSIM-based analyses for the $m = 0, 1$, and 2 perturbations in all the $Re_s = 1733$ cases. The calculations are performed at least up to $m = 3$ perturbations in all the cases to ensure that the leading eigenmodes are captured. The cases $\mu = 0, 0.2, 0.4, -1.0$, and -2 have similarities in the frequency of the leading eigenmodes from the MV- and EARSIM-based analyses, while the cases $\mu = -0.2, -0.4$, and -0.71 do not have any similarities in the stability results from the two analyses. The results for the $\mu = -2$ case cannot be compared with the other cases. This is because the mean velocity in $\mu = -2$ case has no Taylor vortices. Consequently, the stability results for the $\mu = -2$ case are for the primary instability, which is the formation of Taylor vortices, while the stability results in the other cases are for secondary instabilities.

Figure 6.18 shows the growth rates of the leading modes in all the $Re_s = 1733$ cases obtained from the (a) MV- and (b) EARSIM-based analyses. It also shows the azimuthal wavenumbers of the leading eigenmodes. The MV-based analysis predicts that the growth rate increases with the increasing absolute value of μ for all the cases except for the $\mu = -1$ case. Based on these few cases, it predicts that the $Re_s = 1733$ flow cases should become more intermittent with the increase in the outer cylinder rotation, except for the very strong counter-rotation case. The EARSIM-based analysis predicts that the growth rate first decreases for a small change in μ , which is from 0 to -0.2 or 0.2 , then it increases when the magnitude of μ is further increased. Therefore, it predicts that the $Re_s = 1733$ flow cases with small counter- or co-rotation should be less intermittent than the $\mu = 0$ case, and that these flow cases should become more intermittent for the higher values of counter- or co-rotation.

Table 6.2 The growth rates of the leading eigenmodes in the $Re_s = 1733$ flow cases.

Case	Azimuthal wavenumber					
μ	$m = 0$		$m = 1$		$m = 2$	
	MV	EARSM	MV	EARSM	MV	EARSM
0.4	$38 + 0i$	$36 + 0i$	$76 - 616i$	$55 - 611i$	$99 - 1259i$	$51 - 1253i$
	$31 + 430i$	$-10 + 0i$	$39 - 414i$	$-16 - 422i$	$54 - 1095i$	$-40 - 1088i$
	$30 + 284i$	$-20 + 198i$	$20 - 238i$	$-38 - 866i$	$37 - 1433i$	$-78 - 1489i$
	$m = 0$		$m = 1$		$m = 2$	
	MV	EARSM	MV	EARSM	MV	EARSM
0.2	$12 + 0i$	$-21 + 0i$	$-5 + 658i$	$-70 - 344i$	$3 + 306i$	$-91 - 221i$
	$-14 + 0i$	$-52 + 0i$	$-5 - 347i$	$-80 + 149i$	$-29 + 797i$	$-95 - 1075i$
	$-27 + 1508i$	$-87 + 486i$	$-26 + 174i$	$-97 - 791i$	$-33 - 195i$	$-127 - 676i$
	$m = 0$		$m = 1$		$m = 2$	
	MV	EARSM	MV	EARSM	MV	EARSM
0	$-14 + 0i$	$-14 + 0i$	$-25 + 316i$	$-25 + 316i$	$-36 - 1956i$	$-36 - 1956i$
	$-33 + 1025i$	$-33 + 1025i$	$-32 + 814i$	$-32 + 814i$	$-36 + 616i$	$-36 + 616i$
	$-39 + 495i$	$-39 + 495i$	$-35 - 1729i$	$-35 - 1729i$	$-47 + 119i$	$-47 + 119i$
	$m = 0$		$m = 1$		$m = 2$	
	MV	EARSM	MV	EARSM	MV	EARSM
-0.2	$-8 + 345i$	$-22 + 0i$	$-4 - 245i$	$-126 - 99i$	$-14 - 133i$	$-125 - 224i$
	$-10 + 0i$	$-189 + 385i$	$-17 - 19i$	$-174 + 219i$	$-30 - 150i$	$-183 + 111i$
	$-40 + 570i$	$-191 + 0i$	$-31 - 419i$	$-204 - 293i$	$-32 - 487i$	$-298 - 389i$
	$m = 0$		$m = 1$		$m = 2$	
	MV	EARSM	MV	EARSM	MV	EARSM
-0.4	$-12 + 74i$	$-20 + 0i$	$5 + 14i$	$-124 - 152i$	$-9 - 59i$	$-115 - 169i$
	$-23 + 241i$	$-89 + 139i$	$-15 + 186i$	$-130 + 114i$	$-17 + 122i$	$-158 + 201i$
	$-36 + 0i$	$-190 + 284i$	$-24 - 269i$	$-178 + 206i$	$-31 - 311i$	$-247 + 59i$
	$m = 0$		$m = 1$		$m = 2$	
	MV	EARSM	MV	EARSM	MV	EARSM
-0.71	$10 + 69i$	$-19 + 0i$	$22 + 19i$	$-79 - 140i$	$3 - 39i$	$-93 - 128i$
	$-13 + 0i$	$-86 + 102i$	$-7 - 86i$	$-90 + 128i$	$-26 - 196i$	$-124 + 255i$
	$-27 + 126i$	$-106 + 0i$	$-13 - 167i$	$-149 + 40i$	$-30 - 76i$	$-214 - 52i$
	$m = 0$		$m = 1$		$m = 2$	
	MV	EARSM	MV	EARSM	MV	EARSM
-1.0	$-7 + 112i$	$-13 + 0i$	$-16 + 81i$	$-65 - 171i$	$-42 - 194i$	$-91 - 100i$
	$-11 + 0i$	$-78 + 0i$	$-23 - 140i$	$-82 + 160i$	$-44 + 8i$	$-103 - 207i$
	$-48 + 0i$	$-82 + 125i$	$-44 + 169i$	$-125 - 79i$	$-62 - 114i$	$-104 + 324i$
	$m = 0$		$m = 1$		$m = 2$	
	MV	EARSM	MV	EARSM	MV	EARSM
-2.0	$40 + 0i$	$-10 + 0i$	$39 - 63i$	$-34 + 192i$	$31 - 122i$	$-44 - 163i$
	$38 + 0i$	$-44 + 0.3i$	$35 - 57i$	$-47 - 49i$	$27 - 111i$	$-49 + 406i$
	$18 + 0i$	$-66 + 0i$	$15 - 64i$	$-60 - 357i$	$5 - 127i$	$-53 - 115i$

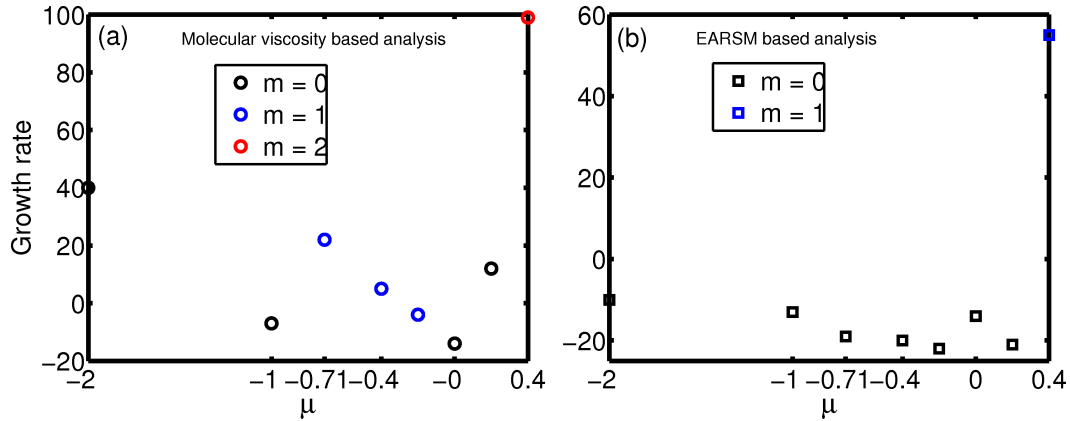


Fig. 6.18 The growth rates of the leading modes predicted by the (a) MV- and (b) EARSM-based analyses. The MV-based analysis predicts co-rotation to be destabilising, which means flows with positive μ should be more intermittent than the $\mu = 0$ flow case. The EARSM-based analysis predicts that small co-rotation ($\mu = 0.2$) is stabilising while the higher co-rotation ($\mu = 0.4$) is destabilising. This means that the flow with small co-rotation should be less intermittent than the $\mu = 0$ case, and the flow with higher co-rotation should be more intermittent than the $\mu = 0$ case. The MV-based analysis predicts counter-rotation to be destabilising except for the $\mu = -1$ case, which means that the flows with higher counter-rotation should be more intermittent except for the $\mu = -1$ flow case. The EARSM based analysis predicts that small counter-rotation is stabilising (up to the $\mu = -0.2$), while higher counter-rotation (up to the $\mu = -1$) is destabilising. Therefore the $\mu = -0.2$ should be less intermittent than the $\mu = 0$ case, and the flows with the $\mu \geq -0.4$ should be more intermittent than the lower negative μ flows. The growth rate for the $\mu = -2$ flow cases are for the primary instability, which means for the formation of Taylor vortices.

Figure 6.19 shows the standard deviation in the torque at the inner (blue squares) and outer (orange rhombuses) cylinders as functions of μ for the $Re_s = 1733$ flow cases. The standard deviation is an indicator of the fluctuations in the torque with respect to the mean torque. The trends of standard deviation in the torque match qualitatively with the trend of growth rates predicted from the MV-based analysis in figure 6.18 (a). Therefore, based on a preliminary comparison with the observations from the DNS data, it again suggests that stability predictions from the MV-based analysis are in a better agreement than those from the EARSM-based analysis.

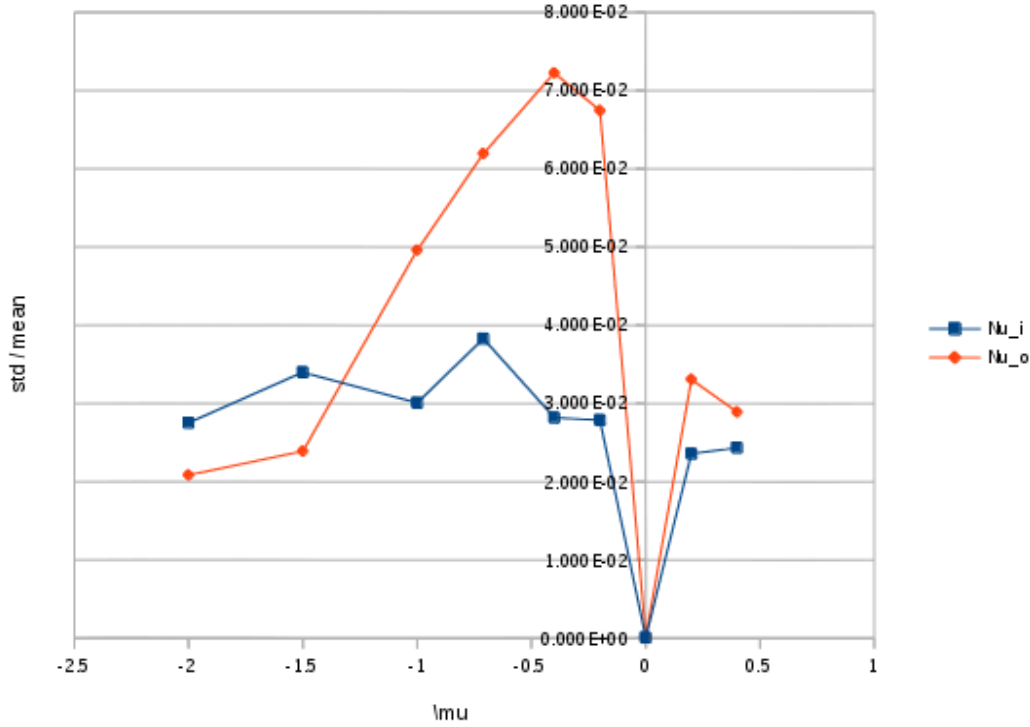


Fig. 6.19 Standard deviation in the torque at the inner (blue squares) and outer (orange rhombuses) cylinders as functions of μ . The standard deviation is an indicator of the fluctuations in the torque with respect to the mean torque. The trends of standard deviation in the torque match qualitatively with the trend of growth rates predicted from the MV-based analysis in figure 6.18 (a). This figure is provided by Mr. Hannes Brauckmann, which is based on the DNS results presented in Ref. [12].

Figures 6.20, 6.21, and 6.22 show the shapes of the leading eigenmodes for the $\mu = 0.2$ and 0.4 cases calculated from the two analyses. The figures show the similarity of eigenmodes from the two analyses. Figures 6.23 and 6.24 show the shapes of the eigenmodes for the $\mu = -0.2, -0.4$, and -0.71 cases calculated from the MV- and EARS-M-based analyses, respectively. The stability results from the two analyses do not have similarities with each other for these cases. Figures 6.25 and 6.26 show the shape of eigenmodes for the $\mu = -1$ and -2 cases, respectively. The stability results from the two analyses again have many similarities. Figure 6.26 shows that stability results for the $\mu = -2$ flow case are for the primary instability, i.e. for the formation of Taylor vortices. Therefore, the results for this flow case cannot be compared with those for the other cases.

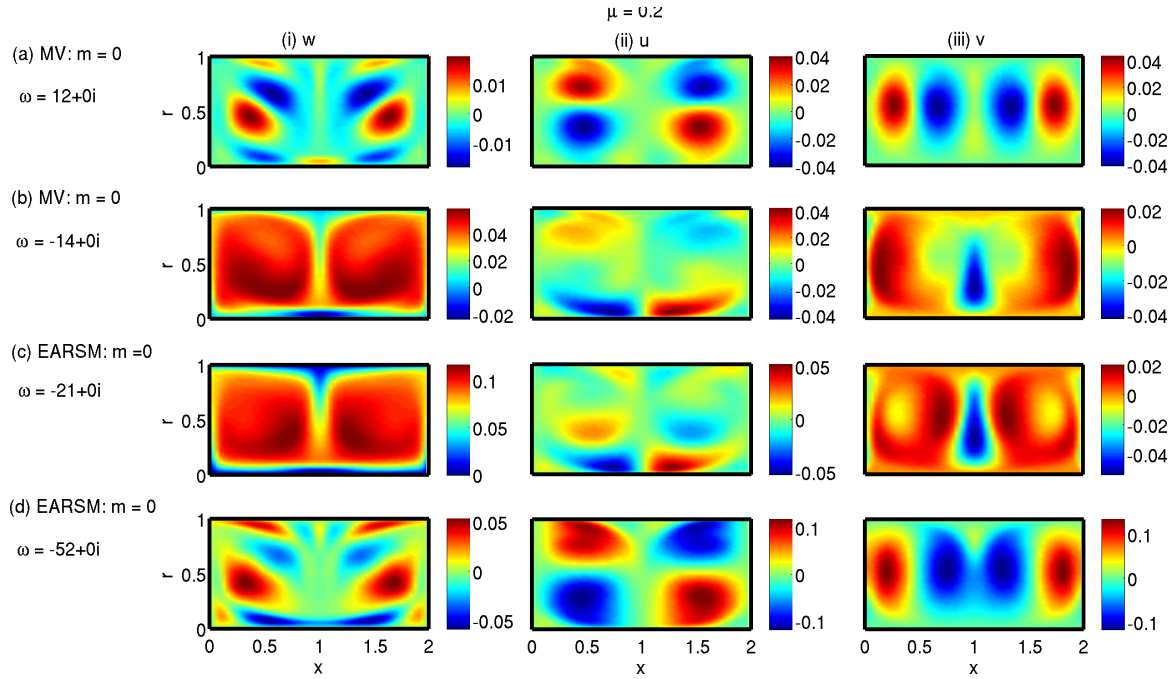


Fig. 6.20 The first two $m = 0$ eigenmodes in the $\mu = 0.2$ flow case calculated from the (a, b) MV- and (c, d) EARSM-based analyses.

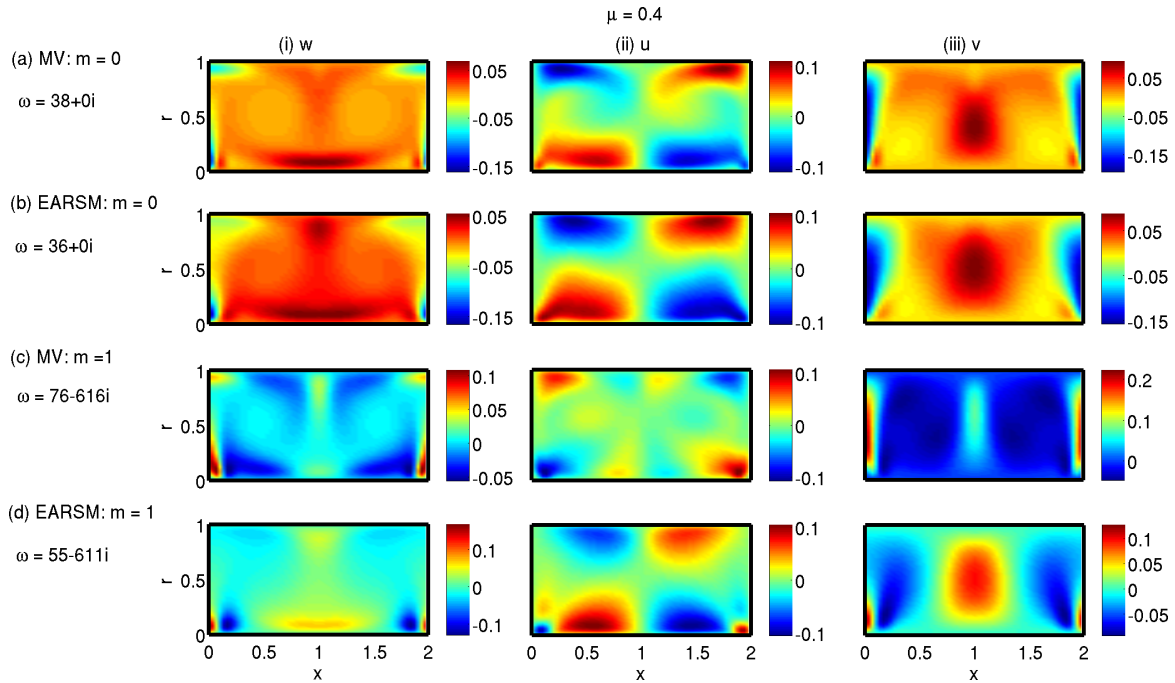


Fig. 6.21 The first eigenmodes in the $\mu = 0.4$ case of the azimuthal wavenumbers (a, b) $m = 0$ and (c, d) $m = 1$ calculated from the (a, c) MV- and (b, d) EARSM-based analyses.

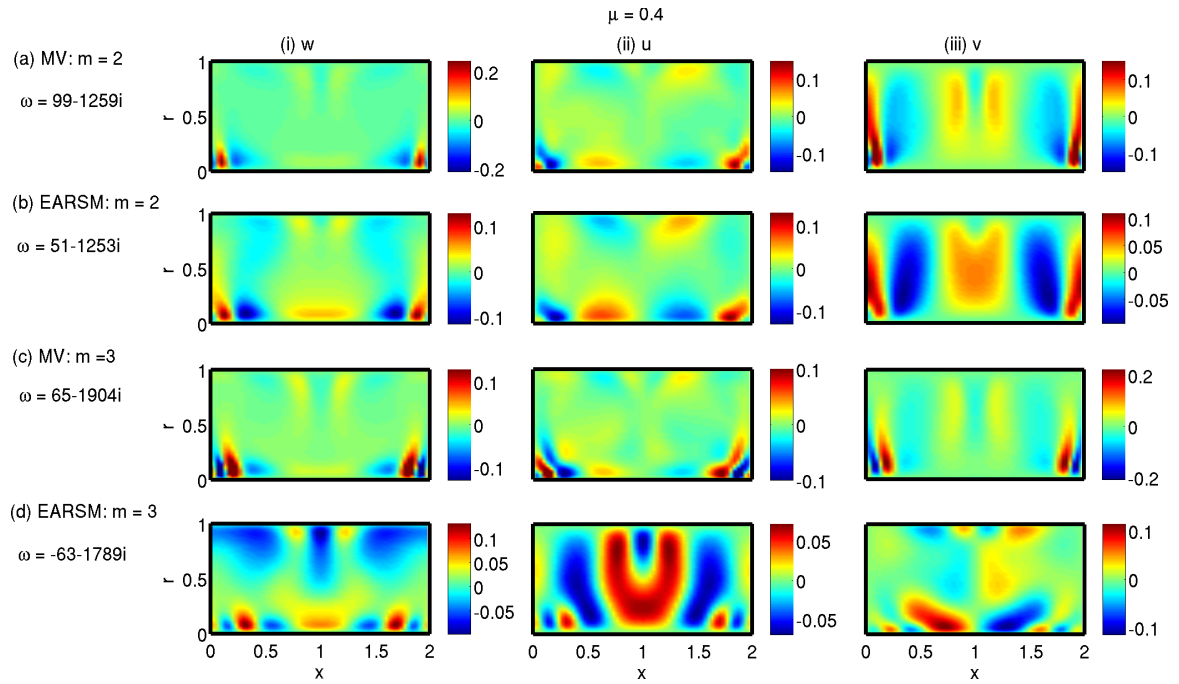


Fig. 6.22 The first eigenmodes in the $\mu = 0.4$ case of the azimuthal wavenumbers (a, b) $m = 2$ and (c, d) $m = 3$ calculated from the (a, c) MV- and (b, d) EARSM-based analyses.

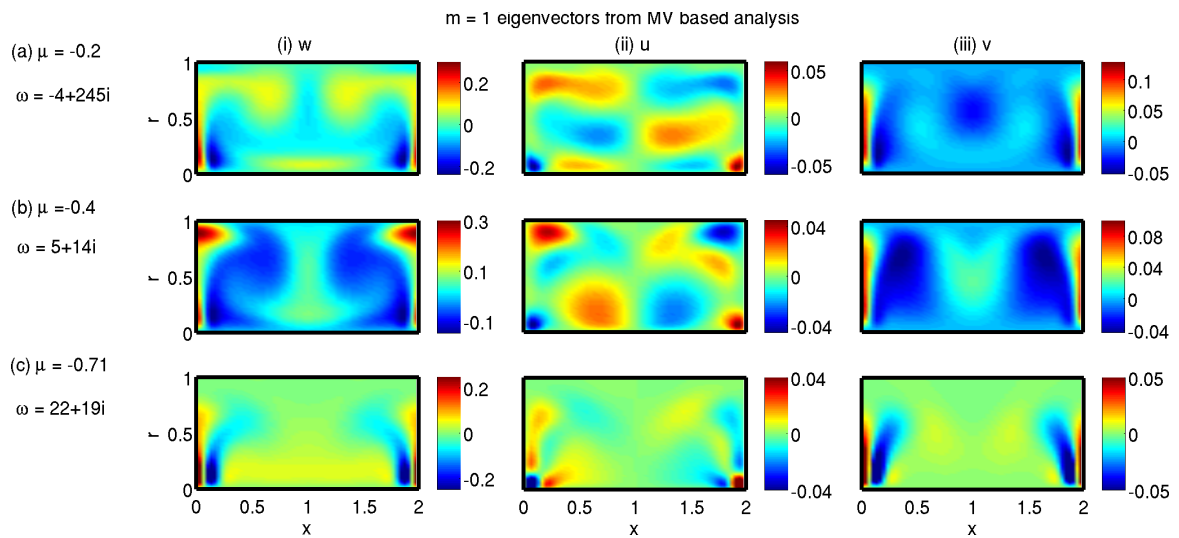


Fig. 6.23 The first $m = 1$ eigenmodes in the (a) $\mu = -0.2$, (b) $\mu = -0.4$, and (c) $\mu = -0.71$ flow cases calculated from the MV based analysis.

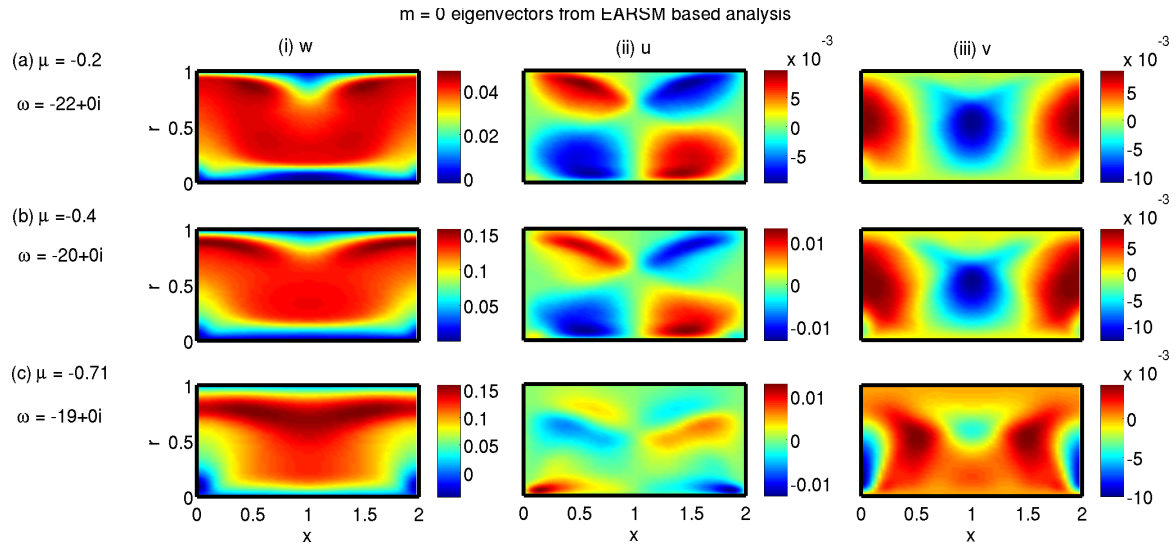


Fig. 6.24 The first $m = 0$ eigenmodes in the (a) $\mu = -0.2$, (b) $\mu = -0.4$, and (c) $\mu = -0.71$ flow cases calculated from the EARSM-based analysis.

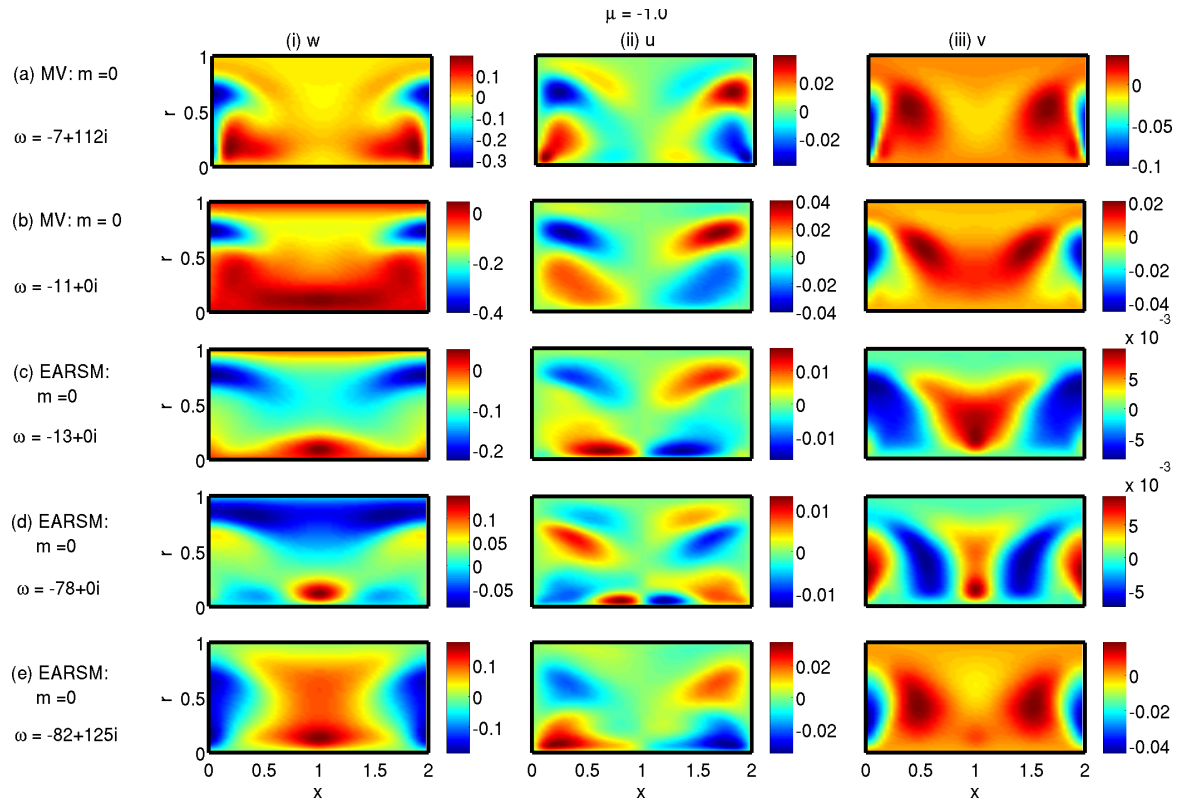


Fig. 6.25 Eigenvectors in the $\mu = -1$ case: (a, b) the first two $m = 0$ eigenmodes calculated from the MV-based analysis, and (c, d, e) the first three $m = 0$ eigenmodes calculated from the EARSM-based analysis.

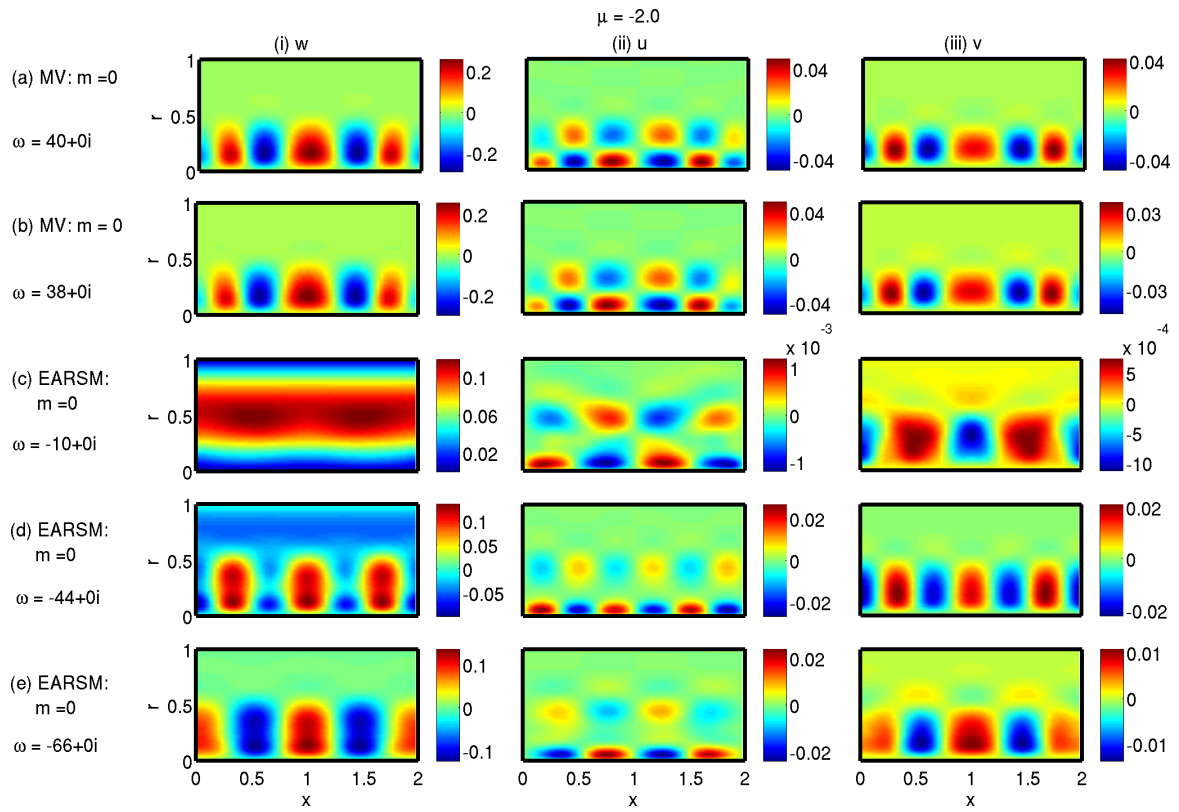


Fig. 6.26 The first few $m = 0$ eigenmodes for the $\mu = -2$ flow case calculated from the MV- and EARSIM-based analyses. The stability results for this case are for the primary instability, i.e for the formation of Taylor vortices.

6.6 Summary and further work

In this chapter, two stability analyses are applied to predict large intermittent turbulent structures over Taylor vortices in flows between two concentric cylinders rotating independently about their axis. The purpose is to discover whether the results from stability analyses, such as growth rate and eigenmodes, are in agreement with the intermittent structures observed from the DNS data, and whether these intermittent structures can be directly linked with the observed fluctuating torque in the flow. The first stability analysis is based on the Navier–Stokes equation linearised over the mean velocity profile. The second stability analysis is based on the RANS equations linearised over the mean velocity and Reynolds stresses profiles, where an EARSM, proposed by Wallin and Johansson (2000) [108], is used to derive the RANS equations.

These stability analyses are applied to the two families of flow cases. The first is with a stationary outer cylinder ($\mu = 0$), and an inner cylinder at various speeds (changing Re_i). On the one hand, the MV-based analysis predicts the flows with higher Re_i should have a higher occurrence of intermittent turbulent structures. On the other hand, the EARSM-based analysis predicts the flows with higher Re_i should have a lower occurrence of intermittent turbulent structures. The second family of flows is the one where the shear Reynolds number (Re_s) is maintained constant for the eight cases of inner and outer cylinder rotation ratios (changing μ). Some conclusions are drawn for the $Re_s = 1733$ flow based on these eight cases. For the co-rotating cases, on the one hand, the MV-based analysis predicts that there should be an increase in intermittency with increasing μ . On the other hand, the EARSM-based analysis predicts that flow should become stabilised for small co-rotation, when μ is changed from 0 to 0.2, then destabilised for the higher co-rotation, when μ is changed from 0.2 to 0.4. For the counter-rotating cases, on the one hand, the MV-based analysis predicts the flow should be more intermittent for higher counter-rotating flows except for the $\mu = -1$ case. On the other hand, the EARSM-based analysis predicts the flow should become stabilised for small counter-rotation, when μ is changed from 0 to -0.2 , then destabilised for the higher counter-rotation.

A preliminary comparison of results from the stability analyses with observation from the DNS data shows that the MV-based analysis is better at predicting the trend of strength of turbulent structures with varying parameters. More thorough comparison of the shapes of the leading eigenmodes from the stability analyses with coherent structures from the DNS, and their precise relation with the torque measurements need to be done. If such comparisons show a conclusive relation between stability analyses results and observed

torque, then an obvious advantage of these stability analyses approaches is that they can be easily extended to the higher Reynolds number flows, where DNS or detailed experimental measurements are not possible. Moreover, these approaches can also give an insight into the physical processes involved in enhancing or reducing the torque.

Chapter 7

Conclusions

Coherent structures in turbulent flows are extracted from analyses that require only the mean velocity and Reynolds stress profiles as input. These are stability analyses over either the linearised Navier–Stokes equations or the linearised RANS equations. In Chapters 2 and 3, the equations are derived, the analyses are explained, and implemented on fully developed turbulent channel flows. In Chapters 4, 5, and 6, these analyses are implemented to extract coherent structures and understand their formation in more complex flows.

7.1 Summary of the work completed

In Chapter 2, linear amplification analysis is performed by linearising the Navier–Stokes equations over the mean velocity profile to extract coherent structures in turbulent channel flow. The use of the linearised equations is justified based on the rapid distortion theory in Refs. [81, 82, 92]. The effect of the neglected nonlinear terms is modelled as the input streamwise wavelengths of the perturbations, where the input values are based on experimental and DNS observations. The most amplified perturbations and the corresponding initial optimal modes from the analysis are interpreted as approximations of coherent structures in fully nonlinear turbulent channel flows. It is acknowledged that modelling the effect of the neglected nonlinear terms as the input streamwise wavelengths is very rudimentary. Nevertheless various kinematic features of the optimal modes and the maxima in energy amplification from the analysis match with those of the observed coherent structures in wall-bounded turbulence DNS and experiments.

The analysis finds three main types of structures in turbulent channel flows. The first type of structures are at the small streamwise wavelengths ($\lambda_x^+ = 200 - 800$) in Section 2.3. These initial and final optimal structures correspond to quasi-streamwise vortices and

near-wall streaks, respectively, and the preferred spanwise wavelength for these structures is found to be equal to one hundred wall-units ($\lambda_z^+|_{peak} \approx 100$ - shown in figure 2.3). This matches well with the observed spanwise spacing of near-wall streaks in experiments [21, 27]. The second type of structures are at the intermediate streamwise wavelengths (from $\lambda_x^+ > 800$ to $\lambda_x < 3$) in Section 2.4.1. These initial and final optimal modes correspond to hairpin vortical and large-scale streaky like structures, respectively, as shown in figures 2.8 and 2.9. The peak in energy amplification in this wavelength range found from the analysis matches well with that from the DNS in Ref. [4]. Various kinematic properties, such as the inclination angle of streaks with the wall and shapes of the streaks, also match with those of large-scale-motions (LSMs) observed in experiments. The third type of structures are at the large streamwise wavelength ($\lambda_x \geq 6$) in Section 2.4.3. The preferred spanwise wavelength of these structures ($\lambda_z|_{peak} \approx 2$), their scaling in outer units, and the fact that they extend to the wall match with the observed features of very-large-scale-motions (VLSMs). All these results show that the most optimal modes obtained from the linearised Navier–Stokes equations, without any turbulence model or eddy viscosity, share many important features (such as their lengths in the homogeneous directions, energy spectra, and shapes) with those of coherent structures in turbulent channel flows.

In Chapter 3, the linearised RANS equations based on a second-order turbulence model, which is explicit algebraic Reynolds stress model (EARSM), are derived. In order to verify the derivation and the associated codes, these equations are applied to an energy amplification analysis in turbulent channel flows in order to find coherent structures. The results from this analysis are compared with those from the eddy viscosity model (EVM)-based analysis derived in this chapter, and also with those of Pujals *et al.* (2009) [2]. The EARSM-based analysis finds that there are two peaks in the transient growth, G_{max} , in the system. A primary peak at the $\lambda_z \approx 4.25$, which scales in outer units, and a secondary peak at the $\lambda_z^+ \approx 170$, which scales in inner units. These results and the shapes of the optimal modes from the EARSM-based analysis match qualitatively with those from the EVM-based analyses. The agreement of the results verifies the derivation and the associated code for the EARSM-based analysis. This analysis is then used in Chapters 5 and 6.

It is also concluded in Chapter 3, that an analysis based on the linearised RANS equations, such as the EVM- and EARSM-based analyses, is better suited for extracting coherent structures that occur at an almost constant frequency, such as vortex shedding behind a cylinder, and not so suitable for extracting coherent structures that occur intermittently, such as streaks and vortices in a turbulent channel flow. The reason for this is based on the derivation for the linearised RANS equations shown in Ref. [76] and Chapter 3, and discussed in

Refs. [4, 98]. The linearised RANS equations are derived for organised wave-perturbations, while intermittent coherent structures are part of the fluctuating perturbations. The intermittent coherent structures, therefore, are not expected to be the solution of the linearised RANS equations.

In Chapter 4, stability analyses based on the linearised Navier–Stokes equations are performed to study the formation of near-wall structures in turbulent pipe flow, and to examine the effect of constant axial rotation of the pipe on their formation. In the first part, the formation of streaks from quasi-streamwise vortices and the effect of constant axial rotation on the formation process are studied. This is done by performing energy amplification analysis based on the Navier–Stokes equations linearised over the mean velocity profile. The effect of the neglected nonlinear terms in this analysis is modelled as the input streamwise wavelengths of the perturbations, as in the analysis in Chapter 2. In the second part, the breakdown instability of streaks, for the formation of quasi-streamwise vortices, and the effect of constant axial rotation on this instability are studied. This is done by performing secondary stability analysis based on the Navier–Stokes equations linearised over the mean velocity profile superimposed with an ideal realisation of the low-speed streaks, such as in Schoppa & Hussain (2002) [11].

It is found from the first part that constant axial rotation causes the widening of streaks, which agree with the observations in Ref. [113], and increases the transient growth, G_{max} , in the system. In laminar flows, rotation is found to be destabilising, which is in accord with this increase in G_{max} . In turbulent flows, however, rotation is found to be stabilising, which is not in accord with this increase in G_{max} . It is found from the second part that constant axial rotation of the pipe has a stabilising role on the breakdown instabilities of streaks, and therefore it prevents the formation of quasi-streamwise vortices. This explains how constant axial rotation causes a reduction in the near-wall structures. In this Chapter, it is shown that simple linear stability analyses, without requiring any turbulence closure model, reproduce many important features of the regeneration cycle of near-wall structures in turbulent pipe flow.

In Chapter 5, approaches based on linearised equations are used to find large hydrodynamic structures in turbulent flows inside gas-turbine injector-combustor systems. These approaches include molecular viscosity based stability analysis, eddy viscosity based stability analysis, and anisotropic eddy viscosity based stability analysis that are derived in Chapter 3. A major assumption in this chapter is that local stability analysis can be applied to the complex flows inside gas-turbine injector-combustor systems. This assumption is based on the success of previous studies on similar flows [123–126].

The motivation behind studying hydrodynamic instabilities and the resultant large-scale coherent structures in gas-turbine flows is for their role in entrainment of fuel into air, which is important for air-fuel mixing at the molecular level for combustion [83–85]. Apart from this desired effect on the air-fuel mixing, hydrodynamic instabilities may also resonate with thermoacoustic oscillations, which can result in dangerously high pressure oscillations in the system. Flows inside gas-turbines are in the turbulent regime and the geometry of gas-turbine systems is usually complicated. This makes studying them computationally expensive, such that DNS is practically impossible and LES is possible only at a few steps in the design process. RANS and URANS solvers are popular methods because they calculate the mean velocity and Reynolds stresses in a turbulent flow in a feasible time as required in the design process. The RANS solvers, however, are usually very dissipative and therefore do not capture hydrodynamic instabilities. The URANS solvers are less dissipative than the RANS solvers, but they can capture only low frequency oscillations. The stability analyses used in the present study require only the mean velocity and Reynolds stress profiles as input and give a quick information on hydrodynamic instabilities in the system.

Based on the results from the stability analyses used in this chapter, it is found that for the flows in gas-turbine systems the inclusion of turbulence models in stability analysis, in order to account for wave-induced fluctuations in the Reynolds stresses, has no significant qualitative effect on the results. This is because these instabilities are driven by regions of high mean shear for which analysis based on the linearised Navier–Stokes equations is sufficient [81, 82]. It is also found that an expansion at the nozzle exit and swirl in the flow are destabilising, and therefore increase hydrodynamic instability.

In Chapter 6, two stability analyses are applied to predict large intermittent turbulent structures over Taylor vortices in flows between two concentric cylinders rotating independently about their axis. The purpose is to find whether the results from stability analyses, such as growth rate and eigenmodes, are in agreement with the intermittent structures observed in DNS, and whether these intermittent structures can be directly linked with the observed fluctuating torque in the flow. The first stability analysis is based on the Navier–Stokes equation linearised over the mean velocity profile, such as in Chapter 2, and is labelled MV-based analysis. The second stability analysis is the EARSM-based analysis derived in Chapter 3, in this chapter an EARSM proposed by Wallin and Johansson (2000) [108] is used. This chapter extends the application of these stability analyses to turbulent flows with the two-dimensional mean velocity profile. The results show that growth rate trend from the MV-based analysis is in good agreement with the trend of torque intermittency in the DNS results.

7.2 Main conclusions

In this thesis various linear amplification analyses are performed on different turbulent flows to find coherent structures. The linear amplification analyses used can be divided into two types. The first is based on the Navier–Stokes equations linearised over the mean velocity profile. The second is based on the RANS equations linearised over the mean velocity and Reynolds stress profiles. This type of analysis requires a turbulence closure model to find the effect of wave-induced perturbations in Reynolds stresses on the stability analysis results. It is concluded that the linearised RANS equations based analyses are not suitable for finding coherent structures that occur intermittently, such as streaks and vortices in wall-bounded turbulence. It is also concluded that the linearised Navier–Stokes equations based analysis finds structures in the region of strong mean shear in the flow that are in good match with the observed coherent structures in fully nonlinear turbulent flows.

7.3 Further work

A major consequence of the results is that the simpler analysis, based on the linearised Navier–Stokes equations, can be used in control applications in place of the EVM-based analysis, such as in Moarref & Jovanovic (2012) [87]. Another consequence is that the linearised Navier–Stokes equations-based analysis can be used for obtaining energy spectra in high Reynolds number turbulent channel and pipe flows, provided that the mean velocity is known for those flows. Work in these directions will justify the work completed in this thesis.

It is also seen that linear stability analysis predicts many useful hydrodynamic instability trends for small changes in operating conditions and system designs in gas-turbine injector-combustor systems, such as expansion at the nozzle exit and swirl in the flow are found to be destabilising. In order to use such tools reliably, it is important to validate the results from the analysis in this study with those from global analysis and experiments or LES or DNS for a number of cases.

Most flows studied in this thesis have only intermittent coherent structures, with the exception of the flows in Chapter 5. In order to see the usefulness of the linearised RANS equations based analysis, it is important to study flows that have coherent structures that occur at almost a constant frequency. Contribution of the constant frequency coherent structure will be in the phase-averaged component of the velocity and pressure fields, as shown in Chapter 3, for which the linearised RANS equations are derived.

References

- [1] K. M. Butler and B. F. Farrell. Optimal perturbations and streak spacing in wall-bounded turbulent shear flow. *Phys. Fluid A*, 5:774–777, 1993.
- [2] G. Pujals, M. Garcia-Villalba, C. Cossu, and S. Depardon. A note on optimal transient growth in turbulent channel flows. *Phys. Fluids*, 21(015019), 2009.
- [3] S. Hoyas and J. Jimenez. Scaling of the velocity fluctuations in turbulent channels up to $Re_\tau = 2003$. *Phys. Fluids*, 18(011702), 2006.
- [4] J. Jimenez. Localized amplification of energy in turbulent channels. *Center for turbulence research: Annual Research Briefs*, pages 1423–433, 2009.
- [5] B. J. McKeon and A. S. Sharma. A critical-layer framework for turbulent pipe flow. *J. Fluid Mech.*, 658:336–382, 2010.
- [6] M. Guala, S. E. Hommema, and R. J. Adrian. Large-scale and very-large-scale motions in turbulent pipe flow. *J. Fluid Mech.*, 554:521–542, 2006.
- [7] D. J. C. Dennis and T. B. Nickels. Experimental measurement of large-scale three-dimensional structures in a turbulent boundary layer. part 2. long structures. *J. Fluid Mech.*, 673:218–244, 2011.
- [8] J. Jimenez, J. C. Del-Alamo, and O. Flores. The large-scale dynamics of near-wall turbulence. *J. Fluid Mech.*, 505:179–199, 2004.
- [9] J. Jimenez and S. Hoyas. Turbulent fluctuations above the buffer layer in wall-bounded flows. *J. Fluid Mech.*, 611:215–236, 2008.
- [10] J. C. del Alamo and J. Jimenez. Linear energy amplification in turbulent channels. *J. Fluid Mech.*, 559:205–213, 2006.
- [11] W. Schoppa and F. Hussain. Coherent structure generation in near-wall turbulence. *J. Fluid Mech.*, 453:57–108, 2002.
- [12] H. Brauckmann and B. Eckhardt. Direct numerical simulations of local and global torque in Taylor-Couette flow up to $Re = 30000$. *J. Fluid Mech.*, 718:398–427, 2013.
- [13] A. K. M. Fazle Hussain. Coherent structures and turbulence. *J. Fluid Mech.*, 173:303–356, 1986.
- [14] R. J. Adrian. Hairpin vortex organization in wall turbulence. *Phys. Fluids*, 19(041301), 2007.

- [15] J. Laufer. Deterministic and stochastic aspects of turbulence. *J. Appl. Mech.*, 50 (4b): 1079–1085, 1983.
- [16] G. M. Corcos and F. S. Sherman. The mixing layer: deterministic models of a turbulent flow. part 1. introduction and the two-dimensional flow. *J Fluid Mech.*, 139: 29–65, 1984.
- [17] G. M. Corcos and F. S. Sherman. The mixing layer: deterministic models of a turbulent flow. part 2. the origin of the three-dimensional motion. *J Fluid Mech.*, 139: 29–65, 1984.
- [18] A. A. Townsend. *The Structure of Turbulent Shear Flow*. Cambridge University Press, Cambridge, UK, 1976.
- [19] A. A. Townsend. The structure of the turbulent boundary layer. *Mathematical Proceedings of the Cambridge Philosophical Society*, 47:375–395, 1951.
- [20] H. L. Grant. The large eddies of turbulent motion. *J Fluid Mech.*, 4:149–190, 1958.
- [21] S. J. Kline, W. C. Reynolds, F. A. Schraub, and P. W. Runstadler. The structure of turbulent boundary layers. *J. Fluid Mech.*, 30:741–773, 1967.
- [22] A. K. Gupta, J. Laufer, and R. E. Kaplan. Spatial structure in the viscous sublayer. *J Fluid Mech.*, 50:493–512, 1971.
- [23] M. K. Lee, L. D. Eckelman, and T. J. Hanratty. Identification of turbulent wall eddies through the phase relation of the components of the fluctuating velocity gradient. *J. Fluid Mech.*, 66:17–33, 1974.
- [24] B. U. Achia and D. W. Thompson. Structure of the turbulent boundary in drag-reducing pipe flow. *J. Fluid Mech.*, 81:439–464, 1977.
- [25] D. K. Oldaker and W. G. Tiederman. Spatial structure in the viscous sublayer in drag-reducing channel flows. *Phys. Fluids*, 20:S133, 1977.
- [26] H. Nakagawa and I. Nezu. Structure of space-time correlations of bursting phenomena in an open-channel flow. *J. Fluid Mech.*, 104:1–43, 1981.
- [27] C. R. Smith and S. P. Metzler. The characteristics of low-speed streaks in the near-wall region of a turbulent boundary layer. *J. Fluid Mech.*, 129:27–54, 1983.
- [28] T. Theodorsen. Mechanics of turbulence. In *2nd Midwest. Conf. Fluid Mech.*, pages 353–375, Ohio State University, Columbus, 1952.
- [29] M. R. Head and P. Bandyopadhyay. New aspects of turbulent boundary-layer structure. *J Fluid Mech.*, 107:297–338, 1981.
- [30] D. J. C. Dennis and T. B. Nickels. Experimental measurement of large-scale three-dimensional structures in a turbulent boundary layer. part 1. vortex packets. *J Fluid Mech.*, 673:180–217, 2011.
- [31] R. E. Falco. Coherent motions in the outer region of turbulent boundary layers. *Phys. Fluids*, 20(S124), 1977.

- [32] K. C. Kim and R. J. Adrian. Very large-scale motion in the outer layer. *Phys. Fluids*, 11:417–422, 1999.
- [33] J. Zhou, R. J. Adrian, S. Balachandar, and T. M. Kendall. Mechanism for generating coherent packets of hairpin vortices in channel flow. *J. Fluid Mech.*, 387:353–396, 1999.
- [34] J. P. Monty, N. Hutchins, H. C. H. Ng, I. Marusic, and M. S. Chong. A comparison of turbulent pipe, channel and boundary layer flows. *J. Fluid Mech.*, 632:431–442, 2009.
- [35] S. C. C. Bailey and A. J. Smits. Experimental investigation of the structure of large- and very-large-scale motions in turbulent pipe flow. *J. Fluid Mech.*, 651:339–356, 2010.
- [36] N. Hutchins and I. Marusic. Evidence of very long meandering features in the logarithmic region of turbulent boundary layers. *J. Fluid Mech.*, 579:1–28, 2007.
- [37] J. P. Monty, J. A. Stewart, R. C. Williams, and M. S. Chong. Large-scale features in turbulent pipe and channel flows. *J. Fluid Mech.*, 589:147–156, 2007.
- [38] J. Lee, J. H. Lee, J. Choi, and H. J. Sung. Spatial organization of large- and very-large-scale motions in a turbulent channel flow. *J. Fluid Mech.*, 749:818–840, 2014.
- [39] B. J. Cantwell. Organized motion in turbulent flow. *Ann. Rev. Fluid Mech.*, 13: 457–515, 1981.
- [40] S. K. Robinson. Coherent motions in the turbulent boundary layer. *Ann. Rev. Fluid Mech.*, 23:601–639, 1991.
- [41] M. GaD el Hak and P. R. Bandyopadhyay. Reynolds number effects in wall-bounded turbulent flows. *Appl. Mech. Rev.*, 47:307–365, 1994.
- [42] R. L. Panton. Overview of the self-sustaining mechanisms of wall turbulence. *Progress in Aero. Sci.*, 37:341–383, 2001.
- [43] A. J. Smits, B. J. McKeon, and I. Marusic. High-reynolds number wall turbulence. *Ann. Rev. Fluid Mech.*, 43:353–375, 2011.
- [44] S. C. Crow and F. H. Champagne. Orderly structure in jet turbulence. *J. Fluid Mech.*, 48:547–591, 1971.
- [45] D. Coles. Prospects for useful research on coherent structure in turbulent shear flow. *Proc. Indian Acad. Sci. (Engg. Sci.)*, 4:111–127, 1981.
- [46] G. L. Brown and A. Roshko. On density effects and large structure in turbulent mixing layers. *J. Fluid Mech.*, 64:775–816, 1974.
- [47] C. M. Ho and P. Huerre. Perturbed free shear layers. *Ann. Rev. Fluid Mech.*, 16: 365–424, 1984.
- [48] G. Kawahara, M. Uhlmann, and L. van Veen. The significance of simple invariant solutions in turbulent flows. *Ann. Rev. Fluid Mech.*, 44:203–225, 2012.

- [49] J. Jimenez. Coherent structures and dynamical systems. *Center for Turbulence Research: Proceedings of the 1987 Summer Program*, pages 323–324, 1987.
- [50] M. Nagata. Three-dimensional finite-amplitude solutions in plane Couette flow: bifurcation from infinity. *J. Fluid Mech.*, 217:519–527, 1990.
- [51] J. Jimenez and M. P. Simens. Low-dimensional dynamics in a turbulent wall flow. *J. Fluid Mech.*, 435:81–91, 2001.
- [52] T. Itano and S. Toh. The dynamics of bursting process in wall turbulence. *J. Phys. Soc. Jpn.*, 70:703–716, 2001.
- [53] F. Waleffe. Three-dimensional coherent states in plane shear flows. *Phys. Rev. Lett.*, 81:4140–4143, 1998.
- [54] F. Waleffe. Exact coherent structures in channel flow. *J. Fluid Mech.*, 435:93–102, 2001.
- [55] H. Wedin and R. R. Kerswell. Exact coherent structures in pipe flow: travelling wave solutions. *J. Fluid Mech.*, 508:333–371, 2004.
- [56] B. Eckhardt, T. M. Schneider, B. Hof, and J. Westerweel. Turbulent transition in pipe flow. *Ann. Rev. Fluid Mech.*, 39:447–468, 2007.
- [57] J. F. Gibson, J. Halcrow, and P. Cvitanovic. Equilibrium and travelling-wave solutions of plane Couette flows. *J. Fluid Mech.*, 638:243–266, 2009.
- [58] T. Itano and S. C. Generalis. Hairpin vortex solution in planar Couette flow: A tapestry of knotted vortices. *Phys. Rev. Lett.*, 102:114501, 2009.
- [59] S. Okino, M. Nagata, H. Wedin, and A. Bottaro. A new nonlinear vortex state in square-duct flow. *J. Fluid Mech.*, 657:413–429, 2010.
- [60] R. M. Clever and F. H. Busse. Three-dimensional convection in a horizontal fluid layer subjected to a constant shear. *J. Fluid Mech.*, 234:511–527, 1992.
- [61] G. Kawahara and S. Kida. Periodic motion embedded in plane Couette turbulence: regeneration cycle and burst. *J. Fluid Mech.*, 449:291–300, 2001.
- [62] D. Viswanath. Recurrent motions within plane Couette turbulence. *J. Fluid Mech.*, 580:339–358, 2007.
- [63] Y. Duguet, C. C. Pringle, and R. R. Kerswell. Relative periodic orbits in transitional pipe flow. *Phys. Fluids*, 20:114102, 2008.
- [64] A. S. Sharma and B. J. McKeon. On coherent structures in wall turbulence. *J. Fluid Mech.*, 728:196–238, 2013.
- [65] R. Moarref, A. S. Sharma, J. A. Tropp, and B. J. McKeon. Model-based scaling of the streamwise energy density in high-reynolds-number turbulent channels. *J. Fluid Mech.*, 734:275–316, 2013.

- [66] Y. Hwang and C. Cossu. Amplification of coherent streaks in the turbulent Couette flow: an input-output analysis at low Reynolds number. *J Fluid Mech.*, 643:333–348, 2010.
- [67] Y. Hwang and C. Cossu. Linear non-normal energy amplification of harmonic and stochastic forcing in the turbulent channel flow. *J Fluid Mech.*, 664:51–73, 2010.
- [68] A. Willis, Y. Hwang, and C. Cossu. Optimally amplified large-scale streaks and drag reduction in turbulent pipe flow. *Physical Review E*, 82(036321), 2010.
- [69] K. M. Bobba. *Robust flow stability: Theory, computations and experiments in near wall turbulence*. PhD thesis, California Institute of Technology, May 2004.
- [70] M. R. Jovanovic and B. Bamieh. Componentwise energy amplification in channel flows. *J. Fluid Mech.*, 534:145–183, 2005.
- [71] P. J. Schmid. Nonmodal stability theory. *Ann. Rev. Fluid Mech.*, 39:129–162, 2007.
- [72] W. V. R. Malkus. Outline of a theory of turbulent shear flow. *J. Fluid Mech.*, 1: 521–539, 1956.
- [73] S. I. Chernyshenko and M. F. Baig. The mechanism of streak formation in near-wall turbulence. *J Fluid Mech.*, 544:99–131, 2005.
- [74] T. Suzuki and T. Colonius. Instability waves models in a subsonic round jet detected using a near-field phased microscopic array. *J Fluid Mech.*, 565:197–226, 2006.
- [75] K. Gudmundsson and T. Colonius. Instability wave models for the near-field fluctuations of turbulent jets. *J Fluid Mech.*, 689:97–128, 2011.
- [76] W. C. Reynolds and A. K. M. F. Hussain. The mechanics of an organized wave in turbulent shear flow. part 3. theoretical models and comparisons with experiments. *J. Fluid Mech.*, 54:263–288, 1972.
- [77] J. D. Crouch, A. Garbaruk, and D. Magidov. Predicting the onset of flow unsteadiness based on global instability. *J Comp. Phys.*, 224:924–940, 2007.
- [78] J. D. Crouch, A. Garbaruk, D. Magidov, and Travin. Origin of transonic buffet on aerofoils. *J Fluid Mech.*, 628:357–369, 2009.
- [79] C. Cossu, G. Pujals, and S. Depardon. Optimal transient growth and very large-scale structures in turbulent boundary layers. *J Fluid Mech.*, 619:79–94, 2009.
- [80] C. Mettot, F. Renac, and D. Sipp. Computation of eigenvalue sensitivity to base flow modifications in a discrete framework: Application to open-loop control. *J Comp. Phys. (in press)*, 2014.
- [81] J.C.R. Hunt and D.J. Carruthers. Rapid distortion theory and the ‘problems’ of turbulence. *J. Fluid Mech.*, 212:497–532, 1990.
- [82] M. J. Lee, J. Kim, and P. Moin. Structure of turbulence at high shear rate. *J. Fluid Mech.*, 216:561–583, 1990.

- [83] J. E. Broadwell and R. E. Breidenthal. A simple model of mixing and chemical reaction in a turbulent shear layer. *J Fluid Mech.*, 125:397–410, 1982.
- [84] H. Aref and S. W. Jones. The fluid mechanics of stirring and mixing. *Phys. Fluids A*, 1(470), 1989.
- [85] K. Midgley. *An isothermal experimental study of the unsteady fluid mechanics of gas turbine fuel injector flow fields*. PhD thesis, Loughborough University, UK, 2005.
- [86] K. R. McManus, T. Poinso, and S. M. Candel. A review of active control of combustion instabilities. *Prog. Energy Combust. Sci.*, 19:1–29, 1993.
- [87] R. Moarref and M. R. Jovanovic. Model-based design of transverse wall oscillations for turbulence drag reduction. *J Fluid Mech.*, 707:205–240, 2012.
- [88] P. Meliga, G. Pujals, and E. Serre. Sensitivity of 2-d turbulent flow past a d-shaped cylinder using global stability. *Phys. Fluids*, 24:061701, 2012.
- [89] V. Parezanovic and O. Cadot. Experimental sensitivity analysis of the global properties of two-dimensional turbulent wake. *J Fluid Mech.*, 693:115–149, 2012.
- [90] A. S. Sharma, J. F. Morrison, B. J. McKeon, D. J. N. Limebeer, W. H. Koberg, and S. J. Sherwin. Relaminarisation of $Re_\tau = 100$ channel flow with globally stabilising linear feedback control. *Phys. Fluids*, 23:125105, 2011.
- [91] J. Kim and T. Bewley. A linear systems approach to flow control. *Ann. Rev. Fluid Mech.*, 39(383–417), 2007.
- [92] J. Jimenez. How linear is wall-bounded turbulence? *Phys. Fluids*, 25:110814, 2013.
- [93] J. Kim and J. Lim. A linear process in wall-bounded turbulence shear flows. *Phys. Fluids Letters*, 12(8), 2000.
- [94] J. M. Hamilton, J. Kim, and F. Waleffe. Regeneration mechanisms of near-wall turbulence structures. *J Fluid Mech.*, 287:317–348, 1995.
- [95] S. Pirozzoli, M. Bernardini, and F. Grasso. Characterization of coherent vortical structures in a supersonic turbulent boundary layer. *J Fluid Mech.*, 613:205–231, 2008.
- [96] J. Jimenez and A. Pinelli. The autonomous cycle of near-wall turbulence. *J. Fluid Mech.*, 389:335–359, 1999.
- [97] J. Jimenez and P. Moin. The minimal flow unit in near-wall turbulence. *J. Fluid Mech.*, 225:213–240, 1991.
- [98] O. Blesbois, S. I. Chernyshenko, E. Touber, and M. A. Leschziner. Pattern prediction by linear analysis of turbulent flow with drag reduction by wall oscillation. *J Fluid Mech.*, 724:607–641, 2013.
- [99] L. N. Trefethen. *Spectral Methods in Matlab*. SIAM, Philadelphia, US, 2000.

- [100] S. C. Reddy and D. S. Henningson. Energy growth in viscous channel flows. *J. Fluid Mech.*, 252:209–238, 1993.
- [101] J. C. del Alamo, J. Jimenez, P. Zandonade, and R. D. Moser. Scaling of the energy spectra of turbulent channels. *J Fluid Mech.*, 500:135–144, 2004.
- [102] M. Bernardini, S. Pirozzoli, and P. Orlandi. Velocity statistics in turbulent channel flow up to $Re_\tau = 4000$. *J Fluid Mech.*, 742:171–191, 2014.
- [103] S. B. Pope. A more general effective-viscosity hypothesis. *J. Fluid Mech.*, 72:331–340, 1975.
- [104] J. V. Boussinesq. Theorie de l’ecoulement turbulent. page 46, 1877.
- [105] Stephen B. Pope. *Turbulent Flows*. Cambridge University Press, Cambridge, UK, 2000.
- [106] A. Hellsten and S. Wallin. Explicit algebraic Reynolds stress and non-linear eddy-viscosity models. *Int. J. Comp. Fluid Dynamics*, 23:349–361, 2009.
- [107] T. B. Gatski and C. G. Speziale. On explicit algebraic stress models for complex turbulent flows. *J Fluid Mech.*, 254:59–78, 1993.
- [108] S. Wallin and A. Johansson. An explicit algebraic Reynolds stress model for incompressible and compressible turbulent flows. *J. Fluid Mech.*, 403:89–132, 2000.
- [109] M. J. Walsh. Riblets as a viscous drag reduction technique. *AIAA Journal*, 21(4): 485–486, 1983.
- [110] H. Choi, P. Moin, and J. Kim. Active turbulence control for drag reduction wall-bounded flows. *J. Fluid Mech.*, 262:75–110, 1994.
- [111] C. Mettot, D. Sipp, and H. Bezaud. Quasi-laminar stability and sensitivity analyses for turbulent flows: prediction of low-frequency unsteadiness and passive control. *Phys. Fluids (in preparation)*, 2014.
- [112] B. P. M. van Esch and J. G. M. Kuerten. Direct numerical simulation of motion of particles in rotating pipe flow. *Journal of Turbulence*, 9, 2008.
- [113] P. Orlandi and M. Fatica. Direct simulations of turbulent flow in a pipe rotating about its axis. *J. Fluid Mech.*, 343:343–372, 1997.
- [114] W. J. Jung and R. Akhavan. Suppression of turbulence in wall-bounded flows by high-frequency spanwise oscillations. *Phys. Fluids*, 4:1605, 1992.
- [115] K. S. Choi and M. Graham. Drag reduction of turbulent pipe flows by circular-wall oscillations. *Phys. Fluids*, 10:7, 1998.
- [116] W. Schoppa and F. Hussain. A large-scale control strategy for drag reduction in turbulent boundary layers. *Phys. Fluids*, 10:1049, 1998.
- [117] G. Iuso, M. Ontario, P. G. Spazzini, and G. M. di Cicca. Wall turbulence manipulation by large-scale streamwise vortices. *J. Fluid Mech.*, 473:23–58, 2002.

- [118] F. Waleffe and J. Kim. How streamwise rolls and streaks self-sustain in a shear flow: Part 2. *AIAA paper*, 1998.
- [119] G. Reich and H. Beer. Fluid flow and heat transfer in axially rotating pipe 1. effect of rotation on turbulent pipe flow. *Int. J. Heat and Mass Transfer*, 32:551–561, 1989.
- [120] K. Kikuyama, M. Murakami, and K. Nishibori. Development of three-dimensional turbulent boundary layer in an axially rotating pipe. *ASME J. Fluids Engineering*, 105:154–160, 1983.
- [121] K. Kikuyama, M. Murakami, K. Nishibori, and K. Maeda. Flow in an axially rotating pipe (a calculation of flow in the saturated region). *Bull. JSME*, 25:506–513, 1983.
- [122] M. Asai, M. Minagawa, and M. Nishioka. The instability and breakdown of a near-wall low-speed streak. *J Fluid Mech.*, 455:289–314, 2002.
- [123] S. J. Rees. *Hydrodynamic instability of confined jets & wakes & implications for gas turbine fuel injectors*. PhD thesis, Department of Engineering, University of Cambridge, July 2009.
- [124] K. Oberleithner, M. Sieber, C. Nayeri, C. O. Paschereit, C. Petz, H.-C. Hege, B. Noack, and I. Wygnanski. Three-dimensional coherent structures in a swirling jet undergoing vortex breakdown: stability analysis and empirical mode construction. *J. Fluid Mech.*, 679:383–414, 2011.
- [125] M. Juniper. Absolute and convective instability in gas turbine fuel injectors. *Proceedings of ASME Turbo Expo*, GT2011:68253, 2012.
- [126] K. Oberleithner, S. Terhaar, L. Rukes, and C. O. Paschereit. Why non-uniform density suppresses the precessing vortex core. *Proceedings of ASME Turbo Expo*, GT2013:95509, 2013.
- [127] N. Syred. A review of oscillation mechanisms and the role of the precessing vortex core (pvc) in swirl combustion systems. *Progress in Energy and Combustion Science*, 32:93–161, 2006.
- [128] S. Chakravarthy, O. Shreenivasan, B. Boehm, A. Dreizler, and J. Janicka. Experimental characterization of onset of acoustic instability in a nonpremixed half-dump combustor. *J. Acoust. Soc. Am.*, (122 (1)):120, 2007.
- [129] M. Juniper, L. Li, and J. Nichols. Forcing of self-excited round jet diffusion flames. *Proc. Comb. Inst.*, 32 (1):1191–1198, 2008.
- [130] P. Huerre and P. Monkewitz. Local and global instabilities in spatially developing flows. *Annu. Rev. Fluid Mech.*, 22:473–537, 1990.
- [131] W. D. Q. Bainbridge. *The numerical simulation of oscillation in gas turbine combustion chambers*. PhD thesis, Department of Engineering, University of Cambridge, August 2013.
- [132] A. J. Chorin. Numerical solution of navier–stokes equations. *Mathematics of Computation*, 22:745–762, 1968.

- [133] L. Lesshafft and P. Huerre. Linear impulse response in hot round jets. *Phys. Fluids*, 19:024102–1–11, 2007.
- [134] M. Ruith, P. Chen, E. Meiburg, and T. Maxworthy. Three-dimensional vortex breakdown in swirling jets and wakes: direct numerical simulation. *J. Fluid Mech.*, 486: 331–378, 2003.
- [135] S. Hochgreb, D. Dennis, I. Ayranci, W. Bainbridge, and S. Cant. Forced and self-excited instabilities from lean premixed, liquid-fuelled aeroengine injectors at high pressures and temperatures. *Proceedings of ASME Turbo Expo*, GT2013:9531, 2013.
- [136] A. Mallock. Determination of the viscosity of water. *Proc. R. Soc. Lond. A*, 45: 126–132, 1888.
- [137] M. Couette. Etudes sur le frottement des liquides. *Ann. Chim. Phys.*, 21:433, 1890.
- [138] G. I. Taylor. Stability of viscous liquid contained between two rotating cylinders. *Phil. Trans. R. Soc. Lond. A*, 223:289, 1923.
- [139] C. D. Andereck, S. S. Liu, and H. L. Swinney. Flow regimes in a circular Couette system with independently rotating cylinders. *J Fluid Mech.*, 164:155–183, 1986.
- [140] P. Bradshaw. The analogy between streamline curvature and buoyancy in turbulent shear flow. *J Fluid Mech.*, 36, part 1:177–191, 1969.
- [141] B. Eckhardt, S. Grossmann, and D. Lohse. Torque scaling in turbulent Taylor-Couette flow between independently rotating cylinders. *J Fluid Mech.*, 581:221–250, 2007.
- [142] D. Haim and L. M. Pismen. Performance of photochemical reactor in the regime of Taylor-Görtler vortical flow. *Chem. Engng. Sci.*, 49 (8):1119–1129, 1994.
- [143] D. P. Lathrop, J. Fineberg, and H. S. Swinney. Turbulent flow between concentric rotating cylinders at large Reynolds numbers. *Phys. Rev. Lett.*, 68:1515–1518, 1992.
- [144] D. P. M. van Gils, S. G. Huisman, S. Grossmann, C. Sun, and D. Lohse. Optimal Taylor-Couette turbulence. *J Fluid Mech.*, 706:118–149, 2012.
- [145] H. Brauckmann and B. Eckhardt. Intermittent boundary layers and torque maxima in Taylor-Couette flow. *Phys. Rev. E*, 87:033004, 2013.
- [146] R. Ostilla, R. J. A. M. Stevens, S. Grossmann, R. Verzico, and D. Lohse. Optimal Taylor-Couette turbulence: direct numerical simulations. *J Fluid Mech.*, 719:14–46, 2013.

Appendix A

Linear perturbation equations for secondary instability

This appendix presents the linearised continuity and momentum equations for the secondary instability analysis for flow in a pipe rotating around its own axis.

The mean flow profile, which represents an idealised realisation of low-speed streaks, is:

$$\begin{aligned} U(r, \theta) &= U_0(r) + \frac{\Delta u_o}{2} \cos(M\theta)g(r) \\ V &= 0, \quad W(r) = W_0(r) \\ g(r) &= (1-r) \exp\left(-\eta(1-r)^2\right) = y \exp(-\eta y^2), \quad \text{where } y = 1-r. \end{aligned}$$

where η is such that the function $g(r)$ has a plateau at $y^+ \approx 20$, and M represents the azimuthal spacing of the streaks as: $\lambda_z^+ = \frac{2\pi}{M} Re_\tau$, and $\Omega_y|_{max} = 0.5M\Delta u_o$ represents the strength of a streak.

The linear perturbations in the velocity and pressure are decomposed as:

$$\begin{aligned}
 u &= \sum_{n=0}^N [u_{nv}(r) \cos(nM\theta) + u_{ns}(r) \sin(nM\theta)] \\
 v &= \sum_{n=0}^N [v_{nv}(r) \cos(nM\theta) + v_{ns}(r) \sin(nM\theta)] \\
 w &= \sum_{n=0}^N [w_{nv}(r) \sin(nM\theta) + w_{ns}(r) \cos(nM\theta)] \\
 p &= \sum_{n=0}^N [p_{nv}(r) \cos(nM\theta) + p_{ns}(r) \sin(nM\theta)] \\
 (u', v', w', p') &= (u, v, w, p) \exp(-i\omega t + ikx)
 \end{aligned}$$

The linearised continuity and momentum equations for the secondary stability analysis are given below.

$$iku_{ns} + \frac{1}{r} \frac{\partial}{\partial r} (rv_{ns}) - nMw_{ns} = 0, \quad iku_{nv} + \frac{1}{r} \frac{\partial}{\partial r} (rv_{nv}) + nMw_{nv} = 0, \quad iku_{0v} + \frac{1}{r} \frac{\partial}{\partial r} (rv_{0v}) = 0 \quad (\text{A.1})$$

$$\begin{aligned}
 -i\omega u_{ns} &= -\frac{dU_o}{dr} v_{ns} - \frac{\Delta u_o}{4} \frac{dg}{dr} (v_{(n+1)s} + v_{(n-1)s}) + M \frac{\Delta u_o}{4} \frac{g}{r} (w_{(n-1)s} T_n - w_{(n+1)s}) - ikU_o u_{ns} - ikp_{ns} \\
 &\quad - ik \frac{\Delta u_o}{4} g (u_{(n-1)s} + u_{(n+1)s}) + \frac{1}{Re} \left[\frac{1}{r} \frac{\partial}{\partial r} \left(r \frac{\partial}{\partial r} \right) - \frac{n^2 M^2}{r^2} - k^2 \right] u_{ns} + nM \frac{W_o}{r} u_{nv} \\
 -i\omega u_{nv} &= -\frac{dU_o}{dr} v_{nv} - \frac{\Delta u_o}{4} \frac{dg}{dr} (v_{(n+1)v} + v_{(n-1)v} T_n) + M \frac{\Delta u_o}{4} \frac{g}{r} (w_{(n+1)v} - w_{(n-1)v}) - ikU_o u_{nv} - ikp_{nv} \\
 &\quad - ik \frac{\Delta u_o}{4} g (u_{(n-1)v} T_n + u_{(n+1)v}) + \frac{1}{Re} \left[\frac{1}{r} \frac{\partial}{\partial r} \left(r \frac{\partial}{\partial r} \right) - \frac{n^2 M^2}{r^2} - k^2 \right] u_{nv} - nM \frac{W_o}{r} u_{ns} \\
 -i\omega u_{0v} &= -\frac{dU_o}{dr} v_{0v} - \frac{\Delta u_o}{4} \frac{dg}{dr} v_{1v} + M \frac{\Delta u_o}{4} \frac{g}{r} w_{1v} - ikU_o u_{0v} - ikp_{0v} - ik \frac{\Delta u_o}{4} g u_{1v} \\
 &\quad + \frac{1}{Re} \left[\frac{1}{r} \frac{\partial}{\partial r} \left(r \frac{\partial}{\partial r} \right) - k^2 \right] u_{0v} \quad (\text{A.2})
 \end{aligned}$$

$$\begin{aligned}
-i\omega v_{ns} &= -ikU_o v_{ns} - ik \frac{\Delta u_o}{4} g(v_{(n+1)s} + v_{(n-1)s}) + \frac{1}{Re} \left[\frac{1}{r} \frac{\partial}{\partial r} \left(r \frac{\partial}{\partial r} \right) - \frac{n^2 M^2 + 1}{r^2} - k^2 \right] v_{ns} \\
&\quad - \frac{dp_{ns}}{dr} + \frac{2}{Re} \frac{nM}{r^2} w_{ns} + nM \frac{W_o}{r} v_{nv} + 2 \frac{W_o}{r} w_{nv} \\
-i\omega v_{nv} &= -ikU_o v_{nv} - ik \frac{\Delta u_o}{4} g(v_{(n+1)v} + v_{(n-1)v} T_n) + \frac{1}{Re} \left[\frac{1}{r} \frac{\partial}{\partial r} \left(r \frac{\partial}{\partial r} \right) - \frac{n^2 M^2 + 1}{r^2} - k^2 \right] v_{nv} \\
&\quad - \frac{dp_{nv}}{dr} - \frac{2}{Re} \frac{nM}{r^2} w_{nv} - nM \frac{W_o}{r} v_{nv} + 2 \frac{W_o}{r} w_{ns} \\
-i\omega v_{0v} &= -ikU_o v_{0v} - ik \frac{\Delta u_o}{4} g v_{1v} - \frac{dp_{0v}}{dr} + \frac{1}{Re} \left[\frac{1}{r} \frac{\partial}{\partial r} \left(r \frac{\partial}{\partial r} \right) - \frac{1}{r^2} - k^2 \right] v_{0v} + 2 \frac{W_o}{r} w_{0s}
\end{aligned} \tag{A.3}$$

$$\begin{aligned}
-i\omega w_{ns} &= -ikU_o w_{ns} - ik \frac{\Delta u_o}{4} g(w_{(n+1)s} + w_{(n-1)s} T_n) + \frac{1}{Re} \left[\frac{1}{r} \frac{\partial}{\partial r} \left(r \frac{\partial}{\partial r} \right) - \frac{n^2 M^2 + 1}{r^2} - k^2 \right] w_{ns} \\
&\quad - \frac{nM}{r} p_{ns} + \frac{2}{Re} \frac{nM}{r^2} v_{ns} - nM \frac{W_o}{r} w_{nv} - \left(\frac{dW_o}{dr} + \frac{W_o}{r} \right) v_{nv} \\
-i\omega w_{nv} &= -ikU_o w_{nv} - ik \frac{\Delta u_o}{4} g(w_{(n+1)v} + w_{(n-1)v}) + \frac{1}{Re} \left[\frac{1}{r} \frac{\partial}{\partial r} \left(r \frac{\partial}{\partial r} \right) - \frac{n^2 M^2 + 1}{r^2} - k^2 \right] w_{nv} \\
&\quad + \frac{nM}{r} p_{nv} - \frac{2}{Re} \frac{nM}{r^2} v_{nv} - nM \frac{W_o}{r} w_{ns} - \left(\frac{dW_o}{dr} + \frac{W_o}{r} \right) v_{ns} \\
-i\omega w_{0s} &= -ikU_o w_{0s} - ik \frac{\Delta u_o}{4} g w_{1s} + \frac{1}{Re} \left[\frac{1}{r} \frac{\partial}{\partial r} \left(r \frac{\partial}{\partial r} \right) - \frac{1}{r^2} - k^2 \right] w_{0s} - \left(\frac{dW_o}{dr} + \frac{W_o}{r} \right) v_{0v}
\end{aligned} \tag{A.4}$$

where $T_n = 2$ for $n = 1$ otherwise $T_n = 1$.

